Investigation of the cellular structures containing the autophagy-related proteins GABARAP and LC3B by single molecule localization microscopy

Inaugural dissertation

for the attainment of the title of doctor
in the Faculty of Mathematics and Natural Sciences
at the Heinrich Heine University Düsseldorf

presented by

Iman Abdollahzadeh
from Dashtestan, Iran

Jülich, February 2020

from the institute for Complex Systems (Structural Biochemistry, ICS-6 and Cellular Biophysics, ICS-4) at the Forschungszentrum Jülich GmbH

Published by permission of the
Faculty of Mathematics and Natural Sciences at
Heinrich Heine University Düsseldorf

Supervisor: Prof. Dieter Willbold
Co-supervisor: Prof. Christoph Fahlke

Date of the oral examination: 27/02/2020

Abstract

The study of GABARAP and LC3B proteins from the mammalian Atg8 protein family showed that single molecule localization microscopy (SMLM) is well suited to be used in autophagy research and provides new insight by size and shape determination of vesicular structures in the range of 50 nm to several µm. GABARAP and LC3B proteins were fused to EYFP and Dendra2 fluorescent proteins (FPs) and transiently or stably overexpressed in HEK-293 cell lines. First, SMLM imaging of EYFP-labelled proteins was optimized by elucidating the SMLM performance of EYFP dependent on the excitation wavelength. Excitation of EYFP molecules at 514 nm was found to be ideal since one detects more single molecule emission events with longer duration and higher signal-to-noise ratio when compared to the commonly used excitation at 488 nm. In addition, two-colour SMLM imaging with a pair of FPs commonly used in live cell fluorescence imaging (EYFP and mCherry) was established with the use of a new imaging buffer supporting the photoconversion of mCherry molecules without any negative effect on the single molecule imaging of EYFP molecules.

The vast majority of FP-GABARAP and FP-LC3B containing cytoplasmic structures detected with SMLM have sizes well below the diffraction limited resolution. It was found that size distributions were very similar for FP-GABARAP and FP-LC3B, independent of FP type or state of the cells (resting or autophagy-induced). It was proven, however, through shape determination that FP-LC3B molecules are dominantly located in asymmetric structures (elliptic or U-shaped in the 2D projection), while FP-GABARAP molecules are mostly part of structures with circular profile. FP-GABARAP and FP-LC3B, therefore, are located to a large extent to different cytoplasmic vesicular structures. This is a clear indication that GABARAP and LC3B play different roles in autopagosome biogenesis, which holds true if the overexpressed FP-GABARAP and FP-LC3B proteins mainly localize to autophagic structures.

Conventional fluorescence imaging detects only the largest and brightest FP-GABARAP and FP-LC3B containing structures. Very importantly, it was demonstrated that the shape classification of cytoplasmic structures in conventional fluorescence images determines the wrong category in > 50% of cases, as judged by the corresponding SMLM images.

Finally, with the analysis of the two-colour SMLM images featuring EYFP-GABARAP or EYFP-LC3B on the one hand and mCherry-LAMP1 on the other, it was shown that EYFP-GABARAP appears to have a higher degree of co-localization with late endosome/lysosome structures compared with EYFP-LC3B.

Abstrakt

Die Untersuchung von GABARAP- und LC3B-Proteinen aus der Atg8-Proteinfamilie von Säugetieren zeigte, dass die Einzelmolekül-Lokalisationsmikroskopie (SMLM) für die Autophagieforschung gut geeignet ist und neue Erkenntnisse über die Größen- und Formverteilung von Vesikelstrukturen im Bereich von 50 nm bis bis zu mehreren µm liefert. GABARAP- und LC3B-Proteine wurden an EYFP- und Dendra2-Fluoreszenzproteine (FPs) fusioniert und in HEK-293-Zelllinien transient oder stabil überexprimiert.

Zunächst wurde die SMLM-Bildgebung von EYFP-markierten Proteinen optimiert, indem die SMLM-Leistung von EYFP in Abhängigkeit von der Anregungswellenlänge untersucht wurde. Die Anregung von EYFP-Molekülen bei 514 nm erwies sich als ideal, da man im Vergleich zur üblicherweise verwendeten Anregung bei 488 nm mehr Einzelmolekül-Emissionsereignisse mit längerer Dauer und höherem Signal-Rausch-Verhältnis detektiert.

Zusätzlich wurde eine zweifarbige SMLM-Bildgebung mit einem Paar von FPs, die üblicherweise in der Fluoreszenzbildgebung von lebenden Zellen verwendet werden (EYFP und mCherry), unter Verwendung eines neuen Bildgebungspuffers etabliert, der die Photokonversion von mCherry-Molekülen unterstützt, ohne die Einzelmolekülbildgebung mit Hilfe von EYFP-Molekülen wesentlich zu beeinflussen. Die überwiegende Mehrheit der FP-GABARAP- und FP-LC3B-haltigen zytoplasmatischen Strukturen, die mit SMLM nachgewiesen wurden, weisen Größen auf, die deutlich unter der beugungsbegrenzten Auflösung liegen. Es wurde festgestellt, dass die Größenverteilungen für FP-GABARAP und FP-LC3B sehr ähnlich waren, unabhängig vom FP-Typ oder Zustand der Zellen (ruhend oder autophagieinduziert). Durch Formbestimmung konnte jedoch nachgewiesen werden, dass FP-LC3B-Moleküle überwiegend in asymmetrischen Strukturen lokalisiert sind (elliptisch oder U-förmig in der 2D-Projektion), während FP-GABARAP-Moleküle meist Teil von Strukturen mit kreisförmigem Profil sind. FP-GABARAP und FP-LC3B befinden sich daher zu einem großen Teil in unterschiedlichen zytoplasmatischen vesikulären Strukturen, die für die Autophagie relevant sind.

Die konventionelle Fluoreszenzbildgebung findet nur die größten und hellsten FP-GABARAP- und FP-LC3B-haltigen Strukturen. Es wurde gezeigt, dass die Formklassifizierung von zytoplasmatischen Strukturen in konventionellen Fluoreszenzbildern in > 50% der Fälle die falsche Kategorie bestimmt, wie anhand der entsprechenden SMLM-Bilder beurteilt wurde.

Schließlich haben wir bei der Analyse der zweifarbigen SMLM-Bilder mit EYFP-GABARAP oder EYFP-LC3B einerseits und mCherry-LAMP1 andererseits gezeigt, dass EYFP-GABARAP im Vergleich zu EYFP-LC3B einen höheren Grad an Kolokalisierung mit späten Endosom / Lysosom-Strukturen zu haben scheint.

Acknowledgement

At this point I would like to express my special thanks to the following people who helped and supported me during my PhD work. The very special thanks go to Dr. Thomas Gensch, my main supervisor, for his intensive scientific, technical and personal supports. Many thanks for the constructive discussions and novel ideas.

My special thanks go to Prof. Dr. Dieter Willbold, my doctor’s father, for his open discussion regarding the project, promoting the work and his personal and scientific supports. The same thank go to Prof. Dr. Christoph Fahlke for his kind supports and discussions about the project as well as facilitating using different microscopy techniques in different labs.

I also thank Dr. Oliver Weiergräber for his always new ideas, excellent scientific challenges, and giving motivations to continue performing new experiments. The same thank go to Dr. Silke Hoffmann for her excellent ideas, nice collaborations, and kindly facilitating a lot of technical and scientific materials.

I would particularly like to thank Dr. Johnny Hendriks, especially for his extensive motivations and technical supports regarding the super-resolution and programming materials. Similar thanks goes to Dr. Alexandra Boeske for her supports in providing different laboratory supports. I would also like to thank Julia Sanwald, Indra Simons and Jochen Dobner for their friendly behaviors and collaborations in the lab and also for providing materials for posters, presentations and articles preparations. Furthermore, I would like to thank Anita Eckert, Dorothea Stobbe, Tugba Özdal, Christoph Aretzweiler, Volker Söhnitz, Gabriel Stölting and all technical and scientific staff at ICS-4 and ICS-6 for good cooperation, helpful support and professional discussion.

I also thank my wife Najmeh for her enthusiastic support of my PhD project and for all personal and mental supports. Words cannot express the excellence of her supports though.

Finally, many nice appreciations go to my family even though they were all away from me, but their personal and mental supports had been always with me.

Table of Contents

List of Tables

List of Figures

1. Introduction

1.1.1. Macroautophagy

Autophagy is a regulatory process present in yeast, animal, and plant cells to degrade cellular components in an ordered fashion and prepare certain constitutions for recycling. Autophagy is a highly conserved catabolic process initiated with the help of core protein machinery in response to a variety of cellular stresses, which prevents cell damage and preserves cell integrity (Dikic 2018). One distinguishes three forms, namely macroautophagy (the topic of this thesis), microautophagy and chaperone-mediated autophagy. Autophagy promotes cellular endurance upon signals indicating energy or nutrient shortage and is also a cellular response to different pathogen infections (He 2009, Ravikumar 2010). The process aims at resupplying energy and essential molecular building blocks such as amino acids, nuecleotides, and fatty acids by breakdown of cargo, e.g. aggregated or misfolded proteins (such as extracellular amyloids, extracellular plaques, or protease-resistant prion proteins), damaged organelles, invading bacteria, to name but a few (Gatica, 2018).

Autophagy starts with the formation of a small, disk-like membranous structure, the so-called isolation membrane (or phagophore) in close proximity to the cargo at a locus which is named phagophore assembly site (PAS) (Nakatagowa 2009, Hurley 2017). The phagophore elongates around the cargo aiming at completely isolating the cargo from the cytosol. Once the growing membrane extremities encounter each other, the fully grown structure closes itself and is then called autophagosome. With the help of motor and other proteins autophagosomes are directed along the cytoskeleton, towards lysosomes, where the isolated cargo is delivered to its final destination (Nakatagowa 2009, Hurley 2017). This stage begins with the fusion of the outer membrane of the autophagosome with the lysosomal membrane, while the inner membrane keeps the cargo (Rubinsztein 2011, Nguyen 2017). The acidic hydrolases present in lysosomes first destroy the former inner autophagosomal membrane and complete the degradation of the cargo molecules, followed by delivery of the resulting low molecular mass compounds to the cytosol of the cell (Nakatagowa 2009, Mauvezin 2015). In figure 1.1 a simplified model of the entire autophagy process is represented.

Autophagosome formation is the hallmark of autophagy. Genetic screening in yeast revealed the involvement of more than 40 proteins (Nakatagowa 2009), which often function in the context of large complexes and have been named autophagy-related (Atg) proteins. Lack of essential Atg proteins will result in impairment or failure of autophagosome formation and therefore in the collapse of the whole autophagy process (Mauthe 2016).

Most of the Atg proteins discovered in yeast are preserved in mammalian cells, but often several different homologues correspond to a single member in yeast (Koyama-Honda 2013).

To give a picture of the involvement of Atg proteins, the contributions of various members from isolation membrane formation until degradation are described below. Note that the explanation is written using the terminology of Atg proteins in yeast, which can be transferred to mammalian cells by introducing the respective homologous mammalian proteins.

Different studies showed that the Atg1 protein kinase (resembling Atg1 in yeast) and the phosphatidylinositol 3-kinase Vps34 are the key regulators for the onset of autophagy (Young 2006, Backer 2008, Hara 2008, Chan 2009). Mammalian cells have two homologues of Atg1, ULK1 and ULK2 (Jan 1999). The activation of Atg1 is governed by a protein complex named target of rapamycin complex 1 (TORC1) and the AMP-activated protein kinase sucrose non-fermenting 1 complex (Snf1) (corresponding to AMPK in mammalian cells), which are the nutrient and energy sensitive kinases, respectively (Ganley 2009, Hosokawa 2009, Jung 2009, Kim 2011, Egan 2011, Russel 2013). Atg1 initiates the transfer of Vps34 to the phagophore and thereby plays an important role in recruitment of other Atg proteins and protein complexes such as Atg8 and Atg5-Atg12 supporting autophagosome growth. To date, it is not yet fully understood how these proteins and their interactions are regulated, by amino-acid starvation which is fully mediated by TORC1.

Another core regulatory machinery in autophagy, which is governed by Atg proteins, depends on Atg2 and Atg18. The Atg2-Atg18 complex localizes to the PAS upon association with phosphatidylinositol-3-phosphate (PI3P), which is produced by the Atg14-containing Vps34 (Suzuki 2007, Obara 2008, Rieter 2012). Atg18 binds to PI3P, a process required for the localization of this protein to PAS, endosomes, and vacuoles (Dove 2004, Efe 2007). The localization of Atg18 also depends on the presence of Atg2 (and vice versa). Yet the interaction of Atg18 with Atg2 is independent of the interaction of Atg18 with PI3P. In the absence of the Atg2-Atg18 complex, the isolation membrane is not formed (Suzuki 2007). Different studies have shown that the Atg2-Atg18 complex localizes to the rims of the isolation membrane, while it is found in the vicinity of sites for vesicle formation in the endoplasmic reticulum (ER) (Graef 2013, Suzuki 2013). It is proposed that the Atg2-Atg18 complex functions as a mediator between PAS and ER and in this way contributes to formation and expansion of the phagophore (Kotani 2018).

Atg9 is another key protein in autophagosome biogenesis. Atg9 binds in a cooperative manner to Atg1 complex, PI3K, and Atg2-Atg18 protein complex (Papinski 2016). Atg9 controls autophagosome growth by mediating the movement of vesicles between PAS and ER or Golgi apparatus. Atg9 is the only known transmembrane protein among the core Atg proteins required for autophagosome formation (Noda 2000) and localizes to the PAS depending on Atg17, which is a member of the Atg1 complex, upon starvation (Sekito 2009). In mammalian cells, the Atg9 homolog ATG9A localizes to phagophores, the *trans*-Golgi network, and endosomes (Young 2006). Atg9 containing vesicles are lipid carriers and bud off Golgi (apparatus) membranes to deliver lipids necessary for the isolation membrane. It was shown that Atg9 activity in autophagy is limited to the initial steps of autophagosome biogenesis, and upon elongation of the phagophore around the cargo, the constant recruitment of Atg9 proteins is gradually disappearing (Mizushima 2011), which leads to lesser and lesser localization of Atg9 to PAS. Only a few Atg9 decorated small vesicles (typical diameter: 30 nm (Yamamoto 2012)) are needed to interact and form the initial PAS, while the bulk source of lipids or membranes, particularly during the elongation and closure phases, has remained ambiguous. In fact, depending on cell type and experimental conditions, most endomembrane compartments as well as the plasma membrane have been found to contribute.

Following the role of other Atg proteins in autophagy, one should briefly explain ubiquitination. Ubiquitin is a small protein that is connected by the cell to certain cellular structure in order to mark them for degradation. Ubiquitination requires three types of enzymes: ubiquitin-activating enzymes, ubiquitin-conjugating enzymes, and ubiquitin ligases, known as E1, E2, and E3, respectively. Ubiquitin is activated in a two-step reaction by ATP dependent E1. The initial step involves production of an ubiquitin-adenylate intermediate.

E1 binds both ATP and ubiquitin and catalyzes the acyl-adenylation of the C-terminus of the ubiquitin molecule. The second step transfers ubiquitin to an active site cysteine residue of E1 accompanied by release of AMP. This step results in a thioester linkage between the C-terminal carboxyl group of ubiquitin and E1. During conjugation, E2 catalyzes the transfer of ubiquitin from E1 to the active site cysteine of E2 via a transthioesterification reaction. In order to perform this reaction, E2 binds to both activated ubiquitin and E1 enzyme. E3 mediates the final step of the ubiquitination cascade namely the formation of an isopeptide bond between a lysine of the target protein and the C-terminal glycine of ubiquitin (Buetow 2016).

Atg12 is one of the ubiquitin-like proteins involved in autophagosome biogenesis. It is covalently linked to Atg5 by the enzymatic action of E1-like protein Atg7 and E2-like protein Atg10 (Mizushima 1998). The Atg12-Atg5 conjugate forms a stable complex with Atg16 (Mizushima 1999) and has critical roles in autophagosome maturation and stability. It has been also clarified that efficient Atg8 lipidation (see next section) requires the presence of the Atg12-Atg5 conjugate (Fujioka 2007, Hanada 2007) as well as Atg16 (Fujita 2008). These observations indicate that the Atg12-Atg5-Atg16 complex functions as an E3-like enzyme to facilitate the lipidation of Atg8, presumably in a two-step process. One is the activation of the conjugating activity of Atg3 by the Atg12-Atg5 conjugate. The second is the targeting of Atg3 to the proper membrane surface containing lipid molecules for conjugation with Atg8 involving also Atg16 (Noda 2013).

Finally, another key protein in autophagy is Atg8, which again is a ubiquitin-like protein. The most well-known function of Atg8 proteins in autophagy is the recruitment of cargo molecules to be degraded in the emerging autophagosome. Atg8 is believed to mediate several crucial steps all the way in autophagosome biogenesis. A prerequisite for Atg8 function in autophagy is its attachment to the growing phagophore by lipidation to lipid phosphatidylethanolamine (PE), which is a requirement for the ability of Atg8 to connect the cargo with the phagophore. One of the major roles of Atg8 is specific targeting of the cargo molecules and hence, engulfment of the cargo. Another role is mediating the expansion of the phagophore by associating it with other Atg proteins. A third function is its involvement in autophagosome-lysosome fusion (Ichimura 2000, Tanida 2003).

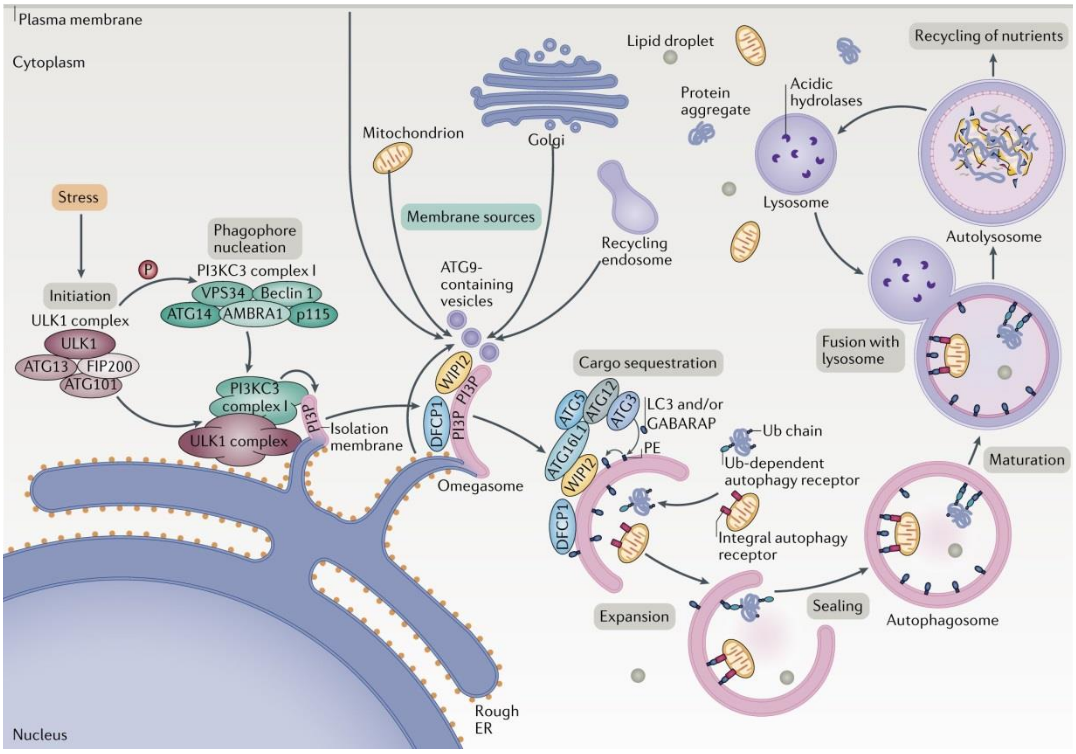

Figure 1.1. The core autophagy machinery proteins and protein complexes that are recruited for engulfment of cargo molecules. Upon stress induction, the ULK complex and PI3KC3 complex cooperatively regulate formation of the isolation membrane. Atg9 containing vesicles move between PAS and Golgi apparatus in order to provide the initial lipid molecules for this structure. Atg8, Atg5, Atg12, and Atg16 are involved in phagophore expansion. Atg8 also plays a major role in cargo sequestration and delivery. Once the growing phagophore is sealed (yielding an autophagosome), it interacts with the cytoskeleton to encounter lysosomes for degradation of the cargo (Dikic, 2018). With publisher permission.

1.1.2. Atg8

Autophagy-related 8 proteins (Atg8s) are one of the most conserved eukaryote-specific protein families (Wood 2002). In the yeast *Saccharomyces cerevisiae* and other fungal species only one Atg8 protein, exists while in mammalian cells two subfamilies have been described, featuring microtubule-associated protein 1 light chain 3 (MAP1LC3, hereafter referred to as LC3) and γ-aminobutyric acid type A receptor-associated protein (GABARAP) proteins, respectively. Proteins of the Atg8 family were among the first components of the core autophagy machinery to be characterized at molecular scale (Sugawara 2004). They are small globular molecules of about 120 amino acid residues containing an ubiquitin-like core (a so-called β-grasp fold) extended by an N-terminal helical domain (Weiergräber 2012). Atg8 family proteins associate with autophagic membranes at all stages of the process. Therefore, Atg8 proteins are often used as markers for visualization of these structures (Abdollahzadeh 2017).

Similar to other ubiquitin-like modifiers, Atg8 family proteins are synthesized as precursors with additional amino acids at their C-termini. In autophagy, Atg8 is proteolytically cleaved by the cysteine protease Atg4, yielding a truncated form (Atg8-I) with a terminal glycine residue. Atg8 proteins are covalently attached to the phospholipid phosphatidylethanolamine (PE) after processing by two proteins, the E1-like Atg7 and the E2-like Atg3 (Ichimura 2000, Tanida 2003), resulting in Atg8-phospholipid conjugates (Atg8-II) that are anchored to the phagophore membrane by its lipid part. After completion of autophagosome formation but before fusion of the autophagosome with lysosomes, the outer membrane Atg8 molecules are delipidated by the action of Atg4 (Kirisako 2000, Kabeya 2004).

The lipidation of Atg8 is tightly regulated by the Atg12-Atg5-Atg16 complex in an E3-like fashion by promoting transfer of Atg8 from Atg3 to PE (Hanada 2007, Fujita 2008). This complex has been found to associate mostly with the convex surface of the isolation membrane (later to be the outer autophagosome membrane), implicating that Atg8 lipidation occurs at this site (Mizushima 2001).

It is believed that Atg8 family proteins are among the major regulatory proteins in autophagy and function at different stages of autophagosome biogenesis, such as elongation, maturation, sealing, cytoskeleton-associated transport, to name a few (Michaeli 2016, Johansen 2019). To shed more light on the mechanisms by which Atg8s play their roles in autophagy, several aspects of this protein family are discussed in more detail below.

1.1.3. Atg8 lipidation

Atg8 proteins are covalently but reversibly bound to PE present in autophagic membranes, enabling the physical attachment of the cargo to the phagophore. This reaction is accomplished via an ubiquitin-like conjugation system (Ichimura 2000) as described above. The final result is the physical anchoring of Atg8 proteins to the membrane of the growing phagophore. Membrane attachment plays a crucial role for many of the biological functions of Atg8 family proteins, such as sequestration of substrates via cargo receptors, or recruitment of components of the autophagy machinery. The amount of membrane attachment is regulated by the lipidation efficiency of Atg8. Experiments *in vitro* suggest that the lipidation reaction is membrane curvature dependent, being most effective at high curvature (Knorr 2012). The shape of the phagophore, a cup-shaped double-bilayer membrane structure with several tens of nanometers of intermembrane space (Nguyen 2016), implies bending of the membrane with moderate curvatures on the convex (outer) and concave (inner) surfaces and with very high curvature at the growing phagophore ends. Atg8-PE tends to be enriched in highly curved regions of the bilayer; furthermore, it is now believed that the curvature sensitivity of Atg8 conjugation *in vitro* may be largely influenced by Atg3, which senses the local curvature via its N-terminal amphipathic helix (Dancourt 2014). Specifically, packing defects of the lipid bilayer that exist in highly curved areas are thought to allow insertion of hydrophobic residues of the N-terminal helix of Atg3 into the membrane interior. On the other hand, despite the sensory role of Atg3, efficient Atg8 lipidation *in vivo* requires the presence of the Atg12-Atg5 complex as well. The Atg12-Atg5 entity is associated with Atg16 to act as an E3-like component (Hanada 2007, Fujita 2008) and facilitates the formation of Atg8-PE by increasing the catalytic activity of Atg3 (Sakoh-Nakatogawa 2013). Atg12-Atg5-Atg16 can be detected only on the outer face (convex face) of the growing phagophore and appears to be recycled with the majority of Atg8 on the outer membrane at the time of phagophore closure (Mizushima 2001). On the contrary, the Atg8 proteins associated with the concave surface of the phagophore, which have a role in cargo recruitment, remain after fusion, thus are degraded (Xie 2008). The structural and functional asymmetry between the two surfaces of the phagophore, connected with different protein interactions, leads to the following model of curvature dependence of Atg8 lipidation efficiency. A membrane sheet (resembling the phagophore at early stages) converts to a curved vesicular shape after reaching a critical size, which depends on the molecular composition of the lipid bilayer on the different faces of the structure (Knorr 2012). It is therefore conceivable that an asymmetry between the numbers of Atg8 molecules on the inner and outer membranes may determine the bending of an expanding phagophore. The role of Atg8 proteins in shaping the phagophore membrane is in agreement with results of a study evaluating the bending energy of lipid bilayers as a function of their curvature (Knorr 2012). Ultimately, cells may regulate autophagosome size by changing, e.g., the rate or spatial distribution of Atg8 conjugation or the availability of partners involved in scaffolds on either surface of the growing phagophore (Xie 2008, Knorr 2012).

1.1.4. Autophagosome rigidity

Autophagosomes are large double bilayer membrane structures with sizes in the range of several tens of nanometers to up 1.5 µm, evolving from a small phagophore to a mature entity that might serve to engulf mitochondria or entire bacteria for example (Bauckman 2015, Yamashita 2016). Autophagosomes may benefit from an enhanced rigidity in order to function properly. As outlined above, Atg12-Atg5 is known to facilitate the efficiency of Atg8 lipidation. Interestingly, Atg12-Atg5 complexes themselves are recruited to autophagosomes by Atg8-PE and in the presence of Atg16, Atg8-PE-Atg12-Atg5 complexes are organized into a two-dimensional mesh-like network of proteins on the membrane, which has been proposed to stabilize the shape of the phagophore (Kaufmann 2014). This scaffold not only plays a role in delivering rigidity, but Atg12-Atg5-Atg16 complexes may also be recruited by Atg8-PE to regulate the efficiency of further lipidation. Atg12-Atg5 and Atg12-Atg5-Atg16 complexes promote Atg8 lipidation by the direct interaction of Atg12 with Atg3. The Atg12-Atg5-Atg16 complex is bound to the phagophore membrane; therefore, it is more efficient than the Atg12-Atg5 conjugate in the recruitment of Atg3 for further increasing Atg8 lipidation. Thus, Atg3-bound Atg8 can be more efficiently brought to the membrane by the Atg12-Atg5-Atg16 complex compared with the Atg12-Atg5 conjugate (Walczak 2013).

1.1.5. Selective autophagy

There are two distinct types of autophagy in cells. One is a global, non-selective autophagy, where upon starvation or stress induction, cells use bulk cytoplasmic components to replenish the necessary sources of energy. The other one is selective autophagy where the cargo is a defined entity such as mitochondria, large aggregates of misfolded proteins, or invading pathogens. It has been previously shown that for damaged mitochondria as cargo (i.e. mitophagy), the Atg8 protein is responsible for selectivity of cargo recruitment, hence preventing the engulfment of other cytosolic material. The involvement of Atg8 molecules in selective autophagy takes place at the concave surface of membrane of the growing phagophore. Selectivity in autophagy is mediated by tethering the cargo to a growing phagophore through the specific interaction of cargo receptor proteins and Atg8. Although several cargo receptors bind to their targets directly, the most common way involves ubiquitination. In mammalian cells ubiquitin chains (polyubiquitination) often mark cellular structures for degradation. Cargo receptors recognize and interact with these ubiquitin chains and hence decorate the cargo in selective autophagy (Grumati 2017). Recently a similar binding motif (GABARAP interacting motif (GIM)) has been identified in the GABARAPs (Wirth 2019). At the same time, they bind to Atg8 family proteins via a conserved LC3-interacting region (LIR) motif, also known as Atg8-interacting motif (AIM) (Pankiv 2007, Ichimura 2008). The 22-amino acid long LIR is an acidic peptide sequence containing three glutamate and four aspartate residues. There are acidic residues such as glutamic and aspartic acids both in the N and C-terminal half of LIR. The presence of negatively charged residues in the proximity of the core LIR sequence has been shown to contribute essentially to the binding to Atg8 family proteins (Pankiv 2007, Ichimura 2008, Wild 2011, Rogov 2013, Rogov 2013). Generally, the Atg8 family proteins decorating the concave surface of the phagophore are avidly bound by the cargo receptors, enabling the autophagosomal membrane to wrap the cargo in tight apposition and thereby exclude non-cargo material from degradation.

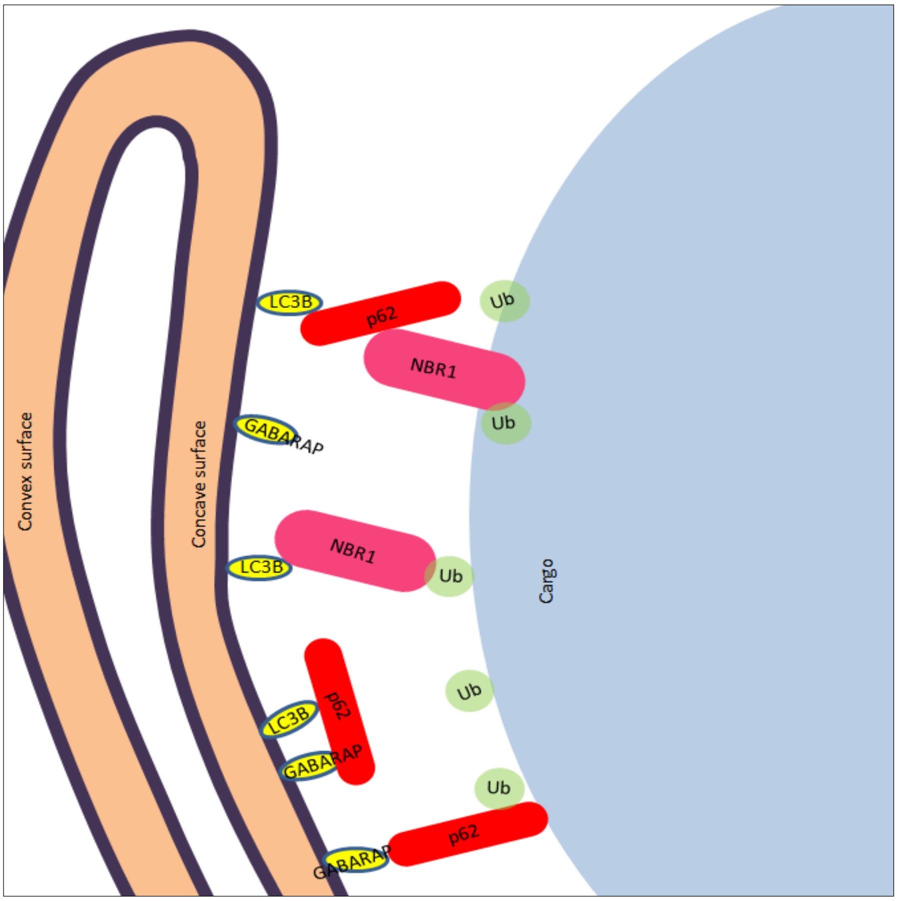

Figure 1.2. The direct involvement of Atg8 (GABARAP and LC3) proteins in selective autophagy. Atg8 proteins on the inner membrane of growing phagophore are attached specifically to cargo receptor molecules (e.g. p62 and NBR1). There are several Atg8 binding sites on a cargo receptor molecule, making it possible that the

growing phagophore engulfs cargo tightly in order to minimize non-specific engulfment of components from cytoplasm.

1.1.6. Interaction of Atg8 with the cytoskeleton

The growing, closure, and trafficking of autophagosomes depend on the activities of several cytoskeletal components such as actin filaments and microtubules (Biskou 2019). The autophagosome interaction with cytoskeleton components in yeast has not been fully explained yet and here it has been focused on findings from autophagy induced in mammalian cells. Matured autophagosomes detach from the ER and are transported by motor proteins using both actin- and microtubule-based mechanisms. Interactions with the cytoskeleton not only occur after closure of the autophagosome, but from the beginning of phagophore formation at the PAS, when many proteins are delivered to the site through actin networks in close proximity of the ER. Autophagosomes are formed throughout the cytoplasm, but the majority of lysosomes are present in the perinuclear region. Thus, autophagosomes need to be transported through the cytoplasm via the cytoskeleton network to fuse with lysosomes. The mature autophagosome connects to the microtubule network by association of dynein, dynactin and kinesin proteins, which are a family of cytoskeletal motor proteins moving along microtubules and thereby dragging connected cellular structures (here autophagosomes). Autophagosome movements are mediated towards the peripheral region (plus end) by connection to microtubules upon attachment to kinesin and towards the perinuclear region (minus end), where lysosomes are populated, by connection to microtubules upon attachment to dynein-dynactin. The link between autophagosome and kinesin is via interaction of Atg8 molecules with FYVE (FYVE: Fab 1, YOTB, Vac 1, and EEA1) and coiled-coil domain-containing 1(FYCO1) protein. FYCO1 proteins are recruited to autophagosomes by Rab7 GTPase molecules. The link between autophagosome and dynein-dynactin is via interaction of RILP and ORP1L. Time-lapse measurements of autophagosome movement showed a strong decrease in the velocity of motion upon injection of anti-LC3 antibody that binds specifically to LC3 molecules (Kimura 2008), which might explain the recruitment of Atg8s to the convex surface and their importance for dynein-dynactin based microtubule-autophagosme connections. On the other hand, it was shown that the low level of cholesterol (which induces autophagy and increases the Atg8s level) prevents dynactin recruitment and, hence, blocks the minus-end transport (Kimura 2008). Therefore, the role of Atg8 protein family in autophagosome-cytoskeleton interaction is not fully understood yet. Apart from the microtubule-driven transport, autophagosomes encounter lysosomes through actin filaments, which are regulated via lipids such as phosphoinositides (PIs). Upon starvation, a series of phosphorylation events turn PIs into different variants and as a result activate actin-associated proteins, which lead to the interaction of autophagosomes and actin filaments (Nakamura 2017, Xu 2013, Kast 2017).

1.2. GABARAP and LC3 subfamilies behave differently in autophagosome biogenesis

Atg8 family proteins in mammalian cells divided into two main subfamilies. They are either the GABAtype(A)receptor-associated protein (GABARAP) or the microtubule associated protein 1 light chain 3 (MAP1LC3, hereafter LC3) subfamily. The members of GABARAP subfamily are GABARAP, GABARAP-like 1 (GABARAP-L1), and GABARAP-like 2 (GABARAP-L2). The two GABARAP-L1 and GABARAP-L2 are often called glandular epithelial cell 1 (GEC1) and Golgi-associated ATPase Enhancer of 16 kDa (GATE-16), respectively. The LC3 subfamily includes three members LC3A, LC3B, and LC3C. All three members of LC3 subfamily are often used as the markers for autophagy (Schaaf 2016), but recently it has been demonstrated that their distribution in cell nucleus and cytoplasm is different, which might be a result of their distinct functionalities (Koukourakis 2015). Most of the findings related to the role of Atg8s in mammalian cells have been assigned to the use of LC3 molecules but it was shown that GABARAP also contributes to the autophagosome biogenesis in several critical stages (Nair 2012).

For the first time, the different functionality of GABARAP and LC3 subfamilies was linked to their different duties in various stages of the autophagosome growth. While the contribution of GABARAP subfamily in autophagy (as presented with GABARAP-L2) was principally linked to the late stages (such as closure, maturation, and transportation), the LC3 subfamily is believed to be assigned to the initiation of autophagosome formation such as nucleation, elongation, and growth (Weidberg 2010). Most specifically, the overexpression of GABARAP-L2 and knock down of LC3 molecules in HeLa cells led to the formation of larger round-shaped autophagosomal structures, while the overexpression of LC3 and knock down of GABARAP-L2 showed higher number of small elongated-shapes autophagosomes. Besides that, findings *in vitro* with the use of large unilamellar vesicles (LUVs) forming from GABARAP-PE-induced lipid mixing and from LC3-PE-induced lipid mixing, revealed that in the former system, there is a clear tendency for the formation of lager and roundish vesicles, while the latter represented nearly small and elongated shaped vesicles (Landajuela 2016).

1.3. Fluorescence from basics to super-resolution microscopy

1.3.1. Fluorescence microscopy

Fluorescence spectroscopy has been rapidly evolved over the past decades to become a major technique in various scientific fields including life science. The application of fluorescence spectroscopy is not only interesting for biochemistry and biophysics but also in biology, biotechnology, flow cytometry, macromolecular structural biology, and genome sequencing (Lacowicz 2006). The sensitivity and specificity of fluorescence spectroscopy detection increased primarily by scientific needs but based on the advancement in sophisticated electronic devices for detection, excitation sources (e.g. lasers), and developments in fast computerized algorithms (Nehme 2018). In general, detectors with small readout noise and therefore high signal-to-noise ratio (SNR) such as monochrome CCD cameras or detectors with moderately high readout noise but compensated by additional signal gain (such as in intensified CCDs or EMCCDs) are very well popularized for using in fluorescence spectroscopy. While CCD detectors are mainly used in widefield fluorescence microscopy methods, the introduction of single-photon-counting avalanche diode (SPAD) for single molecule detection significantly improved the detection efficiency in the visible range and replaced high-voltage, bulky photomultipliers by more compact and simpler devices, permitting a rapid development of the field (Michalet 2012).

There are three families of light sources used for fluorescence spectroscopy. First are broadband sources such as the mercury-arc and tungsten-halogen lamps. Second are the laser excitation sources, which offer one or a few well-defined spectrally narrow emissions (less than 1 nm), allowing selective illumination. Third are the more recently developed, high-output light-emitting diodes, (LED), which have gained popularity due to their selective wavelengths (usually 10-20 nm FWHM), low cost and energy consumption, and long lifetime (Claßen 2019). Before the invention and usage of lasers and LEDs, as the excitation sources that are used nowadays in fluorescence spectroscopy, a gas arc lamp with inherently weak emission and broadened spectra, or spectral filtering of broader and brighter lamps such as the xenon arc lamp by monochromators was the dominant source of excitation. Lasers, in contrast, have intrinsic reduced linewidths and high focused power density.

One of the first observations of fluorescence was made by Stokes in the 19th century. He observed that the mineral fluorspar emits blue light when being irradiated with ultraviolet light and proposed the term fluorescence (Stokes 1852). Moreover, he discovered that the wavelength of the fluorescence light is red-shifted compared to the excitation light, which has been termed Stokes shift (Lavis 2008, Li 2013, Lavis 2014). This is an important fundamental property of fluorescence light which allows separating excitation and emission wavelengths easily using appropriate dichroic beam splitters and optical bandpass, long pass or short pass filters. Nowadays, fluorescence spectroscopy is one of the methods to investigate biological samples in a non-invasive (apart from photo bleaching or photo induced processes at high illumination powers) fashion. Not to mention that almost every protein or nucleic acid can be labeled fluorescently and finally visualized even in living specimen.

Over the years of breakthroughs in optics, material sciences, biology, and laser development, scientists established very well described theories and observations in the field of fluorescence spectroscopy which allowed the development of sophisticated fluorescence microscopy types, all based on techniques previously introduced and verified in spectroscopy studies. At the same time the palette of labels was extended to natural minerals, a great number of organic fluorescent dyes, fluorescent proteins, and semiconductor nanocrystals for probing a plethora of biological, chemical, or biophysical entities.

1.3.2. Absorption and Emission of Light

Light can be described as an electromagnetic wave that interacts with materials consisting of atoms and molecules to elevate their electrons from stable ground states to transient excited states. In that case one speaks of the light energy is absorbed by the matter. The energy of the light is treated as quantized (photon) and is given by Planck's relation

$$E = h\upsilon = \frac{hc}{\lambda} \qquad (1.1)$$

where υ, λ, and c are frequency, wavelength, and velocity (in vacuum) of the light, respectively, and *h* is Planck's constant. For single atoms the total energy is only determined by electronic states which results in discrete line spectra. For molecules (like organic fluorophores), on the other hand, the excitation of molecules involves not only electronic states but also rotational and vibrational states, the latter arising from the quantized angular momentum of the molecule and vibrational motion of its atoms. Thus in general, the excited molecule can enter a multitude of excited states. The energy needed for an electron to be excited from the ground state S_0 to the first excited state S_1, is formulated as

$$\Delta E = E_{S1} - E_{S0} = \frac{hc}{\lambda} \tag{1.2}$$

where λ is the wavelength of the absorbed photon. The required energy for electronic transitions is in the range of 1-5 eV, for vibrational states is 0.1-0.4 eV, and for rotational states only 10^{-3} eV. The latter are therefore occupied equally at room temperature ($E = k_B T$ = 0.025 eV, where k_B is the Boltzmann constant and T is the temperature). On the other hand, energetically higher electronical states have a very low probability to be occupied at room temperature according to Boltzmann-statistics:

$$\frac{N_{S1}}{N_{S2}} = e^{-\Delta E / k_B T} \tag{1.3}$$

N_{S1} and N_{S0} stand for the number of molecules occupying the excited state and the ground state, respectively, k_B is the Boltzmann constant, and T is the temperature.

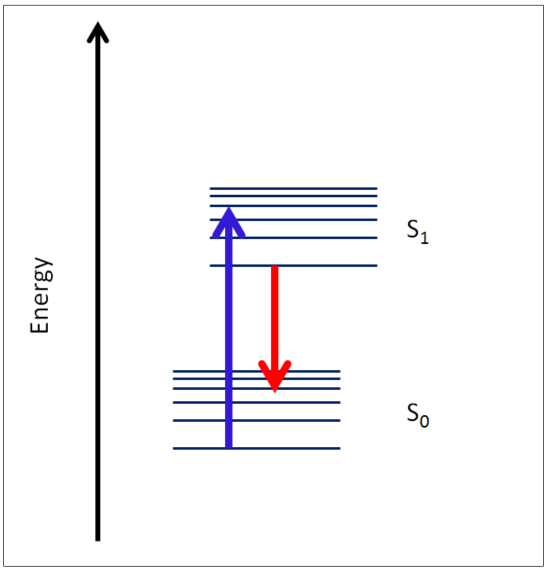

Figure 1.3. Principle of electronic transitions. Light absorption occurs on a timescale of 10^{-15} s and the electronic transition takes place vertically into a higher vibrational and rotational level of the excited state S_1 with no movement of atoms. Next, relaxation to the lowest vibrational level of S_1 takes place prior fluorescence and relaxation into a higher vibrational and rotational level of the ground state S_0 occurs.

Absorption of light is often described by treating the absorbing molecule as an electric dipole, where the electron transition of the dipole moment must oscillate at the frequency equal to the frequency υ of the illuminating photon in order for a successful excitation event. If the charge distribution in ground state S_0 is described by ψ_0 and in the first excited state by ψ_1, then the transition dipole moment μ can be described by

$$\mu = \langle \psi 1 | \hat{\mu} | \psi 0 \rangle \tag{1.4}$$

where $\hat{\mu}$ is the dipole moment operator.

1.3.3. Emission of Light

A molecule that upon absorption of light emits a photon with red-shifted wavelength with a sizable probability (quantum yield > 0.1) is called fluorophore. The probability of a transition caused by a photon is proportional to $|\mu|^2$ and increases with the dipole character of the fluorophore's S_0 to S_1 transition. Excitation is only possible if $\mu \neq 0$ (Atkins 2006).

After an electron is elevated from the lowest vibrational state of the ground state into an excited state, a higher vibrational state is occupied (see figures 1.3 and 1.4). Next, vibrational relaxation will occur to the lowest vibrational level of S_1 followed again by a transition into a higher vibrational level of S_0, which can occur by emission of a fluorescence photon.

In general, an excited fluorophore can relax in different ways to the ground state. This recombination can be radiation-less but with the release of heat or can be accompanied by emission of a photon. A detailed view of all processes of recombination is displayed in an energetic scheme, called Jablonski diagram (figure 1.4).

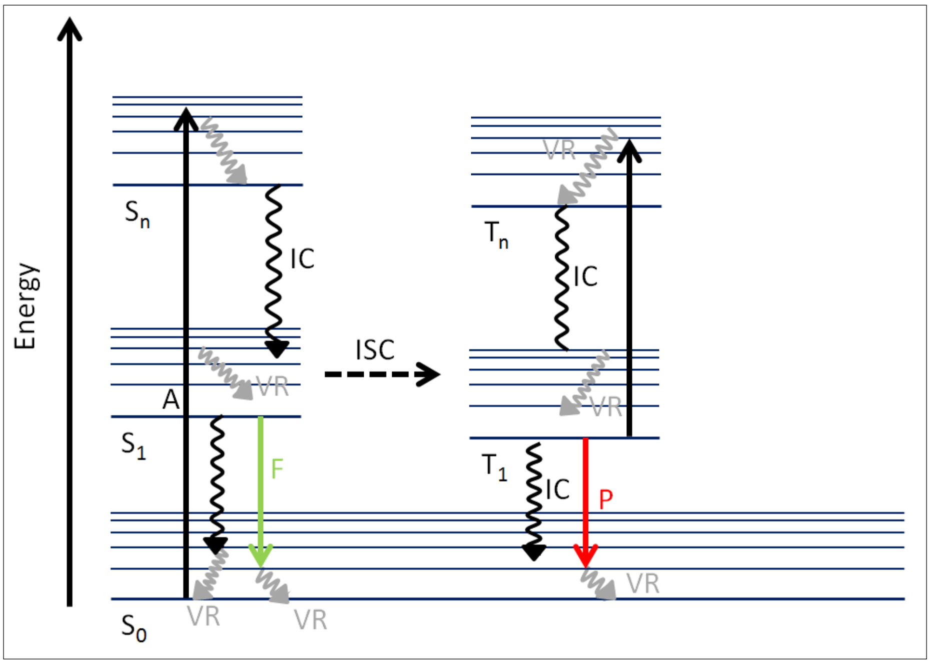

Figure 1.4. Jablonski-diagram: S0/1/n = Singlet ground / first / nth excited state, T = triplet state; absorption (black), IC = internal conversion, VR = vibrational relaxation, ISC = intersystem crossing, A = excitation, F = fluorescence, P = phosphorescence (modified from “Sebastian Van De Linde PhD thesis”, Bielefeld University, Department of physics, 2011).

By absorption of a photon a fluorophore will be excited from the ground state to one of the many vibrational state of a higher electronic state. Most often, fluorophores relax to the lowest state of S_1 by internal conversion (IC) and vibrational relaxation (VR; radiation-less transition between vibrational states within one electronic state) within 1 ps. From the lowest level of the S_1 state there are, in the simplest case, two relaxation pathways to the lowest level of S_0 state possible. The more general one consists of IC and VR, the fluorophore specific pathway includes the emission of a photon followed by VR. VR is caused as the random collisions of the fluorophore with neighboring molecules. As follows obviously from figure 1.4, a fraction of the excitation energy is dissipated as heat because of IC or VR processes; therefore, the wavelength of fluorescence is red-shifted, as described already by Stokes (Stokes-Shift). The fluorescence spectrum of fluorophores usually is a mirror-image of the absorbance spectrum. The reason for this phenomenon relies on similar IC and VR probabilities of electronic transitions in vibrational states for both, absorption and emission. All processes are completed before fluorescence photon emission occurs. This is because the internal conversion occurs on timescales 10^{-12} s versus 10^{-9}-10^{-8} s for emission. Other possible pathways for depopulation of the S_1 state can occur by a deactivation channel termed intersystem crossing (ISC). If intersystem crossing occurs, the spin of the electron in the highest occupied molecular orbital (HOMO) is orientated parallel to the unpaired electron in the lowest unoccupied molecular orbital (LUMO). Therefore, multiplicity changes from 1 to 3. Intersystem crossing is a transition into the triplet state (T_1) which occurs with low probability.

Once the excited electron populates the first triplet state T_1, similar processes for further relaxations can occur as in the singlet excited state. If the electron is at higher vibrational or rotational levels in T_1 ($T_1(1)$), it first relaxes to $T_1(0)$ via VR. The depopulation of the triplet state T_1 to the ground state S_0 again is accompanied by spin conversion (another ISC), which is a forbidden transition and thus results in a longer triplet lifetime, ranging from microseconds to seconds. The long lifetime of the triplet state of fluorophores is the basis for reactions with the environment of a fluorophore, for instance with redox reaction to generate long-lived metastable dark states that is extensively utilized in a novel class of fluorescence microscopy named Single Molecule Localization Microscopy which will be described in later sections. Under constant or repetitive illumination (as in fluorescence microscopy), the probability of transition from T_1 to T_n is not zero due to the long T_1 lifetime and the electron may be excited to higher excited triplet states T_n which often are very reactive leading to irreversible photoproducts (and irreversible photo bleaching. From T_n the electron can also relax back to $T_1(0)$ via internal conversion and vibrational relaxation. From $T_1(0)$, the energy can be either released without irradiation, in a second ISC process, or by emission of a photon, a process termed phosphorescence.

As described above, an excited fluorophore can either relax via emission of fluorescence or in radiation less processes (IC and ISC). A parameter describing the efficiency of the fluorescence emission is the fluorescence quantum yield ϕ, which is the ratio of photons emitted by fluorescence to photons absorbed by the fluorophore. It can be described by two depopulation rates of S_1 to S_0, which are k_r and K_{nr} (non-radiative relaxation):

$$\phi = \frac{k_r}{k_r + k_{nr}} \tag{1.5}$$

k_{nr} is the sum of the rate constants of all non-radiative depopulation processes, that is internal conversion, intersystem crossing and other quenching phenomena and k_r is the radiative rate constant (Lakowicz, 2006). Fluorophores with a quantum yield close to unity exhibit very efficient pathways for photon emission, whereas in fluorophores with low ϕ, non-radiative depopulation dominate.

1.3.4. Quenching of Fluorescence

An excited fluorophore can interact with the adjacent molecules in different ways. If the interaction leads to enhanced non-radiative relaxation of the fluorophore, it is called fluorescence quenching. Molecules in the vicinity of fluorophores that act in this way of a fluorophore are called quenchers.

There are several techniques taking advantage of the presence of quenchers in the neighborhood of the actual fluorophores. One of the most important methods is collisional quenching. The quencher diffuses to the fluorophore during the lifetime of the excited state and upon contact, the fluorophore returns to the ground state, without emission of a photon. This approach is used for the detection of the presence of specific quencher molecules (e.g. Trpyptophan-[Cl^-] (MQAE)). In general, quenching occurs without any permanent change in the molecules, that is, without a photochemical reaction (Lakowicz 2006). Another method of taking advantage of quenchers is energy transfer. In energy transfer processes, for instance, the energy of an excited fluorophore is transferred to a second acceptor fluorophore and can be distinguished in fluorescence resonance energy transfer (FRET) or in electron exchange energy transfer (EEET). Another example is electron transfer processes involving interactions between an excited fluorophore with reducing or oxidizing molecules (quenchers).

1.3.5. Fluorescence Resonance Energy Transfer (FRET)

FRET is a result of interaction between two molecules with permanent absorption and emission dipole, respectively, and hence is formulates as dipole-dipole interaction. In FRET, the excitation energy of a donor molecule (D) will be transferred non-radiatively to an acceptor molecule (A). It was theoretically derived and experimentally proven from classical electrodynamics by Theodor Förster (Förster 1948). For this resonance phenomenon the emission spectrum of the donor and the absorption spectrum of the acceptor fluorophore must overlap. FRET is a type of dynamic quenching effect meaning that the energy transfer takes place while the donor is in the excited state. It is different than static quenching where a complex is formed while donor and acceptor are in the ground state. FRET is extremely sensitive to the distance between donor and acceptor for common fluorophores (Galla 1988, Lakowicz 2006) due to its strong distance dependence ($1/r^6$), which makes it a powerful mechanism to study the conformational changes in macromolecules or the interaction of proteins. The fraction of photons absorbed by the donor fluorophore that are deactivated by transferring their energy to the acceptor fluorophore resulting in an elevation of an acceptor electron from S_0 to S_1 state gives the energy transfer efficiency

$$E_T = \frac{K_{ET}}{K_{ET} + \tau_D^{-1}} = \frac{R_0^6}{R_0^6 + r^6} \tag{1.6}$$

Here, K_{ET} is the rate of FRET and τ_D is donor fluorescence lifetime in absence of acceptor, r is the distance between D and A, R_0 is the Förster radius. $1/\tau_D$ equals the rate of donor deactivation in the absence of acceptor. The Förster radius is the distance between D and A, where the transfer efficiency E_T is 50% and is formulated as $R_0^6 = \frac{9 \log(10) \kappa^2 J\, \phi}{128 \pi^5 N_A n^4}$ where ϕ is the fluorescence quantum yield of the donor in the absence of the acceptor, κ^2 is the dipole orientation factor, n is the refractive index of the medium, N_A is Avogadro's number, and J is the spectral overlap integral between donor and acceptor. Typical R_0 values for fluorophores are about 2–8 nm.

1.3.6. Fluorophores

Fluorescence spectroscopy is performed with entities, which absorb near UV, visible or near-infrared light and have a sizeable ($\phi_{FL} > 0.01$) fluorescence including organic synthetic dyes, metal-ligand complexes, fluorescent proteins (FP), and semiconductor nanocrystals. The latter shows size-dependent optical and physicochemical properties and include quantum dots (QDs) made from II/VI and III/V semiconductors or carbon and silicon nanoparticles (Resch-Genge 2008, Xie 2013, Ren 2018). These probes differ in their photophysical, biological, and chemical properties and consequently also in experimental handling towards receiving optimal fluorescence signal. Organic fluorescent dyes (see 1.3.6.1) have been more than 100 years available and optimized in the past 20 years to match the requirements for fluorescence spectroscopy, in particular fluorescence-based sensing and single molecule fluorescence spectroscopy. The major goal in synthesis of new organic fluorescent dyes development is obtaining molecules with high fluorescence quantum yield and high photo stability issue. Often they have to be chemically introduced into biological samples (e.g. labeling of antibodies or proteins), many localize to cytosol, RNA/DNA, or certain cell organelles due to their chemical properties. On the other hand, fluorescent proteins (FPs, 1.3.6.2) can be tagged to any protein of interest in cells by modification of the genetic code of the cells, who subsequently express the fluorescently tagged, in most cases, functional fusion protein. Organic fluorescent dyes and fluorescent proteins are the main probes in single-molecule based super-resolution microscopy. Since the main focus of this study is based on the FPs, only the classical fluorescent organic dyes and the FPs are introduced in detail.

1.3.6.1. Organic fluorescent dyes

Synthetic organic fluorescent dyes have been used since the beginning of fluorescence microscopy almost 100 years ago (Lakowicz 2006, Martynov 2016) and also as only fluorophores at the beginning of single molecule fluorescence spectroscopy. The most important dye classes are fluoresceines, cyanines, oxazines, rhodamines, and boron-dipyrromethenes (Bodipy) (Lavis 2008).

Common to all these dyes is a conjugated double bond system whose length determines the spectral properties (Locowick 2006, Luo 2019). The absorption of a cyanine dye Cy3, for instance, with five carbon atoms in a chain as $R_2N{-}C{=}C{-}C{=}C{-}C{=}N^+R_2$, is calculated to be 453 nm (550 nm when measured in water) if using only the simplified model of a particle in a box (Kuhn 1948, Kuhn 1949). With increase in the length of this one-dimensional box in molecules of the same family, the absorption is shifted to higher wavelengths. This simple one-dimensional particle in a box model does not exactly explain the experimental results but provides a rough estimation of absorption of a dye and shows the trend of increasing wavelength with increasing length of the polymethine chain. Other values based on the particle in box model are 650 nm for Cy5; $R_2N{-}C{=}C{-}C{=}C{-}C{=}C{-}C{=}CN^+R_2$ (experimentally obtained value is 649 nm) and 706 nm for Cy7; $R_2N{-}C{=}C{-}C{=}C{-}C{=}C{-}C{=}C{-}C{=}N^+R_2$ (experimentally obtained value is 750 nm).

Nowadays, cyanine dyes are widely used in imaging and spectroscopy (Karlsson 2018). Besides Cy3, Cy5 and Cy7, some Alexa dyes such as Alexa 555, Alexa 647, and Alexa 750 are structurally very similar and exhibit very similar spectral properties. However, Alexa dyes are significantly more resistant to photobleaching than their Cy dye counterparts (Berlier 2003). Rhodamine dyes are derived from the xanthene dye family. Many rhodamines exhibit fluorescence quantum yields near to unity. Several functionalized rhodamines are commercially available and already established for biological labeling such as ATTO 520,

ATTO 532, ATTO 550, ATTO 565, ATTO 590, and the Alexa derivatives Alexa 488, Alexa 532, Alexa 546, Alexa 568, and Alexa 594.

Oxazine dyes such as MR121, ATTO 655, ATTO 680, and ATTO 700 are near infrared absorbing dyes with high photostability. Bodipy dyes are notable for their uniquely small Stokes shift, high, environment-independent fluorescence quantum yields, often approaching 100% even in water, sharp excitation and emission peaks contributing to overall brightness, and high solubility in many organic solvents (Boens 2012). Common to all Bodipy dyes such as BODIPY FL, BODIPY R6G, BODIPY TMR, BODIPY 581/591, BODIPY TR, BODIPY 630/650, and BODIPY 650/665, is that the core carries a negative charge on the boron atom and a positive charge on one of the nitrogen atoms (Loudet 2007, Si 2015).

Fluorescein dyes (von Bayer 1871) and its derivatives (such as eosin Y, eosin B, and Fluorescein isothiocyanate (FITC)) have absorption maximum at 486 - 494 nm and emission maximum of 512 - 570 nm (in water). Fluorescein family of dyes have a broad range of applications from usage in solar cells (Pepe 2016), chemical sensors to identify metallic ions (Icart 2016), usage as a fluorescent tracer in medicinal and biological applications and tumor-infected tissues tracer (Falco 2019), etc. They show the fluorescent quantum yield of near to 0.85 when the molecule is free in an alkaline aqueous solution but it decreases to 0.3–0.5 when fluorescein is conjugated to antibodies (Robertson 2013).

1.3.6.2. Fluorescent proteins

Today, fluorescent proteins (FP) are the standard markers when fluorescence microscopy is used in cell biology applications, e.g. to visualize and track proteins and intracellular organelles or prove gene expression. The story of FPs began with the discovery of original green fluorescent protein (GFP). It was found in the early 1960s when researchers (group of Prof. F. H. Johnson, Princeton University, USA) were studying the bioluminescent properties of the *Aequorea victoria* jellyfish. They isolated a blue-light-emitting bioluminescent protein called aequorin which was tightly but non-covalently connected to another protein that they named the green-fluorescent protein (Shimomura 1962). Aequorin and GFP work together in the light organs of *A. victoria* to convert Ca^{2+}-induced blue bioluminescence signals into the green luminescence that is characteristic of the species (Chalfie 1995).

Nowadays a huge number of jellyfish FP variants are in use. For example, BFP (blue FP), CFP (cyan FP), YFP (yellow FP) are all variants of GFP.

For the first time Yang et al. at 1996 solved the crystal structure of recombinant wild-type GFP to a resolution of 1.9 Å. GFP consists of 238 amino acids forming a cylinder, comprised of 11 strands of β-sheet with a central α-helix inside and short helical segments on both ends of the amino acid chain. The chromophore is an imidazolone ring formed by a modification of the tripeptide -Ser^{65}-Tyr^{66}-Gly^{67}- (called maturation) in an autocatalytic, multistep chemical reactions that can only take place once the polypeptide chain has folded to a near-native structure. After folding step, backbone cyclization via covalent bond formation between Gly^{67} and Ser^{65} followed by dehydration of the oxygen of the same carbonyl, and Tyr^{66} oxidation reactions is taking place (Craggs 2009). GFP folding motif, with β-structure on the outside and α-helix on the inside, represents a new protein fold, which was named β-can (Yang 1996). The β-barrel cylindrical structure (figure 1.5) shields the chromophore, which is inside from quenching molecules of the solution consisting of an amino acid trimer, that is serine, tyrosin, and glycine (Prasher 1992). This architecture is common for all FPs, though differences in amino acids sequence can be more than 50 %.

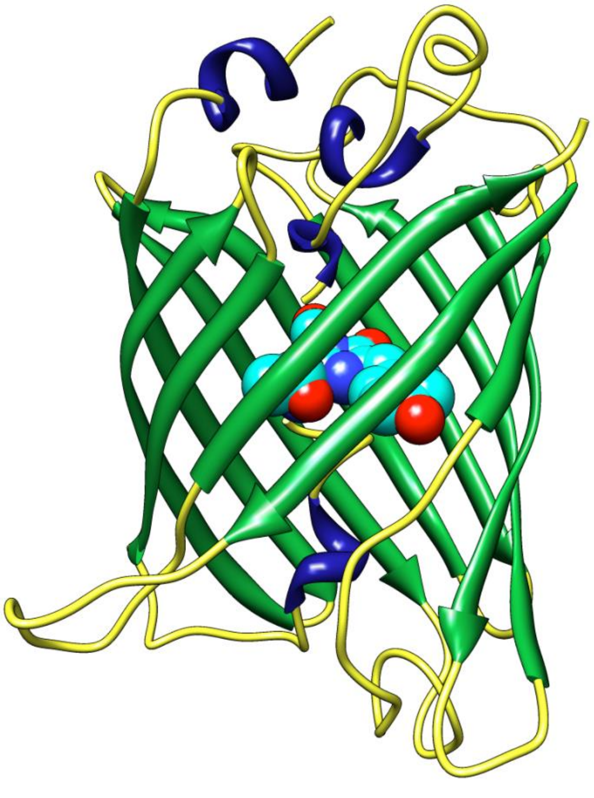

Figure 1.5. The overall shape of the protein GFP. Eleven strands of β-sheet (green) form the walls of a cylinder. Short segments of α-helices (blue) cap the top and bottom of the structure and also provide a scaffold for the

fluorophore, which is near geometric center of the can. Red spheres in chromophore represent oxygen, light blue show carbons, and dark blue show nitrogen. Adopted from (Craggs 2009). Image taken from https://pdb101.rcsb.org/learn/paper-models/green-fluorescent-protein-gfp with the permission from PDB structure: 1 ema.

YFP is the most red-shifted FP derived from avGFP. RFP (red FP), with absorption maximum at 555 nm and fluorescence at 584 nm, belongs to another class of fluorescent proteins derived from *Discosoma*, and was originally named DsRed. There is a red emitting chromophore representing bond between the alpha-carbon and nitrogen of Gln-66 has been dehydrogenated in DsRed, extending the GFP chromophore by forming -C=N-C=O at the second position of the imidazolidinone. This acylimine substituent quantitatively accounts for the red shift (Gross 2000). DsRed-like proteins show much narrower major maxima with smaller Stokes shifts and a characteristic shoulder at 630 nm in the emission spectrum that makes it look remarkably like cyanobacterial phycoerythrins (Alieva 2008). There are some derivatives of the chromophore in the DsRed-like FPs, each observed once among FPs. The first one is the fragmented DsRed chromophore of the kindling fluorescent protein (KFP) from the sea anemone *Anemonia sulcate* (Quillin 2005, Alieva 2008). Another one is a three-ring structure found in the natural yellow fluorescent protein from *Zoanthus sp*. (Remington 2005, Pletneva 2007). The third one is found in a mutant variant of DsRed called mOrange (Piatkevich 2014). Moreover, more red-shifted variants such as mKatushka and mPlum could be classified as another derivative of the chromophore in the DsRed-like FPs (Hense 2015).

One of the major limitations of using wild-type FPs is their low photostability and brightness. There are several genetically modified derivatives for the wild-type FPs called as EFPs (enhanced FPs) with enhanced photostability and brightness of up to 35 times more than that of wild-type (Zhang 1996).

The FP variants in the blue spectrum have been created by single point mutations in tripeptide chromophore of wtGFP (tyrosine residue substitution at position 66 with histidine (Y66H) of GFP yields BFP (Mena 2006), tryptophan (Y66W) substitution yields CFP (Lelimousin 2009)). In table 1.1, various possible GFP mutations and the resulting absorption and emission maxima are given.

Table 1.1. Fluorescence properties of different GFP mutants (adopted from (Heim 1996)). The values in parenthesis are second maxima.

Mutations	Excitation max (nm)	Emission max (nm)	Quantum yield
Wild-type	395 (475)	508	0.77

Y66H	383	447	0.21
Y66H	381	445	0.38
Y66W	433 (453)	475 (501)	0.67
Y66W	432 (453)	480	0.72
S65T	489	511	0.66
S65T	504 (396)	514	0.54

Many more FPs have been identified and cloned from different organisms and even more mutations have been introduced resulting in a broad palette of FPs with fluorescence spanning a broad range of the visible spectrum from 440 to 650 nm (Shaner 2007, Tsien 2009, Constantini 2015).

A major advantage of using FPs in cell and molecular biology is the possibility to fluorescently label any protein of interest with FPs in all organisms with high specificity and hence allowing live cell microscopy. The only prerequisite is the presence of sufficient concentration of molecular oxygen (O_2) needed for chromophore maturation. In addition to the mentioned FPs, a new strategy of producing other types of FPs suitable specifically for single molecule spectroscopy and microscopy has been stablished, which includes photoswitchable, photoactivatable, and photoconvertible FPs. Since the central topic of this study is focused on using single molecule localization microscopy (SMLM), all these three classes of FPs will be explained in the following.

1.3.7. Reversible photoswitchable fluorescent proteins

All photoswitchable FPs exhibit either a reversible or irreversible transition from a non-fluorescent state to a fluorescent state. Photoswitchable FPs undergo an emission spectral redshifted fluorescent state upon excitation by irradiation at most commonly 400 nm violet light. As an example, the photoswitchable FP Dronpa can be switched reversibly between a bright on and non-fluorescent off state applying 400 nm light for activation (on-switching) and 488 nm for read-out (and off-switching) (Habuchi 2006, Rainey 2019). Dronpa, is a monomer and has an absorption maximum at 503 nm due to its anionic, deprotonated chromophore, and a minor absorption maximum at 390 nm due to its neutral, protonated chromophore. Whereas the anionic form has an emission maximum at 518 nm, the neutral form shows no fluorescence. In its anionic state Tyr63 is in cis conformation when it is illuminated there is a cis-trans isomerization connected with the protonation of the chromophore. On the contrary, in the neutral state of the chromophore the Tyr63 side chain is in a trans-form (Wilmann 2006). Upon irradiation with a 405 nm laser pulse Dronpa is forced into its fluorescent deprotonated cis-conformation. A 488 nm laser pulse then switches the Dronpa chromophore back to its non-fluorescent protonated trans-conformation. This cycle can be repeated several hundred times (figure 1.6). In table 1.2 a list of other photoswitchable FPs, their maximum excitation and emission spectrum, as well as the activation and read-out condition is given.

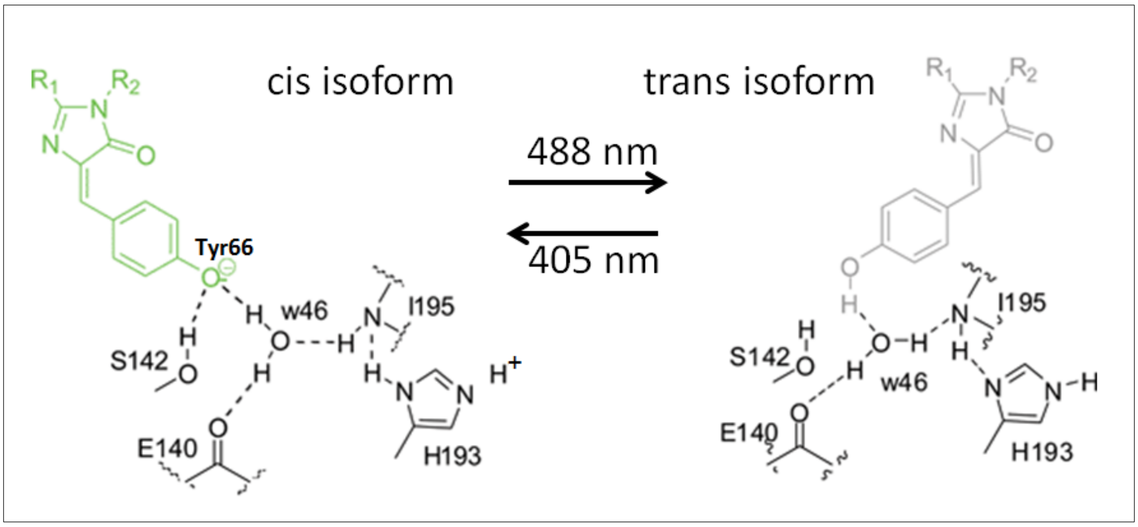

Figure 1.6. Mechanism of reversibly photoswitching of the Dronpa chromophore. Intense blue light (488 nm) converts this FP from a bright on-state (green) to a non-fluorescent off-state (gray). The on-state is attributed to the deprotonated anionic chromophore which adopts a cis-configuration. In the non-fluorescent off-state, the protonated neutral form of the chromophore exists in a trans-configuration (adopted from (Sample 2009)). With publisher permission (Order number: 1011878).

Table 1.2. List of different photoswitchable FPs. Table adopted from https://www.leica-microsystems.com/science-lab/photoactivatable-photoconvertible-and-photoswitchable-fluorescent-proteins/ with their permission under Leica microsystems copyright.

Photoswitchable proteins	Excitation maximum (nm)	Emission maximum (nm)	Photoswitching on-state /off-state formation	References
mTFP0.7	453	488	405 nm / 458 nm	(Henderson 2007)
PDM1-4	503	517	405 nm / 488 nm	(Mizuno 2010)
Dronpa	503	518	405 nm / 488 nm	(Ando 2004)
Dronpa-2	489	515	405 nm / 488 nm	(Ando 2007)
Dronpa-3	489	515	405 nm / 488 nm	(Ando 2007)
bsDronpa	460	504	405 nm / 488 nm	(Andersen 2008)
Padron	503	522	503 nm / 405 nm	(Andersen 2008)

Padron0.9	500	524	500 nm / 400 nm	(Brakemann 2010)
Mut2Q	496	507	405 nm / 478 nm	(Quercioli 2010)
rsFastLime (DronpaV157G)	496	518	405 nm / 488 nm	(Stiel 2007)
rsKame (DronpaV157L)	503	518	405 nm / 488 nm	(Rosenbloom 2014)
Dreiklang	515	529	365 nm / 405 nm	(Brakemann 2011)
mGeos-M	503	514	405 nm / 488 nm	(Chang 2012)
EYQ1	510	524	405 nm / 514 nm	(Abbruzzetti 2010)
KFP1	590	600	532 nm / 458 nm	(Chudakov 2003)
rsCherry	572	610	550 nm / 450 nm	(Stiel 2008)
rsCherryRev	572	608	450 nm / 550 nm	(Stiel 2008)
rsTagRFP	567	585	445 nm / 570 nm	(Pletnev 2012)
mApple	568	592	480 nm / 570 nm	(Shaner 2008)
asFP595	572	595	569 nm / 450 nm	(Yampolsky 2005)
Kindling FP (KFP1)	580	600	green / 450 nm	(Chudakov 2003)
rseGFP	493	510	405 nm / 488 nm	(Grotjohann 2011)
rseGFP2	478	503	408 nm / 478 nm	(Grotjohann 2012)

1.3.8. Irreversible photoswitchable fluorescent proteins

Irreversible photoswitchable proteins can be grouped into two classes, phtoactivatable and photoconvertible fluorescent proteins. Photoactivatable fluorescent proteins (PAFPs) are stimulated by high frequency (e.g. near UV) light excitation to undergo an irreversible switch from a non-emissive off-state to emissive on-state, in most cases resulting in the irreversible decarboxylation of the glutamic acid side chain in residue 222. This loss of a carbon dioxide molecule alters the enrichment of the chromophore and subsequently the chromophore protonation state from a neutral to an anionic state. Among the PAFPs, there are tetramers such as KFP1 (Chudakov 2003) and KikGR (Nowotschin 2009) but also monomeric proteins such as PA-GFP (Patterson 2002) and PA-RFP1 (Verkhusha 2005). The main drawback of tetrameric PAFPs is that they can be thought to disrupt the localization and function of their fusion partner and should not be applied for studies on single proteins are used to label whole cells and organelles. Monomeric PAFPs, however, can be used for labeling an individual protein and monitor its first localization and motion. A general approach to engineer monomeric PAFPs is by mutating selected specific residues in the protein environment of chromophore to achieve photoactivation and secondly by mutagenesis that disrupts other tetramer interfaces yielding monomeric PAFP (Verkhusha2005, Nemet 2015).

A unique application of PAFPs is the kinetic microscopy of living cells, in which proteins (often membrane-associated proteins) can be tracked. This method is widely substituting the traditional Fluorescence recovery after photobleaching (FRAP) technique (Luu 2012), in which a small area of a cell containing fluorescently labeled proteins (e.g. PA-GFP-tagged lipids in cell membrane) is photobleached by long and intense excitation of the FP-tagged molecules in the area. Then due to the diffusion of bleached molecules out of the illuminated area and their substitution with non-irradiated FP-tagged molecules from neighboring, one can measure the time course of the fluorescence intensity which monitors the diffusion of the protein. With PAFPs, on the other hand, it is possible to photoactivate a subset of the cell containing the protein of interest and in real time monitors the diffusion of the protein and also observes where the irradiated FP-fusion proteins are translocated. One of the advantages of using PAFP-based microscopy instead of FRAP is that in the latter, it is impossible to distinguish between proteins which are re-entering the area and newly synthesized molecules. Irreversible photoactivation of PAFPs used in fluorescence microscopy is one way to address this problem. In figure 1.7, a simplified model of tracking a protein of interest labeled with PA-GFP is presented.

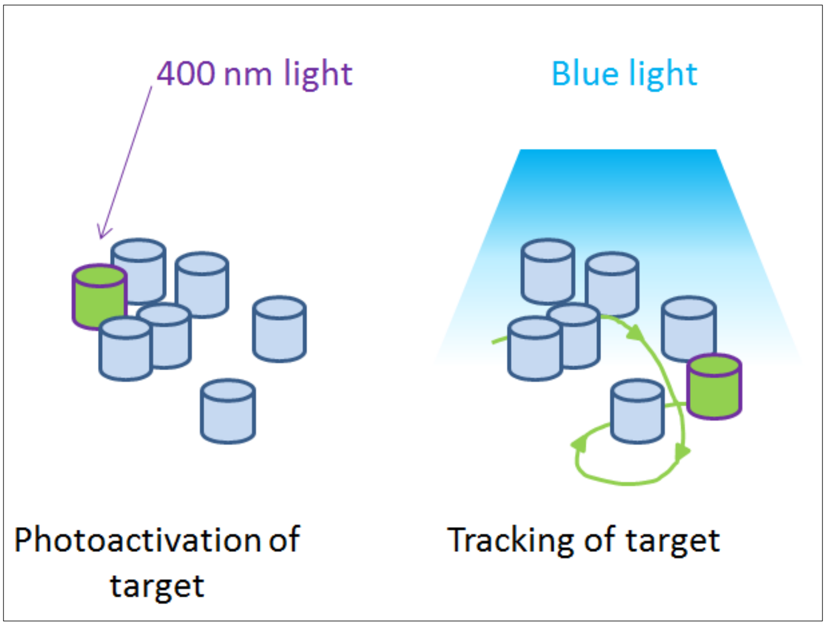

Figure 1.7. Procedures for selective photolabelling using irreversible photoactivatable fluorescent proteins (PAFPs). Cylinders represent a protein that has been tagged with a PAFP. The excitation or activating light is shown above the cylinders.

In table 1.3 a list of several PAFPs, the maximum excitation and emission spectrum and the condition for activation/read-out is given.

Table 1.3. List of different photoactivatable FPs. Table adopted from https://www.leica-microsystems.com/science-lab/photoactivatable-photoconvertible-and-photoswitchable-fluorescent-proteins/. The excitation and emission values are for pre-photoactivation and post-photoactivation, respectively. With their permission under Leica microsystems copyright.

Photoswitchable proteins	Excitation maximum (nm)	Emission maximum (nm)	Photoswitching on-state formation/off-state formation	References
PA-GFP	400 504	515 517	violet	(Patterson 2002)
PAmCherry	404 564	ND 595	350 – 400 nm	(Subach 2009)
PATagRFP	ND 562	ND 595	violet	(Subach 2010)
PAmKate	ND 586	ND 628	405 nm	(Gunewardene 2011)
Phamret (PA-GFP + ECFP)	458 458	475 517	violet	(Matusda 2008)

To give an example, the excitation spectrum of PA-GFP consists of two peaks, one at 400 nm and the other at 504 nm. They correspond to the neutral (protonated) and anionic (deprotonated) chromophore forms, respectively. Ultraviolet (UV) or violet-light irradiation changes the ratio of the peaks slightly in favor of the anionic form. These changes are brought about by Glu222 side chain decarboxylation, which results in the rearrangement of the hydrogen-bonding network and chromophore deprotonation. The proposed mechanism is that the decarboxylation is due to electron transfer between the gamma-carboxylate of Glu222 and the p-hydroxybenzylidene-imidazolidinone chromophore of GFP, followed by reverse transfer of an electron and a proton to the remaining carbon side chain atom of Glu222 (figure 1.8). This basic mechanism apparently underlies the pronounced photoactivation of PA-GFP (Slocum 2017).

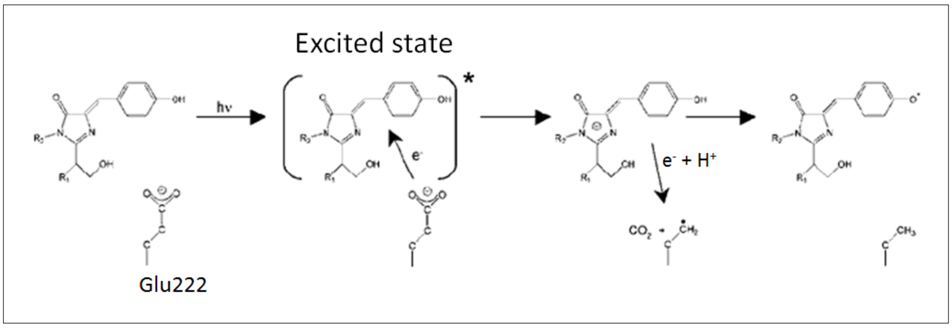

Figure 1.8. R1 and R2 correspond to residues Phe 64 and Val 68. The asterisk denotes the excited state of the neutral, phenolic chromophore. Adopted from (Van Thorr 2002). With publisher permission (License Number 4725801219873).

In contrast to photoactivatable proteins, photoconvertible proteins emit fluorescence already in their non-converted state. Once excited with short pulses of UV or violet light, the irreversible conformational changes in the structure of the fluorophore redshifts the absorption and the emission spectra. Photoconversion was discovered in the stony open brain coral *Trachyphyllia geoffroyi* (Ando 2002). Due to their emission attributes, which are shifting from green to red after photoconversion with UV light, the fluorescent protein was given the name *Kaede* like the leaves of Japanese maple trees (https://dengarden.com/landscaping/japanese-maple-trees). If Kaede is photoconverted with wavelengths between 380 and 400 nm, its emission maximum is shifting from 518 nm to 582 nm. Despite the irreversible nature of photoconversion, its tetrameric nature hampers severely the use of Kaede in live-cell imaging studies (Tomura 2008).

A major advantage of photoconvertible FPs over photoactivatable FPs is that they are emissive prior to the illumination by near UV/violet light, and hence allow selecting a cell region or single protein of interest. Similar to photoswitchable and photoactivatable FPs, the underlying mechanism of photoconversion is a light induced process. In this case a histidine residue inside the tripeptide forming the chromophore (His62-Tyr63-Gly64) is cleaved by irradiation and finally leads to an extension of the conjugated system by formation of a highly conjugated dual imidazole ring system. This process is connected to a red-shift of absorption and fluorescence spectra (Stepanenko 2011).

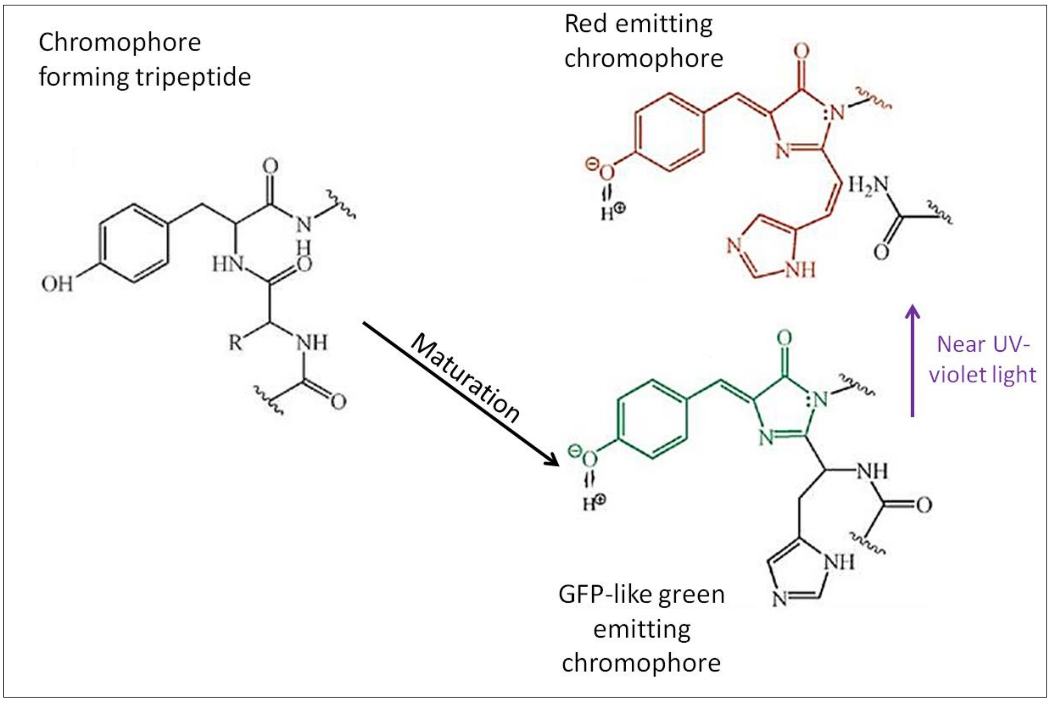

Figure 1.9. General scheme of the autocatalytic synthesis of green and red chromophores. The synthesis comprises three stages: cyclization of the tripeptide to a α-enolate form, oxidation to cyclic imine (carbon-nitrogen double bond), and dehydration of the Cα-Cβ bond of Tyr63 resulting in a mature GFP-like chromophore which is able to emit green light in its deprotonated (anionic) state. Excitation with UV light will result in histidine residue cleavage and formation of conjugated dual imidazole. Adopted from (Stepanenko 2013). With publisher permission (License Number 4725821488993).

Another well charcterized photoconvertible FP is Dendra2. It was derived from the GFP-like dendGFP from octocoral *Dendronephtytha sp*. combining the name of the species and the red activatable property, the name Dendra (Gursakya 2006) was born. dendGFP carries a histidine residue in the chromophore that is characteristic for a group of green-to-red Kaede-like PAFPs. To make dendGFP suitable for protein labeling, a monomeric variant using mutagenesis strategy similar to that for monomerization of green fluorescent protein Azami-Green (Karasawa 2003) was created which was named Dendra. Dendra2, a commercial variant of Dendra, comprises single A224V substitution, which results in better maturation and a brighter fluorescence both before and after photoconversion. Dendra2 undergoes irreversible photoconversion from a green to a red fluorescent form. It provides a unique combination of advantageous properties including monomeric state suitable for protein labeling, high contrast photoconversion with fluorescence in the orange-red spectral region, low phototoxic activation with simultaneous illumination by blue and red light (Virant 2017) or cyan and near-infrared light (Klementieva 2016) nm light available on common confocal microscopes, high photostability of the photoconverted state, and efficient chromophore maturation at 37°C in mammalian cells (Jradi 2019). The peak of the excitation and emission spectrum are 490 and 507 nm, respectively, before photoconversion and 553 and 573 nm, respectively, after the photoconversion (figure 1.10). Dendra2 is believed to be one of the best suited FPs suitable for single molecule microscopy due to its unique blinking behavior which will be explained later. In table 1.4 a list of different photoconvertible FPs is given.

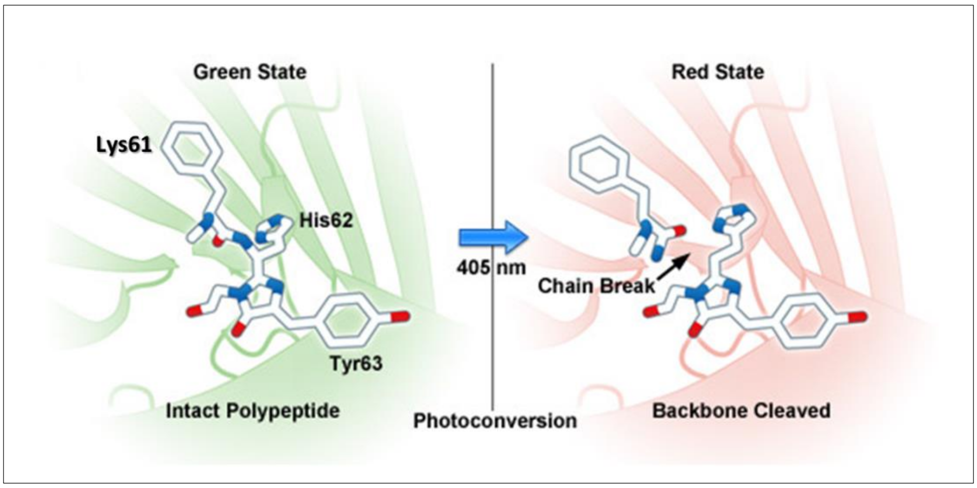

Figure 1.10. Dendra2 chromophore chain break during photoconversion resulting into shortening of the chromophore due to the cleavage of the Phenyl group of Lysine 61 (Pletnev 2015) and the formation of a chromophore with extended π-conjugated system. The permanent chromophore structural change will be resulted into fluorescent emission change from 507 nm to 573 nm. Image taken from http://zeiss-campus.magnet.fsu.edu/articles/probes/highlighterfps.html

Table 1.4. List of different photoconvertible FPs. Table adopted from https://www.leica-microsystems.com/science-lab/photoactivatable-photoconvertible-and-photoswitchable-fluorescent-proteins/ with their permission under Leica microsystems copyright.

Photoconvertible proteins	Excitation maximum (nm) before and after photoconversion	Emission maximum (nm) before and after photoconversion	Photoconversion condition	References
mClavGR2	488 / 566	504 / 583	405 nm	(Hoi 2010)
mMaple	489 / 566	505 / 583	380 nm	(McEvoy 2012)
Dendra2	490 / 553	507 / 573	405 nm	(Gurskaya 2006)
PS-CFP2	400 / 490	468 / 511	405 nm	(Chudakov 2007)
Meos3.2	507 / 572	516 / 580	405 nm	(Zhang 2012)
Kaede	508 / 572	518 / 580	405 nm	(Ando 2002)
EosFP	506 / 571	516 / 581	405 nm	(Wiedenmann 2004)
mEosFP	505 / 569	516 / 581	405 nm	(Wiedenmann 2004)
mEos2	506 / 573	519 / 584	405 nm	(McKinney 2009)
kikGR (Kikume)	507 / 583	517 / 593	365 nm	(Nowotschin 2009)
PSmOrange	548 / 636	565 / 662	blue-green	(Subach 2011)
PSmOrange2	546 / 619	561 / 651	489 nm	(Subach 2012)
mKikGR	505 / 580	515 / 591	405 nm	(Habuchi 2008)

There is another more general mode FPs that unlike photoactivatable and photoconvertible FPs, similar to photoswitchable FPs repeatedly switches between emissive on and non-emissive off states, allowing multiple localizations of the same FP molecule. Although in most photoswitchable FPs, a switch laser light and a read-out laser light exist, in some of reversible photoswitchable FPs, only one laser line is sufficient. Reversible photoswitching in FPs has first been observed on yellow derivatives of Aequora victoria GFP (YFP) at the single-molecule level (Dickson 1997). YFP is generated by the replacement of Thr203 in GFP with Tyr (Sinnecker 2005). Single immobilized YFP proteins excited by light of cyan (488 nm) showed repeatedly cycles of non-emissive/emissive switching on a timescale of several seconds. Bulk photoswitching at room temperature was evidenced for the first time in ECFP and EYFP (Chudakov 2004, Sinnecker 2005). Reversible photoswitching in ECFP and EYFP is evident at physiological pH, but even more obvious at acidic pH. Reversible light-induced cis-trans isomerization of the chromophore and/or chromophore protonation was hypothesized as the most likely reasons for the observed switching (Bourgeois 2012). Illumination of EYFP, for instance, in protonated forms results in reversible photobleaching. The reversible photobleaching rate depends on the illumination intensity and the reversible photobleaching arises from interaction of photons with the protonated ground state (P) and deprotonated ground state (D). Absorption of a photon may lead to the generation of an excited state (P -> P*), which may then relax to a reversibly metastable bleached state (P* -> B). The reversibly bleached state B may return into a fluorescent state by more than one way. First, it was shown that reversibly bleached fluorescent proteins regain their fluorescence in the dark with time constants of several seconds. Because of the fast equilibrium P <-> D and P* <-> D*, it cannot be decided whether the reversibly bleached state relaxes directly to the fluorescent deprotonated ground state (B -> D) or via the protonated states P. Second, the restoration of fluorescence can be accelerated by illumination. This implicates the absorption of a photon by the reversibly bleached state, which presumably leads to the generation of another excited state (B -> B*) which serves as a gateway to more rapidly relax back to the fluorescent ground state (Habuchi 2006, Bourgeois 2012).

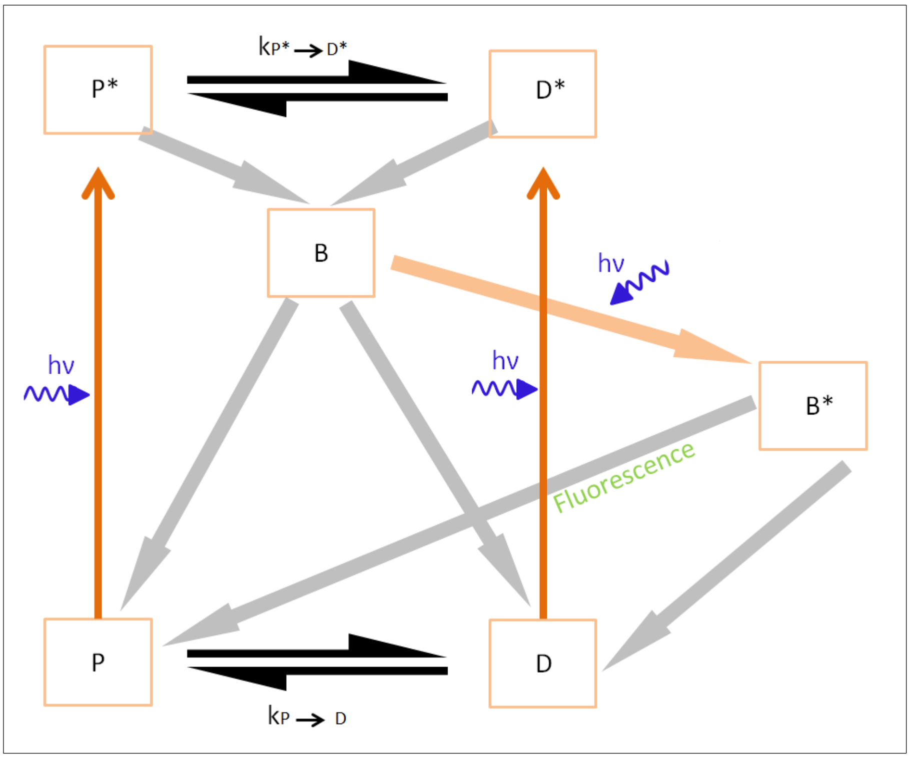

Figure 1.11. Simplifid model of YFP/EYFP reversible photoswitching. In the ground state, the protein is either in neutral deprotonated (D) state or in anionic protonated (P) state. Excitation by light interaction, brings them into excited D* and P* states, respectively. (There is a kinetical balance between two neutral and anionic states in ground state and in the excited state). Once in excited state, YFP/EYFP can relax into a metastable photobleached dark (B) state. There are many possibilities for the molecule in B to come again into the ground state. There is a fraction of B->P, a fraction of B->D and another mechanism, which highly depends on the intensity of the initial excitation light, forcing molecule in B to enter an excited, long lived, non-emissive state (B*). From this state to D state, the relaxation is non-emissive while the fraction of B*->P will be resulted into fluorescence emission. B* can be populated several times and hence the reversible photoswitching of an FP is repeatedly happened.

The overall photoswitching contrast for ECFP compared to EYFP is limited, probably due to the coexistence of non-interchangeable populations of molecules over experimental timescale. EYFP gained a lot of attention for usage in single-molecule microscopy experiments. The first diffraction-limited images with the use of EYFP and single particle tracking of EYFP fused proteins were reported in group of Moerner (Dickson 1997, Shaner 2005, Lew 2011, Gahlmann 2013, Saurabh 2016).

1.3.9. Fluorescence Microscopy

The simplest realization of optical fluorescence microscopy is the widely used widefield microscopy method, which provides a unique, high contrast mechanism based on specific labeling of target structure. In fluorescence microscopy a suitable light source for irradiation of fluorescent probes, filters to separate fluorescence from excitation light, and a detector is required (figure 1.12). Similar to standard transmission light microscopy and in general all microscopy methods that use electromagnetic waves for contrast generation, fluorescence microscopy is subject to diffraction. Even though the lateral resolution for a widefield fluorescence microscope might be about 200 nm, the axial resolution is 4 times worse than the lateral resolution. Although standard fluorescence microscopy has been proven to be a powerful tool in life science since 1970, it is simultaneously, a high demand for imaging below the diffraction limit has developed as well. As it is not possible to break this fundamental limit, various different super-resolution approaches have been established that instead circumvent it in different ways. Some of them briefly introduced here, while this work focuses on the super-resolution method Single Molecule Localization Microscopy (SMLM). Hence there is a more detailed description of SMLM given here in the introduction.

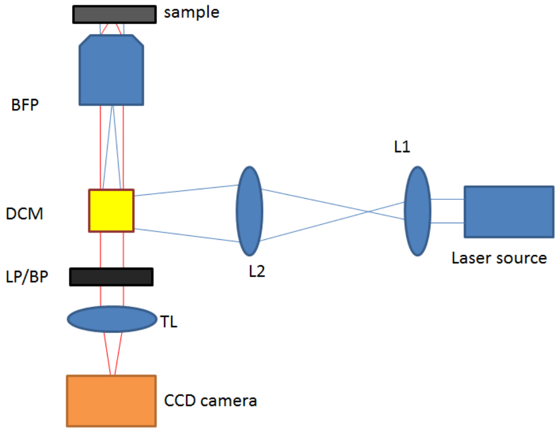

Figure 1.12. Fluorescence widefield microscope. A laser beam is broadened and focused onto the back focal plane (BFP) of the objective. The laser beam is parallelized by the objective (OBJ) resulting in a widefield illumination. Fluorescence light is collected by the objective and displayed on a detector. DCM = dichroic mirror, TL = tube lens, LP = long-pass filter, BP = bandpass filter, CCD = charge-coupled device.

1.3.9.1. Resolution Limit of Light Microscopy

Every imaging system is only able to transmit a certain bandwidth of spatial frequencies due to limiting factors such as diffraction and aberrations, which are direct consequences of the wave nature of light. Chromatic and spherical aberrations are generally not a limiting factor in modern optical imaging systems as highly sophisticated lens systems built into objectives are able to correct most chromatic and spherical differences of the parameters like focal plane, size, and shape of the PSF. Diffraction is still highly challenging in optical imaging and is the reason for a fundamental resolution limit described independently by Abbe (Abbe 1873) and Rayleigh (Rayleigh 1896), respectively:

$$d_{Abbe} = \frac{\lambda}{2n\sin\alpha} = \frac{\lambda}{2NA} \tag{1.7}$$

$$d_{Rayleigh} = \frac{1.22\,\lambda}{2n\sin\alpha} = \frac{1.22\,\lambda}{2NA} \tag{1.8}$$

where λ is the wavelength of the diffracted light, *n* is the refractive index of the medium between object and objective, α is the opening angle of the objective, and NA = *n* · sin α is the objective's numerical aperture.

In reality, single molecules are imaged as point source objects and they are displayed by a circular aperture with finite size. For a circular shape object, the pattern of the displayed image is an Airy diffraction image. The lateral intensity distribution is a Bessel function of the first order as following:

$$I_r \propto \left(\frac{J_1(r)}{r}\right)^2 \tag{1.9}$$

where J_1 is a Bessel function of the first kind of order one, and *r* the distance from the center of the light source. The lateral intensity distribution of a point source is also called point spread function (PSF) of a microscope objective. Since the PSF is fundamentally an estimation based on Airy disc, only a certain band-width of frequencies is transmitted by the optical system. Ideally the diffraction pattern should contain all spatial frequencies contributing to the original object. As a result, information of fine details of the object structure gets lost. (The area inside the first minimum of the diffraction limited focus is called the Airy disc). The distance between the main maximum diffraction pattern and the first minimum is given by

$$r_{Airy} = 0.61\frac{\lambda}{NA} \tag{1.10}$$

Having two equally bright point sources in an image separated by a small distance is subjected to Rayleigh criterion, in which two objects can only be resolved if the distance between them is greater or equal to the radius of the Airy disc (figure 1.13).

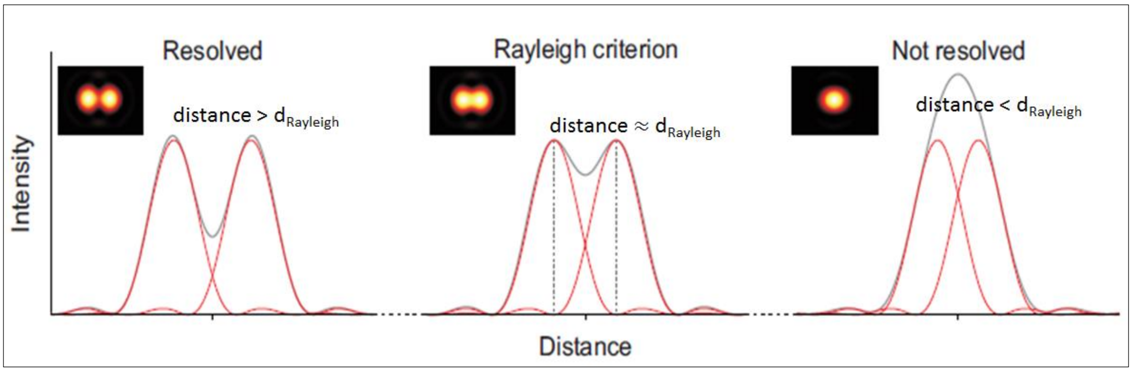

Figure 1.13. Airy discs and Rayleigh criterion. The Airy discs of two equally bright point objects can be just distinguished from each other if their distance is greater than the Rayleigh criterion.

Typical values for lateral resolution in standard light microscopes for NA = 1.2 and n = 1.33 are r_{Airy} = 203 nm for λ = 400 nm (violet), and r_{Airy} = 330 nm for λ = 650 nm (red).

1.3.9.2. Widefield fluorescence Microscopy

In widefield fluorescent microscopy, fluorescent molecules are irradiated using white light sources filtered to desired spectra (light emitting diodes (LEDs) of constrained spectral width (10-30 nm)) and coherent fluorescence light sources (lasers) with very narrow spectrum (< 1 nm). The fluorescence light has to be separated from the incident light by a dichroic filter which is a thin film or a mirror and a bandpass filter reflecting a short range of wavelengths while the other frequencies are transmitted and is placed at a 45° angle. The laser beam is reflected by 90° and passes the microscope objective thus achieving illumination of the sample. The resulting fluorescence light is then collected by the same objective, passes through the dichroic mirror, and is finally detected with the use of (EM)CCD, CMOS cameras, multiarray APD (avalanche photodiodes), or multiarray PMTs (photomultiplier detectors). The widefield microscope is fairly straightforward to implement. Before being reflected by the dichroic mirror, the laser beam is broadened with the use of a beam expander and focused onto the back aperture of the objective, also known as the back focal plane (BFP). The need for expansion of the laser light on BFP of the objective is to illuminate the sample in the center with a nearly uniform profile of incident light. The whole field of view can be irradiated and detected at once. Since in widefield illumination, molecules of long distances (micrometers) along the z-axis of the microscope are excited, not only fluorescence light generated in the focal plane is detected but also signal coming from molecules out of focus contributes to the final image and is blurring it. The axial resolution is formulated as $d_{axial} = \frac{2\lambda}{NA^2}$. The more limited axial resolution with respect to lateral resolution coming from the elongated geometry of the PSF along the optical axis arises from the nature of the non-symmetrical wavefront that emerges from the microscope objective.

1.3.9.3. Total Internal Reflection (TIR) Fluorescence Microscopy

One way to minimize the contribution of the fluorescent molecules out of focus to the final image and to limit the observed volume in widefield microscopy is the use of evanescent waves and total internal reflection (TIR). If an incident light beam encounters at an interface of two materials with different refractive index from a higher (n_1) to a lower refraction index (n_2) under the angle θ_1, θ_2 is larger than θ_1 and is given by Snell's law

$$\theta_1 \sin n_1 = \theta_2 \sin n_2 \tag{1.11}$$

If the angle of the incident beam θ_1 exceeds a critical angle θ_c, total internal reflection occurs (figure 1.14), where the light exits tangentially to the interface. θ_c is specific for the interface and depends only on the refractive indices, with $n_1 > n_2$

$$\theta_c = \sin^{-1}(\tfrac{n_2}{n_1}) \tag{1.12}$$

Considering an incident beam (the excitation light) in the case of fluorescence microscopy of biological samples, encountering a glass/water interface ($n_1 = 1.5$ respectively $n_2 = 1.3$), θ_c is 60.1°. For $\theta_1 > \theta_c$ the excitation light is completely reflected back into the glass medium while the interaction of light with the biological sample near the interface is still ensured, thus generating an evanescent field which propagates parallel to the surface in the plane of incidence. The intensity of light along the z-axis I(z) exponentially decays according to

$$I(z) = I_0 \exp(-\tfrac{z}{d}) \tag{1.13}$$

where I_0 is the intensity at the surface, and *d* is the penetration depth formulated as

$$\frac{\lambda}{4\pi\sqrt{{n_1}^2\, sin^2\theta_1 - \, {n_2}^2\, sin^2\theta_2}}$$

that is a function of refractive indices of both mediums and wavelength of the incident light beam.

Typical values for d are less than the wavelength of light used. For instance, using 488 nm light and an incident angle of 65° for glass/water surface, d is 98.68 nm and the same value for 647 nm, an incidence angle of 65°, and for a glass/water surface d is 130.97 nm. Thus, the observation volume is dramatically reduced and a high signal-to-noise ratio (SNR) is achieved. TIRF microscopy comes in two forms, prism and objective based (Axelrod 2001, Mattheyses 2010). The latter, based on development of microscope objectives with very large NA (larger than 1.4), allows easy implementation in normal fluorescence widefield microscopes and makes a popular tool for cell biologists, especially studying proteins and physiological processes in the plasma membrane and nearby cellular structures, e.g. endo- and exocytosis (Fish 2009), or receptor dimerization (Jaykumar 2016, Tabor 2016, Scott 2018). TIRF is also often used for single molecule fluorescence spectroscopy and microscopy due to its intensity reduction of fluorescence background from deeper sample layers.

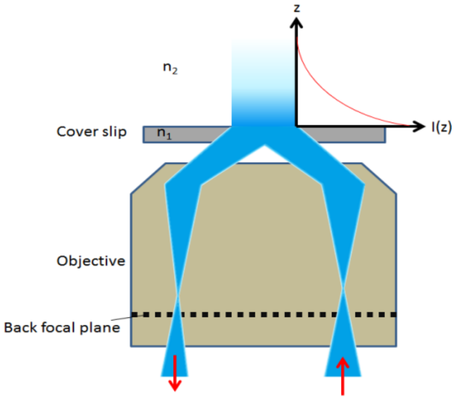

Figure 1.14. Scheme of widefield total internal reflection (TIR) microscopy. The laser is focused onto the back focal plane (BFP; white line). The objective lenses collect the laser light so that the sample is illuminated by a parallel beam. The formed evanescent field decays exponentially thus confining the observation volume.

Nevertheless, the intensity of excitation light spreads over hundreds of nanometer to a few micrometers since d denotes the depth, where the excitation light intensity is decreased to 1/e (i.e. d is far from being 0). If emitter distribution in z-axis is inhomogeneous (e.g. high emitter concentrations at larger axial distances z and low emitter concentrations near the interface (an example is a labeled protein that is localized in cell nucleus but in endoplasmic reticulum and cell plasma membrane), the axial resolution in TIRF microscopy can be severely deteriorated).

1.3.9.4. Scanning Confocal Fluorescence Microscopy

The concept of confocal microscopy was developed more than half a century ago, in the 1940s and 1950s (Goldmann 1940, Koana 1943, Minsky 1957) and was finally patented by Marvin Minsky (Minsky 1988), with first practical realization in 1969 and 1971 (Davidovits 1969). The technique offers rejection of fluorescence light emitted from molecules outside the focal plane. It provides better contrast and resolution (axial but also lateral) compared to fluorescence widefield microscopy (St. Croix 2005). The principal idea of the confocal approach is utilizing a spatial (the confocal pinhole) filter to reject out-of-focus light. The illumination method in confocal microscopy is different from conventional optical microscopes in that in a confocal microscope, a small area of the sample is illuminated while in widefield microscope, a large area of the sample is uniformly illuminated. To achieve the small focus size, low divergence of the excitation source is necessary in confocal microscopy. This and the high power in narrow spectral range are the reason that over decades, the confocal microscopes took advantage of using lasers instead of the initial designed zirconium arc in 1950s by Minsky (Minsky 1988). Nowadays, the confocal microscopes are usually equipped with different fixed-wavelength continuous wave (CW) lasers as excitation light sources but there are also setups with intense LED sources instead of lasers in range 750-850 nm (Vakili 2015).

In the confocal microscope, there is a pinhole in front of the detector. Since light coming from emitters above and below the focal plane is not confocal with the pinhole in front of the detector and will form larger Airy disk on the pinhole plane. Hence, only a small portion of this out-of-focus light will pass through the pinhole to the detector while most of this light will be blocked and will not contribute to the image. The other benefit of using a pinhole is to reject most of the surrounding (e.g. ambient) light that passes through the optical system. The pinhole improves the lateral resolution given by the Rayleigh limit by a factor of $\sqrt{2}$ (Pawley 2006) and for the axial resolution, the improvement of the confocal microscope is nearly the similar $\sqrt{2}$.

Confocal microscopy rapidly became popular especially in cell biology and imaging living cells and tissues because it is non-invasive to live cells and tissues, and technically handling of the device is not elaborate (Wang 2018, Liesche 2014, Zhang 2019). A common confocal fluorescence microscope focuses the beam to a very small spot realizing a detection volume of less than 1 fl (1 μm^3) in the specimen (Merkle 2018). In order to form an image, scanners are used to scan the excitation focal point in two dimensions through the sample. By additionally moving objective or specimen in axial direction one can generate high-resolution three dimensional images of live and fixed biological specimen. Microscopes that use such a scanning method are known as point scanning confocal microscopes or laser scanning confocal microscopes (LSCM) (Claxton 2015). Figure 1.15 shows a typical design for a LSCM.

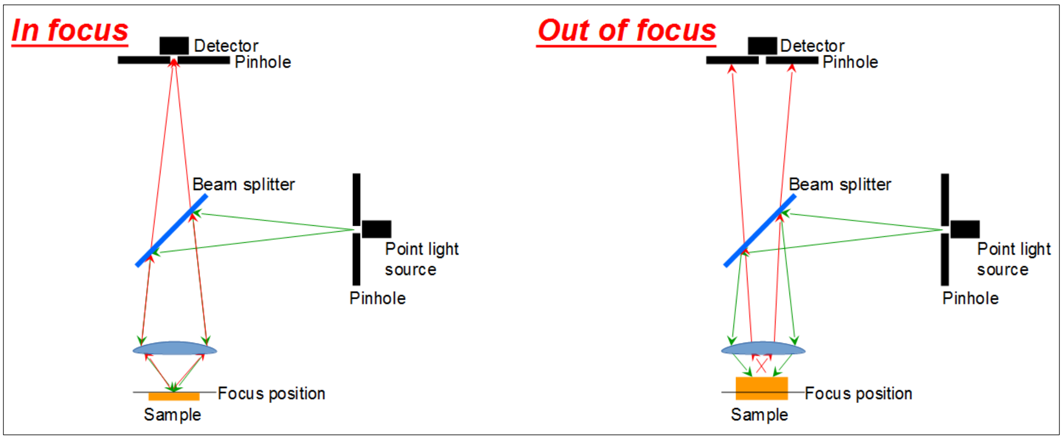

Figure 1.15. Layout of a typical confocal microscope. Excitation light is directed to the sample by a dichroic mirror or beam splitter. The objective lens focuses the beam into a diffraction limited spot on specimen. Light coming back from the specimen, travels the same path back to the dichroic mirror, where the fluorescence light is transmitted while back-scattered excitation light is reflected in this way the fluorescence to scatter ratio is improved by orders of magnitude. The emitted light is further directed towards the confocal pinhole, where only light from the focus in the sample plane can pass and reach the detector.

1.3.9.5. Limitations of confocal fluorescence microscopy

Although the confocal microscope provides slightly better resolution compared to conventional microscopes, its resolution is diffraction limited. For example, illumination of a sample with 488 nm light, while the surface is glass/water (for instance cell interior) with refractive indices 1.52 and 1.38 respectively, and with the incident beam angle 45°, for NA = 1.4, the diffraction limit is 245 nm as described by formula 1.7. In confocal microscopy, to improve the signal-to-noise ratio of the final image, a number of consecutive images of an identical sample's area are averaged. Obviously this approach is time consuming and in case of existence of scatter noises in sample, this noise is also contributing to the final image. As described above, the excitation laser light is focused in a small spot to increase signal to noise and reduce out-of-focus signal contributions. But it has the limitation of rejecting photons emerging from the focal plane by tuning the pinhole's opening to small values. This will cause not detecting from the focal volume for instance photons that are scattered on their way out of the sample and therefore, blocked on a small pinhole (Pawley 2006). Therefore, another drawback of using confocal microscopy would be the quantitative accuracy with which these measurements can be made due to insufficient signal-to-noise, a factor that depends on the ratio of number of photons that pass through the confocal pinhole and the number of photons being blocked, the volume size, and the position of the detection volume within the sample. Another limitation is the discrete nature of the image reconstruction in confocal microscopy which is time consuming. Continuous samples must be measured in terms of discrete volume elements called voxels (i.e. the three-dimensional equivalent of a pixel, which is the smallest element of a two dimensional (2D) digital image). Due to scanning, there is an intrinsic "time smear" between the measured voxels.

Other microscopy approaches such as Electron microscopy (EM) have a much better spatial resolution but need very special sample preparation, allow no observation of living biological specimen, and the investigation of several observables at the same time is slow. Confocal fluorescence microscopes are considerably cheaper, faster, and easier to use than EM and allow to observe living cells. Nevertheless, EM is the gold standard for single particles but also cell structures when it comes to resolution, therefore, in the following section a short introduction to EM technique, its advantages and limitations will be given.

1.3.10. Electron microscopy

Fluorescence microscopy, in general, and confocal fluorescence microscopy, in particular, is one of the techniques for biological imaging. There exist a large number of other methods that rely on different physical phenomena than fluorescence. They range from medical diagnostic tools such as X-ray, magnetic resonance imaging (MRI) (Laurent 2019) and positron emission tomography (PET)(Laurent 2019). More detailed structural determination by nuclear magnetic resonance (NMR) (Marion 2013), atomic force microscopy (AFM) (Matusovsky 2019) and X-ray diffraction (Nicolas 2019) can also be performed. Electron microscopy (EM) can resolve details in fixed and specially prepared structures on an atomic scale (1 Å) and is often be applied complementary to other structure deformation techniques. For example, the surface and morphology of cellular environment can be monitored using light microscopy and then the detailed localization of the molecule of interest inside the cell can be inquired using EM (CLEM, combined light and electron microscopy, Shibata 2019). Electron microscopy can also offer insights into cell architecture (Thiberge 2004, Rikkert 2019).

The Rayleigh criterion for light microscopy (see formula 1.8) states that the smallest distance that can be measured is proportional to the wavelength of the incident electromagnetic beam (λ), the refractive index of the viewing medium and the angle of collection of the magnifying lens. In the early 20th century, Louis de Broglie suggested that electrons behave like a wave with the wavelength proportional to $1/\sqrt{\boldsymbol{E}}$, where E is the energy of a single electron in terms of eV. For instance, for E = 200 keV, the wavelength of the electron's wave is 0.0025 nm, which is smaller than the diameter of an atom. In 1932, Knoll and Ruska developed the first electron microscope based on the wave-like nature of energetically activated electrons (Ruska 1987). Electrons interact with matter via several pathways such as elastic scattering, inelastic scattering, generating Auger electrons, and generation of secondary electrons. The two principle techniques are scanning electron microscopy (SEM) and transmission electron microscopy (TEM). Broadly, SEM analyses the scattered electrons that are emitted from the surface of the sample where a focused electron beam is impinging (the focused beam is scanned over the sample for image generation as in laser scanning confocal microscopy) while TEM analyses those that are transmitted through the sample (Bogner 2007).

Since the current study is not focused on EM techniques, the technical details of different EM microscopies are not explained but just a brief mechanism for TEM is given in the following. In TEM, components are pre-specimen electron lenses, electron source, sample stage, post-specimen electron lenses and a CCD camera to acquire an image. All the components of the microscope need to be contained within a vacuum. The electron beam is focused on a fixed, thin layer of the sample with the use of electron lenses. Due to interaction of the energetically activated electrons the amount of transmitted electrons in changed according to the local sample properties. A part of them are scattered, change direction and do not enter the detection pathway since interaction probability is large, the sample thickness has to be small (less than 100 nm). A sensitive detector then collects the electron signal to reconstruct the final image (figure 1.16).

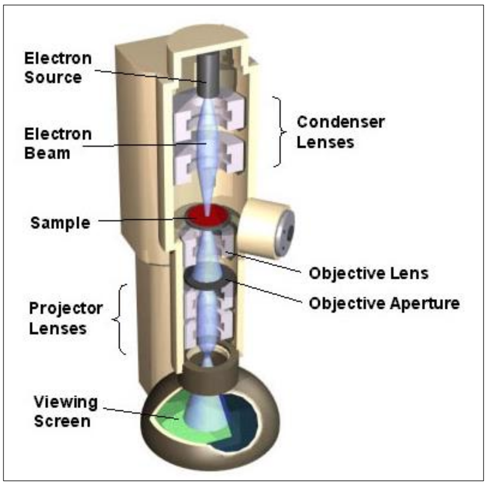

Figure 1.16. A typical TEM schematic. Electron beam originating from electron source (E-gun) is focused onto the sample with the use of condenser lenses (i.e. coil based magnets) and passes through the sample. The electrons that pass through the sample are diverged due to scattering, collision with the atoms in the sample, etc. and must be collected with the projector lenses and finally are detected by a fluorescent screen that is excited by impinging high energy electrons (image from the Barret research group (https://barrett-group.mcgill.ca/tutorials/nanotechnology/nano02.htm)).

Images from SEM and TEM reveal a large number of biological specimen’s structural details, but principally, there are major challenges and limitations inherent in TEM which makes it a challenging technique to use. First, sample preparation for TEM is a complex procedure that needs chemical fixation, dehydration procedure, embedding the sample in resin, sectioning the whole sample in very thin pieces and placing staining thin sections on EM-grids. Second, the final cell's dataset is limited due to the fact that a relatively small area of cells can be imaged in detail (for example 1 µm x 1 µm section in order to see the details of mitochondria). Even for such a small area, to view a sample in TEM, the sections of 60-80 nm thickness must be carefully transferred onto metal grids and subsequently, the adjacent sections adhere to each other to make a ribbon of serial sections. In the end, the throughput of TEM imaging compared with fluorescence microscopy is much lower (Winey 2014).

Besides the limitations described above, due to the dehydration step, many small structures such as proteins go through conformational changes and cannot be resolved properly. Cryogenic TEM (CryoEM) has been developed as a method to immobilize biological molecules in a hydrated state which can be maintained within the vacuum of an electron microscope. The challenge of freezing biological material with a standard protocol is that the formation of ice crystals at best deforms and at worst destroys the sample. Samples are vitrified by plunge freezing into liquid ethane cooled down to liquid nitrogen temperatures, forming non-crystalline ice. Near-atomic resolution has been reached by exploiting the icosahedral symmetry of viral proteins (Zhang 2008). The DNA nanostructure has been studied at high resolution using CryoEM (Kato 2009) and many more detailed biological and cellular structures were revealed (Ciuffa 2015).

1.3.11. Super resolution fluorescence microscopy

In fluorescence microscopy due to the wave nature of light, diffraction at the aperture of the objective and all other optical components of the microscope is an inevitable phenomenon. In an optical system, the dimensions of a point object O(x, y) are broadened in the image I(x, y) due to its convolution with the point spread function (PSF) of the microscope (Pawley 2006).

$$I(x,y) = O(x,y) * PSF(x,y) \tag{1.13}$$

where the operator * is the convolution operator.

Consequently, the image of a structure consisting of several point light sources such as fluorophores appears blurred as well (see figure 1.17).

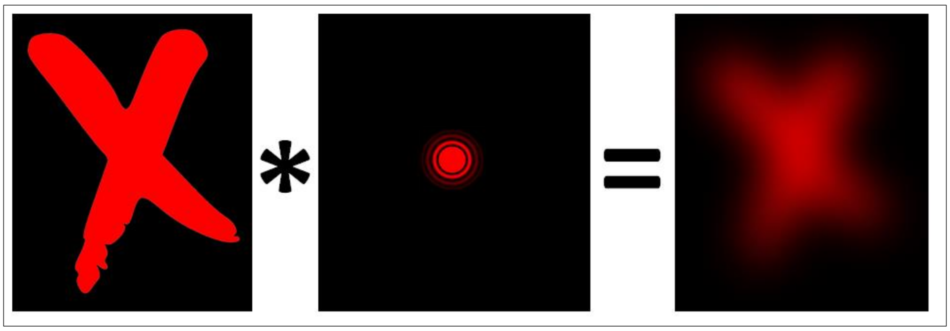

Figure 1.17. The dimensions of a fluorescent object are convolved with the point spread function (PSF) of the optical system. Consequently, a recorded structure appears blurred in the resulting image. Left: Structure (a cross); middle: PSF; right: recorded image.

From the beginning of 1990s, efforts have been made to bypass the resolution limit of fluorescence microscopy beyond the diffraction limit and hence provide a tool to reveal the structural detail of cellular and molecular samples with improved resolution down to single molecules (several nm) while keeping the advantage of fluorescence microscopy. From the innate nature of biological samples and the size of the relevant molecules (e.g. RNA, DNA, proteins) and structures (e.g. filaments, vesicles, membranes, membrane protein complies), it follows inevitably that the cell constituents are in close proximity, which is well below the resolution limit (200-300 nm) of the microscope, hence the spatial resolution is not sufficient for the details of the cellular and physiological processes. In principle, two classes of sub-diffraction resolution fluorescence microscopy techniques exist and many improvements are still implemented to this day in these two classes. First, in deterministic approaches, fluorescence emission is confined by creating a sub-diffraction excitation pattern as in stimulated emission depletion (STED) (Klar 2000) or introduce a known periodic spatial modulation of the excitation light (structured illumination (SIM)) (Gustafsson 2000). Second, in stochastic approaches fluorescence emission of single emitters is randomly read-out in space as in photoactivated localization microscopy (PALM) (Betzig 2006), fluorescence photoactivation localization microscopy (FPALM) (Hess 2006), stochastic optical reconstruction microscopy (STORM)(Rust 2006), and direct stochastic optical reconstruction microscopy (*d*STORM)(Heilemann 2008) and other special cases, all collected as Single Molecule Localization Microscopy (SMLM).

1.3.11.1. Stimulated Emission Depletion (STED) Fluorescence Microscopy

The idea behind STED is to quench a large fraction of excited fluorophore by stimulated emission in a confined spatial region (Hein 2008). This is achieved by using a laser scanning fluorescence microscope lacking a pinhole and two lasers (often pulsed lasers but CW lasers are also used), one laser for excitation and the second laser for de-excitation (parts of the molecules). The second laser beam is modified by a phase mask (for example an optical vortex phase plate composing of spirally constructed plastic sections) to generate a doughnut-shaped focus with a zero intensity mode in the center (figure 1.18). Fluorophores are excited by the first laser from S_0 -> S_1 and will emit normal fluorescence, when present in center of the doughnut profile of the depletion laser. The excited fluorophores, not in the center of the depletion laser, though, irradiated with sufficient powers of the depletion laser, will be depopulated (S_1 -> S_0) by stimulated emission, emitting a photon at the red-shifted wavelength of the depletion laser. A suitable optical bandpass filter in front of the detector will block photons at depletion laser wavelength while be transparent for the major part of the fluorescence spectrum. In order to prohibit re-excitation of the fluorophore after depletion, the pulse length of the excitation laser has to be short enough (usually fs).

Basically, variation of the intensity of the red-shifted depletion laser and engineering of the pupil of the objective modifies the PSF (figure 1.18) and provides a way to control the number of emitting fluorophores and their spatial distribution area. The achievable resolution can be described by

$$d = \frac{\lambda}{2n \sin\alpha \sqrt{1 + \frac{I}{I_{sat}}}} \tag{1.14}$$

where n is the refractive index of the medium, I is the depletion laser (STED beam) intensity and I_{sat} is the saturation intensity, the amount of required depletion laser intensity to outmatch the normal fluorescent S_1 -> S_0 transition (spontaneous emission). High excitation intensities of up to 1 GW/cm^2 for the STED beam are necessary in order to exceed I_{sat} and thus acquiring a resolution < 100 nm (Dyba 2003).

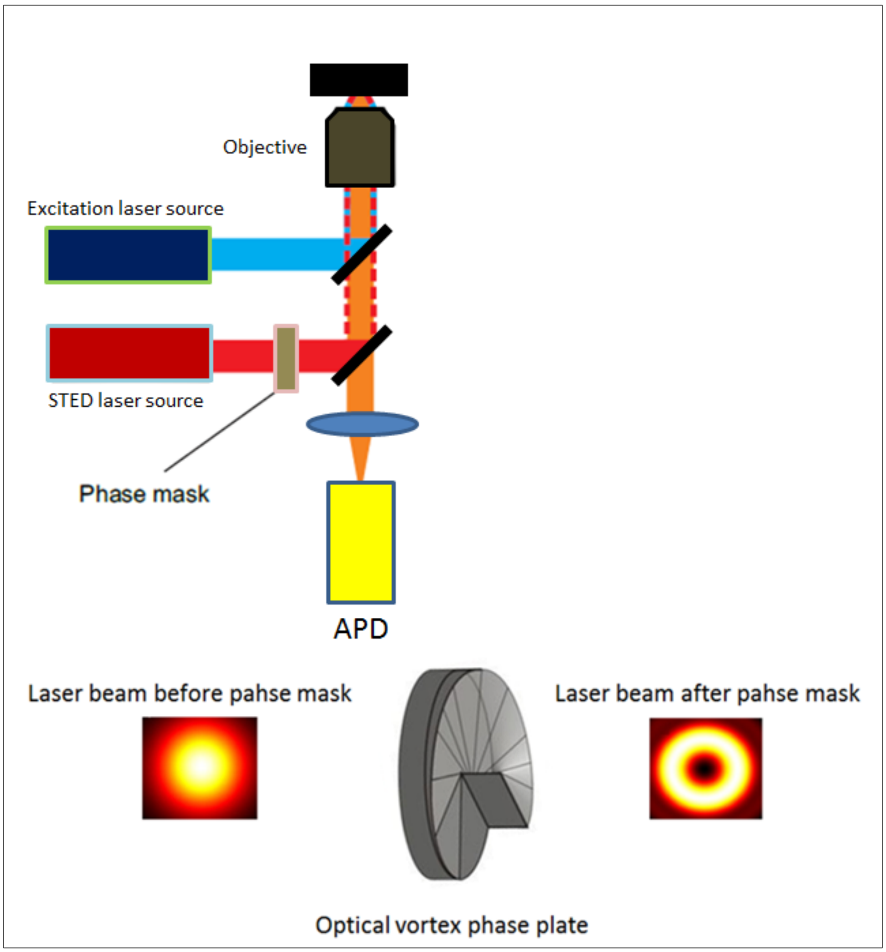

Figure 1.18. Principle of stimulated emission depletion (STED) microscopy. In this setup, two laser pulses are used, one for excitation of fluorophores and a second one for depletion of its excited state. The STED pulse is modified by a phase mask (an optical vortex phase plate depicted in the lower panel) in order to generate a doughnut profile with zero intensity in the center (lower panel, laser beam after phase mask). Therefore, only fluorophores in the center of the doughnut profile remain excited and fluoresce. By using high intensities of the STED beam, the remaining central area from which fluorescence is detected is narrowed. This is done by shrinking the effective PSF size (upper right panel). APD is highly sensitive semiconductor avalanche photodiode used as detector.

1.3.11.2. Structured Illumination Microscopy (SIM)

In structured illumination microscopy (SIM) the illumination pattern of the excitation light is modified. SIM relies on laser-based widefield microscopy setup in which a movable diffraction grating divides the laser beam in two separate beams. The two laser beams interfere with each other at the focal plane of the objective and create an illumination in stripes (intensity following sinusoidal wave). This stripe pattern of light by its superimposition with the sample generates a so-called Moiré effect (Gustafsson 2000, Ströhl 2016). In widefield microscopy, under homogeneous illumination, the PSF of the objective hinders the small spatial details in the sample. But under structured illumination, the overlap between the high frequency organization of the objects within the sample and the high frequency of the illumination stripes creates a pattern of lower frequency which is well collected by the objective (figure 1.19). In another word, the PSF limits the observation of high frequency details (components) of the sample, if one considers the frequency domain. In frequency domain, the maximum observable spatial frequency is formulated by $K_0 = \frac{2NA}{\lambda}$. The widefield microscope acts like a low-pass filter which only allows the detection of spatial frequencies lower equal than K_0. If a structured illumination pattern of frequency K_1 applies at a given orientation, the superposition of frequencies K (a spatial frequency for an object in sample which is between 0 and K_0) and K_1 is resulted to the Moiré patterns observable at frequency $K - K_1$. Therefore, for higher non-observable frequencies, the Moiré patterns observable at lower frequencies reveals some more details of the sample. By repeating the application of structured illumination pattern at various orientations to the sample, a broader range of frequencies can be detected, which in theory enhances the lateral and axial resolutions by a factor of 2 (Gustafsson 2000). To reconstruct the final super-resolved image, several raw images must be collected, each being acquired at different orientation (rotation and translation) of the structured illumination. This is done by moving the diffraction grating. The method is nowadays implemented in commercial microscopes allowing well improved 3D-imaging (comparable or faster than confocal fluorescence microscopy) (Shao 2011, York 2012, Heintzmann 2017, Gottschalk 2019). A disadvantage of the method is the need for very low photobleaching of the sample.

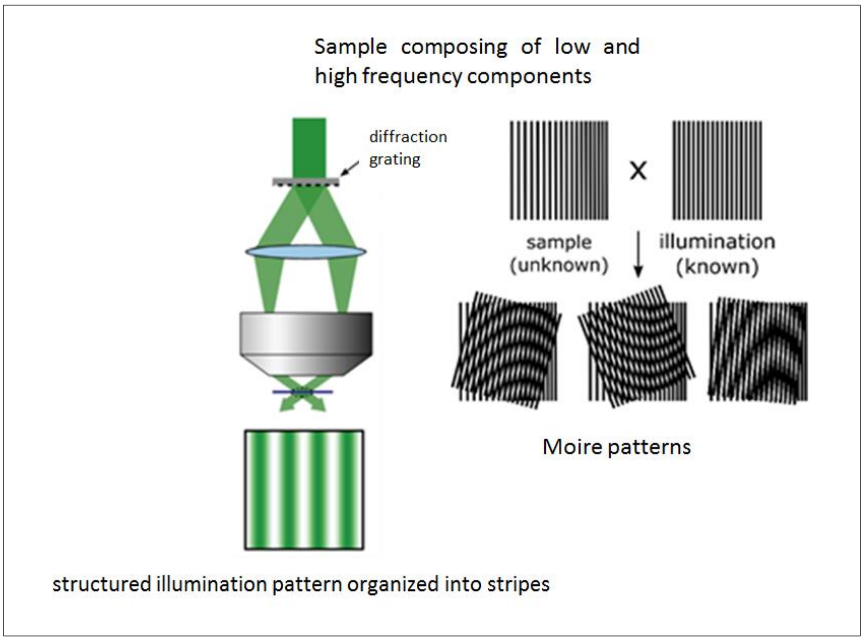

Figure 1.19. A diffraction grating divides incident laser light in two separate beams. The two beams interfere at the focal plane of objective creating interference fringes (stripes) with a fixed, known frequency K1. If

symbolically, a sample is shown by its contributing spatial frequency components (which are unknown), then illumination of sample with the structured pattern will be resulted in creation of Moire stripes with a given frequency. From the obtaining Moire pattern frequency, one can calculate the component frequency by which the final pattern was created. By this method, high frequencies that are not observable by microscope can be calculated by lower frequency Moire patters, expanding the range of details that a microscope can observe. By repeating the illumination of sample with different oriantatin of the structured stripes (both various rotation and translation), it is possible to reconstruct final images with higher frequency components detected which will be resulted to sharper images (image modified from https://andor.oxinst.com/learning/view/article/super-resolution-imaging-structured-illumination-microscopy).

1.3.11.3. Single Molecule Localization Microscopy (SMLM)

Even though single fluorescent molecules appear as blurred spots on a detector, the center of the molecule can be calculated with high precision (Thompson 2002). The intensity distribution of a single emitter is described by an Airy function and the position of the emitter can be approximated by fitting a mathematical model of the PSF to the registered intensity distribution. A simplified approach very often used is to fit a two-dimensional Gaussian function to approximate the PSF as follows:

$$\psi = \frac{A}{2\pi\,\sigma_x\sigma_y}\exp(-\frac{1}{2}\left(\frac{x-x_c}{\sigma_x}\right)^2 - \frac{1}{2}\left(\frac{y-y_c}{\sigma_y}\right)^2) \qquad (1.15)$$

where A is the amplitude, x_c and y_c are the coordinates of the center of the spot and σ_x and σ_y are the standard deviations in x and y direction, respectively. In terminology of single molecule microscopy, such a position determination is termed *localization*.

The fitting of a two dimensional Gaussian distribution to each detected fluorescence intensity point profile is described by an uncertainty termed as the localization precision. One can estimate that the localization precision increases with the number of detected photons from a single molecule. In widefield and TIRF fluorescence microscopy as used in SMLM the photons from a single molecule are collected with a (EM)CCD or CMOS camera and distributed over pixels. When detecting N photons, different noise sources contribute to the total uncertainty of the estimated coordinates. The finite size of the pixels results in pixelation noise, background signal b originates from out-of-focus fluorescence, auto-fluorescence (of usually many but dim emitters) and scattered excitation light, and the camera has its own dark noise. The localization uncertainty in x and y dimensions is given as

$$\sigma = \sqrt{\frac{s^2}{N} + \frac{\left(\frac{a^2}{12}\right)}{N} + \frac{4\sqrt{\pi s^3 b^2}}{aN^2}} \qquad (1.16)$$

where s is the standard deviation of the PSF, a is the size of the pixel, N is the number of detected photon from a single emitter, and b is the background noise (Thompson 2002). For high photon numbers, background noise becomes negligible and the localization uncertainty of single emitters can be approximated by $\sqrt{\frac{s^2}{N}+\frac{\left(\frac{a^2}{12}\right)}{N}}$. For example, detecting 1000 photons for a fluorophore with s = 160 nm predicts σ = 5.1 nm (Thompson 2002).

Localization of single-molecules enables position determination well below the diffraction limit of light microscopy. In reality, in most study objects including biological samples, fluorophores exist very densely within the area of the size of the diffraction limit. Single molecule localization is not possible if all fluorophores are emissive simultaneously. Instead, fluorophores within a diffraction limited region must be distinguishable from each other. This can be realized by using fluorophores which can be switched between emissive (on) and non-emissive (off) states (often called blinking). The mechanism behind the blinking is different for different suitable fluorophores. It has already discussed various FPs in sections 1.3.6 to 1.3.8. All FPs used in SMLM belong to the classes of photoswitchable, photoconvertible, or photoactivatable FPs. The goal however, is the same; reduction of the number of emissive fluorophores in individual images, so that all emitters in the image can be localized. Once such a level of fluorophores in on-state is achieved, one only has to measure enough images, always with different subsets of on-state fluorophores, to generate a high quality image with sub-diffraction limit resolution. From here on, the term single molecule localization microscopy used to refer to a technique that uses such a procedure to localize single molecule emitters for the sake of achieving super resolution images.

Assume a subcellular structure that is densely labeled with photoswitchable fluorophores such as EYFP. To achieve a super-resolution fluorescence images, fluorophore emission has to be separated in time. The majority of photoswitchable molecules are switched into the non-emissive dark state and only a small fraction of molecules is allowed to stay in the fluorescent on-state. A time series of image frames with different subset of fluorophores being in emissive state is recorded. Basically, to resolve single molecules, individual fluorophores must be separated well beyond the distance resolved by the microscope. In every single image of the all recording image series, all single emitter spots from individual molecules are fitted by a two-dimensional Gaussian profile to its emission pattern. Finally, plotting all localizations a single super-resolved image is calculated (see figure 1.20). The resolution of such reconstructed images is considerably better (in the best case a few nm

(Baldering 2019), typically 20-30 nm) than the conventional fluorescence images (200-400 nm).

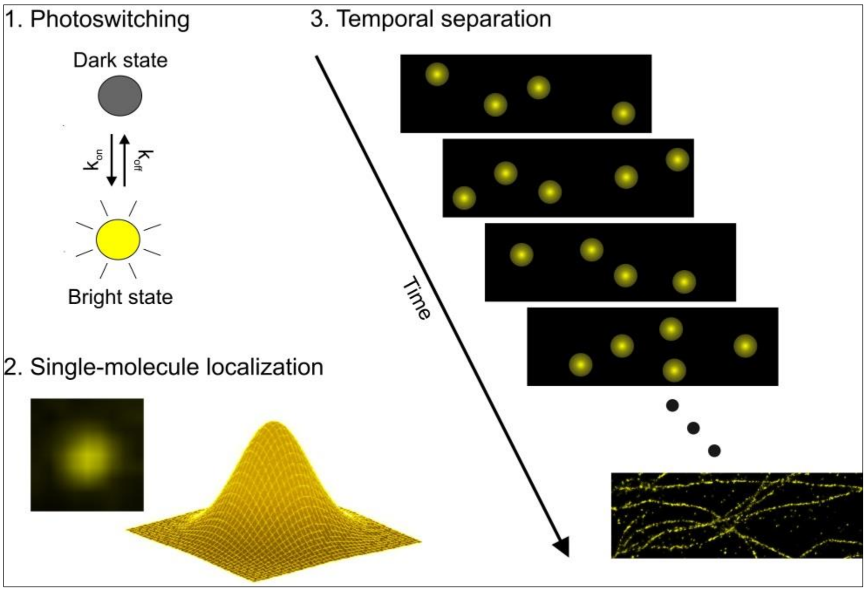

Figure 1.20. Principle of SMLM. Switching fluorophores between a dark and a bright state enables temporal separation of fluorophores. Fitting of point-spread functions of single emitters with a simple 2D Gaussian profile, allows accurate position determination. Super-resolution images can then be reconstructed (image taken from the group of M. Heilemann with his permission (https://www.uni-frankfurt.de/49962827/Methods)).

Single molecule localization microscopy (hereafter SMLM) methods like Stochastic Optical Reconstruction Microscopy (STORM), direct Stochastic Optical Reconstruction Microscopy (*d*STORM), and Photoactivation Localization Microscopy (PALM) allow an increase of optical resolution down to ~20 nm in lateral and ~50 nm in axial direction (Galbraith 2011). In figure 1.21, an example of fluorescence imaging of nuclear pore complexes (NPRs) with conventional microscope and using dSTORM is given. All methods rely on the usage of fluorescent emitters that can be stochastically switched between an emissive bright and a non-emissive dark state.

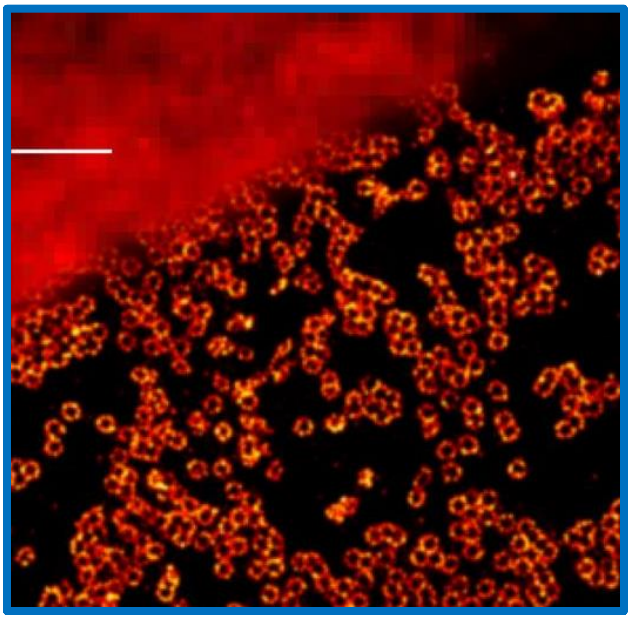

Figure 1.21. Comparison of widefield fluorescence (upper left corner) and dSTORM image (lower right corner) of Nuclear pore complexes isolated from Xenopus laevis oocytes. The structures were labeled by immunofluorescence using the primary antibody X222 directed against an epitope located in the lumen of the nuclear envelope bordering the pore wall and Alexa647 labeled secondary antibodies. Scale bar: 1 µm (adopted from Löschberger 2012). With permission from the publisher (Order license ID 1008461-1).

The difference between STORM, dSTORM, and PALM lays in the nature of the fluorescent label. For a successful STORM measurement and a good blinking behavior, a pair of activator-reporter dyes linked e.g. to an antibody is used. While the multiple activator-reporter pairs allow multicolor STORM applications, this system requires dual labelling of the same target and relies on close proximity of the two fluorophores. The first activator-reporter pair used for STORM was Cy3-Cy5 (Rust 2006, Bates 2011). A series of cyanine dyes (including always Cy5 as reporter fluorophore) with distinct absorption and emission spectra displayed robust photoswitching behavior when paired with a Cy3 molecule in close proximity. The Cy3-Cy5 pair was conjugated to double-stranded DNA or antibody and immobilized on microscope slides for single molecule detection in a buffer solution containing β-mercaptoethanol, a small primary thiol and an enzyme-based system for reduction of O_2 in the solution. Upon illumination with a red laser (657 nm), Cy5 was initially fluorescent and then quickly switched into a non-fluorescent, dark state. A brief exposure to a green laser pulse (532 nm) led to reactivation of the Cy5 back to the fluorescent state through fluorescence resonance energy transfer. Without a proximal Cy3, the reactivation of Cy5 was barely detectable under the excitation conditions. Cy3 dye then was referred as the activator. The reporter typically can be switched on and off for hundreds of cycles before permanently photobleaching. In figure 1.22, a simplified mechanism of Cy5-Cy3 photoswitching is depicted.

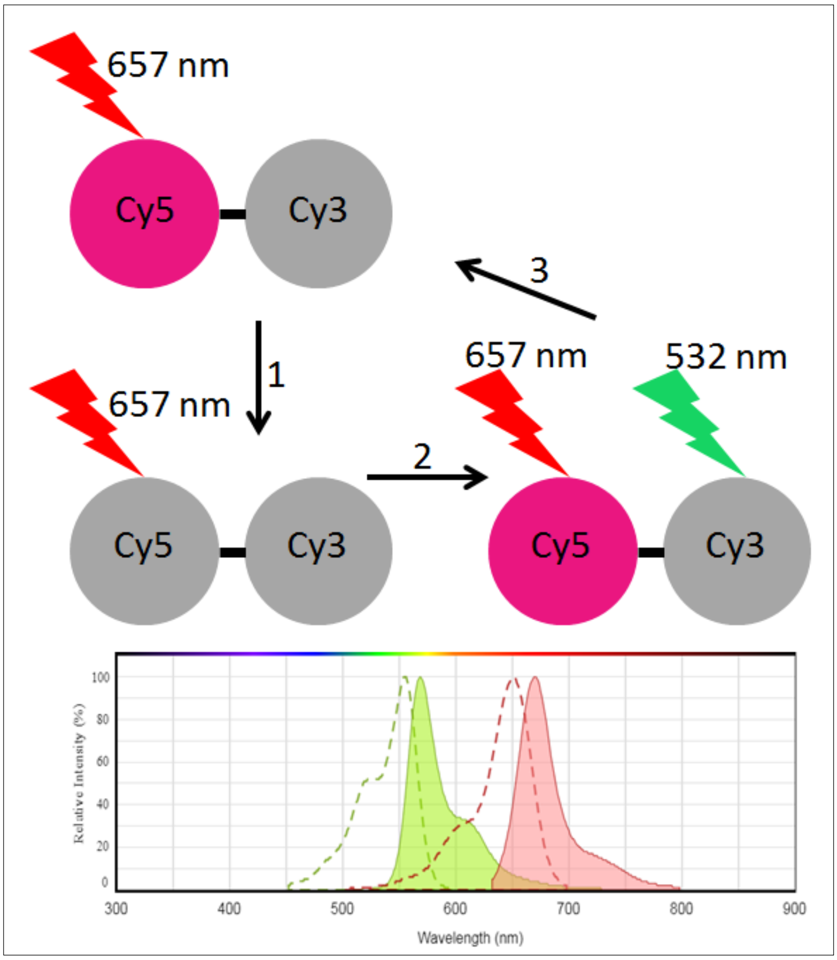

Figure 1.22. Cy3-Cy5 activator-reporter pair enabling the STORM-like SMLM microscopy. Both cyanine dyes are immobilized in close proximity. Excitation of Cy5 with red laser makes it to emit (1) and shortly after to enter a long-lived non-emissive state due to the presence of thiol which covalently alters the chromophore and forced it into dark state (2). Illumination with a low power, short pulse of green laser, which is in the absorption range of Cy3 dye, reactivates Cy5 to the emissive state. The lower panel represents the absorption and emission spectra (dashed graph and solid graph, respectively) for Cy3 (green) and Cy5 (red).

In *d*STORM, on the other hand, only one single dye is presented and the need for an activator dye was eliminated. Fluorophores that can be photoswitched include the widely available carbocyanine dyes (e.g. Alexa Fluor 647, Cy5) and rhodamine class dyes (e.g. Alexa Fluor 488, Atto 532). The conversion to a long-lived dark state is thought to involve photo-reduction of the excited triplet state into energetically stabilized radical anions. The formation of a dark state upon excitation is facilitated by the presence of a thiol group, such as β-mercaptoethylamine. Conversion back to a bright state involves oxidation of the reduced radical back to the singlet ground state (van de Linde 2011). Photoswitchable fluorophores attracted considerable interest as molecular electronic and photonic devices

(Sauer 2005) and are currently the fundament of most SMLM microscopies (Heilemann 2009). As depicted in figure 1.23, common to all photoswitchable fluorophores is a transition from a metastable non-emissive dark state from which no detectable fluorescence is observed to a fluorescent emissive on-state. SMLM imaging requires that most of the fluorophores reside in their dark state and only a fraction of fluorophores is allowed to be fluorescent at any time.

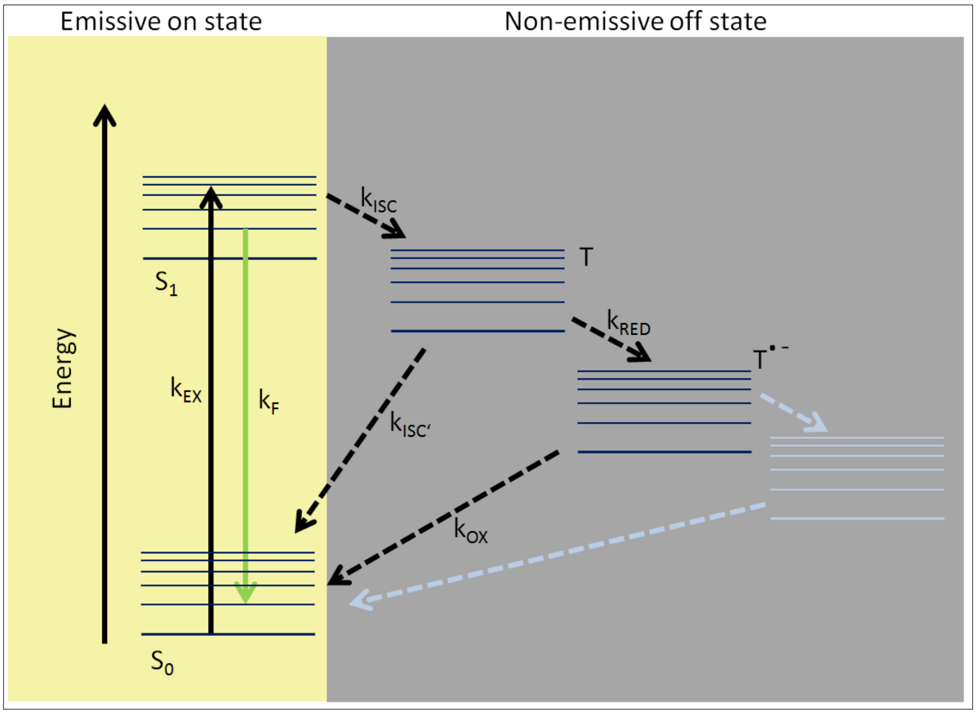

Figure 1.23. Photophysical processes underlying reversible photoswitching of dSTORM dyes (for the sake of simplicity internal conversion processes and phosphorescence are not shown). After excitation of the fluorophores (k_{exc}) into their first excited singlet state S_1, the excited state energy is either depopulated through fluorescence emission with rate k_f, or the triplet state is occupied (k_{ISC}). The triplet state T is either depopulated ($k_{ISC'}$) or reduced by thiol (k_{RED}) to form radical anion T^{*-}, which is reoxidized by molecular oxygen with rate k_{OX} or reacts to other non-fluorescent species (modified from Heilemann 2009) with publisher permission (License number: 4742471050300).

The development of PALM as biophysical super-resolution imaging method with easy and versatile fluorescence targeting abilities and live cell imaging capabilities was largely prompted by the discovery of new fluorescent proteins species and the engineering of mutants of FPs displaying a wide range of emission spectra and controllable blinking such as photoactivatable GFP, Kaede, mEOS, Dendra2. A detailed explanation of these FPs is presented in sections 1.3.7 and 1.3.8. Although the technical handling SMLM measurements using photoactivatable, photoswitchbale, and photoconvertible FPs for PALM is not different from SMLM with synthetic fluorescent dyes suitable for STORM and dSTORM, the biological impacts of using either of mentioned techniques can differ significantly.

A great range of new applications in cell biology took advantage of genetically encoded FPs suitable for PALM (Shcherbakova 2014). In the following section, a short overview on the application of PALM and STORM/dSTORM will be given.

The distribution of Nucleoid-Associated Protein HU in *Caulobacter crescentus* before investigation with the use of PALM received little attention. In group of W.E. Moerner, PALM imaging of EYFP as a reversible photoswitchable FP revealed the spatial distribution of HU2-EYFP in fixed bacteria cells (Lee 2011). In addition, this study proved the suitability of EYFP in a dSTORM-like fashion while illuminated with high laser power in order to force it into non-emissive, slowly returning dark state(s). This example was a good agreement between super resolution images and theoretically modeled distribution of proteins (see figure 1.24).

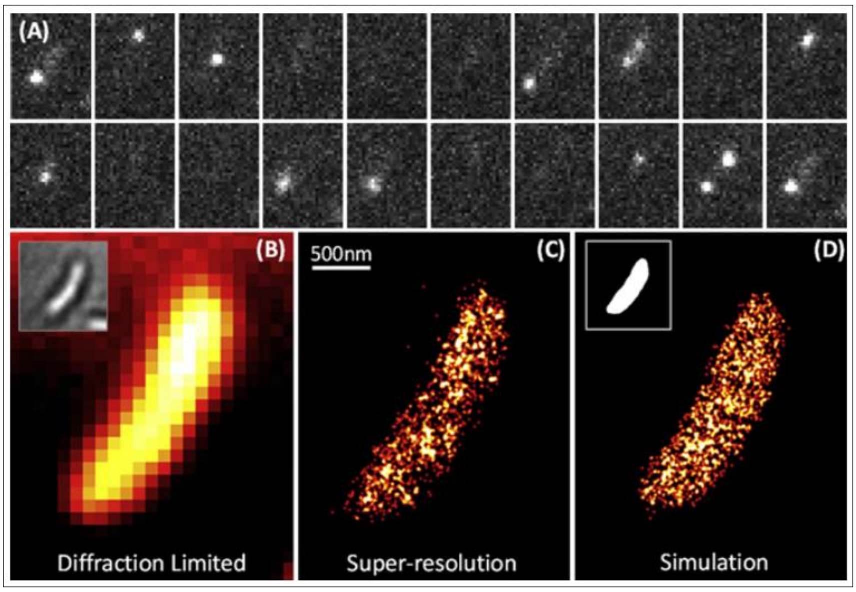

Figure 1.24. PALM imaging of HU2-EYFP in fixed C. crescentus. (A) Frames of raw data (10 ms each) showing the blinking of EYFP achieved through the use of a single 514 nm laser. (B) A diffraction-limited image of HU2-EYFP with a white light transmission image in the inset. (C) PALM image of HU2-EYFP. (D) Monte Carlo simulated image of a random distribution of molecules inside a model cell volume (inset) (modified from (Lee 2011)). With permission from the publisher (License Number 4725820048539).

The list of application of SMLM in cell and molecular biology has been expanded over the years and it is impossible to sort the entire application of SMLM in those areas. In table 1.5, some selected application examples of different SMLM techniques are given. Due to the large number of SMLM users and published papers, there exist no total collection of SMLM-studies with relevant results in cell biology but the following reviews list a few more: Leterrier 2017, Sahl 2017, and Sauer 2017.

Table 1.5. A short selected research articles with the PALM, STORM, and dSTORM as the primarily microscopy technique. With publisher permission (License Number 4725830865064).

Biological super-structure(s)	**Significance/comments**	**References**
Integrin-based focal adhesions	Integrins and actin are vertically separated by a ~40-nm focal adhesion core region consisting of multiple protein-specific strata including integrin talin, a further component, has polarized orientation, indicating a role in organizing the focal adhesion strata	(Kanchanawong 2010)
MreB, CreS, PopZ, FtsZ in *C. crescentus*	Cytoskeletal and polar as well as midplane-located protein superstructures in live bacteria	(Biteen 2008, Lew 2011, Gahlmann 2013, Biteen 2012)
Aggregates of mutant huntingtin exon 1 protein	Fibrillar aggregates, possibly transient protofibrils, with a sharp cut-off length of ~1.5 µm observed to co-exist with mature inclusion bodies	(Duim 2014, Sahl 2012)
Cycling nitro-reductase	Visualization in live *B. subtilis*	(Lee 2013)
Sodium channels in live neuronal model cells by fluorescent saxitoxin	Novel labeling by *de novo* synthesis of fluorescent forms of saxitoxin, fast (<10 s) dynamics of neuritic spine movements	(Ondrus 2012)
Nucleosome-binding protein HU in live *C. crescentus*	Spatial point statistics analysis (2D) of chromosomal DNA	(Lee 2011)
ParA/ParB in live *C. crescentus*	Division spindle components for chromosome segregation	(Ptacin 2010)
Chemotaxis network in *E. coli*	New model triggered for localization patterns	(Greenfield 2009)
Actin and spectrin	Highly periodic protein arrangements in axons	(Xu 2012, Xu 2013)
Synaptic proteins Bassoon and Homer1	Organization of key proteins at the synapse in brain tissue	(Dani 2010)
Spine and excitatory synapse density in the hippocampus (bassoon and glutamate receptor 1/2)	Afadin, a Ras/Rap effector, is a key intracellular signaling molecule for cadherin recruitment and is necessary for spine and synapse formation *in vivo*	(Beaudoin III 2012)
Podosome formation and dissociation	Visualized using an mCherry-tagged truncated talin construct (live cell)	(Cox 2012)
DNA	Direct dye labeling	(Benke 2012)
Various organelles	Live cell, high temporal sampling using membrane probes (1–2 s/SR reconstruction)	(Shim 2012)
Proteins central to centrosome formation	The carboxy terminus of pericentrin-like protein (PLP) is revealed to be at the centriole wall, radiating outwards into a matrix domain where it is organized into clusters having quasi-nine-fold symmetry	(Manella 2012)
Myosin–Actin motility		(Endesfelder 2010)
Formation of a protein corona	dSTORM of Cy5 labeled protein	(Feiner-Gracia 2017)
DHPR and RyR2 clusters with pressure-overload cardiac hypertrophy	dSTORM based on Alexa Fluor 647	(Hadipour-akmehsari 2019)
Structural features of nuclear F-actin at mitotic exit	PALM of nuclear actin filaments in fixed NIH3T3 cells stably expressing nAC-Dendra2	(Baarlink 2017)

1.4. Using super resolution microscopy technique in autophagy

During our literature review on the investigation of autophagy related proteins and autophagosome biogenesis, several studies found using different super-resolution fluorescence microscopy techniques to monitor the role of Atg proteins with high spatial resolution.

To reveal the mechanism of autophagosomes fusion with lysosomes or with endosomes with high resolution, Kumar et. al. used dSTORM to monitor the interaction of Q_a-SNARE syntaxin 17 (Stx17) with mammalian Atg8 family proteins. The conclusion of their study was the existence of an interaction of Stx17 with LC3 molecules. dSTORM images analysis showed that both molecules are in close proximity even though not in perfectly overlapping areas (Kumar 2018).

As discussed earlier (subchapter 1.1.1), regarding the role of Atg9 positive vesicles to regulate the translocation of membrane structures from ER, Karanasios et. al. used super-resolution microscopy (dSTORM) and classified the autophagic structures with their geometrical parameters. They showed that the accumulation of ULK1 compartments progressively turning into spherical structures in association with Atg9 molecules in early stages of autophagy is responsible for the initiation of autophagy (Karanasios 2016).

The interaction of LC3 molecules with actin filaments has been investigated with the help of SIM microscopy to reveal that the actin positive punctae are inside the isolation membranes. In this study, Mi et. al. represented the contribution of the actin-capping protein (CapZ) as the regulators of actin polymerization with PtdIns(3)P, which is enriched in omegasomes and one of the key proteins in autophagy (Mi 2015).

The formation of autophagosome at PAS is believed to be the result of plasma membranes mainly coming from ER. Nascimbeni et. al. by using STED microscopy studied the regulation of the pool of PI3P proteins, which are engaged in autophagosomes growth, by ER-plasma membrane contact sites (Nascimbeni 2017).

Using 3D-SIM microscopy, Smith et. al. enlightened the role of cargo receptor cell-cycle progression gene 1 (CCPG1) and its direct binding to core autophagy proteins via an LIR motif to mammalian Atg8 proteins (Smith 2018).

There are studies by using SIM microscopy to reveal the suggested interaction between autphagosome and several intracellular organelles for platelet adhesion to the injured vessel wall by monitoring the proximity of autophagic structure with the injured vessel wall (Torisu 2013).

1.5. Scientific questions that will be addressed in the current work

In the current study, SMLM technique is used to investigate several scientific questions in the field as follows:

(1) The distributions of sizes and shapes of structures labelled by different Atg8 protein family GABARAP and LC3B.

(2) The differential localization of GABARAP and LC3B (representing the two Atg8 subfamilies), which is closely related to their functions on a molecular level.

(3) To which extent, monitoring the localization of different Atg8 family proteins GABARAP and LC3B using SMLM can be linked to their distinctive roles in autophagy.

(4) Are there real advantages of using super-resolution (in our case SMLM) microscopes instead of conventional fluorescence widefield or confocal microscopes?

(5) How to optimize the EYFP usage in SMLM measurements.

2. Materials and Methods

2.1. Eukaryotic Plasmids

The plasmids used for transient transfection of mammalian cells in this thesis and for generation of stably HEK-293 transfected cell lines which are used in this thesis are given in table 2.1.

Table 2.1. Genetically encoded fluorescent protein fusion plasmids that are utilized for both transient transfection of mammalian cell lines and for generation of stably transfected HEK-293 cell lines.

Plasmid	**Restriction sites for FP fusion protein (insertion of FP-Atg8 in plasmid)**	**Manufacturer of the plasmid**	**Manufacturer of the FP**
peYFP-C1-GABARAP	XhoI and BamHI	Addgene plasmid #73948, Addgene, Watertown, MA, USA	Clontech, Mountain View, CA, USA
peYFP-C1-LC3B	XhoI and BamHI	Addgene plasmid #73948, Addgene, Watertown, MA, USA	Clontech, Mountain View, CA, USA
pDendra2-C-GABARAP	XhoI and BamHI	Addgene plasmid #73948, Addgene, Watertown, MA, USA	Evrogen JSC, Moscow, Russia
pDendra2-C-LC3B	XhoI and BamHI	Addgene plasmid #73948, Addgene, Watertown, MA, USA	Evrogen JSC, Moscow, Russia
mCherry-LAMP1	--	R. Guzman (ICS-4) Based on RFP-LAMP1 (Addgene 1817)	Clontech, Mountain View, CA, USA

2.2 Cell lines

For SMLM microscopy three different cell lines were used to visualize GABARAP and LC3B proteins in cells, their distribution, and their interaction with other cellular structures. They are listed in table 2.2.

Table 2.2. Different cell lines used in this work.

Cell line	**Fusion protein to be transfected in or to be expressed stably**
HEK-293	EYFP-GABARAP, EYFP-LC3B, mCherry-Lamp1
HEK-293 stably expressing Dendra2-GABARAP	Dendra2-GABARAP
HEK-293 stably expressing Dendra2-LC3B	Dendra2-LC3B
HEK-293 stably expressing EYFP-GEC1	EYFP-GEC1

2.3. Phosphate-Buffered Saline

Phosphate-Buffered Saline (PBS) was used as the primary buffer solution for cell washing, dilution of other solutions, and imaging buffer for EYFP and Dendra2 in all experiments in this work. For a PBS 10X stock solution, the following chemicals were used. Amount of 80.1 g NaCl (CAS No. 7647-14-5, Sigma-Aldrich, Munich, Germany), 2 g of KCl (CAS No. 7447-40-7, Sigma-Aldrich), 14.4 g of Na_2HPO_4 (CAS No. 7558-79-4, Sigma-Aldrich), and 2.4 g of KH_2PO_4 (CAS No. 7778-77-0, Sigma-Aldrich) were added to 800 ml distilled water. The pH value was adjusted to 7.4 by addition of several droplets of 1M HCl and finally, the final volume, by addition of distilled water, brought to 1 l.

2.4. Cell Culture and Transfection

Human embryonic kidney 293 cells (HEK-293 (Graham 1977); Leibniz-Institute DSMZ–German Collection of Microorganisms and Cell Cultures, Braunschweig, Germany) and HEK-293 cells stably expressing Dendra2-GABARAP and HEK-293 cells stably expressing Dendra2-LC3B were cultivated at 37 °C in a 95% humidified incubator at 5% CO_2 in Dulbecco's Modified Eagle's Medium (DMEM, Cat. No. D5796, Sigma-Aldrich) supplemented with 1% (v/v) penicillin/streptomycin (P/S, Sigma-Aldrich) and 10% (v/v) Fetal Calf Serum (FCS, Sigma-Aldrich). This medium was utilized in all experiments of this work as the fed condition medium. HEK-293 cells are adherent cells and need to be seeded on a surface to grow. HEK-293 cells were split regularly in a 1:10 ratio every 48 h (10% of cells were kept with fresh medium in a new cell culture flask while 90% were discarded) in order to reach ~ 85% confluence at the point of splitting, when being ready for imaging or for the next round of cultivation. The splitting protocol consists of two stages, namely harvesting and seeding. Cells that had reached the desired confluence after 48 h were taken out of the incubator and first washed one time with PBS 1X pH 7.4 solutions. Then subsequently 1 ml Trypsin/EDTA (MDL: MFCD00130286, Sigma-Aldrich) was added and stayed for three minutes in incubator of the cells in order to let them detach from the surface of the cell culture flask. After incubation, 9 ml of medium was added to the Trypsin/EDTA solution. The entire solution containing cells were mixed gently by pipetting two to three times, and finally re-cultivated in a new culture flask with the 1:10 ratio or seeded on a ibidi container (µ-dish; glass bottom for microscopy, Cat. No. 81158, ibidi, Martinsried, Germany) for further imaging experiments with ~ 4 or 5 x 10^4 cells per chamber. For transient transfection of HEK-293 cell, 6 x 10^5 HEK-293 cells were seeded into a 6-well culture plate (Cat. No. 10062-892, VWR, Randor, PA, USA) containing DMEM with 10% FCS and 1% Penicillin-Streptomycin (P/S). On the next day, transfection with 1.2 µg of either EYFP-GABARAP or EYFP-LC3B or 0.5 µg mCherry-Lamp1 DNA constructs was performed using the transfection reagent Polyfect (Cat. No. 301107, QIAGEN, Hilden, Germany) according to the manufacturer's instructions as follows:

1. The day before transfection, seed 6 x 10^5 cells per 35 mm dish in 3 ml of the growth medium.
2. Incubate the cells at 37°C and 5% CO_2 in an incubator. The dishes should be 40–80% confluent on the day of transfection.
3. Dilute 2 µg of DNA (minimum DNA concentration: 0.1 µg/µl) with cell growth medium containing no serum, proteins, or antibiotics to a total volume of 100 µl. Mix and spin down the solution for a few seconds to remove drops from the top of the tube.
4. Add 20 µl of PolyFect transfection reagent to the DNA-containing solution. Mix by pipetting up and down five times, or by vortexing for 10 sec.
5. Incubate samples for 5–10 min at room temperature (20–25°C) to allow complex formation.
6. While complex formation takes place, gently aspirate the growth medium from the dish and add 3 ml of fresh cell growth medium (containing serum and antibiotics).
7. Add 1 ml of cell growth medium (containing serum and antibiotics) to the reaction tube containing the transfection complexes. Mix by pipetting up and down twice, and immediately transfer the total volume to the cells in the 35 mm dishes. Gently swirl the dish to ensure uniform distribution of the complexes.
8. Incubate cells for 24 h with the complexes at 37°C and 5% CO_2 to allow for gene expression.

The following day, 4-5 x 10^4 of the transfected cells were seeded into a fibronectin (Fibronectin bovine plasma; CAS No. 0086088837, Sigma-Aldrich) coated µ-dish (ibidi) containing DMEM with 10% FCS and 1% P/S. They were cultivated for another day in the incubator. The fibronectin solution was 1:1000 (v/v) of fibronectin in PBS 1X pH7.4. All ibidi containers were coated with this solution for 1 h at 37 °C to prepare an adhesive bottom for cells to grow on.

2.5. Starvation and autophagosome-lysosome fusion blockage

Transfected HEK-293 cells with EYFP-GABARAP, EYFP-LC3B, or mCherry-Lamp1 as well as HEK-293 cells stably expressing Dendra2-GABARAP and stably expressing Dendra2-LC3B were starved with Hank's Balanced Salt Solution (HBSS, Cat. No. 14025050, Thermo Fisher Scientific, Waltham, MA, USA). It was previously established in our research group that incubation of cells with HBSS for 2 h at 37 °C in incubator is enough to stress HEK-293 cells and enhance autophagy. For accumulation of autophagic structures in cells, 100 nM bafilomycin A1 (CAS No. 0088899552, Merck KGaA, Darmstadt, Germany) was used as an autophagosome-lysosome fusion blocking agent along with HBSS (Klionsky 2008). In all experiments of this work the term starved-blocked is used to indicate the presence of bafilomycin inside HBSS solution as the agent to starve cells and to prevent the autophagosome-lysosome fusion.

It was not found any meaningful effect on the quantity and quality of autophagic structures when starvation prolonged for more than 2 h (it was stablished by former PhD student in our group; Dr. Alexandra Boeske (ICS-6)). Instead, when the starvation process performed for more than 3 h, cells started to change their morphology to round shape and detached from the surface of the chamber, which is a signature for cell degradation. In order to minimize initiation of starvation of cells through other stresses, the processes of cell culture such as rinsing, seeding, starvation-blockage buffer addition, etc. were performed as quick and gentle as possible. Starved-blocked solution warmed up at 37 °C prior to the usage to minimize any unwanted stress on cells.

2.6. Fixation

A fixation procedure was previously used in our group that minimizes alterations to cytoskeleton components (Allen 2013) suitable for preserving SMLM measurement of cytoskeleton (Tang 2016, Conard 2018). In all the experiments in this work, the same fixation protocol was used in order to follow the standard protocols that have been already established in our group. Prior to the fixation, the cells were incubated in pre-warmed cytoskeleton buffer at 37 °C (phosphate-buffered saline (PBS, 137 mM NaCl, 2.7 mM KCl, 1.8 mM KH_2PO_4, 10 mM Na_2HPO_4, pH 7.4) containing 4 mM EGTA) for 5 min. Subsequently, cytoskeleton buffer was replaced with fixation solution (4% (w/v) paraformaldehyde in cytoskeleton buffer). Fixation took place at room temperature for 10–15 min. After that, cells were rinsed three times with 1 M glycine in PBS 1X pH 7.4 in order to wash entirely the remaining PFA solution off cells to minimize their desturbing fluorescence signals, and two times with PBS 1X pH 7.4.

2.7. Microscope components and setup for super-resolution imaging

The microscopy setup is based on an inverted microscopy body (Olympus IX-71, Olympus, Hamburg, Germany). Schematic drawings of the microscopy setup are shown in figures 2.1 and 2.2. The samples are mounted on a nano-positioning system (Physik Instrumente (PI) GmbH & Co., Karlsruhe, Germany) for precision motion and control of lateral and axial position. Four different lasers - 405 nm diode laser, a 454/488/514 nm argon-ion laser, a 561 nm diode laser and a 642 nm diode laser (table 2.3) are used as excitation sources. The 405 nm diode laser is controlled digitally via computer and its power supply, while an acousto-optic tunable filter (AOTF; AA OPTO-ELECTRONIC, Orsay, France) is used to switch between the three other laser lines (561, 642, and one of the Argon laser lines) and control their output intensity. The laser light is guided to the back focal plane of the microscopy via broadband dielectric mirrors (reflective in 450-700 nm range) (figure 2.1 and table 2.4; (5); Thorlabs, Dachau, Germany) and appropriate dichroic mirrors. The laser beams are expanded (~ 10-fold) via the incorporation of two achromatic lenses (figure 2.1 and table 2.4; (2) and (3)) with different focal lengths (20 mm and 200 mm). Another lens (figure 2.1 and table 2.4, (4), focal length 500 mm) is used to focus the expanded laser beams on the back focal plane of the objective (60x Apo N TIRF, NA 1.49, Olympus, Hamburg, Germany). Lens (4) and an adjustable mirror are located on a movable stage. Positioning the stage allowed the laser beam to hit the objective either in the center (widefield mode), or off-center near the rim (in figure 2.1, the widefield configuration is shown). For excitation of the samples, laser light is guided onto the objective by a dichroic mirror placed in the microscopy body (figure 2.1 and table 2.4; (6)). Emitted fluorescent light is collected by the objective and passed through the dichroic mirror (transparent for fluorescence light) in the microscopy to ensure separation from the excitation laser light and is then guided to the left output of the microscope port of the IX-71 body. Light is filtered by a suitable emission multi-bandpass filter (table 2.4, (9)) before it was detected. The emitted fluorescence light is detected with a cooled (-75 °C) AndorTM iXon EMCCD camera (Andor Technology, Belfast, Northern Ireland; 512 x 512 pixels per image; figure 2.1), which is mounted on a moveable stage. In combination with a moveable achromatic lens ((8), focal length 50 mm; figure 2.1 and table 2.4), a variable post- objective zoom of 2.05x to 4.2x is achieved, which results in a variable effective size of the object in the image plane on the EMCCD camera. Together with a 60x objective the final pixel size of the images can be varied between approximately 63 nm and 130 nm. In the experiments of this thesis usually a pixel size of 80 nm (200-fold magnification) was used. The whole system is controlled with a program developed by Dr. Johnny Hendriks (ICS-4, Research Centre Jülich).

Table 2.3. Light sources for excitation.

Light Source	Product	Control	Company	No. in figure 2.2
405 nm diode laser	Cube 405-100C, 100 mW	Digital	Coherent	22
Ar ion laser (488 nm and 514 nm)	Innova 70C, 5 W	AOTF	Coherent	23
561 nm diode laser	Sapphire 561-200 CDRH-CP, 200 mW	AOTF	Coherent	24
642 nm diode laser	LBX-642-130 CIR-PP, 130 mW	AOTF	Oxxius	25
Cold white (6500K) LED	MCWHL2, 650 mW	Analog	Thorlabs	

Table 2.4. Components for the super-resolution microscopy.

Type	Product	Remark	Company	No. in figures 2.1 and 2.2
mirror	BB1-E02	400-750 nm	Thorlabs	7, 11, 15, 17, 18-21, adjustable mirror
	BB2-E02	400-750 nm	Thorlabs	5, adjustable mirror
dichroic mirror	DMLP605	50% trans. 605 nm	Thorlabs	16
	DMLP505	50% trans. 505 nm	Thorlabs	14
	DMLP405	50% trans. 405 nm	Thorlabs	12
	F73-866	BS R405/488/561/633	Analyzentechnik	6, carousel
	BrightLine triple-edge laser-flat dichroic beamsplitter	Di01 R442/514/561	Semrock	6, carousel
emission filter	BrightLine fluorescence filter	FF03-525/50	Semrock	9
	BrightLine fluorescence filter	FF01-550/88	Semrock	9

	BrightLine multiband filter	485-537-627	Semrock	9
achromatic lenses	ACN127-020-A	ARC: 400-700 nm	Thorlabs	2
	AC508-200-A-ML	ARC: 400-700 nm	Thorlabs	3
	AC508-500-A-ML	ARC: 400-700 nm	Thorlabs	4
	AC254-050-A-ML	ARC: 400-700 nm	Thorlabs	8
EMCCD	iXonEM+DU897E-COO-#BV		Andor Technology	10
AOTF	AOTF nC-VIS-TN 1001		AA OPTO-ELECTRONIC	13
Objective	60x ApoN TIRF, NA 1.49		Olympus	1

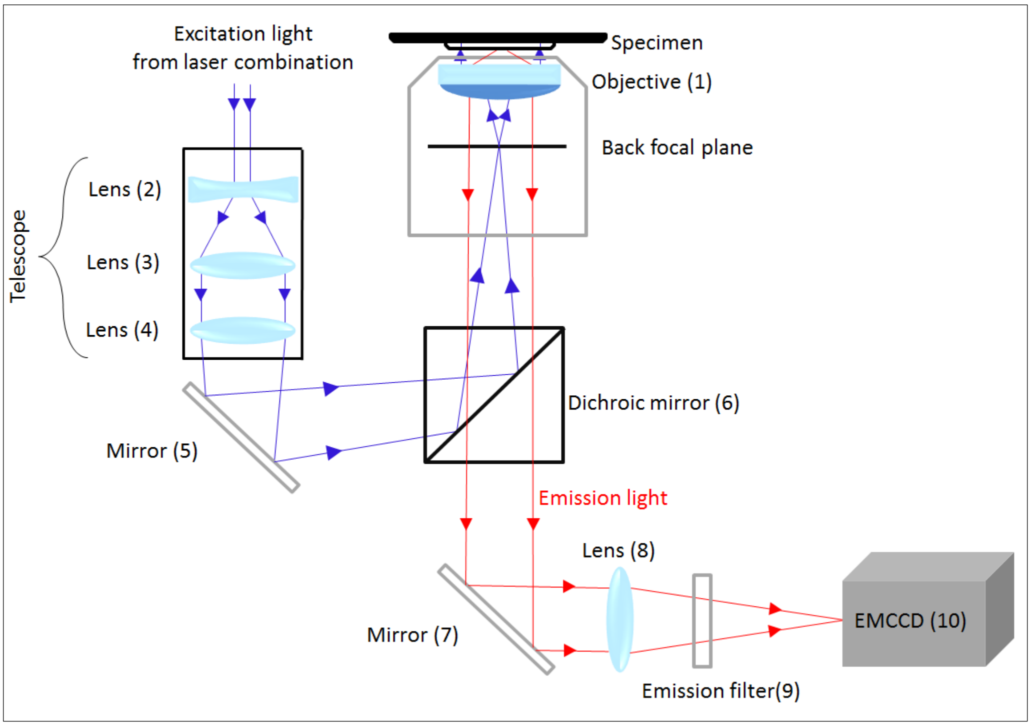

Figure 2.1. Schematic of the optical configuration. The beam from laser combination (upper left corner of the schematic) will be shown in more details in figure 2.2.

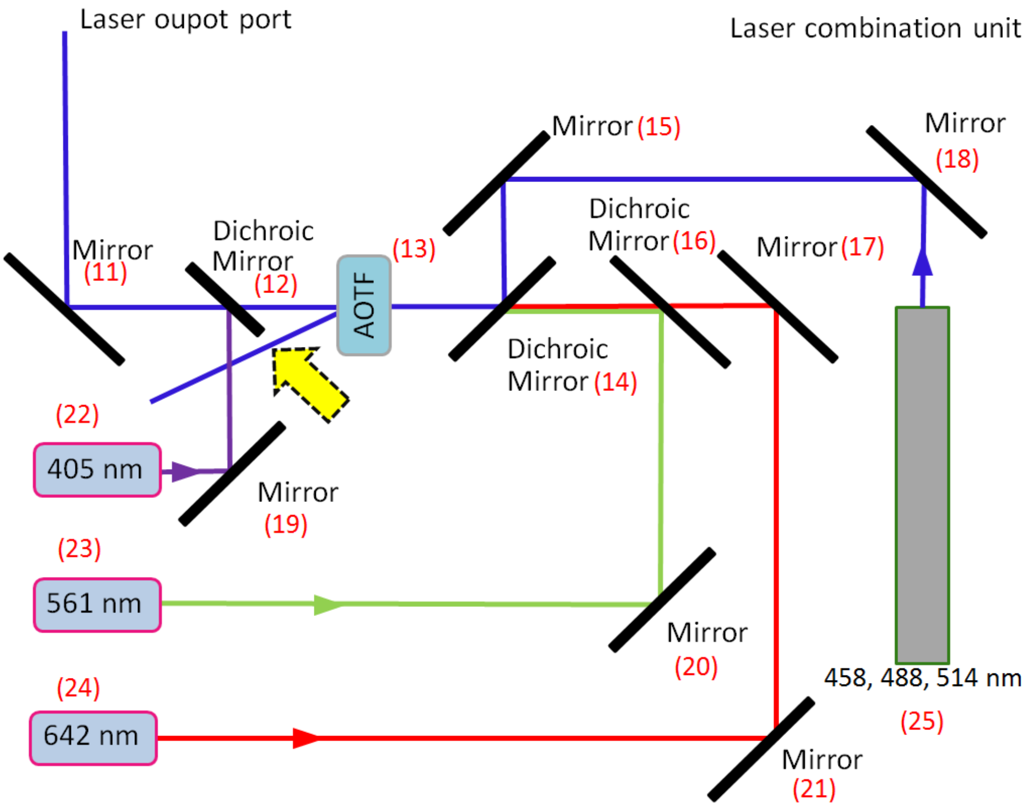

Figure 2.2. Combining the excitation lasers. The highlighted beam with the yellow arrow shows the percentage of the deviated beam by AOTF device. For instance, if the desired power percentage set to 20 %, the highlighted beam is the remaining 80% of the original output laser beam before AOTF.

2.8. Algorithm for image reconstruction

Sub-diffraction image reconstructions were calculated using SNSMIL (Tang 2015) method and rapidSTORM version 1.4.9 (Wolter 2012). A further user-friendly, console-based command of the package was developed by J. Hendriks (unpublished). SNSMIL algorithm is based on the Poisson characteristics of noise or shot noise and greatly improves the identification accuracy of single fluorescent molecules even in data with high and inhomogeneous background. The method determines different parameters of single emitters such as position x (nm), position y (nm), standard deviations of x and y (nm), total number of detected photons, etc. The noise of background (BN) for the estimation of EMCCD noise is calculated and the SNR value could then be calculated as amplitude / BN. While in rapidSTORM a non-maximum suppression algorithm was utilized and spot candidates were determined according to their intensity, SNSMIL is selectively independent of the emitter candidates' intensity and therefore is suitable for the super-resolution analysis when the images have very low SNR.

2.9. SMLM imaging procedure

Once cell samples had been prepared and fixed the SMLM setup was used as explained above. Prior to measurements, several experimental parameters adjusted. After switching all components of the system on, a waiting time of one hour was utilized for warming up of lasers and EMCCD camera. Next the position of the excitation profile was centered. For this purpose, a multicolor plastic slide was illuminated with the z-focus at position of maximum signal. The fluorescence maximum was observed on the EMCCD camera image and aligned to the center of the image by adjusting the respective mirrors (405 nm laser: M12 and M19; Ar ion laser: M15 and M14; 561 nm laser; M16 and M20; 642 nm laser: M17 and M21; see figure 2.2). The pixel size in the SMLM measurements was set to 80 nm/pixel, the camera exposure time was set to 50 ms, the EMCCD camera gain was set to 300, and the effective dark time (readout time) of the camera was 35 ms. The quality parameter (Q) was set to 1, and the final pixel size of reconstructed images was 16 nm (rendering: 5).

In order to minimize mechanical lateral and axial drifts, the sample was kept at room temperature for approximately 30 min and afterwards put it on the microscope's stage for at least one hour before starting a measurement. When this caution was not taken large lateral and, to a lower extent, axial drifts during the recording of images occurred frequently.

The imaging buffer used for the measurement of EYFP and Dendra2 samples was PBS 1X pH 7.4, filtered with 0.22 µm pore filters (Rotilabo Spritzenfilter, KH54.1, Carl Roth GmbH, Cat. No. SE2M035107, Karlsruhe, Germany). For mCherry measurement, 284 mM β-mercapto-ethanol (βME) (CAS No. 60-24-2, Sigma-Aldrich) diluted in PBS 1X pH 7.4 was used as imaging buffer. mCherry samples was kept at βME solution for 30 min prior to the measurement.

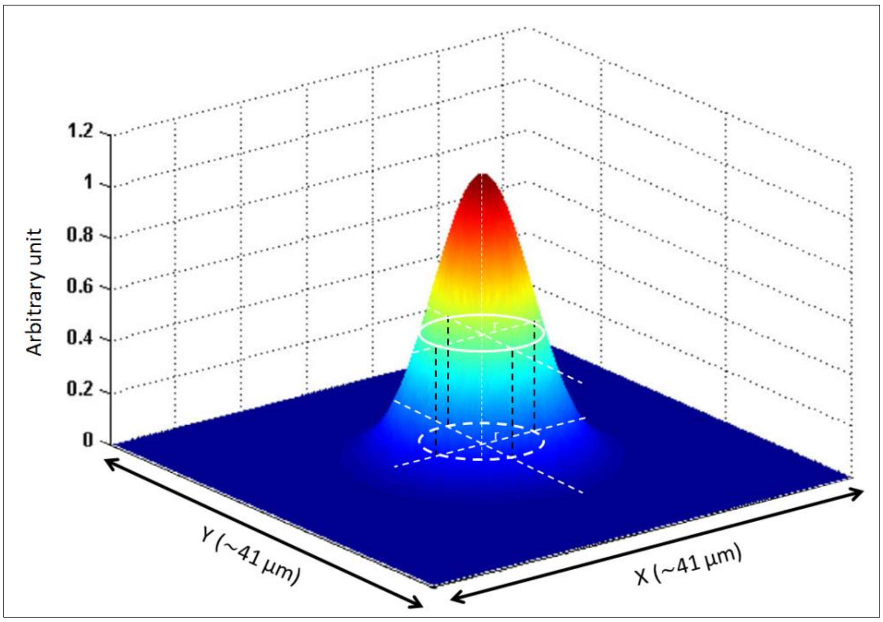

Figure 2.3. 3D profile of the excitation laser beam. The area of the cross section of the beam where the intensity is half of the maximum intensity is considered as the effective area to calculate the power density of the beam. For instance, if the power of the laser beam is 1 mW and the radius of the cross section circle is 5 µm, the power density is given by 1.27 x 10^6 mW.cm^{-2}.

2.9.1. Imaging of mammalian Atg8 proteins fused to EYFP protein

To measure mammalian Atg8 proteins fused to EYFP fluorescent protein, the Argon ion laser producing beams with the wavelengths 488 nm and 514 nm was used (see table 2.3). As it will be explained in chapter 3, section 1, 514 nm laser light is advantageous in SMLM for excitation of EYFP compared to 488 nm. Therefore, in all experiments with EYFP measurement with SMLM in this work, 514 nm for EYFP excitation was used.

To generate a high quality conventional widefield image to be used for further analysis, 50 frames with low power density of 15 W/cm^2 of 514 nm were recorded and then averaged. The single molecule images, on the other hand, measured with a high power density of 1113.7 W/cm^2 of 514 nm laser light. Before start the recording, the cell was illuminated with this laser power for 20 to 120 s in order to reach a state of well separated single blinking events with an acceptable. Once the cell shows an appropriate blinking rate, the recording of 4000 frames began.

2.9.2. Imaging of mammalian Atg8 proteins fused to Dendra2 protein

To perform SMLM measurements of mammalian Atg8 proteins fused to Dendra2 fluorescent protein, one needs to apply two different lasers, the 561 nm laser as the fluorescence readout laser and the 405 nm laser as the photoconversion laser.

In addition, to generate the conventional widefield image, 50 frames with low power density of 45 W/cm^2 of 488 nm without 405 nm illumination were recorded and averaged. This widefield image of non-photoconverted Dendra2-Atg8 fusion proteins registered the spatial distribution of Atg8 and was used as conventional fluorescence image of the cell for further analysis. The single molecule images, on the other hand, measured with a high power density of almost 3341 W/cm^2 of 561 nm laser light while the sample was exposed to illumination by 405 nm laser as well. Before recording, the sample was illuminated with the 561 nm laser only (high power) for 20 to 120 s in order not to photobleach any false single molecule emitters from non-Dendra2 impurity fluorophores. Once the cell shows no blinking, the recording of typically 8000 to 12000 frames began. The photoconversion started with very low power density of 1.1 W/cm^2 of 405 nm were observed as long as sufficient, but not too many fluorescing photoconverted Dendra2 molecules, the 405 nm laser power was kept constant. When nearly all Dendra2 molecules were photobleached at a certain 405 nm power the power of the 405 nm laser was increased by 5 to 10 percent and this procedure was repeated until the entire Dendra2 molecules had been photoconverted by 405 nm laser and subsequently readout and photobleached by 561 nm laser (the maximum 405 nm laser power density is 113.4 W/cm^2).

Our findings revealed that when the measurement with a higher power density of 405 nm laser or when the 405 nm illumination increased steps by a larger percentage (since it was started to photoconvert a large fraction of Dendra2 protein simultaneously) the quality of the final reconstructed super-resolved image was deteriorated.

2.9.3. Imaging of LAMP1 protein fused to mCherry protein

mCherry is a widely used FP for labeling of proteins in conventional microscopy (e.g. widefield and confocal fluorescence microscopy). It has recently been shown that in addition mCherry can be converted into a photoconvertible dark state in the presence of high concentration of βME, i.e., mCherry is driven to a non-emissive dark state upon interaction with βME from which up to 80% of the fluorophores can be recovered to the fluorescent state by photoconversion (with 405 nm light) (Cloin 2017). Incubating with βME quenches the fluorescence maximum at 610 nm (excitation 561 nm) and introduces a weak fluorescence maximum at 460 nm (excitation 405 nm). Illumination with 405 nm or washout of βME recovers the normal highly fluorescent state of mCherry.

To measure SMLM images of the lysosomal protein LAMP1 fused to mCherry, two different lasers, the 561 nm laser as fluorescence readout laser and the 405 nm laser as the photoconverting laser were utilized.

To generate the conventional widefield image, 50 frames with low power density of 45 W/cm^2 of 561 nm without presence of 405 nm in the presence of βME were recorded and averaged. The resulting image was of lower quality compared to EYFP or Dendra2 measurements, but still useful in judging the correctness of the mCherry-SMLM image. The single molecule images measured with a high power density of 3341 W/cm^2 of 561 nm laser light while the sample is exposed to 405 nm laser light as well. Before recording, the cell was illuminated with the 561 nm laser with high power for 20 to 120 s in order to reduce single molecule emission events from fluorescent impurities. Once the cell showed no fluorescent signals anymore, the recording of typically 8000 to 12000 frames was started. The photoconversion was begun with very low power density of 1.1 W/µm^2 of 405 nm then as long as no sufficient but not too many fluorescing mCherry molecules were observed, the 405 nm laser power was kept constant. After photobleaching of nearly all mCherry molecules with the current 405 nm laser power, the power density was increased by 5 to 10 percent and the procedure was repeated until all mCherry molecules had been photoconverted by 405 nm laser and readout and photobleached by 561 nm laser.

The advantage of using photoswitchable mCherry with the use of SMLM is not only the presence of a large number of mCherry fused plasmids in our institute and the entire life science community, but in case another FP fusion protein coexists with mCherry in cell (like EYFP in our case), chemically inducing mCherry into non-emissive dark state would not affect the fluorescence of the other protein (EYFP in this case). Our experimental evaluation of using βME to photoconvert mCherry showed that the destructive effect on the fluorescent intensity of EYFP is almost negligible and therefore, one can safely use both EYFP and mCherry for SMLM measurement.

2.10. Shape and Size Analysis

The flowchart model for the evaluation of shape and size of EYFP-Atg8 and Dendra2-Atg8 containing cytoplasmic structures is shown in figure 2.4. Once the super-resolution reconstructed image was obtained as the output of the SNSMIL software, several macros (see appendix 7.7, for the source codes) written in ImageJ (Schneider 2012) and C programming language was applied to perform the shape and size analysis in a semi-automated approach. The reconstructed SMLM image intensity ranges between 0 and 255. The SMLM image file was first converted to a binary image (applying an intensity cut-off 128, where values below, will be set to 0 and values above, will be set to 1 in the binary image, respectively). A lower size cut-off must be applied in order to discard very small structures originating from isolated EYFP, Dendra2 and mCherry emitters not linked to EYFP-Atg8s and Dendra2-Atg8s containing structures, respectively, as well as structures from auto-fluorescence or electrical noise signals. 50 nm as such cut-off was chosen, well above the positional uncertainty for single molecule emitters in our setup (20-30 nm). In the case of asymmetric objects, the longest dimension of the structure had to be larger than this cut-off value. Subsequently every single detected structure larger than 50 nm was saved separately in a single image Tiff file for further analysis. Depending on the size of the measured cell and the nature of the protein construct, the total number of all single generated files can amount to several thousand single files. For every single detected structure, the parameters area (in pixel or nm^2), x and y coordinates (in pixel or nm) were saved in a separate single LibreOffice Calc (Version 5.2; The Document Foundation, Berlin, Germany) file for further analysis. An input/output (I/O) streaming routine supplied by a C program was called for every single shape saved file and the shape classification for both EYFP- and Dendra2-Atg8 proteins was performed by visual inspection by the experimenter based on three different geometrical patterns, named circles (c), ellipses (e), and U-shapes (u) (see chapter 3.2). A typical example of determining the shape for isolated EYFP-GABARAP structures is shown in figure 2.5. The statistical significance of differences in relative abundances of shapes (figures 3.7-3.8, 3.13, 3.15, 3.20-3.27) was assessed with the two-tailed t-test function of LibreOffice Calc.

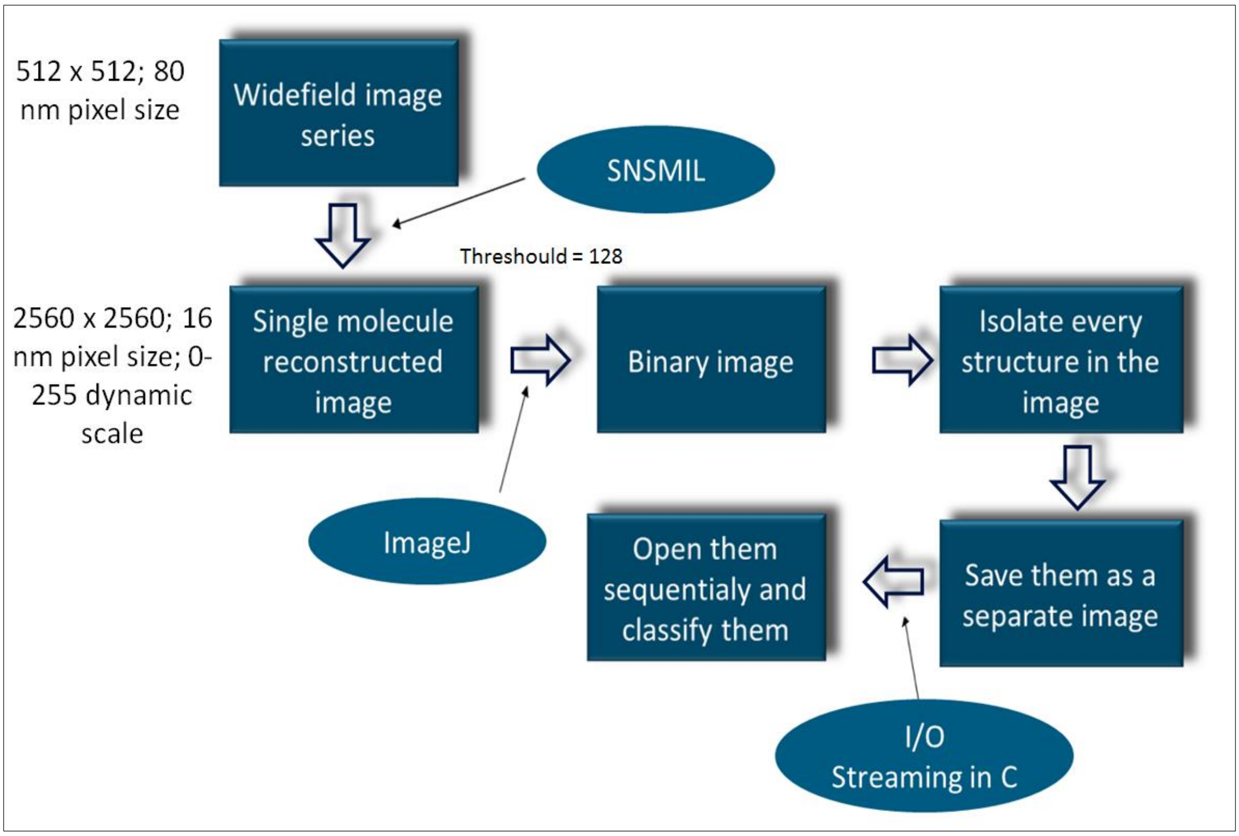

Figure 2.4. Flowchart model of the shape and size analysis

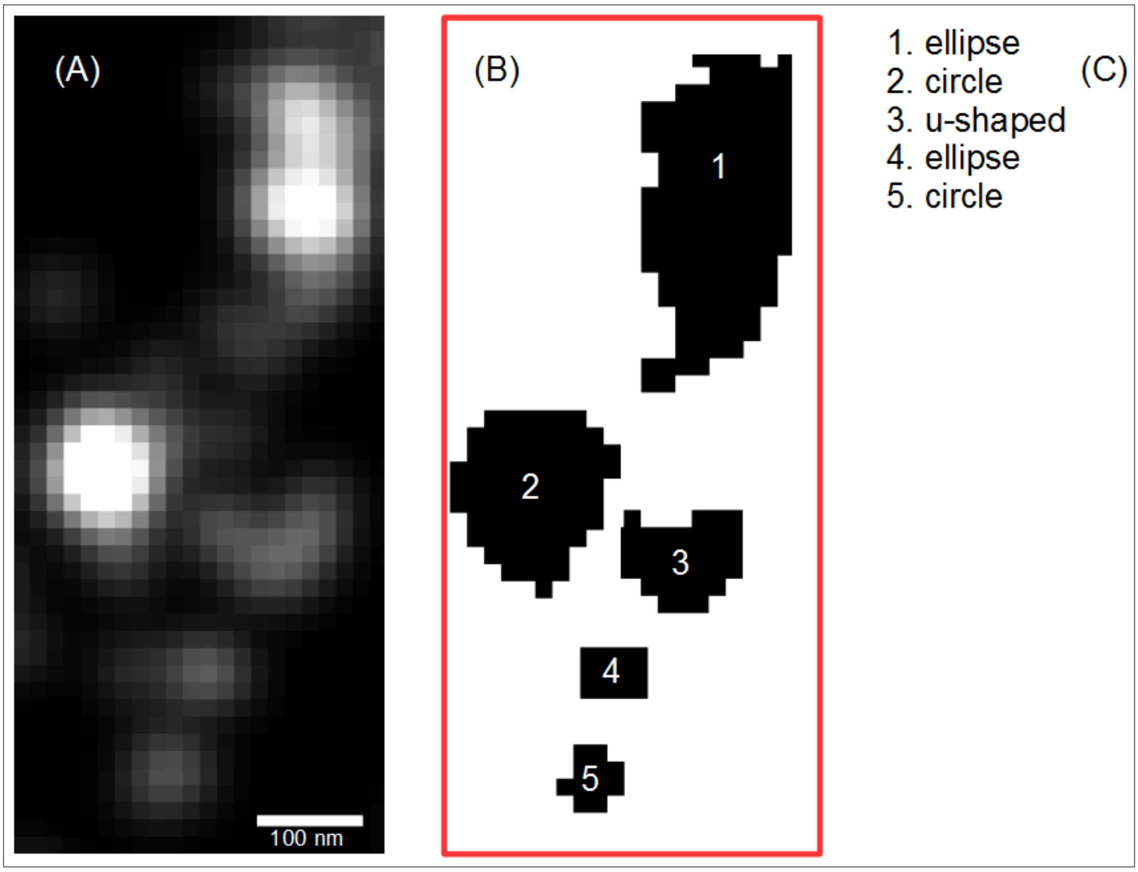

Figure 2.5. Typical example of shape identification based on super-resolution image (A) and its corresponding binary image (B). The shape classification based on visual inspection is given in (C).

2.11. Selection of cytoplasmic containing EYFP and Dendra2, respectively, fused to mammalian Atg8-proteins

Since autophagy is a cellular process that takes place in the cytoplasm (i.e. the whole cell except the nucleus) the selection of cytoplasmic structures containing EYFP or Dendra2 fused Atg8-proteins for shape and size analysis was limited. The identification of the nucleus was done with the use of conventional transmission image of the cells. In figure 2.6, the entire process of nucleus identification is given for a typical example of EYFP-Atg8. As shown in figure 2.6(A), a freehand contour was drawn around the nucleus of the cell identified in transmission image by the option *Edit->Selection->Make Band* with *Band Size = 1 pixel*. Subsequently, in the corresponding super-resolution image an identical contour can be generated by option *Edit->Selection->Restore Selection* (figure 2.6(B)). Having selected nucleus by drawing a contour around it, in ImageJ, the option *Edit->Clear* performed to have only the cytosolic structures identified.

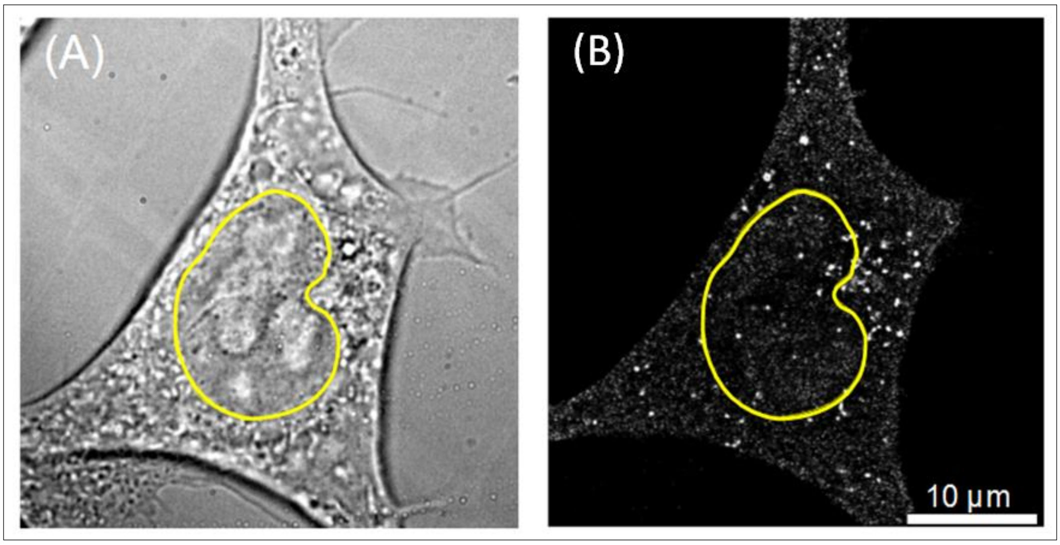

Figure 2.6. Identification of cell's (here: HEK-293 cell transiently transfected with EYFP-LC3B) nucleus from the transmission image (A) and highlighting a similar contour in the corresponding super-resolution SMLM image (B).

2.12. Selection of the structures based on the conventional fluorescence widefield images

The identification of structures in conventional fluorescence widefield images was performed visually. To identify as many structures as possible, especially for structures with their overall sizes close to the spatial resolution of the widefield images, the brightness and contrast of every widefield image was adjusted for maximal visibility of structures. The size of the identified structure was calculated by drawing a freehand contour around the shape of the structure and calculating the pixel count for the selected region. The size of identified object in widefield images are all above 50 nm because the pixel size of images is 80 nm. In figure 2.7 a typical example of fluorescence widefield image of an EYFP-GABARAP containing structure for identification and size and shape determination.

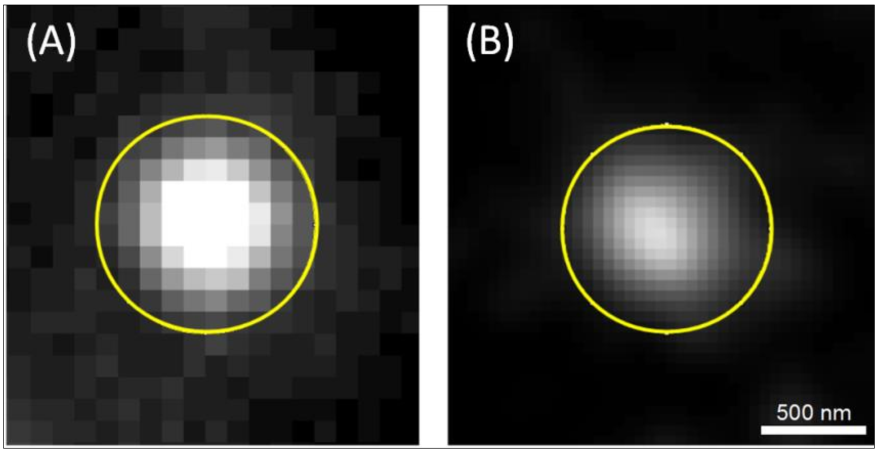

Figure 2.7. Identification and shape classification of a typical structure (EYFP-GABARAP) in conventional fluorescence widefield image (A) drawing a contour around it and reading the pixels inside the contour as the area for the structure. In the corresponding super-resolution image (B), the contour from (A) is depicted for comparison.

2.13. Chromatic aberration correction

Correction of chromatic aberration in images of optical microscopes is a challenging task. The presence of a radial component in the aberration (especially when using microscope objectives of high NA) requires a good calibration measurement that contains information for every region of the recorded image. Especially in super-resolution microscopy correction of chromatic aberration is essential, as even small aberrations not visible in regular microscopy with diffraction limited resolution become visible. Here a method that greatly simplifies correction of chromatic aberration was used. It was developed and implemented by Dr. Johnny Hendriks under guidance of Dr. Thomas Gensch (both ICS-4).

To determine the pixel-size of an image using reference microscope slide containing a 10 x 10 µm grid array applied (Article No. R1L3S3P - Grid Distortion Target, Lübeck, Germany). The analysis of bright-field grid images was performed via regression analysis with a simulated grid using least squares optimization (Levenberg-Marquardt algorithm). Parameters needed for the simulated grid are explained in figure 2.8.

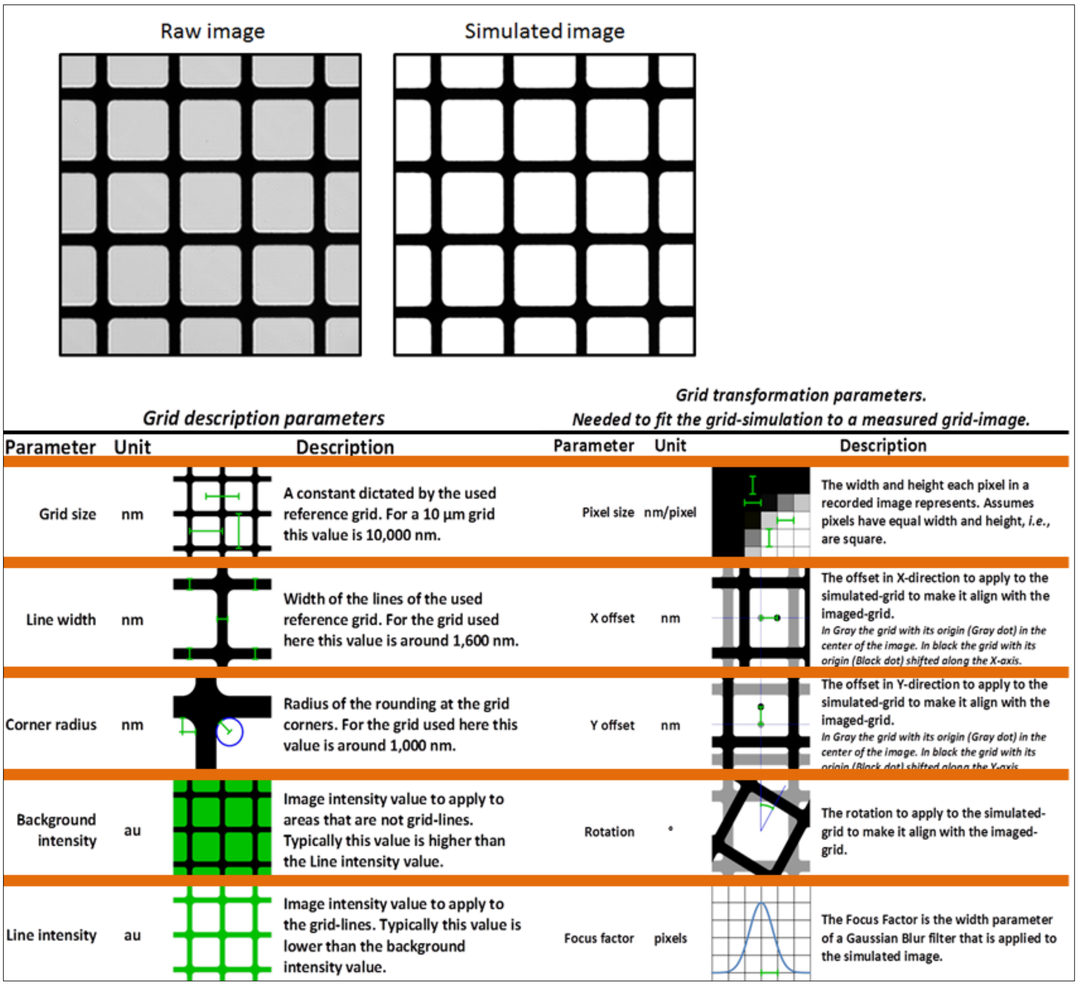

Grid description parameters

Parameter	Unit	Description
Grid size	nm	A constant dictated by the used reference grid. For a 10 µm grid this value is 10,000 nm.
Line width	nm	Width of the lines of the used reference grid. For the grid used here this value is around 1,600 nm.
Corner radius	nm	Radius of the rounding at the grid corners. For the grid used here this value is around 1,000 nm.
Background intensity	au	Image intensity value to apply to areas that are not grid-lines. Typically this value is higher than the Line intensity value.
Line intensity	au	Image intensity value to apply to the grid-lines. Typically this value is lower than the background intensity value.

Grid transformation parameters.
Needed to fit the grid-simulation to a measured grid-image.

Parameter	Unit	Description
Pixel size	nm/pixel	The width and height each pixel in a recorded image represents. Assumes pixels have equal width and height, *i.e.*, are square.
X offset	nm	The offset in X-direction to apply to the simulated-grid to make it align with the imaged-grid. *In Gray the grid with its origin (Gray dot) in the center of the image. In black the grid with its origin (Black dot) shifted along the X-axis.*
Y offset	nm	The offset in Y-direction to apply to the simulated-grid to make it align with the imaged-grid. *In Gray the grid with its origin (Gray dot) in the center of the image. In black the grid with its origin (Black dot) shifted along the Y-axis.*
Rotation	°	The rotation to apply to the simulated-grid to make it align with the imaged-grid.
Focus factor	pixels	The Focus Factor is the width parameter of a Gaussian Blur filter that is applied to the simulated image.

Figure 2.8. Upper panels: Bright field raw and simulated images of the reference grid. Each box in images show a square of 10 µm side length. Lower panels: The parameters used to simulate a reference grid. A successful regression analysis requires that the starting parameters for the model are already relatively close to the final results. A good estimation of the starting parameters can generally be made automatically based on the raw reference grid image.

Fluorescence detection at different wavelengths typically also requires use of different emission filters. As such, to study the effect of the detection wavelength on the reference grid image, a variety of optical configurations was tested. Plotting the pixel size of the reference grid image as a function of detection wavelength shows that there is a significant change that happens to be linear between 500 and 700 nm. The slope of this linear dependence is also dependent on pixel size (see figure 2.9). Furthermore, addition of an emission filter will also cause a significant change in pixel size. Different emission filters appear to cause a similar change. This effect is however additive i.e. the pixel size changes by a similar amount for each emission filter that is added to the optical path between the sample and the detector.

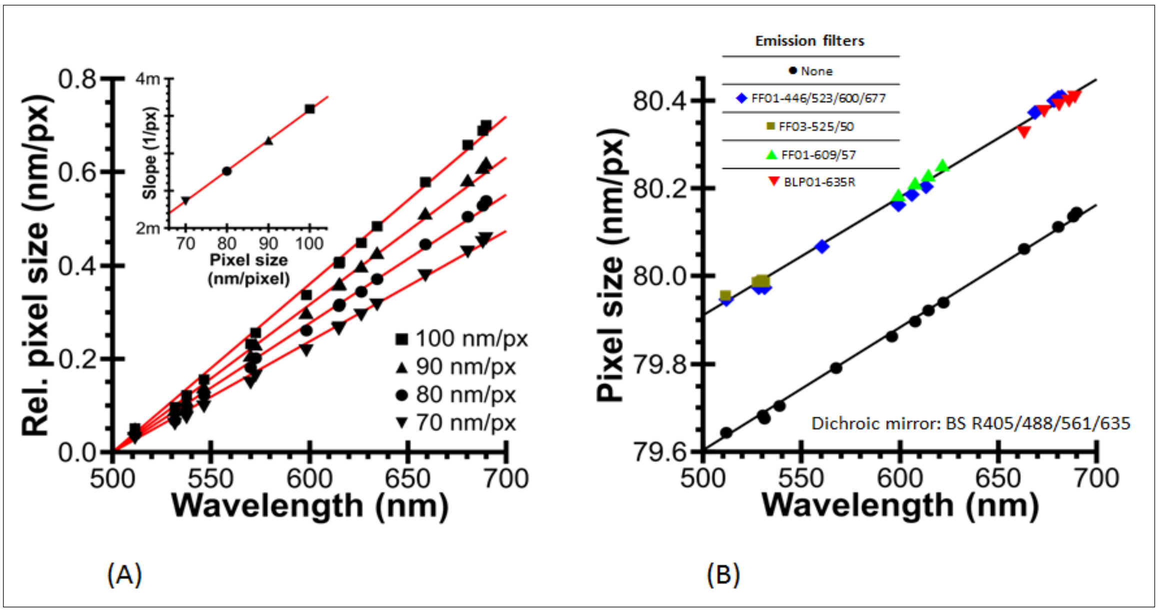

Figure 2.9. (A) Average detection wavelength vs. pixel size change relative to fitted pixel size at 500 nm. Inset: slope of fitted lines vs. fitted pixel size at 500 nm. Optical configuration for this dataset is no dichroic mirror and no filter. (B) Average detection wavelength vs. pixel size for several optical filter configurations used in our setup. Fitted lines are through the data points with no emission filter, and through the data with use of a single emission filter.

Typical multi-color SMLM data are processed using the same pixel size for all images irrespective of the emission wavelength of the fluorophores. This leads to the typical chromatic aberration effect shown in figure 2.10. Correction then requires a calibration measurement that covers the entire area of the recorded images. When SMLM data is processed using the appropriate pixel size for the emission wavelength of the fluorophores, the observed chromatic aberration effect is a simple offset that is the same for the entire area of the recorded image as shown in figures 2.10(A), 2.10(B). Therefore, in principle, a single reference point could be used to calibrate for chromatic aberration.

Finally, the chromatic aberration correction problem is a basic scaling issue. To scale an image, one requires both a scaling factor and an origin point from which to perform the scaling. Here the pixel size is effectively a scaling factor. When analyzing SMLM data, the top-left corner of the image is generally defined as the origin point. It is rarely the case that the actual scaling origin for the change in pixel size is at the top-left corner.

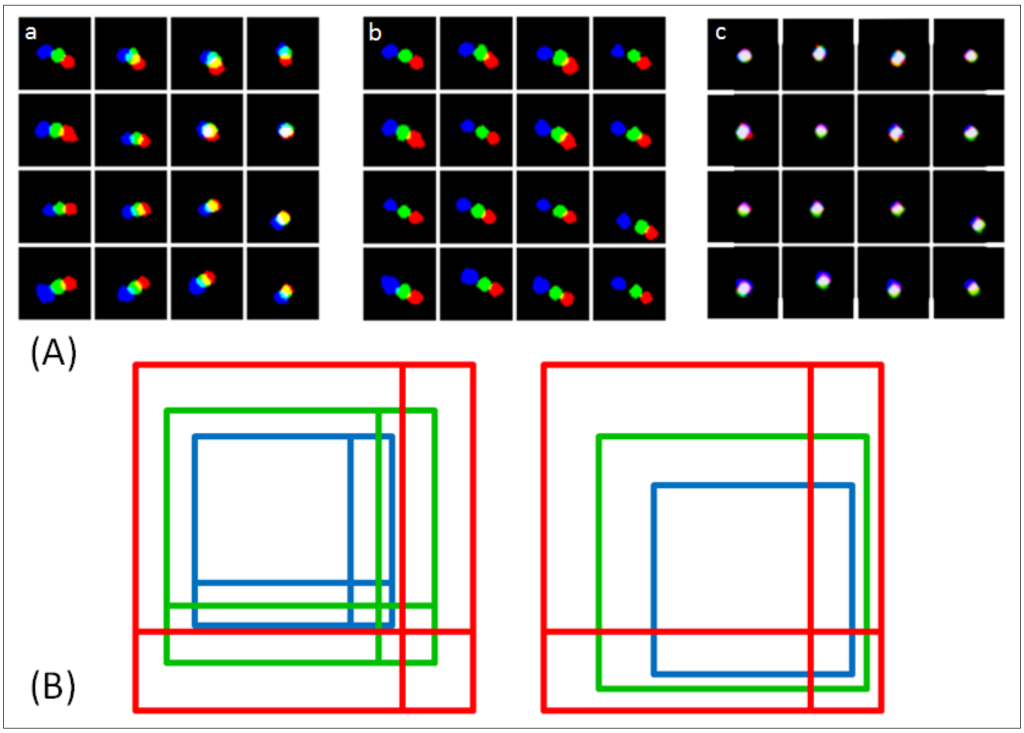

Figure 2.10. (A). Analysis of multi-color beads (0.1 µm TetraSpec Microspheres (Cat. No.: T7279, ThermoFisher Scientific)). Boxes are representative reconstructed SMLM images of beads (621 x 621 nm) in 16 different grid-sections of the original image (~ 41 x 41 µm). Source images (512 x 512 px; pixel size ~ 80 nm/px) were recorded with excitation wavelength of 488 nm (blue spots), 561 nm (green spots), and 642 nm (red spots). Panel a: SMLM analysis using 80 nm/px for all colors. Panel b and c: SMLM analysis using 79.969 nm/px for blue, 80.208 nm/px for green and 80.377 nm/px for red. Panel c: An offset was applied tp green and red localizations. (B) A cartoon simply shows how an offset applying at origin point bottom-right, will align all three blue, green, and red signals.

3. Results

3.1. Excitation of EYFP at 514 nm and 488 nm

In the visible spectral region, only a few (about 10) laser lines are used in commercially available, high performance fluorescence microscopes such as confocal laser-scanning (CLS) or Total Internal Reflection Fluorescence (TIRF) microscopes, but also in super-resolution fluorescence microscopes the 488 nm laser line is standard. The Ar-ion laser is among them. It has many transitions suitable for lasing (between 454 nm and 529 nm) but the most powerful transition at 488 is by far the most commonly used. Another reason for popularity of using the 488 nm laser line of the Ar-ion laser stems from the fact that it is perfect for excitation of fluorescein. Fluorescein and its many derivatives are since many decades and still to date, the most widely used fluorescence molecules in scientific and analytical applications of fluorescence in life sciences. Part of the popularity of the 488 nm excitation laser line also stems from the fact that the most often used fluorescent protein EGFP can be ideally excited by the 488 nm line of the Ar-ion laser.

In chapter Introduction, GFP and many of the fluorescent proteins among them EYFP, were introduced and the reversible photoswitching of EYFP between emissive ON-states and non-emissive OFF-states was highlighted. Due to this behavior, EYFP became a popular FP in SMLM (Lee 2011). As shown in figure 3.1, the EYFP absorption spectrum has a maximum at 514 nm and a shoulder (vibrational band of S_1 state) at 488 nm (relative absorption 38 %). The relative absorption at 488 nm for Aequorea victoria (av) GFP and several others of its variants are reported in table 3.1. As it can be seen from table 3.1, one of the reasons why 488 nm light is used so commonly in life science fluorescence microscopy is that with this wavelength many FPs from the family of GFP can be excited.

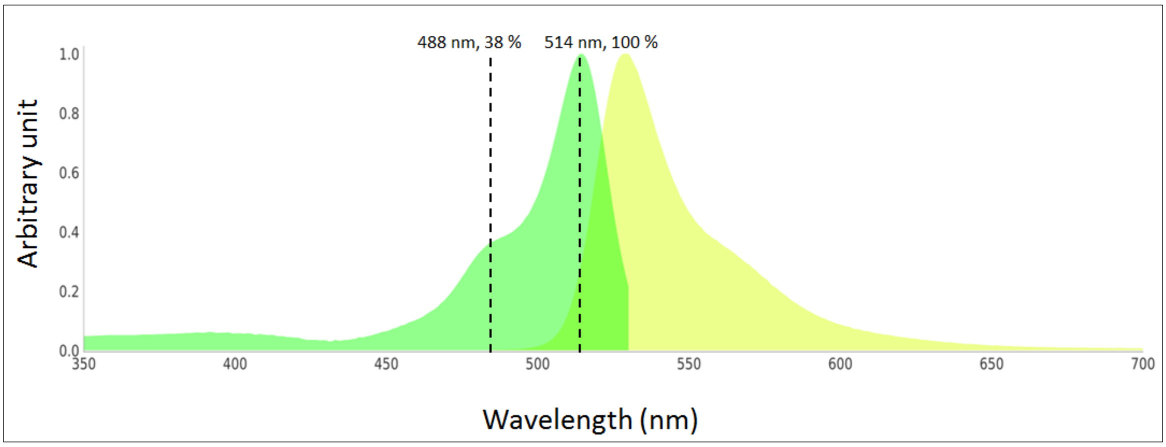

Figure 3.1. The absorption and emission spectra for EYFP (green and yellow graphs, respectively).

Another strong output of the Ar-ion laser is at 514 nm. It allows excitation of EYFP right at its absorption maximum. In addition, the background from cellular auto-fluorescence detected at 528 nm (EYFP's fluorescence maximum) will be weaker with 514 nm excitation compared to 488 nm, since some of the most abundant and fluorescent endogenous chromophores (e.g. nicotinamide adenine dinucleotide (NADH) and flavin adenine dinucleotide (FAD)) are well excited with 488 nm but hardly with 514 nm (Islam 2013).

Table 3.1. The absorption properties for Aequorea victoria GFP, EGFP, PA-GFP, and Dendra2 at 488 nm.

Fluorescent protein	Fluorescence maximum (nm)	Absorption coefficient at 488 nm	Absorption maximum (nm)
avGFP	509	23.1 %	395
EGFP	507	99.8 %	488
PA-GFP	517	72 %	504
Dendra2	507 (non-photoactivated) / 573 (photoactivated)	96.5 %	490/553

The original motivation for the experiments presented in this chapter arose from seemingly better quality SMLM images and longer acquisition times with sufficient single molecule blinking events with excitation at 514 nm compared to 488 nm, when samples with EYFP-fusion proteins (in mammalian cells and bacteria) were subjected to super-resolution imaging. While in the beginning it was believed in our lab and the SMLM community that there is no dependence on excitation wavelength, experimental evidence from SMLM imaging of different EYFP-tagged proteins in our lab pointed towards advantages of using 514 nm vs. 488 nm. In this chapter, a quantitative comparison of SMLM imaging using 514 nm and 488 nm, respectively, is performed, where the total number of detected single molecules and the length of the EYFP blinking period are taken as quantitative measures.

Here, it is investigated whether exciting EYFP with 514 nm light instead of conventionally used 488 nm will have an effect on number single molecule detection efficiency. A HEK-293 cell stably expressing EYFP-GEC1 was used as sample after fixation with PFA based on the fixation protocol explained in chapter Materials and Methods. GEC1 (also named GABARAPL1) is an estrogen regulated gene which shares a high sequence similarity with the

GABARAP gene (Chakrama 2010) and is one of the GABARAP subfamily members in mammalian cells (Boyer-Guittaut 2014). Cells were starved and autophagosome-lysosome fusion was blocked as described in chapter Materials and Methods.

The output power of the laser was measured after the objective lens and adjusted accordingly to verify excitation with identical powers at the two laser lines. Two power values used were 1888 W/cm^2 (hereafter low power) and 4432 W/cm^2 (hereafter high power). Prior to the measurements, each sample was illuminated for a time period of 10-100 s for pre-bleaching of EYFP. During pre-bleaching phase, many EYFP molecules were driven into non-emissive dark states, while a fraction of them stochastically returned to emissive on state. The measurements were performed, by recording a series of widefield fluorescence images of fixed HEK-293 cells stably expressing EYFP-GEC1, each image containing several (10-100) single molecule fluorescent spots. The same experimental procedure was performed for sample excitation at 488 nm with low power, excitation at 488 nm with high power, excitation at 514 nm with low power, and excitation at 514 nm with high power. In figure 3.2, an example of HEK-293 cells stably expressing EYFP-GEC1 excited with 488 nm and 514 nm laser light is given.

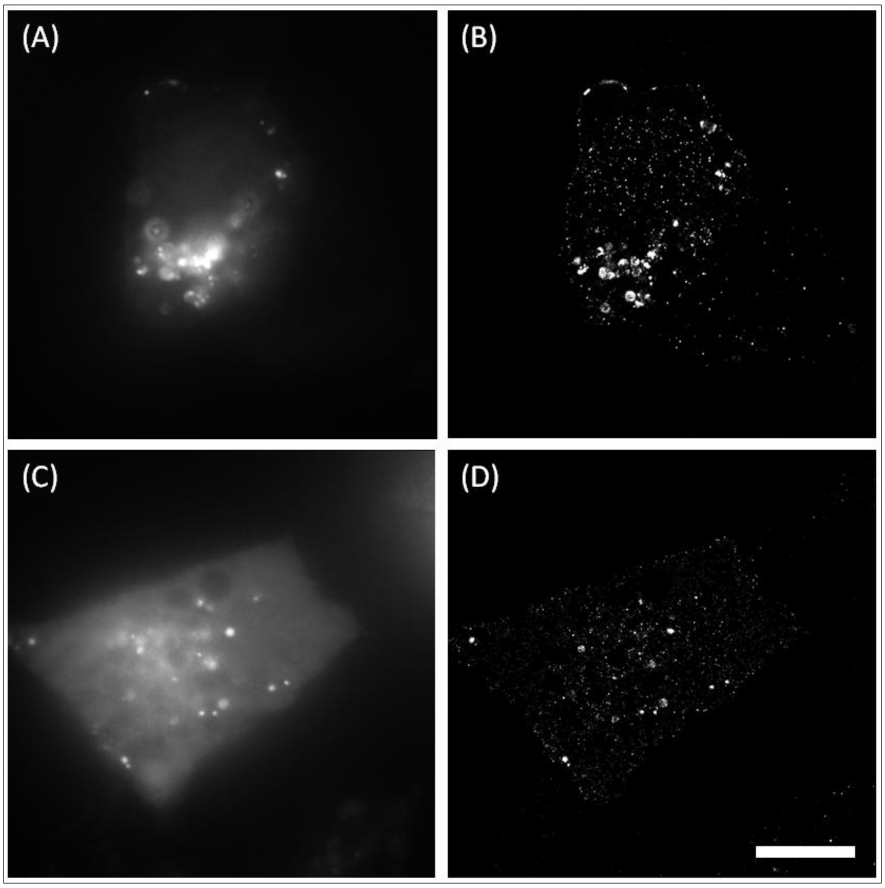

Figure 3.2. Widefield (A, C) and super-resolution images (B, D) of two HEK-293 cells stably expressing EYFP-GEC1 excited with 488 nm laser light, high power (C,D) and 514 nm laser light, high power (A,B), respectively, in starved-blocked condition. The total number of localizations detected in super-resolution images is 8252 and 44889, for 488 nm and 514 nm excitation laser light, respectively. The average cell's fluorescence signal intensity is 649 (a.u.) for (C) and 270 (a.u.) for (A). Scale bar shows 10 µm.

The measurement for each sample was stopped as soon as the number of single molecule blinking events was almost zero or remained at a very low count for 20 or more consecutive frames. The frame number in which the recording was stopped is different for each sample measured in a particular condition and for different cells in a given condition. Although the number of EYFP molecules is larger for the cell excited with 488 nm compared to that with 514 nm and fluorescent signal is larger (650 vs. 270) while the excitation coefficient is smaller (31700 $M^{-1}cm^{-1}$ vs. 83400 $M^{-1}cm^{-1}$ (Day 2009)), the number of detected single molecule events is much smaller (8252 vs. 44889).

The number of localizations for the two cells shown in figure 3.2 is plotted in figure 3.3 as a function of frame number. This number is first nearly constant but starts to decrease significantly after ca. 50 frames and reaches a low but constant value after 1000 or more frames. For the cell excited at 488 nm the total number of localizations as well as the maximum number per frame are distinctively lower compared to the cell excited at 514 nm. In addition, the period of low, constant number of localizations sets in earlier for excitation at 488 nm.

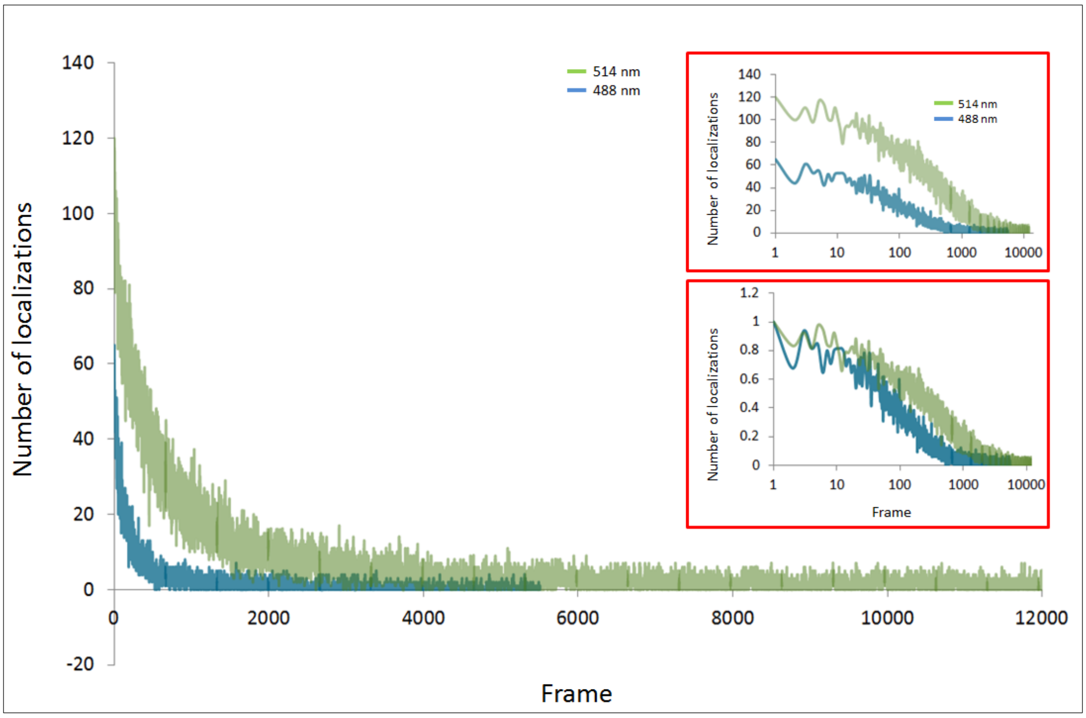

Figure 3.3. Number of localizations detected per frame for the measurement of HEK-293 cells stably expressing EYFP-GEC1 (cells that were shown in figure 3.2). The green and blue graphs show the data for the cells excited with 514 nm and 488 nm laser light, respectively. The upper inset shows the same graphs but the x-axis in logarithmic scale and the lower inset shows the same graphs with the y values additionally normalized for each data set by dividing by the respective maximum values.

The comparison with two different excitation powers (4432 W/cm^2 and 1888 W/cm^2) was performed. 15 cells were measured and analyzed for each excitation wavelength and power, respectively. These power values are the powers usually used in dSTORM experiments at our setup. The analysis of the SMLM measurements of these 60 cells can be found in appendix 7.1.

In the previous section, two arbitrarily chosen cells were compared. In the following three different objective measures are introduced to compare the behavior of EYFP in SMLM imaging with 488 nm and 514 nm excitation. First, the average of the 15 curves of number of localizations vs. frame number for each condition was calculated. They are depicted in figure 3.4. Each dataset has been normalized by dividing the localization counts per frame by the maximum number of localizations per frame in that dataset. In this way all the curves show a normalized number of localizations per frame between 0 and 1, and therefore, it is straightforward to compare all four datasets. Since observation times for the 60 cells measured were different, the four average curves also end at different frame numbers, i.e. the frame number of the experiment with the shortest observation time among the 15 cells measured. In the beginning of the measurement (frame number 1 to 30), the number of localizations detected per frame for the four different conditions showed a similar decrease. From frame number 31 to 2000, there is a strong difference in the number of sample molecules per frame decay. The fastest decay is for cells excited at 488 nm with high power, followed by the experiment where the cells were excited at low power of 488 nm with low power. Excitation at high power 514 nm light was next, while excitation with low power 514 nm light resulted in the most delayed decay of number of localizations per frame. From frame number 2000 to the end of the measurement, curves are more similar. In the final frames a constant value of 0.5 (488 nm excitation) or 1 (514 nm excitation) localization per frame is reached. This value is too low to further improve SMLM imaging and therefore the measurements were irrelevant. Another more quantitative parameter to characterize the time of useful EYFP blinking events is derived from analysis of the individual $N_{loc./frame}$ vs. frame curves by fitting them with a set of exponential decay functions, namely a mono-exponential ($y = y_0 + Aexp(-Bf)$) and a bi-exponential decay function ($y = y_0 +$

$Aexp(-Bf) + Cexp(-Df)$), where A and C are the amplitudes of the fast and slow decreasing exponential functions, respectively, B and D are the rate constants for slow and fast decays in terms of frame^{-1} (1 frame = 85 ms), respectively, f represents the frame, and y_0 is the final constant number of localizations per frame at the end of several thousands of image acquisitions.

In figure 3.5 examples for fitting a mono-exponential and a bi-exponential decay function are depicted together with their residuals for an SMLM imaging experiment of a cell excited at 514 nm. The same analysis was performed for all samples of each condition and the results of mono- and bi-exponential decay function fittings are presented in appendix 7.1 (performed with python programming language). When comparing mono- and bi-exponential fitting functions in figures 3.5 (A) and 3.5 (B), one easily recognizes the non-ideal description of the data by the mono-exponential function in the range of 200 to 4000 frames. This manifests as systematic “undershooting” and “overshooting” in the respective residuals (3.5 (C)), while the residuals of the bi-exponential fitting are evenly distributed around 0, indicating a satisfying description of the data. In figure 3.6 a similar analysis is shown for one cell imaged with excitation at 488 nm. Again a bi-exponential function is necessary and at the same time sufficient to describe the data. The analysis was performed for all samples of each condition and the resulting mono- and bi-exponential decay curve fittings are presented in appendix 7.1.

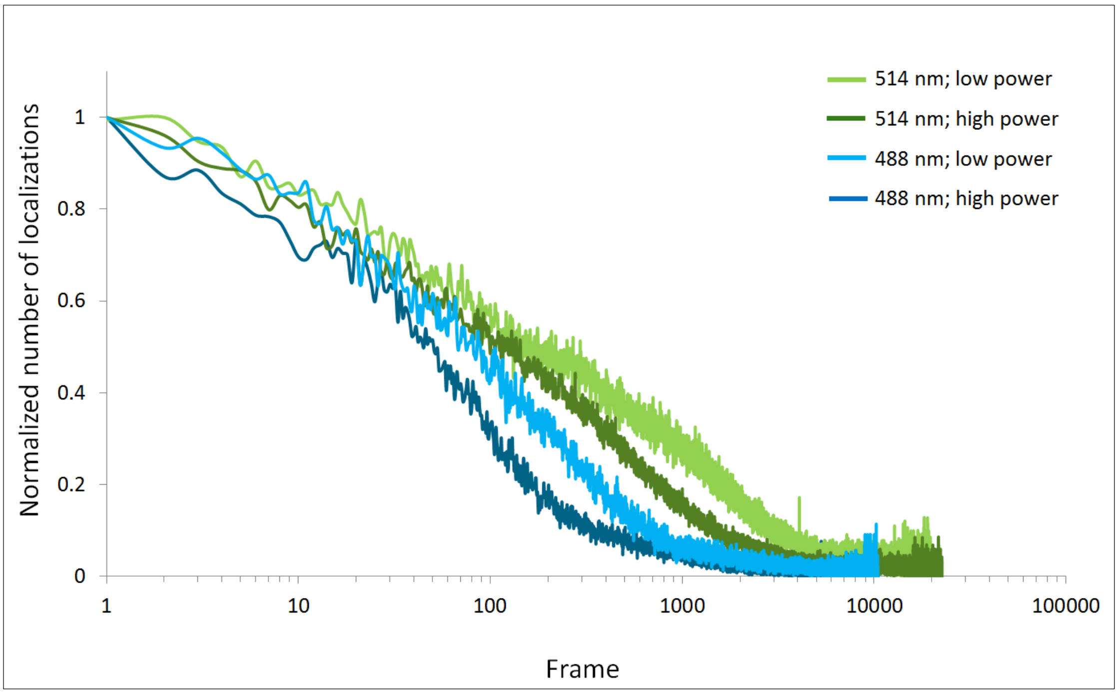

Figure 3.4. The normalized number of localizations per frame for the average of 15 measurements for HEK-293 cells stably expressing EYFP-GEC1 excited with 514 nm low power light (light green), 514 nm high power light (dark green), 488 nm low power light (light blue), and 488 nm high power light (dark blue), respectively.

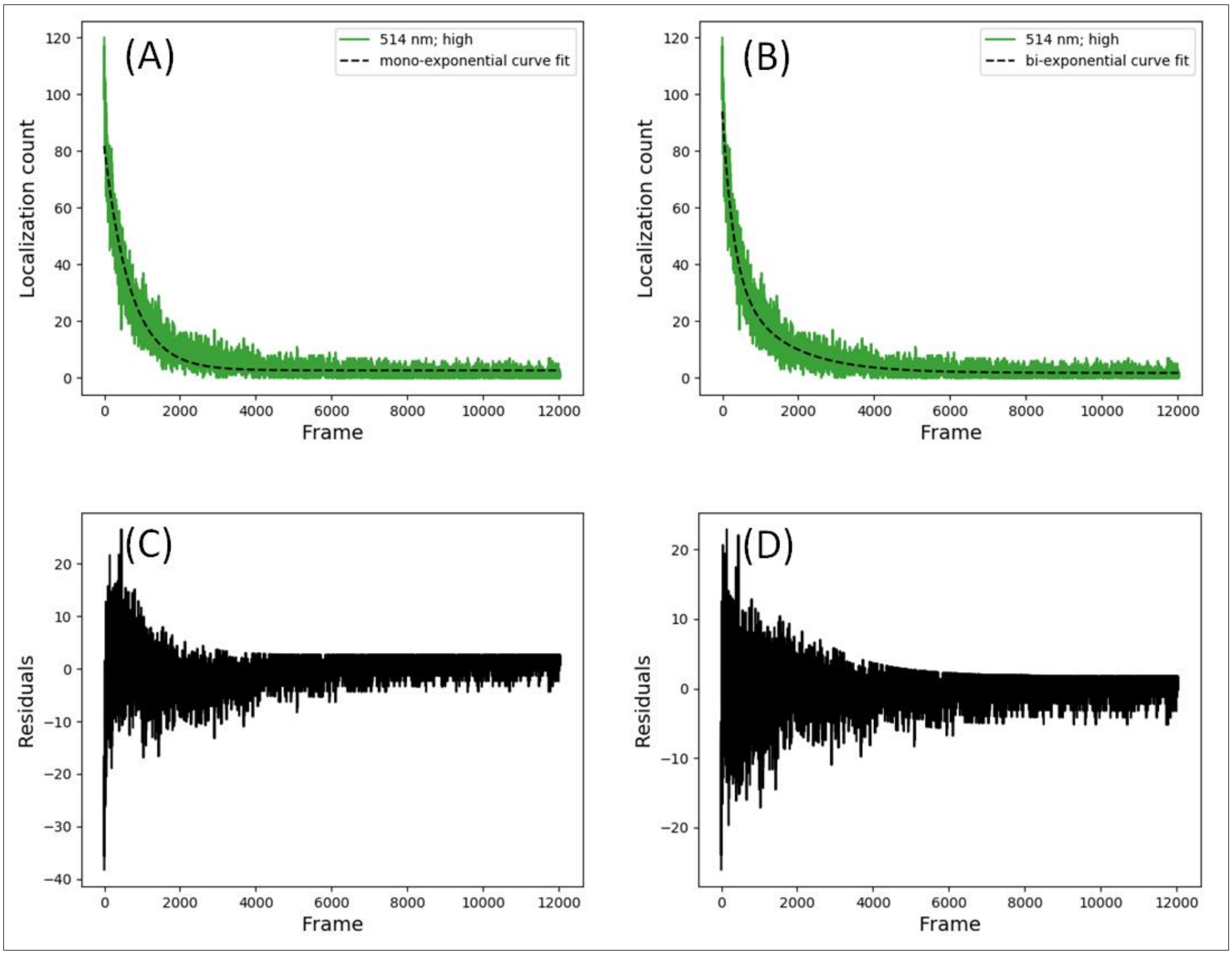

Figure 3.5. Mono-exponential (A), and bi-exponential (B) decay curve fit of a dataset measured from HEK-293 cells stably expressing EYFP-GEC1 with 514 nm excitation light. The residuals of the fitted curves are represented in (C) for mono-exponential decay curve fitting and in (D) for bi-exponential decay curve fitting.

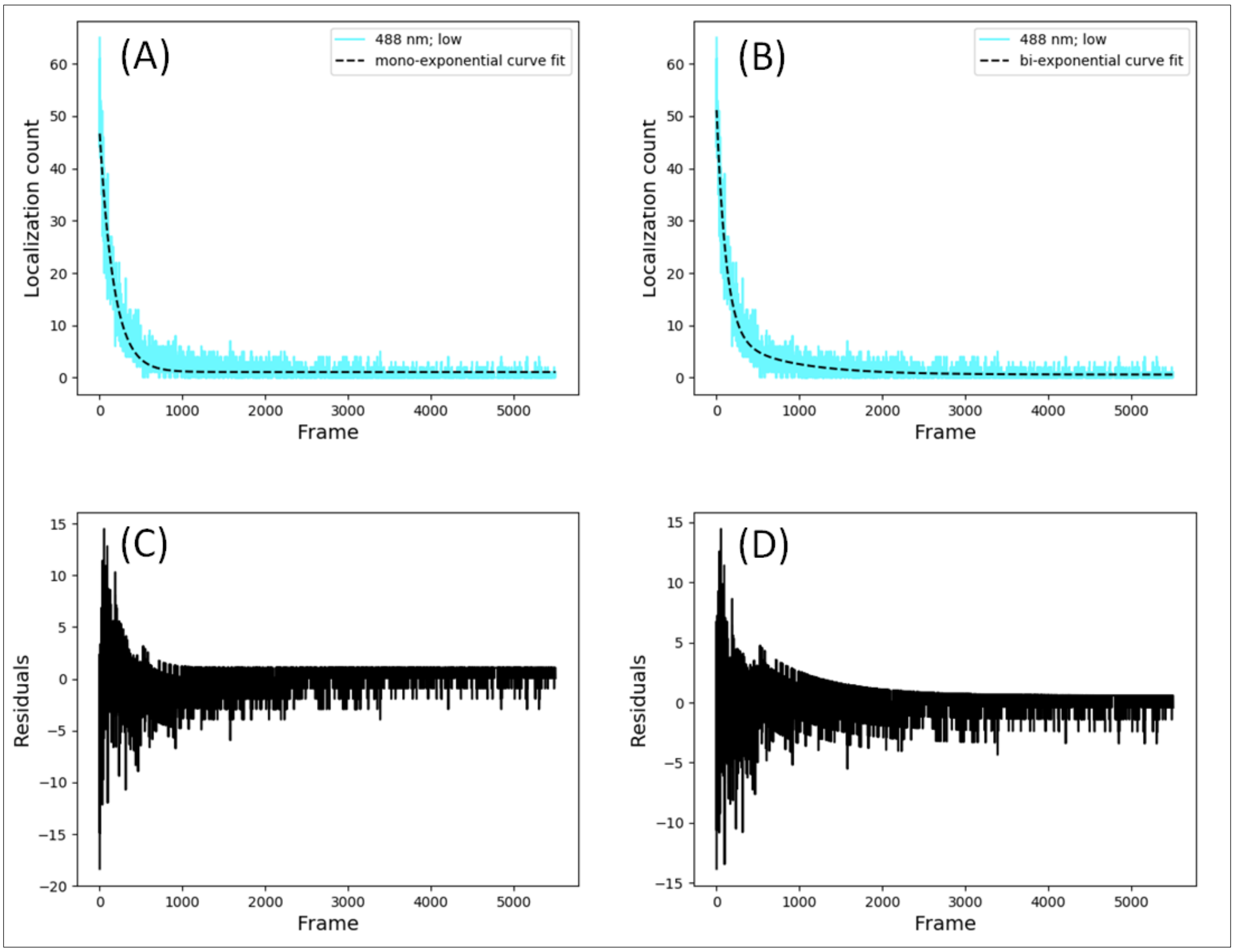

Figure 3.6. Mono-exponential (A), and bi-exponential (B) decay curve fit of a dataset measured from HEK-293 cells stably expressing EYFP-GEC1 with 488 nm excitation light. The residuals of the fitted curves are represented in (C) for mono-exponential decay curve fitting and in (D) for bi-exponential decay curve fitting.

From the results of the bi-exponential fitting one can derive the amplitude of the "weighted characteristic frame" defined by $\frac{A\frac{1}{B}+C\frac{1}{D}}{A+C}$, as an objective parameter to characterize the useful single molecule blinking period for each cell. In appendix 7.1, all values for weighted characteristic frame are given. Figure 3.7 shows the average of the weighted characteristic frame numbers for all cells measured with one of the four experimental conditions. The error bar represents the standard error of mean.

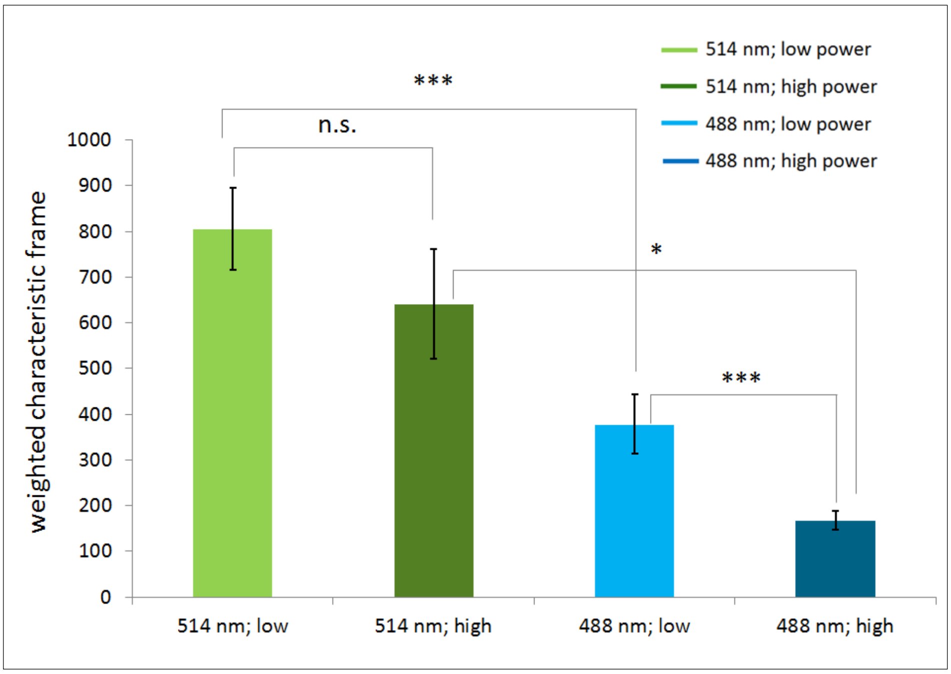

Figure 3.7. Characteristic frame numbers obtained from the bi-exponential decay curve fitting of Nloc./frame vs. frame datasets for HEK-293 cells stably expressing EYFP-GEC1 excited with high and low power of 514 nm (green) and 488 nm (blue) light. Error bars represent standard error of the mean. Statistical significance is represented as $p \leq 0.01$ (***); $p \leq 0.05$ (**), and $p \leq 0.1$ (*) from two-tailed t-tests (n.s., not significant).

In a final approach to find an objective parameter for EYFP blinking of HEK-293 cells stably expressing EYFP-GEC1, the total number of detected localizations was counted and divided by the average fluorescence intensity of the cell obtained from its corresponding fluorescent widefield image before SMLM imaging. ImageJ was used to obtain the average fluorescence intensity from the widefield image by drawing a freehand contour around the cell that defines the cell area and calculating the average fluorescence intensity value in this area. In this way one can compare the total number of localizations for all cells under the four experimental conditions since the number of detected localizations is normalized to the number of EYFP molecules (represented by the average fluorescence intensity). Excitation with low power of 514 nm leads to nearly 9-fold more detected localizations (normalized to number of EYFP molecules) when compared to a similar analysis for excitation with low power of 488 nm. For the high power experiments this difference is similarly high (7.5-fold).

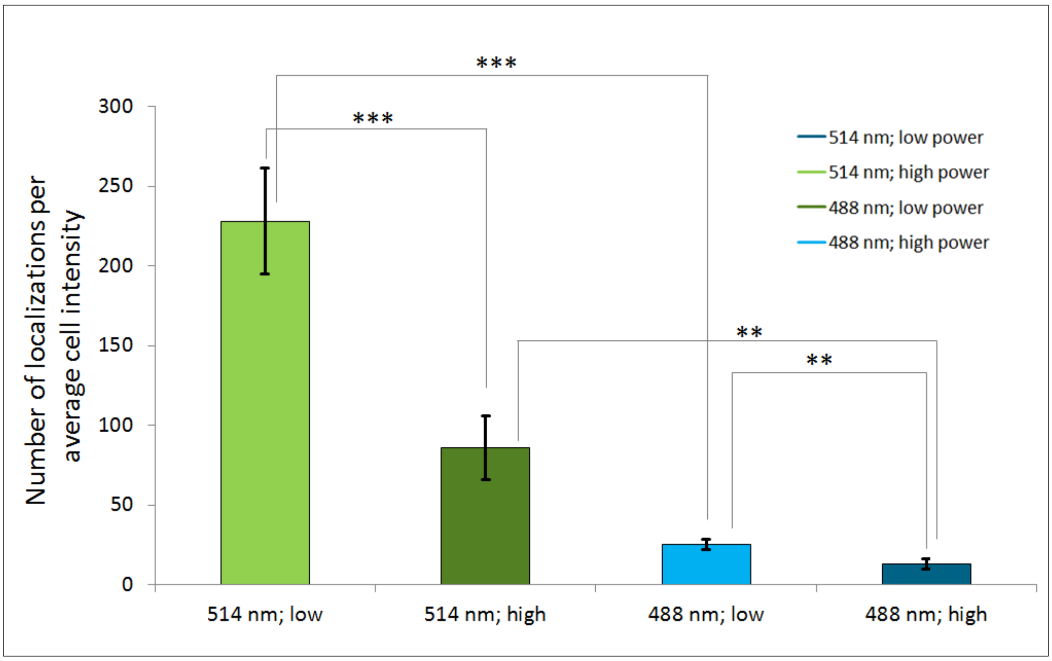

Figure 3.8. Total number of localizations per average cell intensity for high and low power of excitation HEK-293 cells stably expressing EYFP-GEC1 with 514 nm (green) and 488 nm (blue) light. Error bars represent standard error of the mean. Statistical significance is represented as $p \leq 0.01$ (***); $p \leq 0.05$ (**), and $p \leq 0.1$ (*) from two-tailed t-tests.

3.2. Shape and size distributions of EYFP-GABARAP and EYFP-LC3B containing structures

The shape and size distributions of cytoplasmic EYFP-GABARAP containing structures (CS-EYFP-GABARAP) and cytoplasmic EYFP-LC3B containing structures (CS-EYFP-LC3B) were investigated in fixed HEK-293 cells. Only starved-blocked samples were used for this investigation to enhance the number of autophagic structures. Cells labeled as starved-blocked were subjected to a standard protocol for enrichment of autophagic structures (starvation and blockage of autophagosome-lysosome fusion by application of bafilomycin A1) for 2 h right before fixation. The reasoning for investigating only cytoplasmic structures is given below. For both proteins, ten cells were selected for the analysis. The selection of the cells was done with care in order not to bias it with certain features such as high (or low) number of fluorescent structures, accumulation of structures only outside the nucleus, etc.

First, a fluorescence widefield image (with diffraction-limited resolution) of the cell of interest was recorded using low excitation power. The widefield images would be later used for the analysis of the EYFP-containing structures in a method called conventional analysis. Subsequently, a pre-acquisition illumination (with 75-fold higher excitation power) of 20 to 120 s was performed, in which most of the EYFP molecules were photoswitched to metastable, non-emissive dark state. From here the EYFP molecules in the fluorescent state were suitably well separated in order to be appropriately detected by the software for reconstruction of the super-resolution image. SMLM pictures of the EYFP-containing structures with super-resolution, i.e., resolution better than the diffraction limit, were obtained from a series of widefield images with high illumination power (4432 W/cm^2). The fluorescence of all single EYFP molecules was registered in each frame. Measurement series of such images (typically 4000 frames with 50 ms observation time each) was started at the end of the pre-acquisition illumination period. The adjustment of the pre-acquisition time period might be varied according to our former single molecule studies on EYFP.

The SNSMIL software developed several years ago in our institute (ICS-4) (Tang 2015), was used to calculate the super-resolution SMLM picture from the image series (see chapter 2, section 2.8). Representative images of fixed HEK-293 cells (starved-blocked) expressing EYFP-GABARAP and EYFP-LC3B, respectively, are given in figure 3.9. The super-resolved SMLM images (figures 9B, 9D) reveal a much higher total number of CS-EYFP-GABARAP (75 times more) and CS-EYFP-LC3B (89 and 78 times more for the left and right cell, respectively), compared to the corresponding widefield images. A similar increase is found for all cells expressing one or the other fluorescent Atg8 construct. The number of CS-EYFP-LC3B per cell (2898 ± 844) is significantly larger compared to the number of CS-EYFP-GABARAP (1777 ± 356). All samples for both EYFP-GABARAP and EYFP-LC3B in fed and starved-blocked conditions are given in appendix 7.2.

The subcellular distributions of the two overexpressed Atg8 proteins fused to EYFP are quite different. While EYFP-GABARAP structures are mainly found in the cytoplasm, EYFP-LC3B structures are presented in a higher density in the nucleus than in the cytoplasm. The larger labelled structures, which typically are also seen in the widefield images, however, are exclusively found in the cytoplasm for both proteins. These findings are in good agreement with data reported in the literature (He 2009, Nakatogawa 2009, Ravikumar 2010, Weiergräber 2012, Schaaf 2016, Abdollahzadeh 2017). Indeed, LC3B is thought to localize to the cell nucleus in an inactive acetylated form, which serves as a reservoir to be mobilized upon autophagy stimulation (Huang 2015); similarly, LC3 association with nuclear insulin receptor substrate 1 (IRS-1) has been suggested to attenuate autophagy in certain tumor cells (Lassak 2018). GABARAP reservoirs, by contrast, have been identified on the ER and in the pericentriolar matrix (Joachim 2015), but not in the nucleus. Since the entire process of autophagosome biogenesis ranging from initiation to elongation, maturation and degradation is known to take place outside the nucleus, concentration was on the cytoplasmic fraction of the fluorescently labelled objects for further analysis of overexpressed Atg8 proteins fused to EYFP and to omit the fraction localized in the nucleus. Re-examination of the SMLM images under this premise yields much more similar values of 1550 ± 286 cytoplasmic EYFP-GABARAP containing structures (CS-EYFP-GABARAP) and 1813 ± 233 cytoplasmic EYFP-LC3B containing structures (CS-EYFP-LC3B), respectively (see table 3.2). Thus, the previously determined higher number of fluorescently labelled structures in EYFP-LC3B expressing cells, compared to EYFP-GABARAP expressing cells, is caused, to a large extent, by the nuclear protein fraction in the former case. In figures 3.9(C) and 3.9(D), which show widefield and SMLM fluorescence images of EYFP-LC3B expressing cells, the fluorescence intensity contrast between nucleus and cytoplasm is considerably larger in widefield than in SMLM. This can be explained by properties of the widefield and SMLM detection methods. In widefield imaging, the focal depth of fluorescence imaging is larger compared to that of the single molecule detection, in addition, an excessive density of emitters may lead to a decreased single molecule detection efficiency when a large number of molecules emit in the vicinity of each other.

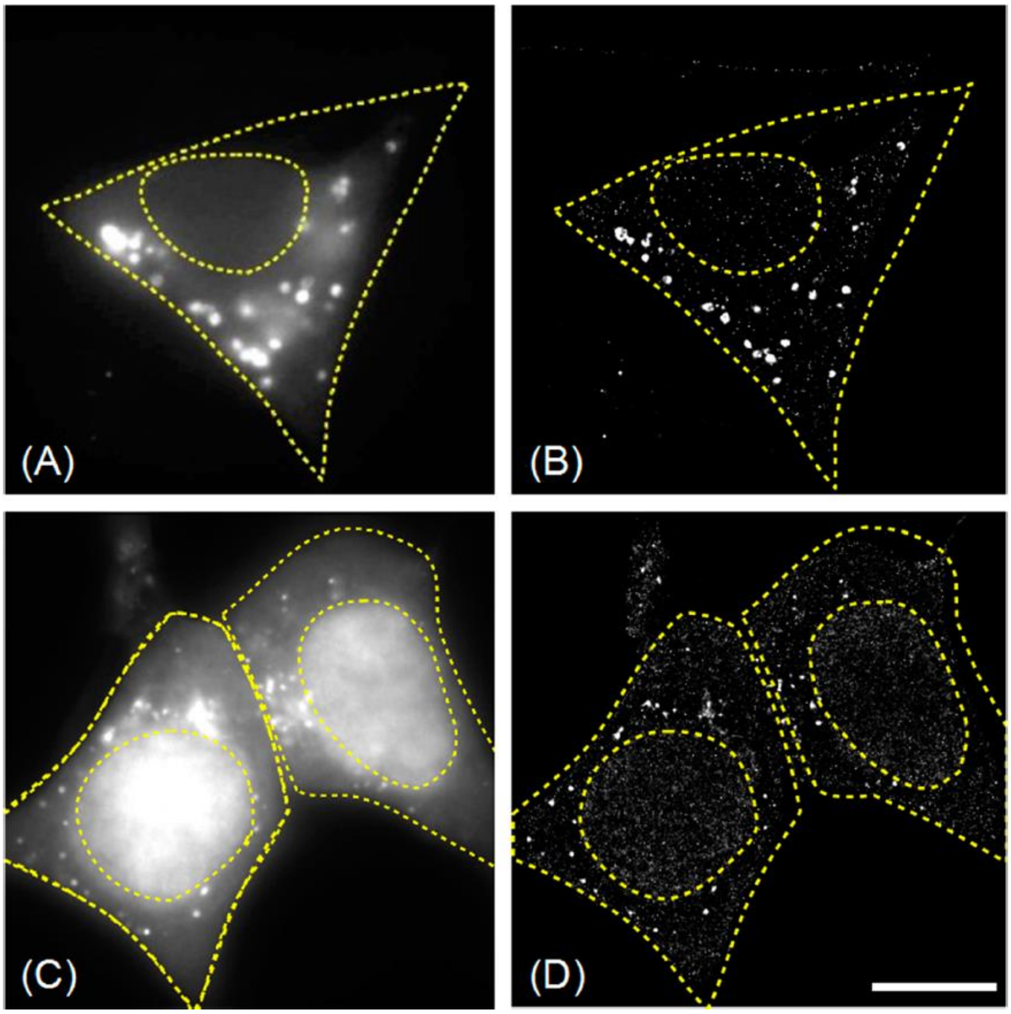

Figure 3.9. Widefield (A,C) and SMLM (B,D) images of fixed HEK-293 cells (starved and bafilomycin A1-treated) expressing EYFP-GABARAP (A,B), and EYFP-LC3B (C,D). In the widefield fluorescence images only a few labelled structures are found (**A**: 22; **C**: 35 and 20 in the left and right cell, respectively), while in the corresponding super-resolution images (**B**,**D**) the numbers of CS-EYFP-GABARAP (1640) and CS-EYFP-LC3B (3100 and 1564) are almost two orders of magnitude larger. Scale bar (valid for **A**–**D**): 10 µm. With the permission from the publisher under CC-BY-ND 2.0 license.

3.2.1. Size distribution of CS-EYFP-GABARAP and CS-EYFP-LC3B

The size distribution analysis of fluorescent protein tagged Atg8 proteins has been performed for EYFP-GABARAP and EYFP-LC3B in starved-blocked condition. The analysis mainly considers the diameter of a virtual circle with an area exactly equal to the area of the classified structure. In this section all sizes of structures are given in units of nm.

Generally, CS-EYFP-GABARAP and CS-EYFP-LC3B represent a similar distribution with mean and median slightly above and below 100 nm, respectively. Notably and interestingly, a large number of structures are smaller than the diffraction limit (~200 nm for fluorescence imaging of EYFP).

The structure size is in the range from 50 nm up to 2800 nm. The reasoning for the selection of 50 nm as the lower limit is based on the limited resolution and pixel size (16 nm in SMLM images). For instance, a circle structure with 50 nm diameter can only be detected by a 3 x 3 pixels area. On the other hand, the precision of single EYFP localization with our setup is ~ 30 nm. Therefore, selection of 50 nm as the lower limit for the size of structures appears to be well above the precision limit of localization for a single EYFP molecule.

In order to enable direct comparison between structures from the widefield images and structures identified from the SMLM images, and for a more appropriate and meaningful comparison of the shape distributions of CS-EYFP-GABARAP and CS-EYFP-LC3B (see section 3.2.2), the fluorescently labelled structures was divided into two groups based on their size, namely small and large structures. First of all, there might be a bias towards assigning circular shape to small fluorescently labelled structures originating from the limited resolution and pixel size. For instance, a very small circular structure can be detected from only one single molecule during the measurement and on the other hand there might be small circular structures with nearly the same size but constructed from much more single molecules. Both categories counted as small circular structures, but this might not be completely meaningful and true for the former. Second, large and small fluorescently labelled structures might well have different origins or functions all the way during autophagosome biogenesis and, as a result, also different shape distributions. To tackle this issue, two different splitting values was applied, namely, 100 nm and 300 nm. The fraction of fluorescently labelled structures larger than 300 nm will contain principally all structures whose shapes could be also classified with conventional fluorescence microscopy techniques like laser-scanning confocal or widefield fluorescence microscopy. On the other hand, 100 nm is the upper size limit for most common intracellular vesicles in endocytic and secretory pathways. Table 3.2 reveals that the value of 100 nm splits the CS-EYFP-GABARAP in almost equally large groups, while splitting at 300 nm classifies only 2% of the CS-EYFP-GABARAP in the group of the large structures and 98% belong to the small structures. For CS-EYFP-LC3B almost the same behavior was found with about 40% and 3% of the structures larger than 100 nm and 300 nm, respectively.

Imaging based on super-resolution techniques has several differences compared to the conventional widefield imaging techniques, which affect the quantity of information provided by the two methods. One of the main differences concerns the detection probability of structures as a function of their size. Another factor is the better resolution, affecting the apparent shapes of visible objects. For a meaningful comparison of the information provided by the two methods, sets of CS-EYFP-GABARAP and CS-EYFP-LC3B identifiable on widefield fluorescence images of the cells generated (see table 3.2).

Table 3.2. Number of cytoplasmic structures containing EYFP-GABARAP and EYFP-LC3B identified in SMLM images. Numbers are given for the entire size range considered (50 nm–2.8 µm) as well as for two sub-ranges (split alternatively at 100 nm or at 300 nm). For comparison, the numbers of cytoplasmic EYFP-GABARAP and EYFP-LC3B identified in the corresponding widefield fluorescence images (named "conventional selection") are also given. With the permission from the publisher under CC-BY-ND 2.0 license.

Overexpressed Protein	Size Category	Number of Structures	Fraction of Structures (%)
EYFP-GABARAP	50 nm–2.8 µm	15,501	100
	50 nm–100 nm	8009	51.66
	100 nm–2.8 µm	7492	48.33
	50 nm–300 nm	15,153	97.75
	300 nm–2.8 µm	348	2.25
	Conventional selection	348	
EYFP-LC3B	50 nm–2.8 µm	18,129	100
	50 nm–100 nm	11,579	63.87
	100 nm–2.8 µm	6550	36.13
	50 nm–300 nm	17,643	97.32
	300 nm–2.8 µm	486	2.68
	Conventional selection	486	

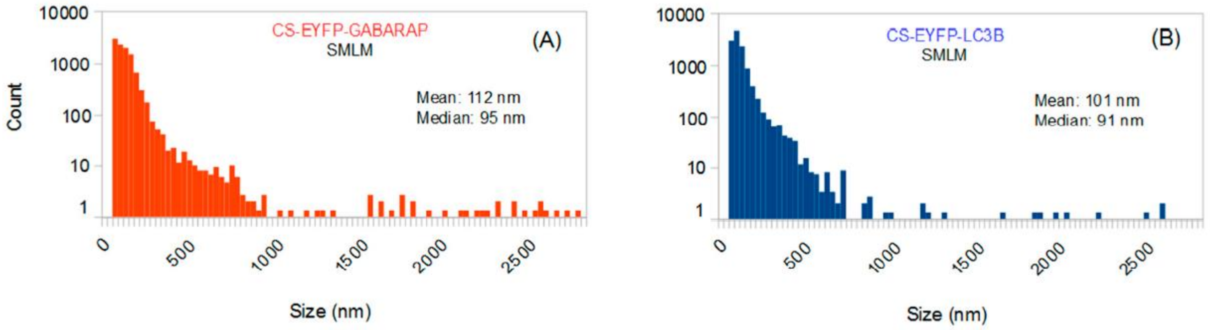

Figure 3.10. Size distributions of all cytoplasmic, fluorescently labelled structures identified in the SMLM images of ten EYFP-GABARAP expressing (A) and ten EYFP-LC3B expressing HEK-293 cells (B) under starvation and bafilomycin A1 treatment. The diagram shows the total count of structures on a logarithmic scale, with a 32 nm binning of radii. With the permission from the publisher under CC-BY-ND 2.0 license.

The size distributions of the "conventionally selected" CS-EYFP-GABARAP and CS-EYFP-LC3B are given in figure 3.11. The sizes of the structures in widefield images were obtained by drawing a freehand border around a detected structure, and determining its area in terms of pixels or nm^2. With x and y coordinates of the structure's position, it was possible to obtain the corresponding size in the super-resolved image. All four size distributions, either acquired in widefield images (figure 3.11 (A), 3.11(C)) or (structures in SMLM images larger than 300 nm) (figure 3.11(B), 3.11(D)) show clear and expected differences when compared to the size distributions of all structures in SMLM images (figure 3.10(A), 3.10(B)). Indeed, no small structures (less than 300 nm) are found in the conventionally selected set. Interestingly, for structures detected in widefield images, the size distributions of the conventionally selected CS-EYFP-GABARAP and CS-EYFP-LC3B were different from those using the respective super-resolution images (compare figure 3.11(A) with figure 3.11(B) and figure 3.11(C) with 3.11(D)). Mean and median are shifted towards higher values (between 455 and 533 nm). There are an increased number of structures smaller than 500 nm in the SMLM images, even though mean and median did not change dramatically.

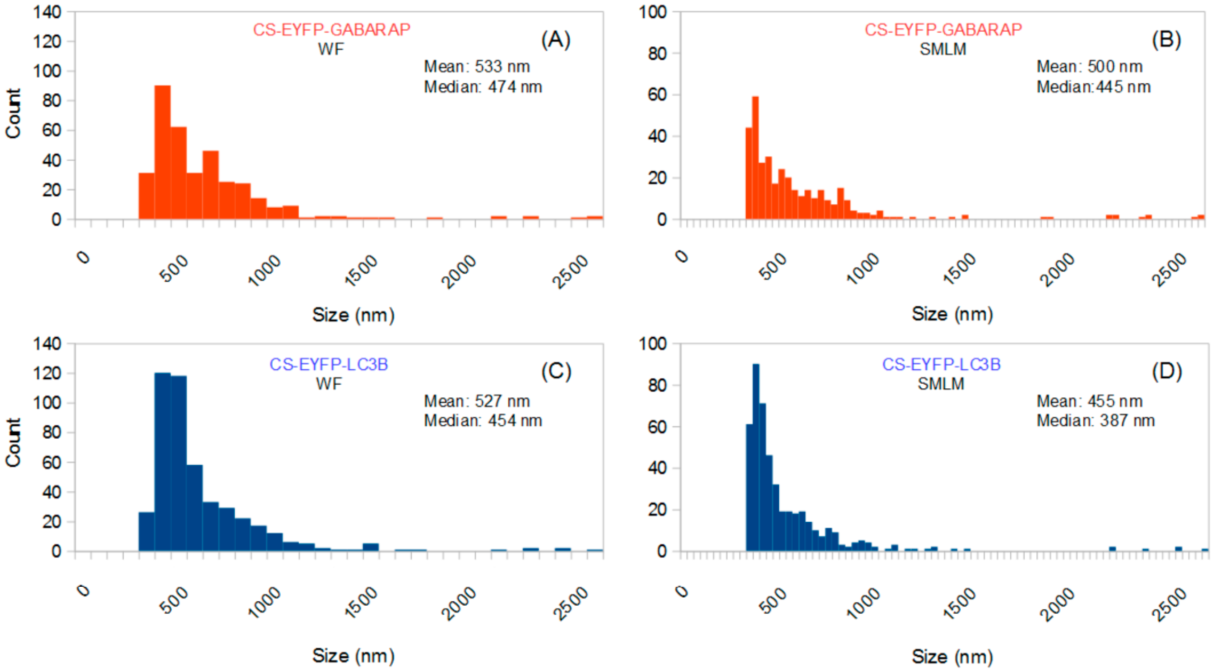

Figure 3.11. Size distributions of all conventionally selected fluorescently labelled structures (identified in widefield images) of ten EYFP-GABARAP expressing (A,B) and ten EYFP-LC3B expressing fixed HEK-293 cells (C,D) under starvation and bafilomycin A1 treatment, where size was determined in the widefield fluorescence (A,C) and the SMLM images (B,D), respectively. Note the different binning used in A/C (80 nm) and B/D (32 nm), respectively, caused by the different image resolution in widefield fluorescence compared to super-resolution microscopy. With the permission from the publisher under CC-BY-ND 2.0 license.

3.2.2. Shape distributions of CS-EYFP-GABARAP and CS-EYFP-LC3B selected in super-resolution fluorescence microscopy images

The shape classification used in this study has been limited to three geometrical categories, namely U-shape, circle and ellipse (abbreviated: u, c and e, respectively). This shape classification is based on the well-established mechanism of autophagosome formation (figure 3.13 and (Shibutani 2014, Carlsson 2015, Abdollahzadeh 2017), where the three shape geometries reflect all possible autophagic structures. In the beginning of autophagosome formation, which is called nucleation, a flat membrane vesicle (i.e., a phagophore) grows around the cargo, and appears either as a U-shape structure (when viewed from the side) or as a circular (when viewed along is longitudinal axis) or elliptical object (when viewed at intermediate angles) in the two-dimensional SMLM imaging mode. During the elongation phase, the phagophore geometry is approaching a half-moon or elliptical shape. Once the autophagosome is mature, its shape will be very similar to a sphere that would be a circle in our 2D-projection SMLM imaging mode, except for very large and asymmetrical cargo. For some relatively large-sized cargo such as entire bacteria, in case of xenophagy, the identified shape would be completely a function of the cargo. In all experiments in this work, autophagy induced in cells by starvation and therefore, bulk autophagy is the dominant pathway and contribution of cargo to the shape is negligible. In figure 3.12, typical examples for the three categories of CS-EYFP-GABARAP and CS-EYFP-LC3B, respectively, from SMLM images of fixed HEK-293 cells are depicted.

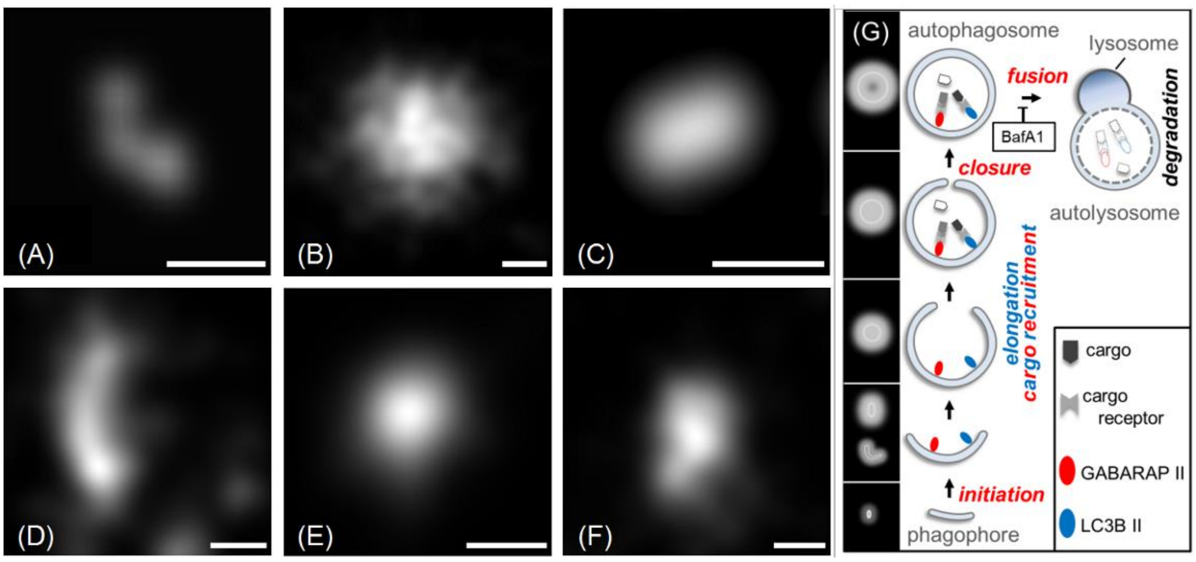

Figure 3.12. Examples for the three shape categories (A, D: U-shape; B, E: circle; C, F: ellipse). Structures in A, B, and C are from EYFP-GABARAP expressing cells, structures in D, E, and F are from EYFP-LC3B expressing cells (scale bars: 100 nm). In G, the presumed roles of GABARAP and LC3B at distinct stages of the autophagy pathway (phagophore initiation, elongation, closure, and fusion of the mature autophagosome with a lysosome to yield an autolysosome) are depicted. Steps that are assumed to require GABARAP and LC3B on the convex face of the isolation membrane (not drawn for clarity reasons) are highlighted in blue and red, respectively. As shown, GABARAP and LC3B can both link cargo materials to the concave face of the isolation membrane during selective autophagy in a cargo receptor-mediated manner. The various autophagic structures drawn as cross-sections are assigned to the respective 2D projections as anticipated in SMLM reconstructions (with a marked direction-dependence in the case of an early phagophore). Note, however, that SMLM cannot strictly distinguish between these membrane-bound autophagic organelles and other (vesicular or non-vesicular) structures populated by Atg8 proteins. With the permission from the publisher under CC-BY-ND 2.0 license.

Classification of all CS-EYFP-GABARAP in the SMLM images, as depicted in figure 3.13, resulted in a shape distribution similarly found in all ten fixed HEK-293 cells analyzed. The number of CS-EYFP-GABARAP per cell varied between 350 and 2300 with a total number of 15,501 in all ten cells (table 3.2). In order to better evaluate the shape distributions of CS-EYFP-GABARAP, it was considered useful to divide the CS-EYFP-GABARAP in two groups based on the size of the structures, namely small and large structures, with two different splitting values, 100 and 300 nm, respectively (see section 3.2.1 for more explanation). In figure 3.13, the shape classification in the five size cases (i.e. all structures, and structures smaller/larger than 100 nm/300 nm) can be generally described as follows: The majority of CS-EYFP-GABARAP appear as circles, lesser structures as ellipses and a minor fraction shows U-shape (only for CS-EYFP-GABARAP larger than 300 nm, circles and ellipses have similar occurrence; figure 3.13(E)). Generally speaking, U-shape structures appear to represent the lowest percentage among CS-EYFP-GABARAP (only 9 to 23%), with the highest value in the group of the largest CS-EYFP-GABARAP (larger than 300 nm).

Classification of all CS-EYFP-LC3B was performed in the same way as described above for CS-EYFP-GABARAP (applying again the separation values of 100 nm and 300 nm, respectively). The total number of CS-EYFP-LC3B in the ten analyzed transiently transfected HEK-293 cells is equal to 18,129 and was hence slightly (∼20%) larger compared to the experiments with EYFP-GABARAP. In general, comparison of the total numbers of labeled structures in an experiment based on overexpression of proteins would not reveal a meaningful result, since a number of experimental parameters may vary in transient transfections (e.g., quality of DNA, efficiency of plasmid uptake, yield of chromophore maturation), preventing the reproducibility of absolute protein numbers. This issue was addressed with the use of HEK-293 cell lines stably expressing Atg8 proteins, in this case fused with the Dendra2 protein (section 3.3).

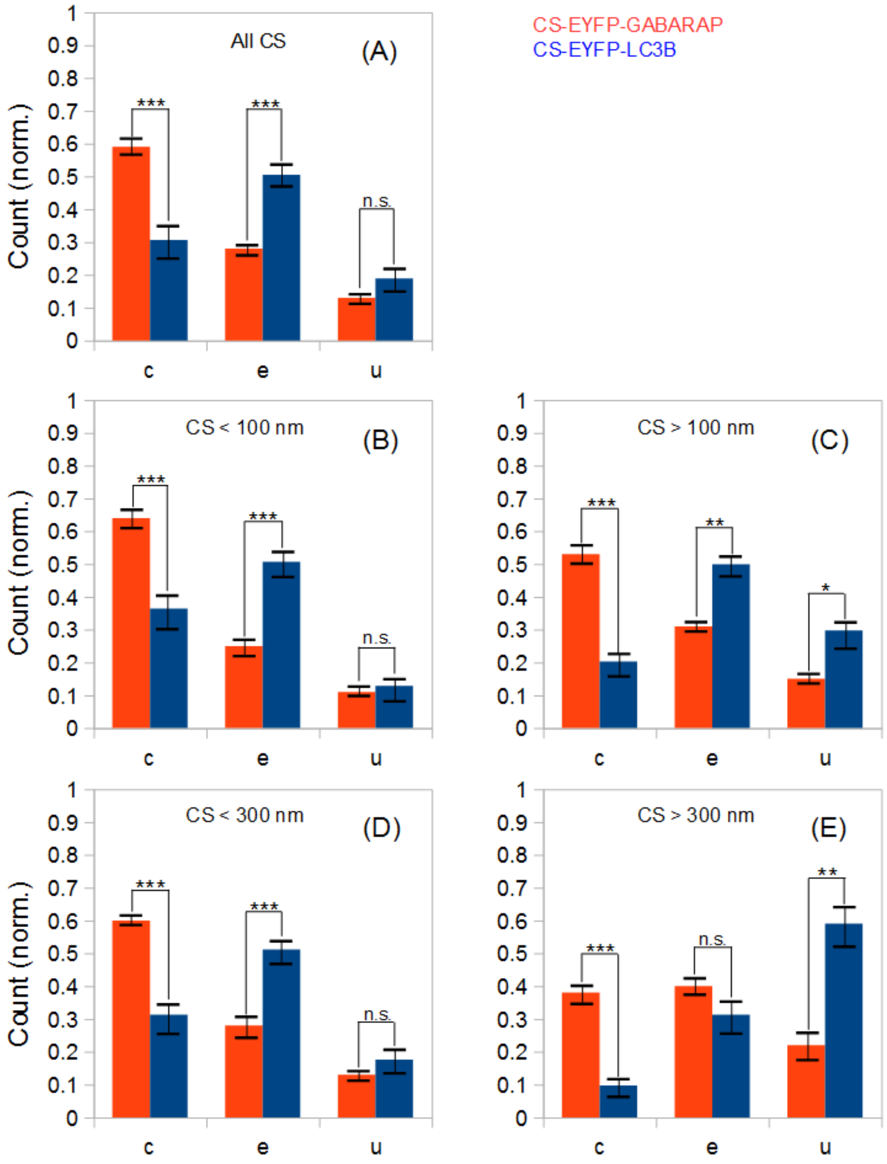

Figure 3.13. Shape analysis of all cytoplasmic fluorescent structures observed in SMLM images of ten HEK-293 cells expressing either EYFP-GABARAP (red) or EYFP-LC3B (blue) under starvation and bafilomycin A1 treatment. (A) All CS-EYFP-GABARAP (15501) and CS-EYFP-LC3B (18129); (B) CS-EYFP-GABARAP (8009) and CS-EYFP-LC3B (11579) smaller than 100 nm; (C) CS-EYFP-GABARAP (7492) and CS-EYFP-LC3B (6550) larger than 100 nm; (D) CS-EYFP-GABARAP (15153) and CS-EYFP-LC3B (17643) smaller than 300 nm; (E) CS-EYFP-GABARAP (348) and CS-EYFP-LC3B (486) larger than 300 nm. Error bars represent standard error of the mean (N=10) mean. Statistical significance is represented as $p \leq 0.01$ (***); $p \leq 0.05$ (**), and $p \leq 0.1$ (*) from two-tailed t-tests (n.s., not significant). c, e and u stands for circles, ellipses and U-shapes. With the permission from the publisher under CC-BY-ND 2.0 license.

In figure 3.13, the five shape distributions for different size categories of CS-EYFP-LC3B are plotted next to the corresponding classification of CS-EYFP-GABARAP. Direct comparison of the shape distributions of the two proteins immediately shows that the two Atg8 proteins are present in different subsets of the vesicular system of the cell. For all five categories of CS-EYFP-LC3B, ellipses constitute the major fraction (31–51%), while circles—the major fraction for CS-EYFP-GABARAP—were only the second most prevalent for total and the small-size groups of CS-EYFP-LC3B (~30%) and even the minor fraction for the large-size groups of CS-EYFP-LC3B (10–20%). U-shape objects among the CS-EYFP-LC3B were found to be present in higher relative amounts (13–59%) compared to CS-EYFP-GABARAP, being the most abundant shape for CS-EYFP-LC3B larger than 300 nm.

The total number of analyzed structures, as was seen from table 3.2, is relatively high and the shape distributions for CS-EYFP-GABARAP and CS-EYFP-LC3B, respectively, appear visually different, especially for the large-size structures. On the other hand, the number of cells analyzed (10 for each protein), is only moderate. In order to assess the effect of the number of cells analyzed for each protein, two-tailed t-tests performed to judge whether the differences in the relative abundances of circles, ellipses and U-shapes are statistically significant. Generally speaking, although the cell numbers appear not very high, the total number of detected structures for all ten cells is high and made it feasible to perform such a classification and statistical analysis. The results are given in numbers in table 3.3, and most of them are also shown graphically in figure 3.13.

Table 3.3. P-values from two-tailed t-tests to assess the statistical significance of differences in the shape distributions (c, circles; e, ellipses; u, U-shapes) of (i) CS-EYFP-GABARAP vs. CS-EYFP-LC3B (various size classes), (ii) different size classes of CS-EYFP-GABARAP, (iii) different size classes of CS-EYFP-LC3B, and (iv) CS-EYFP-GABARAP or CS-EYFP-LC3B structures classified in widefield vs. SMLM. With the permission from the publisher under CC-BY-ND 2.0 license.

	c	**e**	**u**
CS-EYFP-GABARAP vs. CS-EYFP-LC3B (50 nm–2.8 µm)	0.0026	0.00050	0.21
CS-EYFP-GABARAP vs. CS-EYFP-LC3B (< 100 nm)	0.010	0.0053	0.66
CS-EYFP-GABARAP vs. CS-EYFP-LC3B (> 100 nm)	0.000026	0.019	0.10
CS-EYFP-GABARAP vs. CS-EYFP-LC3B (< 300 nm)	0.0024	0.00035	0.29
CS-EYFP-GABARAP vs. CS-EYFP-LC3B (> 300 nm)	0.000023	0.49	0.04
CS-EYFP-GABARAP: CS < 100 nm vs. CS > 100 nm	0.29	0.54	0.20
CS-EYFP-GABARAP: CS < 300 nm vs. CS > 300 nm	0.0042	0.02	0.23
CS-EYFP-LC3B: CS < 100 nm vs. CS > 100 nm	0.09	0.71	0.04
CS-EYFP-LC3B: CS < 300 nm vs. CS > 300 nm	0.03	0.08	0.02
CS-EYFP-GABARAP: WF vs. SMLM	0.000010	0.50	0.0018
CS-EYFP-LC3B: WF vs. SMLM	0.000010	0.70	0.01

As both table 3.3 and figure 3.13 reveal, the five shape classifications based on size of the structures have at least one P-value smaller than 0.01 or in weaker cases a P-value less than 0.05. For all categories except shapes larger than 300 nm, the circular structures appear to be significantly different for both proteins, with higher abundance for EYFP-GABARAP than for EYFP-LC3B. For the same size classes, the ellipse structures are also significantly different for both proteins, with less abundance for EYFP-GABARAP than for EYFP-LC3B. Interestingly, the higher amount of U-shapes for larger cytoplasmic structures containing EYFP-LC3B compared to those containing EYFP-GABARAP is significant too, though with a higher P-value (< 0.05). Thus, although the number of investigated cells is only moderate (due to the time-consuming and elaborate size and shape analysis), the differences in the shape distributions of the cytoplasmic structures labelled by the two proteins are highly significant and relevant.

3.2.3. Shape distributions of CS-EYFP-GABARAP and CS-EYFP-LC3B selected in widefield fluorescence microscopy images

GABARAP and LC3B fused to fluorescent proteins are very popular in autophagy research since the early 2000s. In almost all fluorescence microscopy studies, conventional methods with limited resolution like widefield or confocal fluorescence microscopy were applied. Therefore, the majority of the existing fluorescence microscopy images of structures containing Atg8 proteins have diffraction-limited resolution. A direct comparison of conventional widefield imaging data and super-resolution non diffraction-limited imaging data appeared advisable. The size of every CS-EYFP-GABARAP and CS-EYFP-LC3B that were identifiable in the conventional widefield fluorescence images was determined twice, first in the widefield and second in the corresponding SMLM images (figure 3.11). First, all cytoplasmic EYFP-GABARAP and EYFP-LC3B containing structures were identified in the widefield fluorescence images. For both EYFP-GABARAP and EYFP-LC3B proteins, the group of cytoplasmic fluorescent structures identified in widefield images is identical to the group of cytoplasmic fluorescent structures larger than 300 nm identified in SMLM images. As expected from other studies using conventional microscopy for fluorescently labeled autophagic proteins, the number of cytosolic fluorescently labelled structures detected by “conventional selection” was found largely reduced and is well below 50 per cell. A little surprising, however, was the finding that roughly 10-fold better spatial resolution of SMLM led to a significant difference in the shape analysis of structures compared to the shape analysis in the widefield images. The result of the shape classification for one and the same structure can be different in a widefield fluorescence image and its corresponding SMLM image, respectively. In fact, this is the case for about 50 % of all structures.

To demonstrate this issue, widefield and super-resolution fluorescence images of five conventionally selected CS-EYFP-LC3B are depicted in figure 3.14 (similar examples can be found for CS-EYFP-GABARAP (not shown)). From the widefield images the structures represented in figures 3.14(A) and 3.14(C) are classified as circle while the structures in figures 3.14(B), 3.14(D), and 3.14(E) are classified as ellipse. This simple picture changes when examining the fluorescent structures in the respective SMLM images. While structures in figure 3.14(A) (circle) and figure 3.14(B) (ellipse) appear to have the same shapes in super-resolution, the other three structures have a different shape when imaged and analyzed with higher spatial resolution. The ellipse in figure 3.14(D) turns into a U-shape in figure 3.14(I), while the circle in figure 3.14(C) resolves into an inhomogeneous ellipse in figure 3.14(H). The ellipse in figure 3.14(E) even appears to be clearly two objects in figure 3.15(J), a U-shape and a smaller circle.

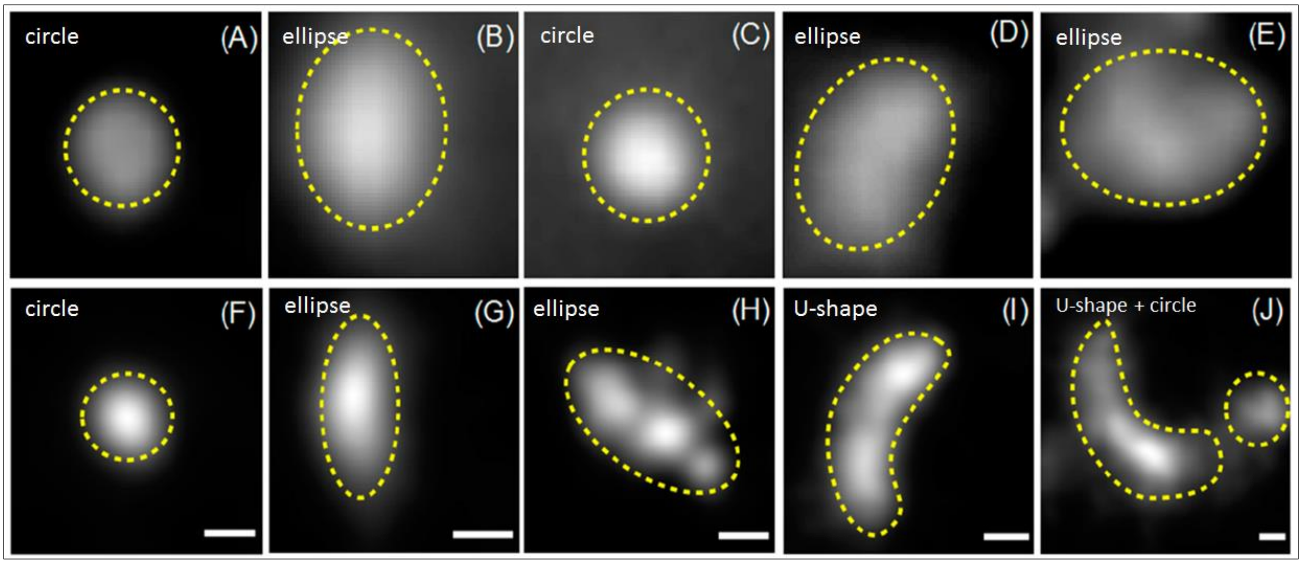

Figure 3.14. Widefield fluorescence (A–E) and corresponding SMLM images (F–J) of five CS-EYFP-LC3B that were identified on the basis of the widefield image (scale bars: 100 nm). With the permission from the publisher under CC-BY-ND 2.0 license.

The shapes of all “conventionally selected” CS-EYFP-GABARAP and CS-EYFP-LC3B analyzed and made a notable observation. First of all, for both Atg8 proteins, the shape distribution is statistically significantly different when the classification is performed based on widefield or SMLM images. These shape distributions and the result of a two-tailed t-test analysis is given in figure 3.15 (see also last two rows in table 3.3). In widefield fluorescence images, U-shapes are very rare (less than 3%) for CS-EYFP-GABARAP but increase to nearly 20% in super-resolution images. The amount of elliptical structures increases from below 25% to almost 40% while the circular shapes percentage drops from above 70% to less than 40%

(figure 3.15(A)). The difference between structures analyzed in widefield and super-resolution images is even more pronounced for CS-EYFP-LC3B (figure 3.15(B)). Here, circular shapes turn from the dominant fraction (65%) in widefield fluorescence to the minor fraction (~10%) in super-resolution fluorescence, while, on the contrary, the percentage of U-shape grows from less than 5% to almost 65% and the percentage of elliptical structure stays nearly the same (30% vs. 35%) when switching from widefield images to super-resolution images. For the two proteins, the relative abundances for both circles and U-shapes are different with very high statistical significance (figure 3.15 and table 3.3).

A closer look at the data presented in figure 3.15 and table 3.3 reveals one more interesting fact when using widefield and super-resolution images with structures larger than 300 nm as the sources of shape classification of both Atg8 proteins. The shape distributions of the structures containing the two Atg8 proteins appear similar upon examination in conventional fluorescence microscopy with diffraction-limited resolution. None of the three shape categories has a statistically different relative abundance, but they are different when shape is classified based on super-resolution SMLM fluorescence microscopy. Specifically, the fractions of circles and U-shapes are significantly different in the latter case. To summarize, our data based on super-resolved images support the idea of involvement of GABARAP and LC3B in different stages of autophagosome biogenesis and/or participation in further, non-autophagy related processes.

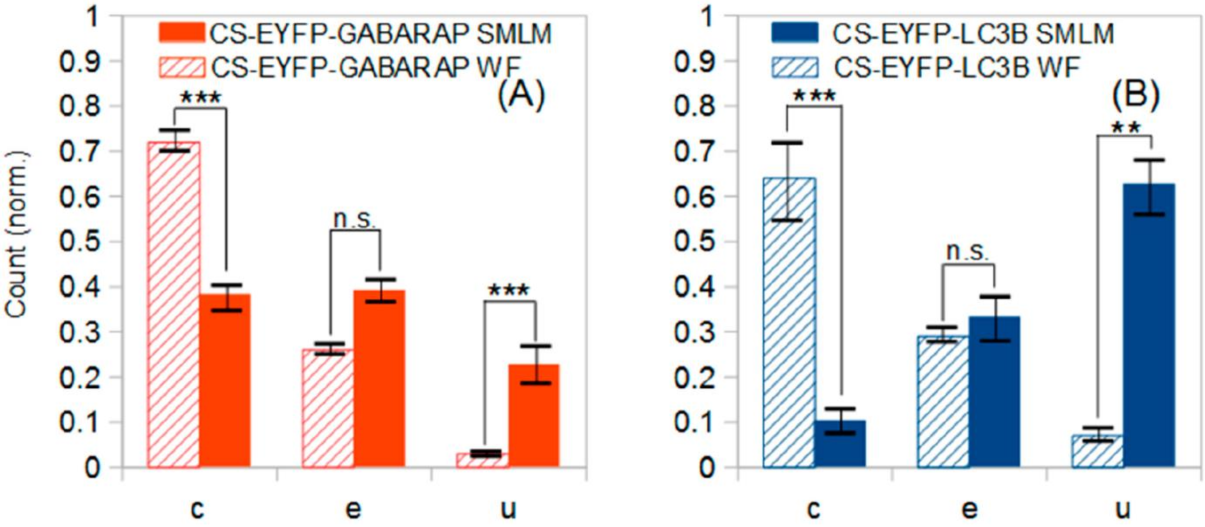

Figure 3.15. Shape distributions of fluorescently labelled cytoplasmic structures identified in the widefield images of ten EYFP-GABARAP expressing and ten EYFP-LC3B expressing HEK-293 cells, respectively, under starvation and bafilomycin A1 treatment. (**A**) Conventionally selected CS-EYFP-GABARAP (348) classified in widefield fluorescence (hatched bars) and the same structures classified in the respective SMLM (full bars) images; (**B**) Conventionally selected CS-EYFP-LC3B (486) classified in widefield fluorescence (hatched bars) and the same structures classified in the respective SMLM (full bars) images. Error bars represent standard error of the mean. Statistical significance is represented as $p \leq 0.01$ (***); $p \leq 0.05$ (**), and $p \leq 0.1$ (*) from two-tailed

t-tests (n.s., not significant). c, e and u stands for circles, ellipses and U-shapes. With the permission from the publisher under CC-BY-ND 2.0 license.

3.3. Shape and size distributions of CS-Dendra2-GABARAP and CS-Dendra2-LC3B

In this section the shape and size analysis for structures detected in super-resolution images of HEK-293 cells stably expressing Dendra2-GABARAP or Dendra2-LC3B is described. During the initial phase of evaluating these cell lines in fed and starved-blocked conditions, it was found that there is reproducibly a distinct difference, in terms of the number of the structures and the fluorescence signal intensity, between fed and starved-blocked cells, as described in the literature (Li 2014, Cohen-Kaplan 2016, Lamb 2017). In contrast, this was not the case when HEK-293 cells were transiently transfected (as in the experiments described in the previous chapter (3.2)). Often, cells in fed condition had similar numbers of FP-GABARAP or FP-LC3B containing cytoplasmic structures. This finding may be rationalized by cellular stress due to the transient transfection period. In appendix 7.3, a set of fluorescent images acquired with the use of confocal laser scanning microscopy (LSM) is depicted, which exemplary visualizes the lower number and fluorescence intensity of the CS-Dendra2-GABARAP and CS-Dendra2-LC3B found in fed conditions in comparison to the starved-blocked conditions. Both fixed cells stably expressing Dendra2-GABARAP and fixed cells stably expressing Dendra2-LC3B kept at fed and starved-blocked condition, respectively, were measured with similar experimental parameters and results plotted with identical scaling in order to allow for a valid comparison. Since both cell lines showed a different phenotype of fed samples compared to the starved-blocked samples (e.g. fluorescence intensity of structures and the total number of structures detected per cell) they were measured with SMLM in fed and starved-blocked conditions. In figure 3.16, representative conventional widefield and SMLM images of fixed HEK-293 cells stably expressing Dendra2-GABARAP or Dendra2-LC3B in fed and starved-blocked conditions, respectively, are given.

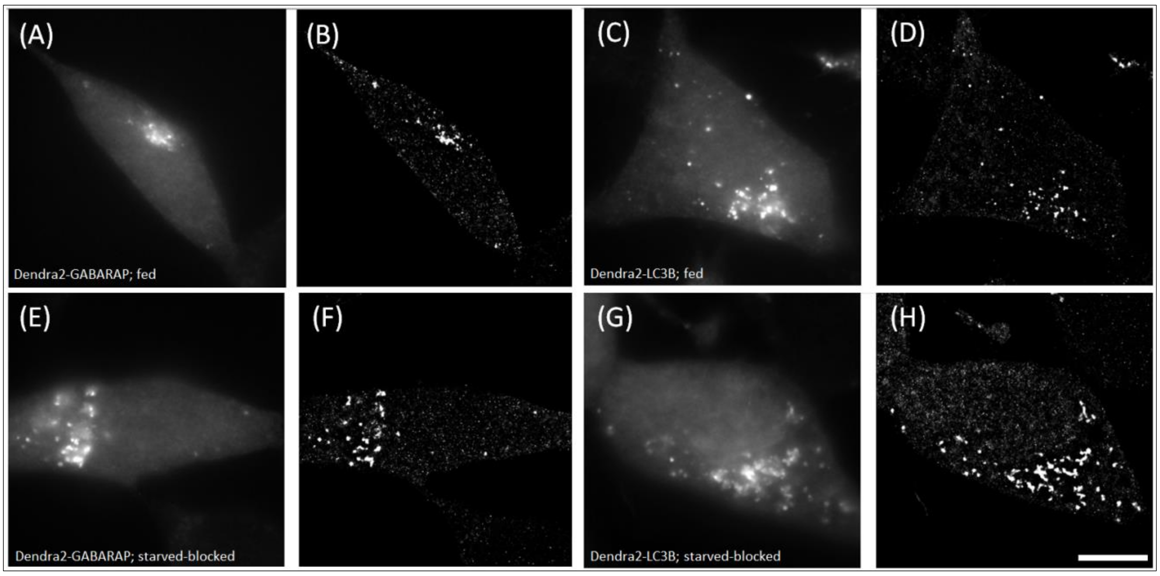

Figure 3.16. Widefield (A,C,E,G) and SMLM (B,D,F,H) images of fixed HEK-293 cells stably expressing Dendra2-GABARAP (A,B,E,F) and Dendra2-LC3B (C,D,G,H). The images in (A,B,C,D) are at fed condition and images in (E,F,G,H) are at starved-blocked condition, respectively. Scale bar: 10 µm.

3.3.1. Size distributions of CS-Dendra2-GABARAP and CS-Dendra2-LC3B

The size analysis for structures detected in super-resolution images of HEK-293 cells stably expressing Dendra2-GABARAP or Dendra2-LC3B is given in this section. In figure 3.17, the entire size distributions for structures larger than or equal to 50 nm for CS-Dendra2-GABARAP (fed and starved-blocked conditions, A) and CS-Dendra2-LC3B (fed and starved-blocked conditions, B)), obtained from ten evaluated cells per condition, are shown.

There is not a large difference between CS-Dendra2-GABARAP and CS-Dendra2-LC3B size distributions for fed or starved-blocked conditions (The average and median are 106.93 nm / 90.51 nm, 104.87 nm / 89.08 nm, 108.01 nm / 91.91 nm, and 122.23 nm / 89.08 nm, for CS-Dendra2-GABARAP-fed, CS-Dendra2-GABARAP-starved-blocked, CS-Dendra2-LC3B-fed, and CS-Dendra2-LC3B-starved-blocked conditions, respectively). Nevertheless, comparing structures detected in fed versus starved-blocked conditions reveals that there is a difference, clearly visible, for larger structures. The number of structures larger than 800 nm is indeed much higher for starved-blocked cells compared with the corresponding fed cells (12 CS-Dendra2-GABARAP-fed vs. 42 CS-Dendra2-GABARAP-starved-blocked; 19 CS-Dendra2-LC3B-fed vs. 165 CS-Dendra2-LC3B-starved-blocked), a much larger difference than what is found when the classification into small and large cytosolic structures was performed with splitting at 300 nm (284 CS-Dendra2-GABARAP-fed vs. 406 CS-Dendra2-GABARAP-starved-blocked; 495 CS-Dendra2-LC3B-fed vs. 682 CS-Dendra2-LC3B-starved-blocked). This finding is valid for structures in both cell lines. Based on this finding, additional classes added containing structures smaller and larger than 800 nm for the analysis of the shapes of CS-Dendra2-GABARAP and CS-Dendra2-LC3B.

The size distributions of the “conventionally selected” CS-Dendra2-GABARAP and CS-Dendra2-LC3B are shown in figures 3.18 (for fed condition) and 3.19 (for starved-blocked condition). The selection of these structures was performed in a similar manner as explained in section 3.2.1 for CS-EYFP-Atg8 structures. First, all structures that could be selected in widefield images were categorized and subsequently the corresponding super-resolved structures were classified. Figures 3.18(A) (mean: 481 nm, median: 418 nm) and 3.18(B) (mean: 493 nm, median: 425 nm) represent the conventional widefield and super-resolution size distribution for CS-Dendra2-GABARAP structures in fed condition and figures 3.18(C) (mean: 432 nm, median: 381 nm) and 3.18(D) (mean: 458 nm, median: 405 nm) represent the conventional widefield and super-resolution size distribution for CS-Dendra2-LC3B structures in fed condition. Figures 3.19(A) (mean: 452 nm, median: 393 nm) and 3.19 (B) (mean: 504 nm, median: 431 nm) represent the conventional widefield and super-resolution size distribution for CS-Dendra2-GABARAP structures in starved-blocked condition and figures 3.19(C) (mean: 600 nm, median: 513 nm) and 3.19(D) (mean: 633 nm, median: 542 nm) represent the conventional widefield and super-resolution size distribution for CS-Dendra2-LC3B structures in starved-blocked condition. Notably, while the CS-Dendra2-GABARAP and CS-Dendra2-LC3B numbers were distinctively (300 nm splitting) or even largely different (800 nm splitting) in the class of large structures, the total number was not (CS-Dendra2-GABARAP: 16205(fed) vs. 16386 (starved-blocked); CE-Dendra2-LC3B: 18563 (fed) vs. 11712 (starved-blocked)).

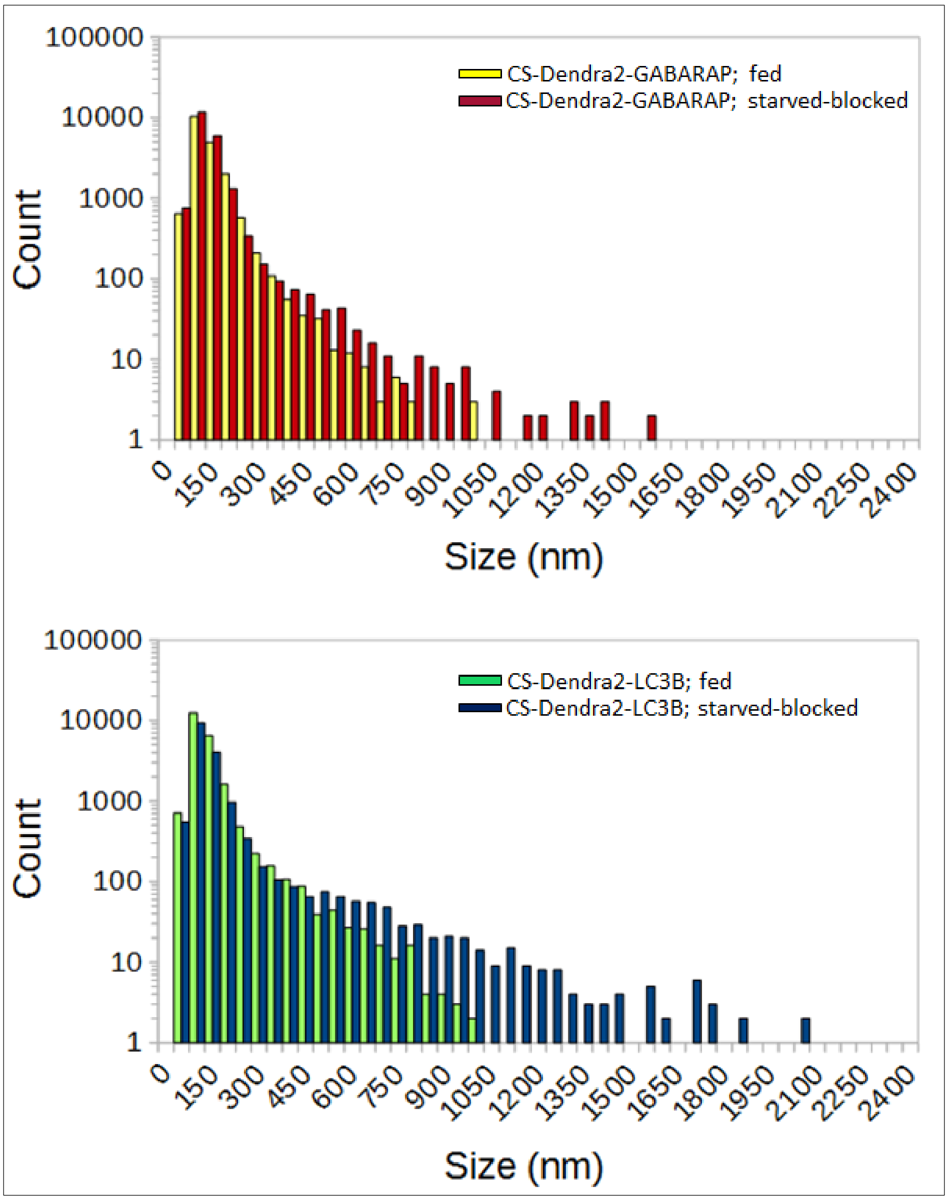

Figure 3.17. Size distributions (binning 32 nm) of all cytoplasmic, fluorescently labelled structures identified in the SMLM images of ten Dendra2-GABARAP expressing (upper graph) and ten Dendra2-LC3B expressing HEK-293 cells (lower graph) under fed (yellow and green bars for Dendra2-GABARAP and Dendra2-LC3B, respectively) and starved-blocked (red and blue bars for Dendra2-GABARAP and Dendra2-LC3B, respectively) conditions. The mean and median values are 106.93 nm / 90.51 nm, 104.87 nm / 89.08 nm, 108.01 nm / 91.91 nm, 122.23 nm / 89.08 nm for CS-Dendra2-GABARAP-fed, CS-Dendra2-GABARAP-starved-blocked, CS-Dendra2-LC3B-fed, and CS-Dendra2-LC3B-starved-blocked, respectively.

Table 3.4. Number of CS-Dendra2-GABARAP and CS-Dendra2-LC3B identified in SMLM images for fed and starved-blocked conditions. Counts are given for the entire size range considered (50 nm–2.8 µm) as well as for three sub-ranges (split alternatively at 100 nm, 300 nm, or at 800 nm). For comparison, the numbers of CS-Dendra2-GABARAP and CS-Dendra2-LC3B identified in the corresponding widefield fluorescence images (named “conventional selection”) are also given.

Overexpressed Protein	Size Category	Number of Structures	Fraction of Structures (%)
CS-Dendra2-GABARAP; fed	50 nm–2.8 µm	16205	100
	50 nm–100 nm	9477	58
	100 nm–2.8 µm	6728	42
	50 nm–300 nm	15921	98

	300 nm–2.8 µm	284	2
	50 nm–800 nm	16193	99
	800 nm–2.8 µm	12	1
	Conventional selection	284	
CS-Dendra2-LC3B; fed	50 nm–2.8 µm	18563	100
	50 nm–100 nm	11015	59
	100 nm–2.8 µm	7548	41
	50 nm–300 nm	18068	97.3
	300 nm–2.8 µm	495	2.7
	50 nm–800 nm	18544	99.9
	800 nm–2.8 µm	19	0.1
	Conventional selection	495	
CS-Dendra2-GABARAP; starved-blocked	50 nm–2.8 µm	16386	100
	50 nm–100 nm	10174	62
	100 nm–2.8 µm	6212	38
	50 nm–300 nm	15980	97.5
	300 nm–2.8 µm	406	2.5
	50 nm–800 nm	16344	99.7
	800 nm–2.8 µm	42	0.3
	Conventional selection	406	
CS-Dendra2-LC3B; starved-blocked	50 nm–2.8 µm	11712	100
	50 nm–100 nm	7653	65
	100 nm–2.8 µm	4059	35
	50 nm–300 nm	11030	94
	300 nm–2.8 µm	682	6
	50 nm–800 nm	11547	98.6
	800 nm–2.8 µm	165	1.4
	Conventional selection	682	

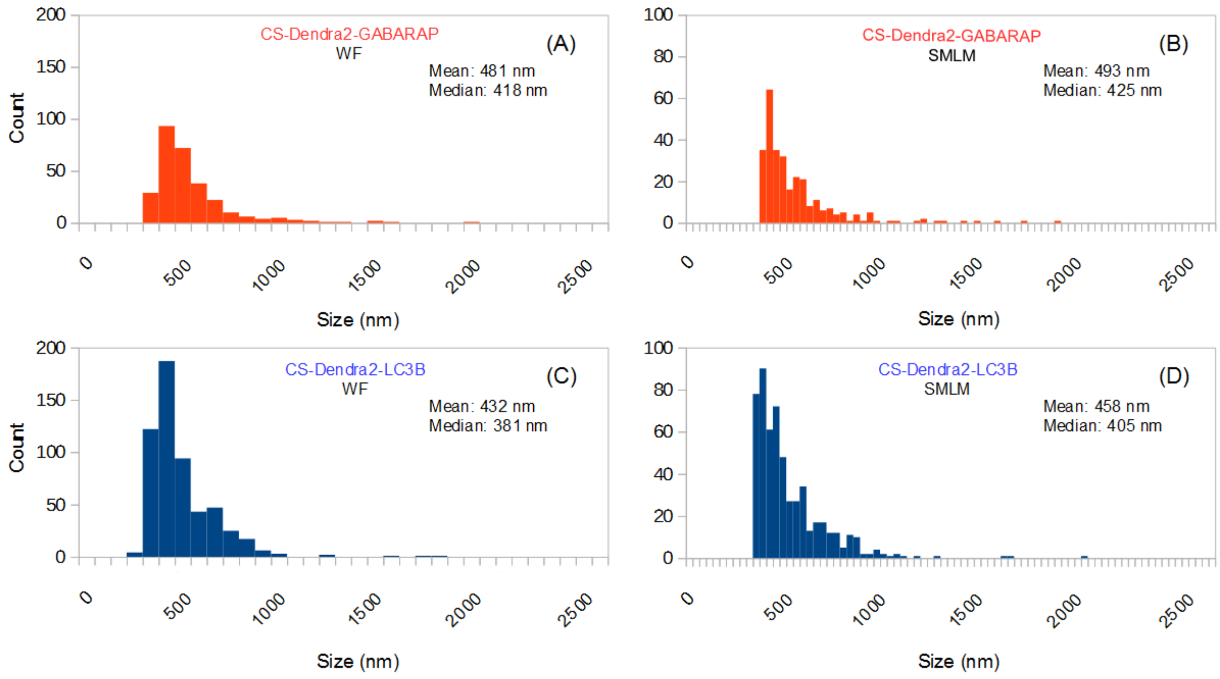

Figure 3.18. Size distributions of all conventionally selected fluorescently labelled structures (identified in widefield images) of ten Dendra2-GABARAP expressing (A, B) and ten Dendra2-LC3B expressing fixed HEK-293 cells (C,D) in fed condition, where size was determined in the widefield fluorescence (A,C) and the SMLM

images (B,D), respectively. Note the different binning used in A/C (80 nm) and B/D (32 nm), respectively, caused by the lower resolution in widefield fluorescence compared to super-resolution microscopy.

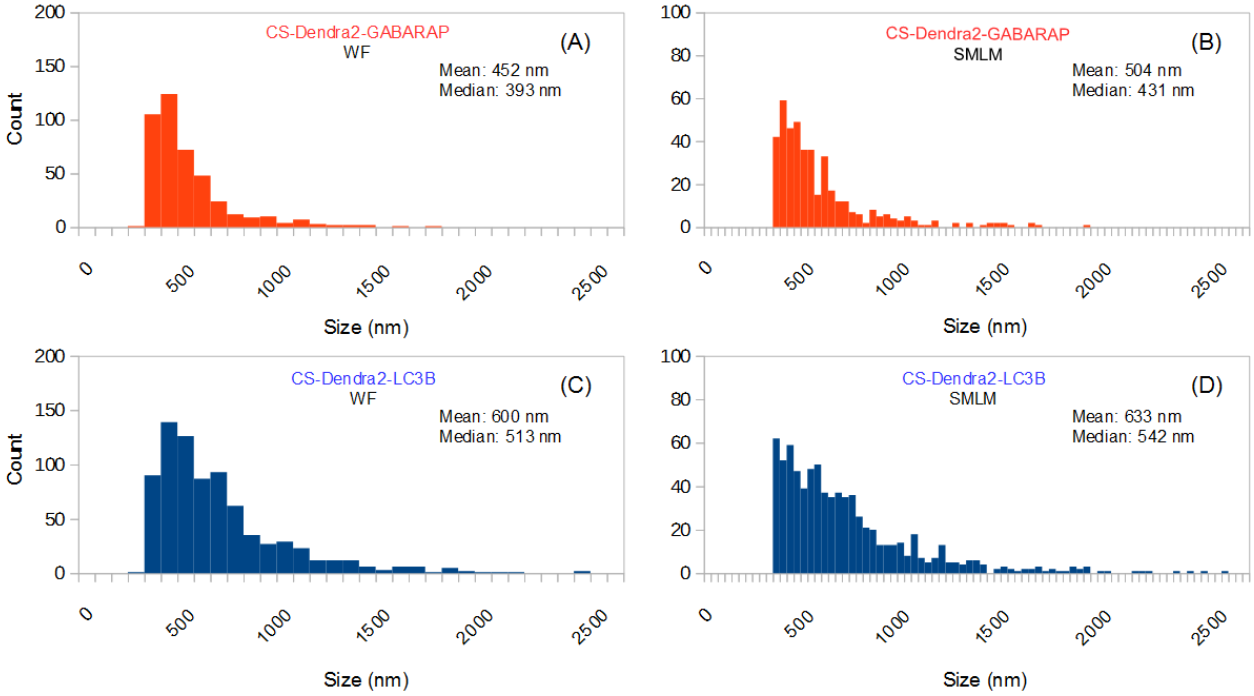

Figure 3.19. Size distributions of all conventionally selected fluorescently labelled structures (identified in widefield images) of ten Dendra2-GABARAP expressing (A, B) and ten Dendra2-LC3B expressing fixed HEK-293 cells (C,D) in starved-blocked condition, where size was determined in the widefield fluorescence (A,C) and the SMLM images (B,D), respectively. Note the different binning used in A/C (80 nm) and B/D (32 nm), respectively, caused by the lower resolution in widefield fluorescence compared to super-resolution microscopy.

3.3.2. Shape distributions of CS-Dendra2-GABARAP and CS-Dendra2-LC3B selected in super-resolution fluorescence microscopy images

The shape classification for structures labeled by Dendra2-GABARAP and Dendra2-LC3B was performed using the same methodology as for the evaluation of Atg8 proteins fused to EYFP. The classification categories are again circular (c), elliptic (e), and U-shaped (u). Interestingly, in contrast to the SMLM measurements after transient transfection with EYFP-GABARAP or EYFP-LC3B, the cell lines stably expressing Dendra2-GABARAP or Dendra2-LC3B displayed only modest variation of fluorescence intensity between cells, thus alleviating concerns regarding sample selection.

Since most remarkable size distribution differences found between fed and starved-blocked conditions at very large sizes for both CS-Dendra2-GABARAP and CS-Dendra2-LC3B (figure 3.17), a new size classification category added, namely smaller/larger than 800 nm, in addition to the categories of smaller/larger than 100 nm and 300 nm, and performed the shape classification for all sizes as well as for the three size-related splitting (in total seven). The results of the shape classifications of CS-Dendra2-GABARAP and CS-Dendra2-LC3B in fed and starved-blocked conditions are summarized in table 3.4 and the shape distributions are depicted in figures 3.20-3.25.

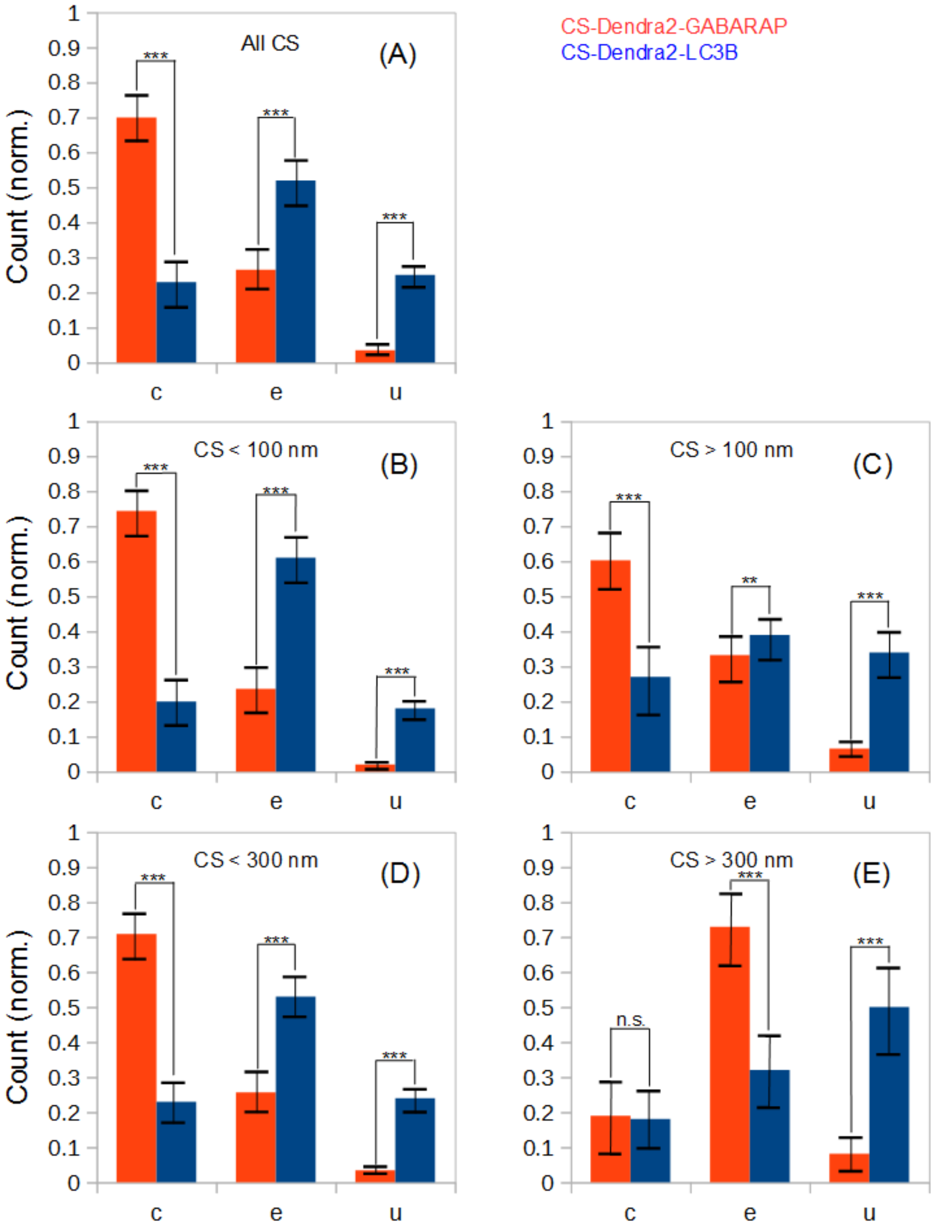

Figure 3.20. Shape analysis of all cytoplasmic fluorescent structures observed in SMLM images of ten HEK-293 cells stably expressing either Dendra2-GABARAP (red) or Dendra2-LC3B (blue) under fed condition. (A) All CS-Dendra2-GABARAP (16205) and CS-Dendra2-LC3B (18563); (B) CS-Dendra2-GABARAP (9477) and CS-Dendra2-LC3B (11015) smaller than 100 nm; (C) CS-Dendra2-GABARAP (6728) and CS-Dendra2-LC3B (7548) larger than 100 nm; (D) CS-Dendra2-GABARAP (15921) and CS-Dendra2-LC3B (18068) smaller than 300 nm; (E) CS-Dendra2-GABARAP (284) and CS-Dendra2-LC3B (495) larger than 300 nm. Error bars represent standard error of the mean. Statistical significance is represented as p ≤ 0.01 (***); p ≤ 0.05 (**), and p ≤ 0.1 (*) from two-tailed t-tests (n.s., not significant). c, e and u stand for circles, ellipses and U-shapes.

In fed condition, the number of CS-Dendra2-GABARAP per cell varied between 736 and 2702 with an average number of 1620 ± 660. According to figure 3.20, the shape distributions of the five size cases that were also considered in chapter 3.2 (i.e. all structures, and structures smaller/larger than 100 nm/300 nm) can be generally described as follows: The majority of CS-Dendra2-GABARAP structures appear as circles, to a lesser extent they are ellipses and a minor fraction shows U-shape (only for CS-Dendra2-GABARAP larger than 300 nm, the relative abundance of ellipses is highest; figure 3.20(E)). Generally, U-shape structures represent the lowest percentage among CS-Dendra2-GABARAP (only 3 to 10%).

Classification of all CS-Dendra2-LC3B followed the same way as described above for CS-Dendra2-GABARAP (applying again the separation values of 100 nm and 300 nm, respectively). In fed condition, the number of CS-Dendra2-LC3B per cell varied between 1413 and 4078 with an average number of 1856 ± 710 in all ten cells, while was slightly (~14 %) larger compared to the shape distributions of CS-Dendra2-LC3B show two differences compared to CS-Dendra2-GABARAP. First, ellipse (and not circle) was the most abundant shape (except for objects larger than 300 nm, where U-shape was), and second, relative abundance of U-shapes was generally higher (18-50 %).

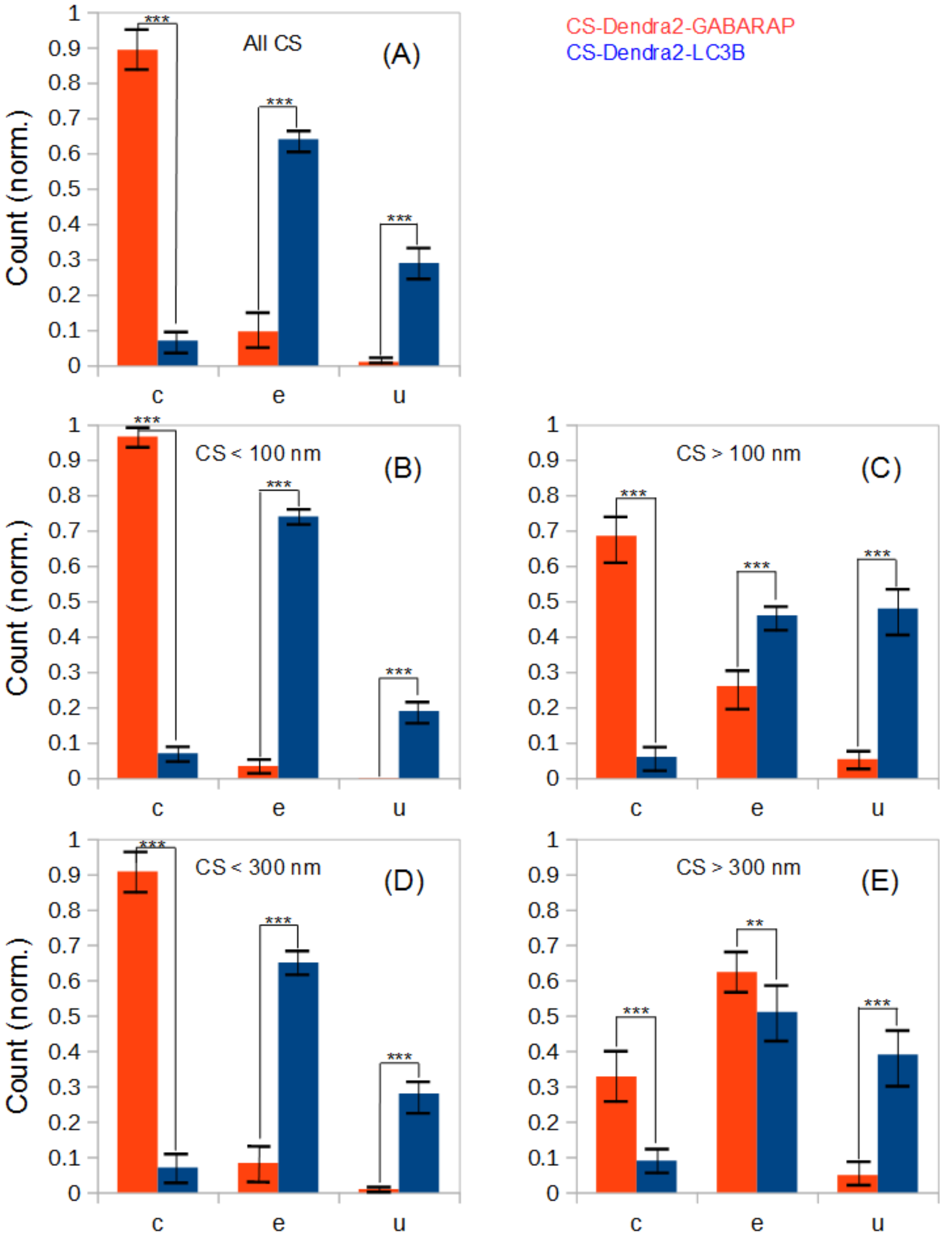

Figure 3.21. Shape analysis of all cytoplasmic fluorescent structures observed in SMLM images of ten HEK-293 cells stably expressing either Dendra2-GABARAP (red) or Dendra2-LC3B (blue) under starvation and bafilomycin A1 treatment. (A) All CS-Dendra2-GABARAP (16386) and CS-Dendra2-LC3B (11712); (B) CS-Dendra2-GABARAP (10174) and CS-Dendra2-LC3B (7653) smaller than 100 nm; (C) CS-Dendra2-GABARAP (6212) and CS-Dendra2-LC3B (4059) larger than 100 nm; (D) CS-Dendra2-GABARAP (15980) and CS-Dendra2-LC3B (11030) smaller than 300 nm; (E) CS-Dendra2-GABARAP (406) and CS-Dendra2-LC3B (682) larger than 300 nm. Error bars represent standard error of the mean. Statistical significance is represented as $p \leq 0.01$ (***); $p \leq 0.05$ (**), and $p \leq 0.1$ (*) from two-tailed t-tests (n.s., not significant). c, e and u stand for circles, ellipses and U-shapes.

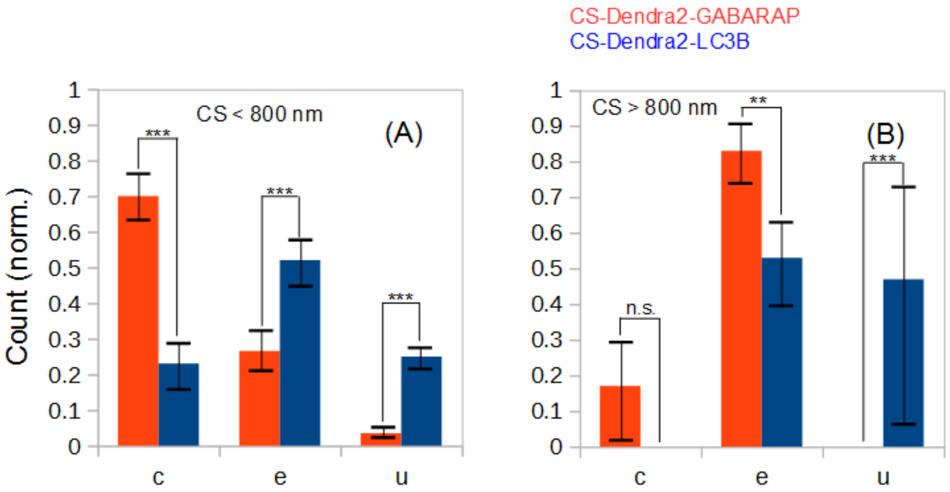

Figure 3.22. Shape analysis of all cytoplasmic fluorescent structures observed in SMLM images of ten HEK-293 cells stably expressing either Dendra2-GABARAP (red) or Dendra2-LC3B (blue) under fed condition. (A) CS-Dendra2-GABARAP (16193) and CS-Dendra2-LC3B (18544) smaller than 800 nm; (B) CS-Dendra2-GABARAP (12) and CS-Dendra2-LC3B (19) larger than 800 nm. Error bars represent standard error of the mean. Statistical significance is represented as p ≤ 0.01 (***); p ≤ 0.05 (**), and p ≤ 0.1 (*) from two-tailed t-tests (n.s., not significant). c, e and u stand for circles, ellipses and U-shapes.

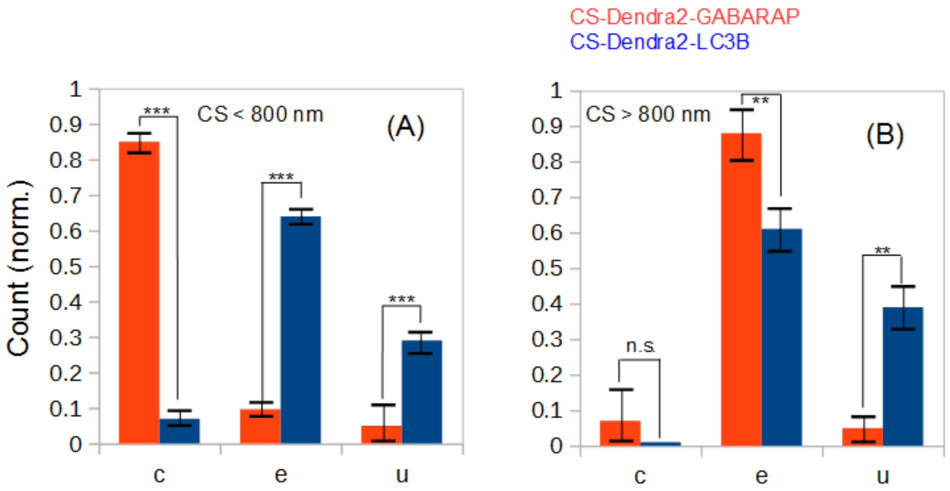

Figure 3.23. Shape analysis of all cytoplasmic fluorescent structures observed in SMLM images of ten HEK-293 cells stably expressing either Dendra2-GABARAP (red) or Dendra2-LC3B (blue) under starved-blocked condition. (A) CS-Dendra2-GABARAP (16344) and CS-Dendra2-LC3B (11547) smaller than 800 nm; (B) CS-Dendra2-GABARAP (42) and CS-Dendra2-LC3B (165) larger than 800 nm. Error bars represent standard error of the mean. Statistical significance is represented as p ≤ 0.01 (***); p ≤ 0.05 (**), and p ≤ 0.1 (*) from two-tailed t-tests (n.s., not significant). c, e and u stand for circles, ellipses and U-shapes.

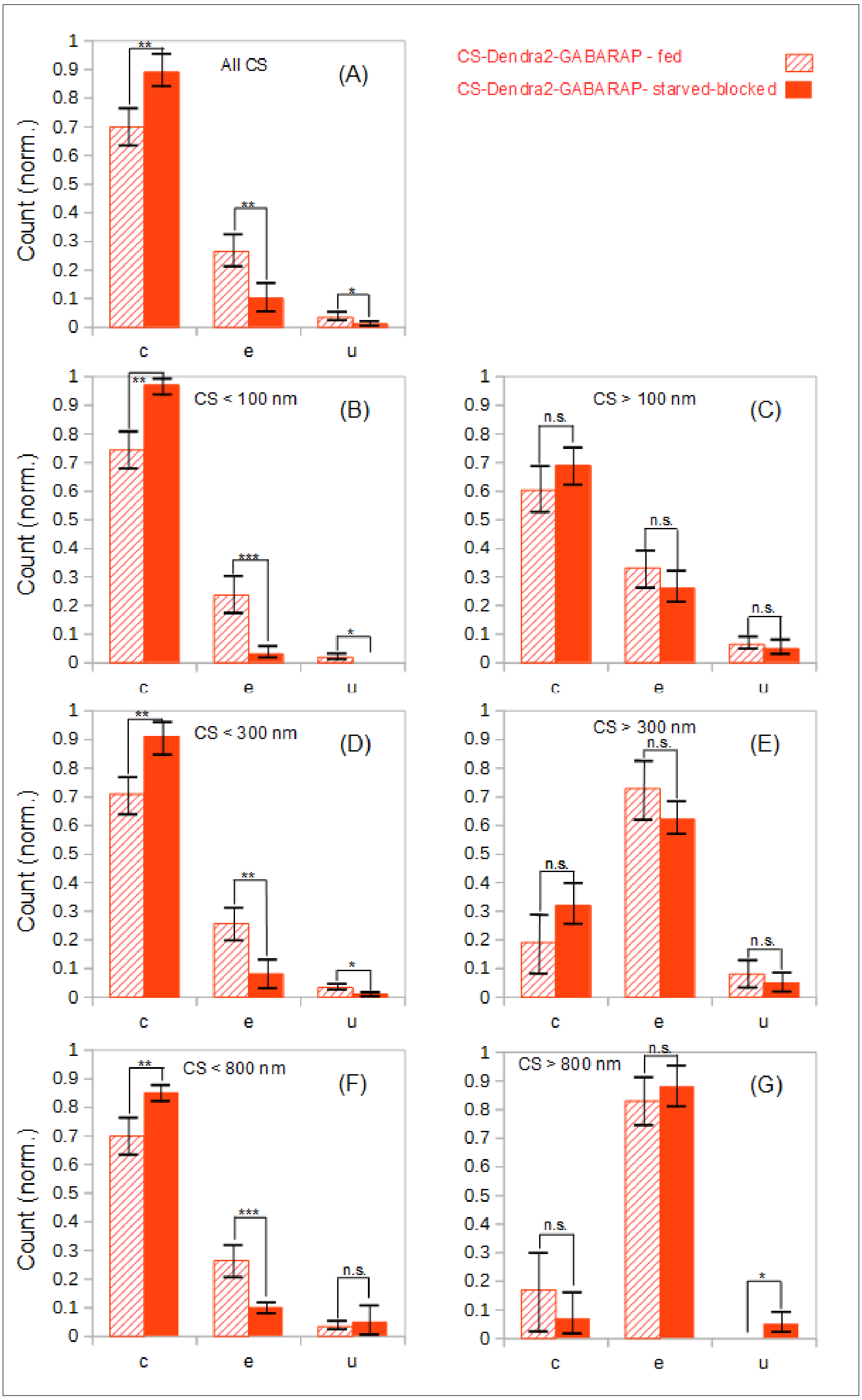

Figure 3.24. Shape analysis of all cytoplasmic fluorescent structures observed in SMLM images of ten HEK-293 cells stably expressing Dendra2-GABARAP in fed condition (dashed bars) and Dendra2-GABARAP in starved-blocked condition (solid bars). (A) All CS-Dendra2-GABARAP-fed (16205) and CS-Dendra2-GABARAP-starved-blocked (16386); (B) CS-Dendra2-GABARAP-fed (9477) and CS-Dendra2-GABARAP-starved-blocked (10174) smaller than 100 nm; (C) CS-Dendra2-GABARAP-fed (6728) and CS-Dendra2-GABARAP-starved-blocked (6212) larger than 100 nm; (D) CS-Dendra2-GABARAP-fed (15921) and CS-Dendra2-GABARAP-starved-blocked (15980) smaller than 300 nm; (E) CS-Dendra2-GABARAP-fed (284) and CS-Dendra2-GABARAP-starved-blocked (406) larger than 300 nm; (F) CS-Dendra2-GABARAP-fed (16193) and CS-Dendra2-GABARAP-starved-blocked (16344) smaller than 800 nm; (G) CS-Dendra2-GABARAP-fed (12) and CS-Dendra2-GABARAP-starved-blocked (42) larger than 800 nm. Error bars represent standard error of the mean. Statistical significance is represented as $p \leq 0.01$

(***); p ≤ 0.05 (**), and p ≤ 0.1 (*) from two-tailed t-tests (n.s., not significant). c, e and u stand for circles, ellipses and U-shapes.

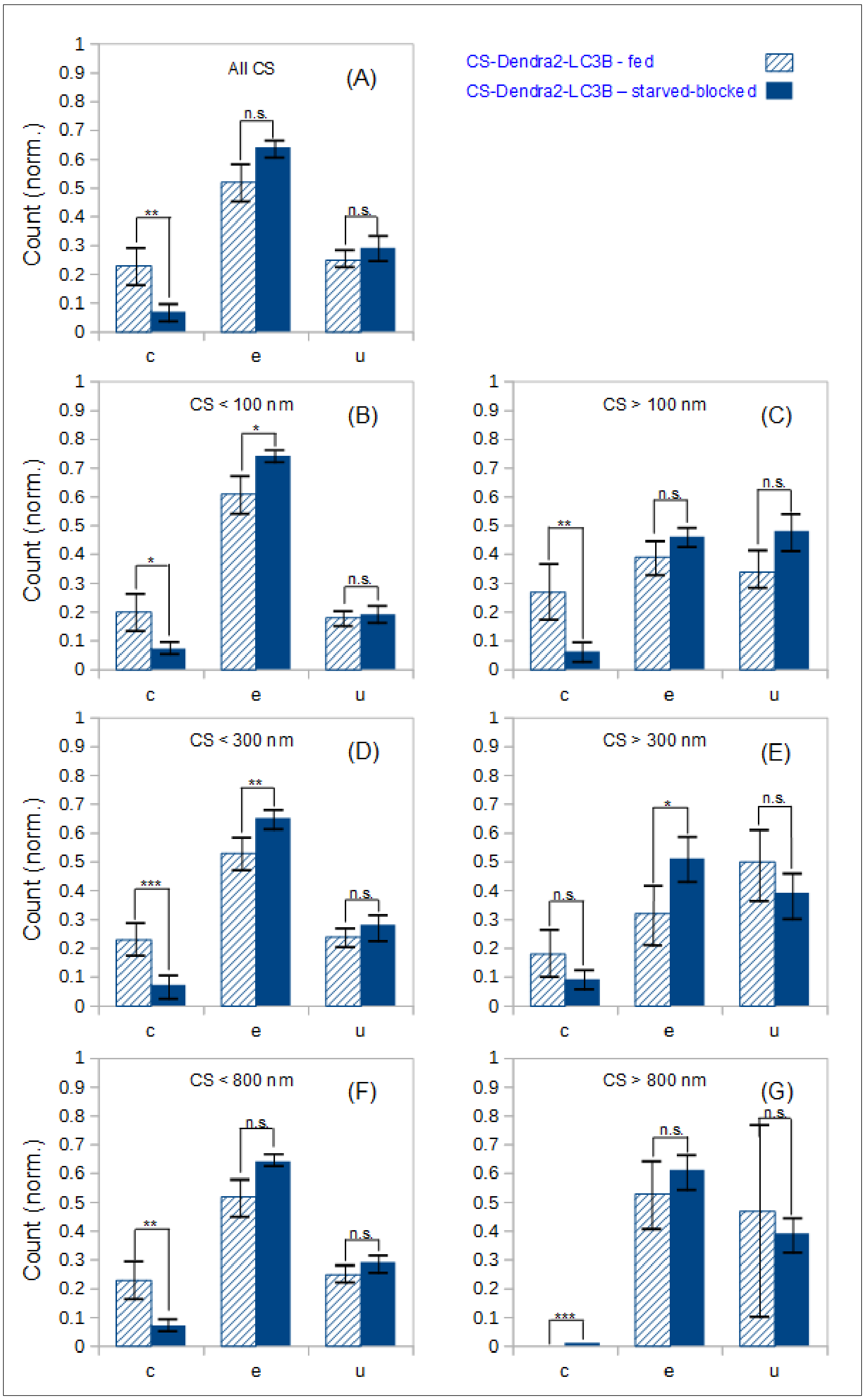

Figure 3.25. Shape analysis of all cytoplasmic fluorescent structures observed in SMLM images of ten HEK-293 cells stably expressing Dendra2-LC3B in fed condition (dashed bars) and Dendra2-LC3B in starved-blocked condition (solid bars). (A) All CS-Dendra2-LC3B-fed (18586) and CS-Dendra2-LC3B-starved-blocked (11712); (B) CS-Dendra2-LC3B-fed (11015) and CS-Dendra2-LC3B-starved-blocked (7653) smaller than 100 nm; (C) CS-Dendra2-LC3B-fed (7548) and CS-Dendra2-LC3B-starved-blocked (4059) larger than 100 nm; (D) CS-Dendra2-LC3B-fed (18068) and CS-Dendra2-LC3B-starved-blocked (11030) smaller than 300 nm; (E) CS-Dendra2-LC3B-fed (495) and CS-Dendra2-LC3B-starved-blocked (682) larger than 300 nm; (F) CS-Dendra2-LC3B-fed (18544) and CS-Dendra2-LC3B-starved-blocked (11547) smaller than 800 nm; (G) CS-Dendra2-LC3B-fed (19) and CS-

Dendra2-LC3B-starved-blocked (165) larger than 800 nm. Error bars represent standard error of the mean. Statistical significance is represented as p ≤ 0.01 (***); p ≤ 0.05 (**), and p ≤ 0.1 (*) from two-tailed t-tests (n.s., not significant). c, e and u stand for circles, ellipses and U-shapes.

In starved-blocked condition, the number of CS-Dendra2-GABARAP per cell varied between 1088 and 2926 with an average number of 1639 ± 618 (see table 3.4). In figure 3.21, the shape classification for the five sizes that were also used for analysis in chapter 3.2 (i.e. all structures and structures smaller/larger than 100 nm/300 nm) reveals the following picture: The majority of CS-Dendra2-GABARAP appear as circles, to a lesser extent they are ellipses and a minor fraction shows U-shape (only for CS-Dendra2-GABARAP larger than 300 nm, the relative abundance of ellipses is highest; figure 3.21(E)). Generally, U-shape structures represent the lowest percentage among CS-Dendra2-GABARAP (only 1 to 6%).

The majority of CS-Dendra2-LC3B structures appear as ellipses, to a lesser extent they are U-shaped and a minor fraction shows circular distribution, the latter with a percentage of only 7 to 9 %. In starved-blocked condition, the number of CS-Dendra2-LC3B per cell varied between 1203 and 2199 with an average number of 1171 ± 366, which was ~29 % smaller compared to the cells expressing CS-Dendra2-GABARAP.

In figure 3.22, the shape distributions for detected structures of CS-Dendra2-GABARAP and CS-Dendra2-LC3B smaller and larger than 800 nm in fed condition are shown. The majority of CS-Dendra2-GABARAP smaller than 800 nm appear as circles, to a lesser extent they are ellipses and a minor fraction shows U-shape. For the structures larger than 800 nm, on the other hand, the majority of CS-Dendra2-GABARAP structures appear as ellipses, to a lesser extent they are circles and not a single U-shape was found. CS-Dendra2-LC3B smaller than 800 nm appear mostly as ellipses, while circles and U-shapes are nearly similarly abundant. For the structures larger than 800 nm, on the other hand, the majority of CS-Dendra2-LC3B appears as ellipses or U-shapes, while no circle was found. The situation for starved-blocked conditions is very similar.

In figure 3.23, the shape distributions for detected CS-Dendra2-GABARAP and CS-Dendra2-LC3B smaller and larger than 800 nm in starved-blocked condition are given. The majority of CS-Dendra2-GABARAP smaller than 800 nm appears as circles, and minor fractions are ellipses and U-shapes. For the structures larger than 800 nm, on the other hand, the vast majority of CS-Dendra2-GABARAP is ellipses, while very small fractions appear as circles or U-shapes. The majority of CS-Dendra2-LC3B smaller than 800 nm appear as ellipses, to a lesser extent they are U-shapes, and very few circles are identified. For the structures larger than 800 nm, a very similar shape distribution as for CS-Dendra2-LC3B smaller than 800 nm is observed. To better compare the shape distributions between fed and starved-blocked conditions for the two proteins, the data presented in figure 3.20-3.23 were replotted. For both proteins, the changes upon induction of autophagy are modest. Most differences in relative abundance of shapes are statistically not significant at all. There are two trends worth mentioning: for CS-Dendra2-GABARAP, a modest increase of circular shapes and for CS-Dendra2-LC3B a considerable decrease of circular shapes when autophagy was induced (starved-blocked condition) compared to resting state (fed condition).

Table 3.5. P-values from two-tailed t-tests to assess the statistical significance of differences in the shape distributions (c, circles; e, ellipses; u, U-shapes) of (i) CS-Dendra2-GABARAP vs. CS-Dendra2-LC3B (various size classes), (ii) different size classes of CS-Dendra2-GABARAP, (iii) different size classes of CS-Dendra2-LC3B, and (iv) CS-Dendra2-GABARAP or CS-Dendra2-LC3B structures classified in widefield vs. SMLM. The cells with yellow background represent fed condition and those with green background show starved-blocked condition.

	c	e	u
CS-Dendra2-GABARAP vs. CS-Dendra2-LC3B (50 nm–2.8 µm)	0.0009	0.0061	0.0003
	0.0001	0.0001	0.0007
CS-Dendra2-GABARAP vs. CS-Dendra2-LC3B (< 100 nm)	0.0005	0.0023	0.0009
	0.0001	0.0001	0.0015
CS-Dendra2-GABARAP vs. CS-Dendra2-LC3B (> 100 nm)	0.0072	0.2541	0.0022
	0.0002	0.0040	0.0003
CS-Dendra2-GABARAP vs. CS-Dendra2-LC3B (< 300 nm)	0.0008	0.0053	0.0003
	0.0001	0.0001	0.0008
CS-Dendra2-GABARAP vs. CS-Dendra2-LC3B (> 300 nm)	0.9048	0.0104	0.0081
	0.0082	0.1530	0.0039
CS-Dendra2-GABARAP vs. CS-Dendra2-LC3B (< 800 nm)	0.0009	0.0061	0.0003
	0.0001	0.0001	0.0007
CS-Dendra2-GABARAP vs. CS-Dendra2-LC3B (> 800 nm)	0.4354	0.0217	0.0035
	0.8162	0.0162	0.0520
CS-Dendra2-GABARAP: CS < 100 nm vs. CS > 100 nm	0.0847	0.1661	0.0520
	0.0034	0.0034	0.0363
CS-Dendra2-GABARAP: CS < 300 nm vs. CS > 300 nm	0.0023	0.0037	0.1647
	0.0006	0.0003	0.1682
CS-Dendra2-GABARAP: CS < 800 nm vs. CS > 800 nm	0.0529	0.0008	0.0213
	0.0065	0.0001	0.6688
CS-Dendra2-LC3B: CS < 100 nm vs. CS > 100 nm	0.2921	0.0082	0.0145
	0.8090	0.0003	0.0022
CS-Dendra2-LC3B: CS < 300 nm vs. CS > 300 nm	0.4353	0.0356	0.0347
	0.5265	0.0629	0.1379
CS-Dendra2-LC3B: CS < 800 nm vs. CS > 800 nm	0.0033	0.8967	0.0461
	0.7626	0.1963	0.8185
CS-Dendra2-GABARAP: WF vs. SMLM	0.0126	0.0201	0.8503
	0.0179	0.0073	0.8002
CS-Dendra2-LC3B:WF vs. SMLM	0.0011	0.2941	0.0039
	0.0001	0.1032	0.0032

3.3.3. Shape distributions of CS-Dendra2-GABARAP and CS-Dendra2-LC3B selected in widefield fluorescence microscopy images ("conventional selection")

The motivation to perform such an analysis for the Dendra2-Atg8s is the same as that given for EYFP-Atg8s, i.e. an appropriate comparison of our results with previous reports on FP-GABARAP and FP-LC3B expressing cells. Similarly, as in subchapter 3.2.3., it was found that because of the ability of SMLM to detect and localize single fluorophores, in contrast to conventional fluorescence microscopy, many of the structures fall into a different shape category when classified in widefield images and in the corresponding SMLM images.

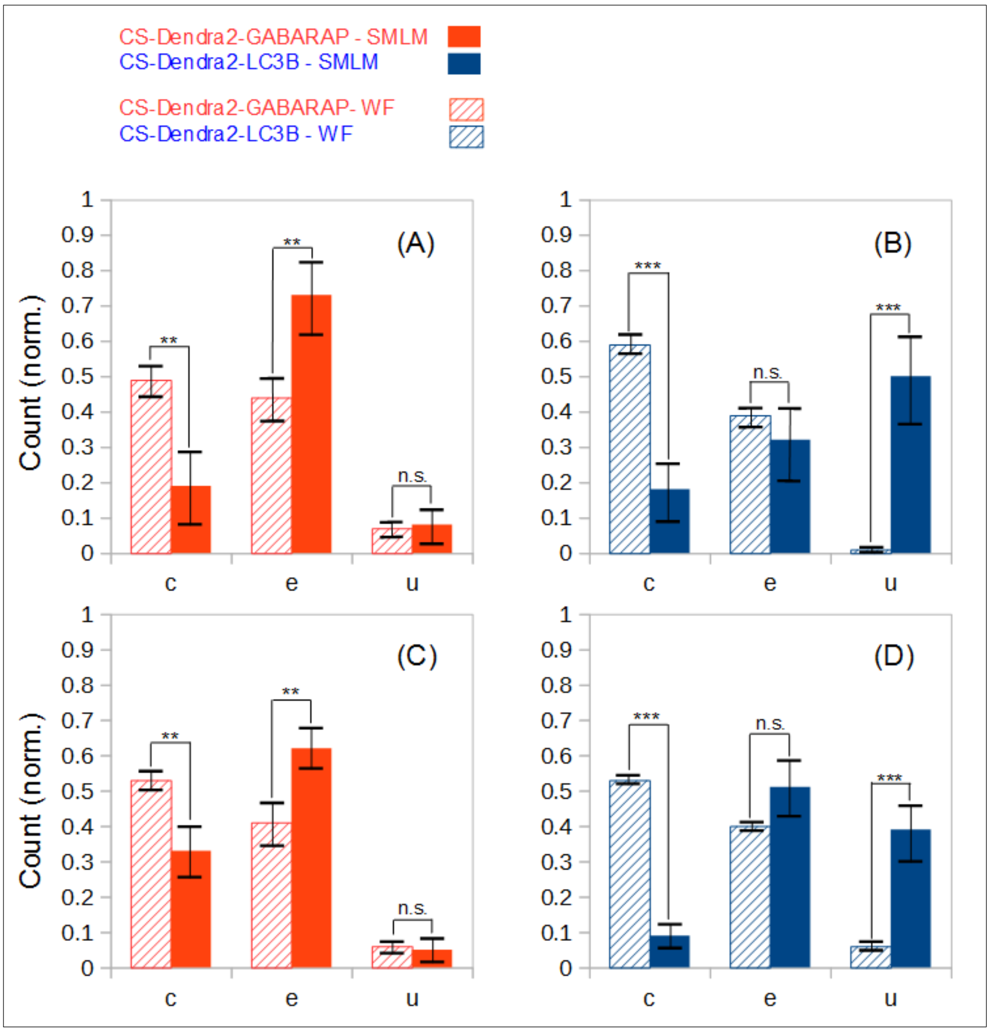

Figure 3.26. Shape distributions of fluorescently labelled cytoplasmic structures identified in the widefield images of ten HEK-293 stably expressing Dendra2-GABARAP and Dendra2-LC3B, respectively, under fed (A, B) and under starved-blocked conditions (C,D). (A) Conventionally selected CS-Dendra2-GABARAP (284) classified in widefield fluorescence (hatched bars) and the same structures classified in the respective SMLM (full bars) images; (B) Conventionally selected CS-Dendra2-LC3B (495) classified in widefield fluorescence (hatched bars) and the same structures classified in the respective SMLM (full bars) images for fed condition. (C) Conventionally selected CS-Dendra2-GABARAP (406) classified in widefield fluorescence (hatched bars) and the same structures classified in the respective SMLM (full bars) images; (D) Conventionally selected CS-Dendra2-LC3B (682) classified in widefield fluorescence (hatched bars) and the same structures classified in the respective SMLM (full bars) images for starved-blocked condition. Error bars represent standard error of the

mean. Statistical significance is represented as $p \leq 0.01$ (***); $p \leq 0.05$ (**), and $p \leq 0.1$ (*) from two-tailed t-tests (n.s., not significant). c, e and u stand for circles, ellipses and U-shapes.

The shapes of all “conventionally selected” CS-Dendra2-GABARAP and CS-Dendra2-LC3B analyzed in fed and starved-blocked conditions. First of all, for both Atg8 proteins, the shape distribution is statistically significantly different when the classification is performed based on widefield or SMLM images. The shape distributions along with two-tailed t-test analyses are given in figures 3.26 and 3.27 and table 3.5. For CS-Dendra2-GABARAP, U-shapes are rare (less than 9 % for fed condition and 4 % for starved-blocked condition) in widefield fluorescence and remain almost the same in SMLM images. The elliptical structures are 45 % and 40 % for classification based on widefield images for fed and starved-blocked conditions, respectively, but increase significantly to more than 70 % and 60 % when classified based on SMLM images for fed and starved-blocked conditions, respectively. The circular shapes’ percentage is nearly 50 % for classification based on widefield images for fed and starved-blocked conditions, respectively, and drops to 20 % and 32 % (again statistically significant), when classified based on SMLM images for fed and starved-blocked conditions, respectively. A similar analysis for CS-Dendra2-LC3B was performed as well. U-shapes are 1 % and 4 % for classification based on widefield images for fed and starved-blocked condition. This percentage turns into 50 % and 40 % for classification based on SMLM images for fed and starved-blocked condition, respectively. Ellipses amount to 40 % for classification based on widefield images for both fed and starved-blocked conditions, and are 32 % and 51 % (differences not statistically significant), respectively, when classified based on SMLM images for fed and starved-blocked conditions. The circular shapes’ percentage is nearly 60 % and 53 % for classification based on widefield images for fed and starved-blocked conditions, respectively, and largely decreases to 19 % and 9 % when classified based on SMLM images for fed and starved-blocked conditions, respectively.

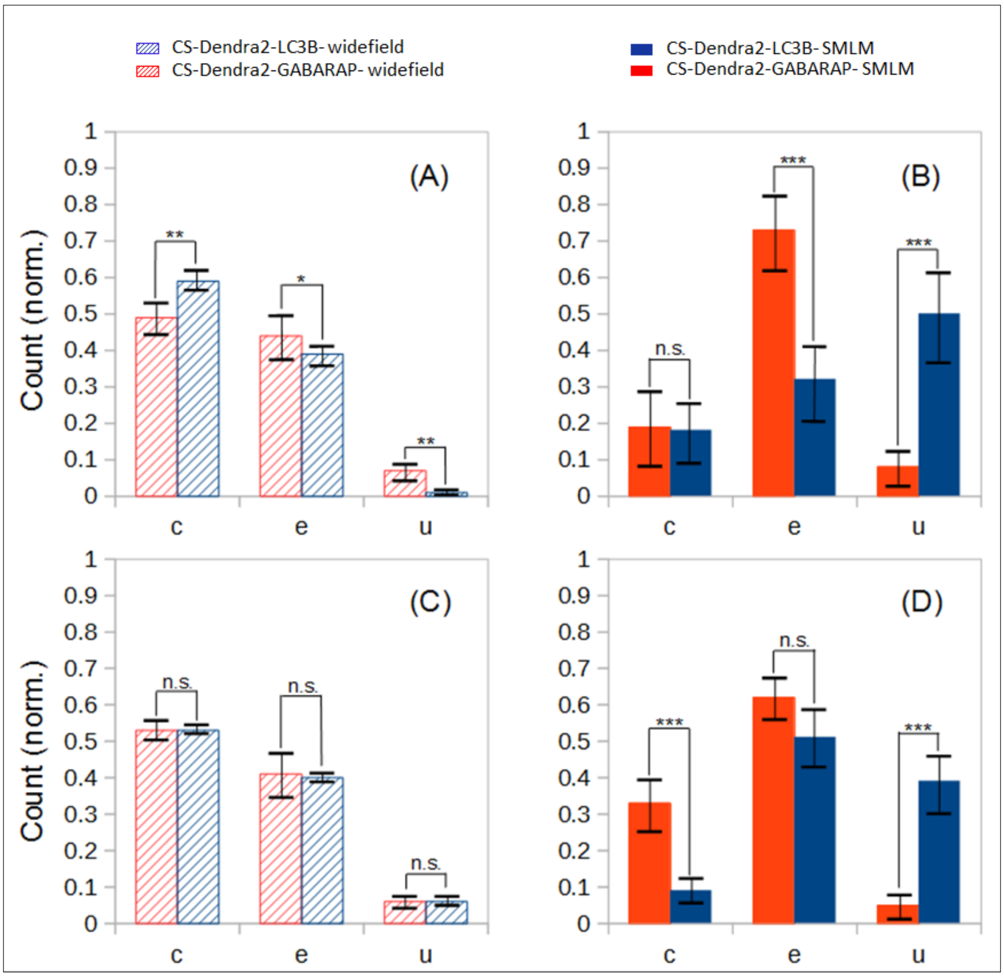

Figure 3.27. Shape distributions of fluorescently labelled cytoplasmic structures identified in the widefield images of ten CS-Dendra2-GABARAP and ten CS-Dendra2-LC3B stably expressed by HEK-293 cells, respectively, under fed (A,B) and under starved-blocked conditions (C,D). (A) Conventionally selected CS-Dendra2-GABARAP (284) classified in widefield fluorescence (red) and conventionally selected CS-Dendra2-LC3B (495) classified in widefield fluorescence (blue) images; (B) selected CS-Dendra2-GABARAP (284) classified in SMLM (red) and selected CS-Dendra2-LC3B (495) classified in SMLM (blue) images. (C) Conventionally selected CS-Dendra2-GABARAP (406) classified in widefield fluorescence (red) and conventionally selected CS-Dendra2-LC3B (682) classified in widefield fluorescence (blue) images; (D) selected CS-Dendra2-GABARAP (406) classified in SMLM (red) and selected CS-Dendra2-LC3B (682) classified in SMLM (blue) images. Error bars represent standard error of the mean. Statistical significance is represented as $p \leq 0.01$ (***); $p \leq 0.05$ (**), and $p \leq 0.1$ (*) from two-tailed t-tests (n.s., not significant). c, e and u stand for circles, ellipses and U-shapes.

Figure 3.27 depicts a comparison of the shapes of the cytoplasmic structures labeled by Dendra2-GABARAP and Dendra2-LC3B, respectively, performed with widefield fluorescence microscopy (figures 3.27(A) and 3.27(C)) or with SMLM (figures 3.27(B) and 3.27(D)). While the shape distributions of the labeled structures are very similar for the two proteins when classified in fluorescence images with diffraction-limited resolution, they are highly and statistically significantly different when judged in super-resolution SMLM images. In general, the fraction of circles, even for these objects larger than the diffraction limit, is highly overestimated in conventional fluorescence microscopy.

Figures 3.27(A) and 3.27(C) shows that the shape classifications in conventional analysis for CS-Dendra2-GABARAP vs. CS-Dendra2-LC3B in fed condition are similar but statistically significantly different values. The majority of structures are circles (50 % for CS-Dendra2-GABARAP and 60 % for CS-Dendra2-LC3B). Ellipses are the second abundant class (41 % for CS-Dendra2-GABARAP and 40 % for CS-Dendra2-LC3B), and U-shapes are the minor fraction of the classified structures. The shape classifications for CS-Dendra2-GABARAP vs. CS-Dendra2-LC3B in starved-blocked condition are similar and they are statistically significantly non-different. The majority of structures are circles (52 % for both CS-Dendra2-GABARAP and CS-Dendra2-LC3B). Ellipses are the second abundant class (45 % for CS-Dendra2-GABARAP and 40 % for CS-Dendra2-LC3B), and U-shapes are the minor fraction of the classified structures (6 % for both CS-Dendra2-GABARAP and CS-Dendra2-LC3B).

3.4. HEK-293 cells transiently transfected with EYFP-GABARAP/LC3B and mCherry-LAMP1

LAMP1 is established as a marker for lysosomes and late endosomes (Dunster 2001, Cheng 2018). Since autophagosomes fuse with late endosomes and lysosomes to achieve finally cargo degradation, two-colour fluorescence imaging (SMLM) performed to observe such interactions with super-resolution. Another motivation was to test whether or not any differences between the distributions of GABARAP and LC3B exist with respect to late endosomes and lysosomes. In figure 3.28 typical examples of HEK-293 cells are depicted that were transiently co-transfected with EYFP-GABARAP and mCherry-LAMP1 or EYFP-LC3B and mCherry-LAMP1, respectively, starved/fusion-blocked and finally fixed. Transmission, fluorescence widefield, and SMLM images of the rest of the cells measured and analyzed for this experiment are given in appendices 7.5 and 7.6.

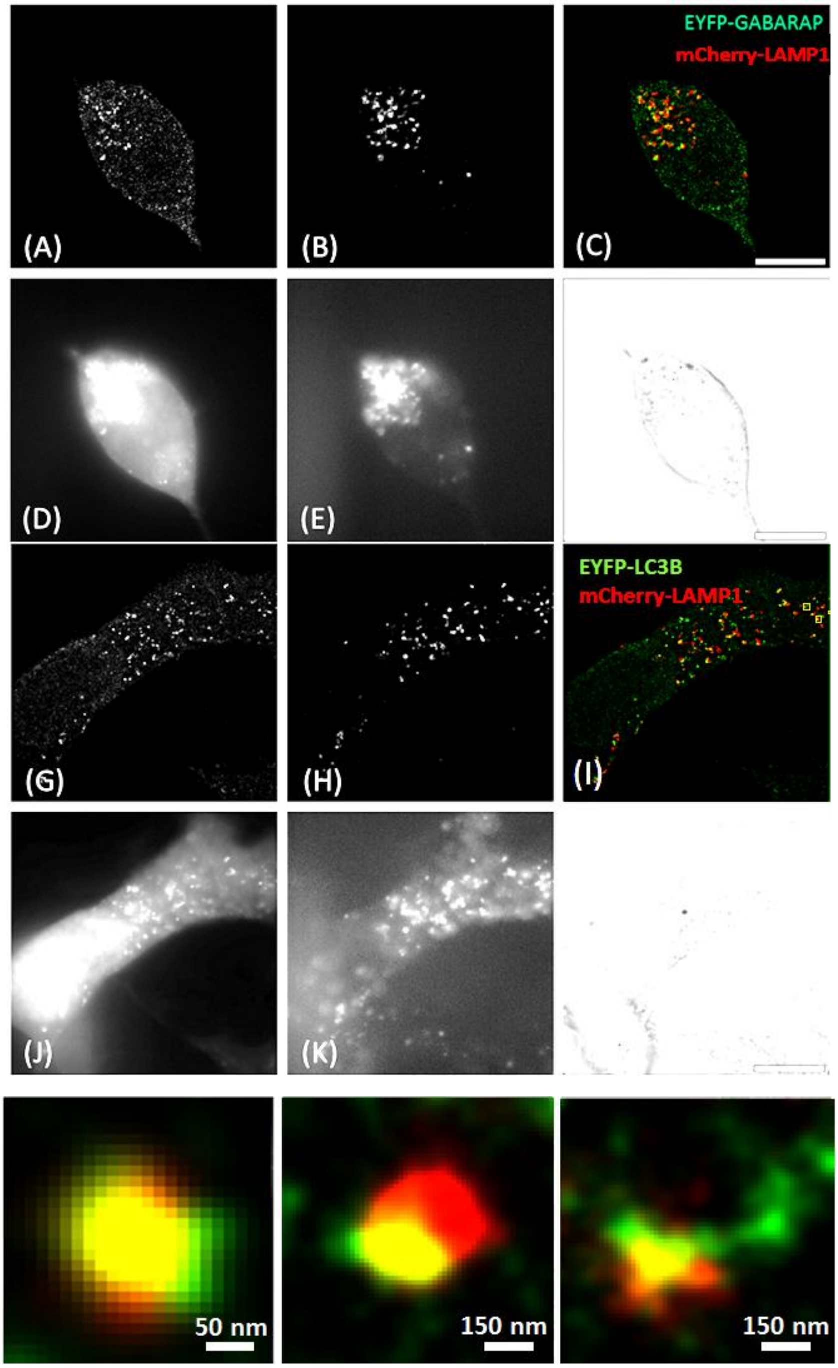

Figure 3.28. A fixed HEK-293 cell transiently co-transfected with EYFP-GABARAP and mCherry-LAMP1 (starved/fusion-blocked; A - F) and a fixed HEK-293 cell transiently co-transfected with EYFP-LC3B and mCherry-LAMP1 (starved/fusion-blocked; G - L). A shows the SMLM image of EYFP-GABARAP, B shows the SMLM image of mCherry-LAMP1, C is the superposition of A and B, D shows the widefield fluorescence image of EYFP-GABARAP, E shows the widefield fluorescence image of mCherry-LAMP1, and F shows the transmission image of the cell. G shows the SMLM image of EYFP-LC3B, H shows the SMLM image of mCherry-LAMP1, I shows the superposition of G and H, J is the widefield fluorescence image of EYFP-LC3B, K is widefield fluorescence image of mCherry-LAMP1, L is the transmission image of the cell. Note that in addition three non-transfected cells are visible. Scale bar: 10 µm.

Three co-localized structures from image (I) are presented highly magnified at the bottom panel depicting co-localization of mCherry-LAMP1 structure and the EYFP-LC3B structures of the same size, of mCherry-LAMP1 structure larger than the EYFP-LC3B structure, and of mCherry-LAMP1 smaller than the EYFP-LC3B structure.

As figure 3.28 reveals, both Atg8 proteins behave similar with respect to co-localization with LAMP1-positive structures, namely they show partial co-localization. There are four cases found, namely structures positive for both overexpressed proteins and similar size and shape, double positive but with different size and shape and only positive for either LAMP1 or only positive for the Atg8 protein (GABARAP or LC3B). The quantitative analysis of five HEK-293 cells transiently co-transfected with EYFP-GABARAP and mCherry-LAMP1 and five HEK-293 cells transiently co-transfected with EYFP-LC3B and mCherry-LAMP1 is given in figures 3.29 and 3.30 and table 3.6.

The partial co-localization can in part be explained, in a simple manner, since the number of cytosolic EYFP-GABARAP and EYFP-LC3B structures is larger compared to that labeled with mCherry-LAMP1 (in both relevant size categories, less than 300 nm and larger than 300 nm; table 3.6). The size distributions of EYFP-GABARAP and EYFP-LC3B, respectively, in these co-transfection experiments look very similar to those of the experiments (cells starved/fusion-blocked) with transient single transfection in chapter 3.2 (figure 3.10) and stable single transfection in chapter 3.3 (figure 3.17). Mean and median values (EYFP-GABARAP: 126/107 nm; EYFP-LC3B: 137/102 nm) are in the same range though a little larger as determined in the single transfection experiments. The percentage of large (larger than 300 nm) CS-EYFP-GABARAP and CS-EYFP-LC3B in the co-transfection experiment is at least doubled when compared to single transfection experiment (table 3.2). Interestingly, the total number of cytosolic mCherry-LAMP1 positive structures is only one quarter of CS-EYFP-GABARAP and CS-EYFP-LC3B, respectively; while the size distribution is shifted towards larger structures with 16% of the LAMP1-positive structures larger than 300 nm.

Table 3.6. Total number of EYFP-GABARAP, EYFP-LC3B, and mCherry-LAMP1 structures smaller and larger than 300 nm in SMLM images.

HEK 293 cells transiently co-transfected with EYFP-GABARAP and mCherry-LAMP1	EYFP-GABARAP < 300 nm	7996
	EYFP-GABARAP > 300 nm	406

	Total mCherry-LAMP1	1313
	mCherry-LAMP1 < 300 nm	1102
	mCherry-LAMP1 > 300 nm	211
	Number of EYFP-GABARAP < 300 nm co-localized with mCherry-LAMP1	469
	Number of EYFP-GABARAP > 300 nm co-localized with mCherry-LAMP1	347
HEK 293 cells transiently co-transfected with EYFP-LC3B and mCherry-LAMP1	EYFP-LC3B < 300 nm	6575
	EYFP-LC3B > 300 nm	591
	Total mCherry-LAMP1	1565
	Total mCherry-LAMP1 < 300 nm	1313
	Total mCherry-LAMP1 > 300 nm	252
	Number of EYFP-LC3B < 300 nm co-localized with mCherry-LAMP1	257
	Number of EYFP-LC3B > 300 nm co-localized with mCherry-LAMP1	293

The purpose of this co-localization experiment is to investigate whether GABARAP and LC3B have the same or a different probability to be present in joint vesicular structures with LAMP1, a late endosome and lysosome marker. It has been shown, by us and others, that bafilomycin treatment is not completely preventing autophagic cargo degradation, i.e., fusion of autophagosomes with late endosomes and lysosomes is hampered but not completely blocked. In our SMLM experiments here it was found that co-localization is found rarely for small structures (less than 300 nm; 6% (EYFP-GABARAP) and 5% (EYFP-LC3B)). On the contrary, co-localization is very prominent for large structures (larger than 300 nm), especially for EYFP-GABARAP (85%; EYFP-LC3B: 50%). For this quantitative analysis it was used in both cases the number of small (smaller than 300 nm) and large (larger than 300 nm), respectively, CS-EYFP-GABARAP and CS-EYFP-LC3B as reference. Alternatively, one can use the total number of cytosolic mCherry-LAMP1 structures as scale basis. When doing so, EYFP-GABARAP co-localizes to a larger extent with mCherry-LAMP1 for both size classes. In total, 61% of mCherry-LAMP1-positive structures are EYFP-GABARAP-positive, while only 35% are EYFP-LC3B-positive. Altogether, a higher tendency for co-localization of GABARAP with LAMP1-positive vesicular structures than for LC3B was found.

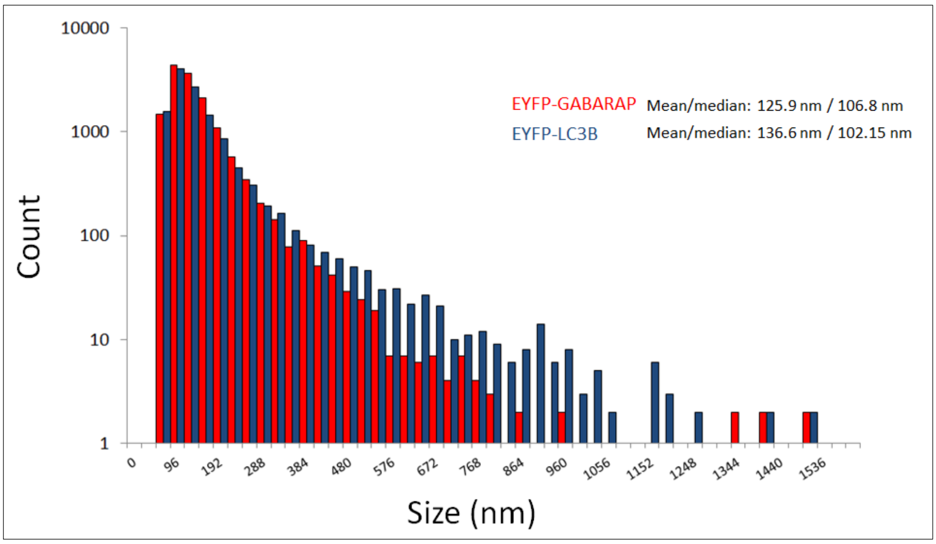

Figure 3.29. The size distributions of EYFP-GABARAP (red) and EYFP-LC3B (blue) cytosolic structures for five measured cells for each protein. The mean and median values are 125.9 nm / 106.8 nm and 136.6 nm / 102.15 nm, for EYFP-GABARAP and EYFP-LC3B cytosolic structures, respectively.

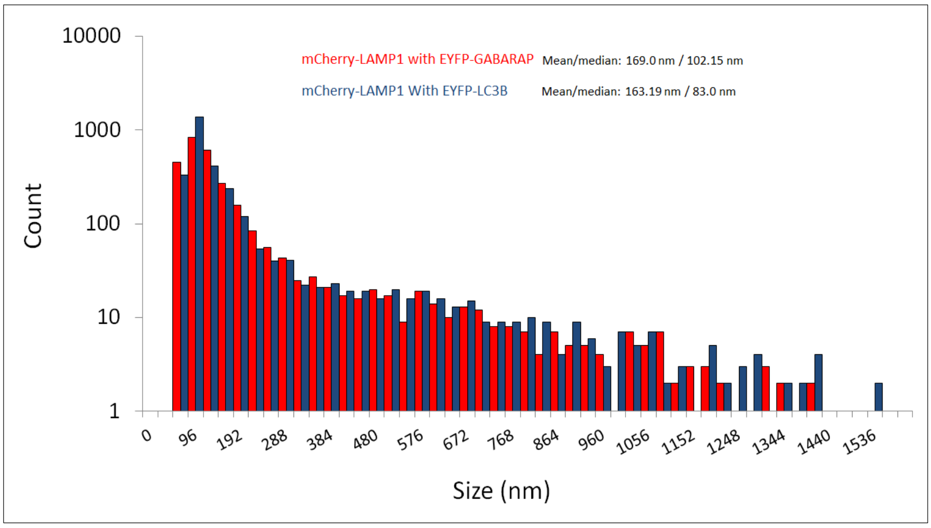

Figure 3.30. The size distributions of mCherry-LAMP1 cytosolic structures in HEK-293 cells co-transfected with mCherry-LAMP1 either and EYFP-GABARAP (red) or EYFP-LC3B (blue) cytosolic structures. The mean and median values are 169.0 nm / 102.15 nm and 163.19 nm / 83.0 nm, for mCherry-LAMP1 co-transfected with EYFP-GABARAP and mCherry-LAMP1 co-transfected with EYFP-LC3B cytosolic structures, respectively.

4. Discussion

Fluorescence microscopy offers nondestructive and label-specific investigation of localization and movement of proteins, cell organelles and cellular structures in living cells, tissues and organisms. In addition, a multitude of fluorescent biosensors exist, differing in environment sensitivity of fluorescence or more complex photophysical processes (e.g. anisotropy, FRET). These and the relatively, easy implementation of simultaneous monitoring of two or three observables (multi-colour fluorescence imaging) lead to the important role fluorescence microscopy plays in the life sciences since 30 years. The datasets acquired from fluorescence microscopy images often contain information on a large number of cells or cellular compartments in the field of view for further analysis. Super-resolution fluorescence microscopy enlarges the amount of data enormously (10- to 100-fold). A large number of details below the diffraction limit are detectable and distinguishable by super-resolution (especially single molecule localization) microscopes, offering the opportunity to analyze the dataset to get more insight into the organization of cellular or molecular compartments of interest. Precise estimation of the localization of proteins in their cellular context or even *in vivo* nowadays is easily performed with various super resolution fluorescence microscopy methods.

The research in autophagy, to a large extent, has also been significantly influenced by fluorescence microscopy as an imaging, spectroscopy, and analysis tool (Nair 2011). Autophagic organelles are dynamic complex (double and single bilayer) membrane structures, which undergo geometrical transformations during the different stages of their existence, and both morphogenesis and functionality of the surrounding membranes are believed to be regulated not only by the so-called autophagy-related proteins, but also by many other regulatory proteins. The number of autophagic structures in one cell varies significantly, but with better resolution and analysis methods it becomes clear that they are at least in the hundreds. Super-resolution microscopy detection of autophagy-related proteins will reveal the dynamic interactions and subcellular distribution of these molecules and hence contribute to the establishment of a model to understand their functionalities in the autophagy process. This study is one of the first attempts to apply single molecule localization microscopy (the fluorescent super-resolution microscopy type that delivers currently the highest resolution in practical applications) to autophagic proteins and structures.

Because of their involvement in many different functional stages in the autophagosome biogenesis, members of the Atg8 protein family are supposed to initiate or be involved in morphology alteration of autophagosomes during their development. As an example, with *in-vitro* experiments, Atg8 (from yeast) in several biophysical model systems revealed involvement in modulating membrane properties in curved membrane sections as well as a tendency of curvature sorting of lipidated Atg8 proteins (Knorr 2014). A sometimes proposed enrichment of Atg8 proteins specifically at the edges of expanding phagophores has not been demonstrated in a precise systematic model or in cells. Over almost two decades, the study of Atg8 by using different fluorescence imaging techniques has contributed to a huge body of literature, the vast majority of which, however, has been compromised by the diffraction limit of conventional optical microscopy. Not until recently, with the advent of different, now commercialized super-resolution microscopy techniques, people started to observe the spatial organization of different Atg and other autophagy-relevant proteins in detail. The existence of several, partly contradictory, hypotheses about the different roles of several members of the Atg8 protein family at different stages of autophagosome biogenesis was the starting point for the research topic presented in this thesis. GABARAP and LC3B as prototypical members of the two subfamilies of Atg8 proteins were selected to test the existing models in more detail by investigating their localization in mammalian cells by using SMLM. Large datasets were acquired based on SMLM imaging of cells during autophagy with a lot of spatial details well below diffraction limit. In the following sections, first the technical aspects of EYFP excitation in SMLM are considered, and subsequently, our findings and results about GABARAP and LC3B localization and the different shape and size distributions in HEK-293 cells are discussed.

4.1. 514 nm excitation of EYFP makes better SMLM images than 488 nm excitation

As described in chapter 3.1, excitation of EYFP FPs with less common light 514 nm gave a higher number of localizations per frame with a larger characteristic frame number for the fading out of the “blinking phase” – the suitable time for image generation in an SMLM measurement. The blinking period is two- to threefold longer when excitation at 514 nm is applied (figure 3.7). In figure 3.8, the number of localizations per cell intensity for low and high power excitation of EYFP with 488 and 514 nm light are depicted. These powers refer to the powers typically used on our setup for SMLM-imaging with excitation at 488 nm (high power) and 514 nm (low power). Two things are evident. First, higher excitation power does lead to lower number of detected localizations from single EYFP emitters pointing towards the necessity to optimize excitation power for every sample and fluorophore in SMLM. Secondly, there are 9- and 7.5-fold more localizations detected with 514 nm than with 488 nm excitation for the same power. This is the basis for the observed much better SMLM image quality for excitation at 514 nm compared to 488 nm excitation.

To explain the empirically found and not expected wavelength dependence of SMLM image quality the nature of the EYFP “blinking” has to be considered. In the literature there is evidence for dark (or non-emissive) metastable states of yellow fluorescent proteins that live for seconds, minutes or even hours. No conclusive, all-encompassing model exists since these results have been obtained for different mutants and different experimental conditions. These dark states may include chromophore protonation, isomerization, and decarboxylation of amino acids near by the chromophore and formation of radical states. A common theme though is the signature of a protonated YFP chromophore with absorption at 360 – 400 nm (figure 4.1).

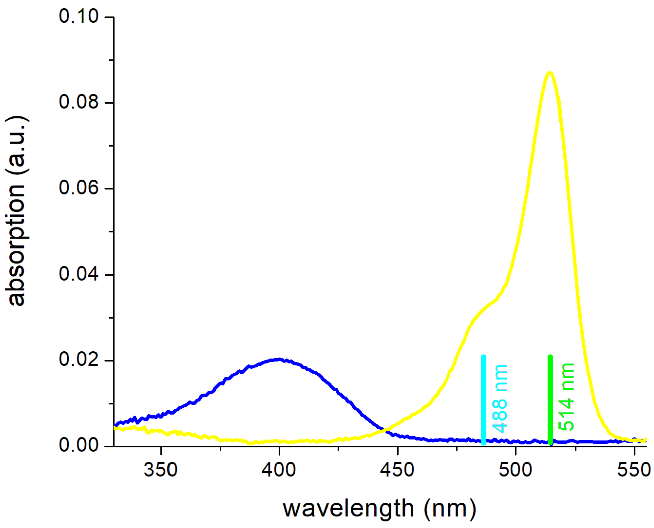

Figure 4.1. The absorption spectra of EYFP.

Though 488 nm and 514 nm are far red-shifted to this absorption band there is still a remaining absorption probability, which of course is higher for 488 nm light, since it is nearer to the absorption maximum. When exciting the dark states, of course, they can be permanently photobleached. In fact, it is well known for many fluorophores, that permanent photobleaching is occurring with much higher likelihood from long-lived triplet or radical states, which were formed after absorption of a first photon, by absorption of a second photon exciting these metastable states. By this process 488 nm excitation destroys more of the non-emissive dark states compared to the more red-shifted 514 nm excitation. But these dark states are the ones that return during the blinking period back to the emissive cycle with normal absorption spectrum (yellow curve in figure 4.1; peaking at 514 nm) and very high fluorescence quantum yield. In other words, they make the SMLM-imaging capability of EYFP so good.

Further evidence for the above described model was established in an experiment inspired by a recent observation in the laboratory of Prof. Philip Tinnefeld (Jusuk 2015). There it was reported that blinking periods and total number of fluorescent photons of EYFP (using 488 nm excitation) are enlarged when SMLM imaging was performed in so-called dSTORM-buffer that is with low molecular oxygen concentration and electron donating (reducing) molecules present. While the usefulness of the effect for SMLM imaging quality was demonstrated the photophysical context and origin was not discussed. The latter, however is of great interest with respect to the here in this thesis reported excitation dependent quality of SMLM imaging using EYFP and the hypothetical model to explain it (see above).

The dSTORM buffer allows high quality SMLM imaging with a number of fluorescent organic dyes based on the formation of radical anion states of the fluorophore from the triplet state by interaction with the electron donor (here mercaptoethanol)(Heilemann 2017). The radical anion state typically has largely blue-shifted absorption spectra and is therefore not excited nor does it fluoresce. In other words, a dark or OFF state is generated from the fluorophore – a prerequisite for SMLM. The absence (or low concentration) of molecular oxygen prolongs the lifetime of both triplet and radical anion state, which favors the formation of the dark state and prolongs its lifetime – thus modulating the blinking behavior. In principle, such anion radicals can also be formed in GFP-like fluorescent proteins. Appendix 7.7 presents preliminary data that clearly hint towards involvement of radical-involving photophysical phenomena in the EYFP photophysics leading to blinking as well as the excitation wavelength-dependent SMLM imaging performance. Figure 7.7.1 shows that the period of constant number of localizations per frame is considerably prolonged in dSTORM buffer compared to PBS, especially for excitation at 488 nm, where the prolongation is more than threefold. This is also reflected in the characteristic frame time (figure 7.2) and the total number of single molecule localizations (figure 7.3). The effect as such and the much larger prolongation of the EYFP-blinking period for 488 nm excitation (compared to 514 nm excitation, were the effect is only moderate) strongly support the above given model excitation dependence in EYFP SMLM imaging. Obviously, radical anion formation of EYFP chromophore (a dark state by itself), which occurs most probably from EYFP triplet state, competes with formation of other, more long-lived dark states of EYFP. The latter are the suggested cause of permanent photobleaching due to excitation under the strong illumination as in SMLM imaging – and much more with 488 nm light than with 514 nm light. Excitation of the radical anion state of EYFP, on the other hand, is relatively unlikely, since it is a short-lived metastable state with off-times below 1 s (Jusuk 2015). Though, by this competition the excitation wavelength dependence of EYFP-based SMLM imaging is reduced. To sum up, the best SMLM imaging with EYFP is achieved by using 514 nm excitation and dSTORM buffer (when applicable, i.e., in fixed cells).

4.2. Advantages of SMLM

Our data demonstrate that application of SMLM has the potential to provide superior results in comparison with conventional widefield fluorescence microscopy, in terms of both completeness of observations (figures 3.10 and 3.17, 3.29, 3.30) and wealth of associated information (figures 3.11, 3.13, 3.14, 3.15, 3.18-3.27). The reason is obviously the better spatial resolution and detection efficiency of the respective images, when acquired in SMLM mode. Observational completeness can be defined as the fraction of the items of interest that can be detected using the method in question. Quantification of the results showed that SMLM captures about 50 times the number of EYFP-labelled structures found via widefield microscopy, and this number is about 35 times for the Dendra2-labelled structures. Looking more carefully at the analysis of the size distributions revealed this difference to be mainly due to a large number of smaller structures (those with size smaller than 300 nm) which are not visible in the widefield images (tables 3.4 and 3.6, figures 3.11 and 3.17). This is a huge limitation given that a significant portion (most probably the larger fraction) of autophagy-related structures should fall into this size range, including early isolation membranes, growing phagophores and even the smaller-sized mature autophagosomes. The information content of the structures originating from the super-resolution images is interestingly different and more complete. The observation of a set of larger structures, which are readily visible on both widefield and SMLM images, yields quite different data depending on the fluorescence method used for acquisition. In addition to a slightly changed size distribution at lower resolution (figure 3.12, 3.18, 3.19), there is a large difference in the assignment of shapes to the detected structures (figures 3.14, 3.15, 3.26, and 3.27). These findings can be summarized to a very important result of this thesis. Although many structures, with dimension close to the diffraction limit or above, are detectable by conventional fluorescence microscopy, the information extracted from these structures should be treated with caution because numbers, sizes and shapes of structures might be biased. This is obviously very important when the information from fluorescence images is analyzed quantitatively and the observed structures are near the diffraction limit or below. For example, in autophagy as a dynamic process in which the morphology of structures directly reflects their functional state, misinterpretation of, e.g., a U-shape structure (commonly assigned to an early phagophore viewed from the side) as an elliptical object (usually assigned to a late phagophore or autophagosome) may affect biological conclusions drawn from experiments. As is shown for example in figures 3.15, 3.26, and 3.27, based on the analysis of the detected structures from the widefield images, one would conclude that, the majority of the labelled structures (both GABARAP and LC3B) appear to be circular or elliptical and therefore might correspond to late steps of the process.

Nonetheless, such interpretations are rejected by the more detailed analysis of labelled structures based on SMLM images. Although the large class of structures for GABARAP labelled structures are indeed circular or ellipse in widefield images, this classification and as a result, the functionality of the GABARAP is not similar for the corresponding structures outcome from SMLM images. This discussion could be with higher certainty applied for the LC3B labelled structures. Interpretation based on the widefield images clarifies the majority of these structures as circular, while based on the SMLM images; the dominating fraction is U-shaped or ellipses, depending on the starvation state.

Besides these methodological aspects, our SMLM analysis using EYFP and Dendra2 fusion proteins revealed important differences between the two Atg8 orthologues investigated. While the total structures size distributions behave similarly, the shape distributions of the respective labelled structures are quite disparate, indicating differential (but possibly overlapping) localization: GABARAP and LC3B may appear on phagophores at different stages of their evolution, but could also support distinct autophagic channels or participate in non-autophagy-related pathways.

4.3. GABARAP and LC3B functioning differently

Detailed electron microscopy-based experiments as well as experiments supported by fluorescence microscopy in cultured cells suggested that LC3 proteins were often engaged in phagophore expansion, whereas GABARAP proteins acted at a later stage, such as maturation, closure, and autophagosome-lysosome fusion (Weidberg 2010, Nguyen 2016). These differential functions of the two subfamilies from literature results are in good agreement with the shape distributions of cytoplasmic structures containing FP-GABARAP and FP-LC3B in our SMLM images after transient overexpression of EYFP-GABARAP and EYFP-LC3B, respectively, as well as in cell lines stably (over)expressing Dendra2-GABARAP and Dendra2-LC3B, respectively. Regarding their functions in cargo recruitment, GABARAP and LC3B differ in dynamic distribution by modulating the target structures, often with marked subfamily specificity (Birgisdottir 2013), supporting the idea that the prevalence of different Atg8 orthologues on individual phagophores or autophagosomes may be modulated by the type of substrate.

The overall accumulation of Atg8 proteins in punctate objects does not necessarily highlight phagophores or autophagosomes. The co-transfection of HEK-293 cells with mCherry-LAMP1 and EYFP-GABARAP or EYFP-LC3B (see section 3.4) showed the existence of many large EYFP labeled structures not associating with any of LAMP1 labeled structures, the latter most probably lysosomes or late endosomes. This might be due to the existence of GABARAP or LC3B in non-phagophore or non-autophagosome intracellular structures. The centrosomal pool of GABARAP, e.g., which is thought to play a critical role in autophagosome biogenesis, presumably consists of non-lipidated protein (Joachim 2015), and indeed, neither the centrosomal matrix nor the centriolar satellites shuttling GABARAP along microtubules contain membrane-terminated vesicles. Similarly, nuclear association of LC3 with insulin receptor substrate 1 (IRS-1) leads to the formation of layered clusters, again not involving biological membranes (Lassak 2018). Mammalian Atg8 proteins have also been found to associate with immunity-related GTPase M (IRGM) and the Qa-SNARE syntaxin-17 (Stx17) in large protein complexes (so-called autophagosome recognition particles, ARPs) which deliver

Stx17 to mature autophagosomes, thus enabling fusion with lysosomes (Kumar 2018). Again, these structures are assumed to be without membranes, with IRGM shielding the transmembrane domain of Stx17. Finally, both GABARAP and LC3B participate in cellular processes that are unrelated to autophagy but do involve vesicular structures. Prominent examples include trafficking of vesicles carrying transmembrane receptors towards the plasma membrane, which is typically mediated by GABARAP subfamily proteins (Schaaf 2016), and LC3-associated phagocytosis, which is usually engaged if membrane-wrapped extrinsic cargo is to be degraded (Fazeli 2017). A more general function in cellular signaling has emerged for GABARAP-type proteins, which are able to recruit an ubiquitin ligase targeting the RAC1-specific guanine nucleotide exchange factor TIAM1 (T-lymphoma invasion and metastasis-inducing protein 1). This process has been suggested to occur on non-autophagic membranes, although mechanistic connections to autophagy regulation may exist (Genau 2015). Based on these considerations, it seems very likely that a certain fraction of the objects labelled by EYFP-fused and Dendra2-fused Atg8 proteins actually constitute non-membranous autophagic or membranous non-autophagic structures, and thus do not represent phagophores or autophagosomes.

The abundance of fluorescently labelled particles in the sub-100 nm range, for instance, may be explained to a large part by non-vesicular structures such as centriolar satellites or ARPs. While protein complexes of the size between 50 nm (our SMLM spatial resolution limit) and 100 nm are clearly resolved in our SMLM images, they only contribute to a diffuse background in conventional diffraction-limited microscopy, preventing their differentiation from the cytosolic Atg8 pool. Despite the significant gain in spatial information provided by super-resolution fluorescence imaging, unambiguous assignment of structures to specific pathways still requires secondary labelling for a number of markers, and will not be covered in this work.

4.4. Size and shape distribution of Atg8 family proteins in fed condition and during starvation

Analyzing the data for CS-Dendra2-GABARAP and CS-Dendra2-LC3B shows that when cells are in fed or staved-blocked condition, there is no difference in size distribution for GABARAP and LC3B. Key parameters of autophagosomes or in general autophagic structures, while comparing cells in fed condition and in starvation, are the levels of protein expression, the numbers of punctate structures, and the size variation of such structures in fluorescence based images. Indeed, while working with cells transiently over-expressing EYFP-fused Atg8 proteins, since very often almost no such distinction was observed between fed and starved conditions. A possible reason could be that the transient transfection of cells constitutes a stress in itself and is inducing autophagy in the transfected cells, which also as a consequence produce an FP-Atg8 protein that serves a multitude of functions, i.e., might mis-trigger certain cellular behaviors (see also subchapter 4.5). To minimize such a limitation, HEK-293 cells stably expressing Dendra2-fused Atg8 proteins were investigated instead.

The basal level of autophagy, which occurs in mammalian cells at rest, plays various roles in regulation of inflammation (Into 2017), turnover of cytoplasmic contents in neuronal cells (Casares-Crespo 2018), and cell differentiation (Morgado 2015). This level of autophagy can be monitored principally in cells while they are kept at fed condition and no external or internal stimulus enforces cells to induce autophagy.

By inspection of our date of CS-Dendra2-Atg8s, a clear difference between fed and starved-blocked conditions was observed (figures 3.17, 3.20, and 3.21, but also appendix 7.3). The size distribution of all detected structures showed that splitting structures at 800 nm and classifying them as below and above 800 nm highlights the number and size differences of the structures in fed and starved-blocked conditions best. From our finding it immediately follows, that the basal level of autophagy does not result in formation of autophagosomes as large as 800 nm and above. This is a profound effect in CS-Dendra2-LC3B while in a lower extent can be also generalized to CS-Dendra2-GABARAP structures. On the other hand, the assumption that GABARAP functions and associates at late stages of autophagosome growth can be supported with these new findings from the shape classification of the structures in fed versus starved-blocked conditions. To our surprise, the picture of association of GABARAP with mainly circular shapes and to a lesser extent as ellipse from one hand, and the association of LC3B with shapes of mostly U-shaped structures (and to a lesser extent ellipses), was observed at both basal levels of autophagy and in autophagy-induced condition, supporting the critical role of the basal autophagy process for cell survival. The statistically significant differences between the shape classes of CS-Dendra2-LC3B and CS-Dendra2-GABARAP (figures 3.20 and 3.21, and table 3.7) demonstrated that GABARAP and LC3B contribute to autophagy at different time points of autophagosome biogenesis and/or are involved in different autophagy or non-autophagy related processes channel or pathway for GABARAP and LC3B for both autophagy-induced (starved/blocked) as well as at fed conditions.

4.5. Validity of using overexpressed Atg8 family proteins

In order to assess the localization of GABARAP and LC3B, the overexpression of fluorescent fusion proteins regulated by a non-natural promoter (CMV chosen for high protein expression levels) was utilized, which is part of the standard toolkit in cell biology research. This is valid for both transiently transfected fusion proteins and stably expressed fusion proteins. In comparison to immunolabelling of endogenous protein, this strategy ensures decent signal strength and excellent specificity of detection, but comes with the disadvantage of potentially non-specific localizations of the overexpressed protein – due to its unnaturally high intracellular concentrations - and a non-physiological regulation of fusion protein expression. The fusion proteins might accumulate at sites which are not significantly populated in parent cells, and even at physiological locations pathways may suffer from an overload of protein as well as the presence of the fusion partner. For instance, the experiments with co-transfection of EYFP labelled Atg8 proteins on one hand and mCherry-LAMP1 on the other hand (high rate of overexpression of different proteins), showed the presence of structures positive in EFYP signals that did not overlap with corresponding LAMP1 signals (see figures 3.26 and 3.27). Since the size of such structures varied from small to very large structures, it might be related to the above-discussed reasons that the overexpression of extra proteins follows several non-autophagic pathways.

The strength of nuclear staining that was observed when overexpressing EYFP-LC3B, for example, even after autophagy stimulation may indicate such an effect of overexpression since it exceeds what has been described previously for endogenous LC3 detected by immunofluorescence.

On the other hand, the numbers of cytoplasmic structures populated with EYFP-GABARAP and EYFP-LC3B are quite similar despite the fact that total cytoplasmic fluorescence (representing the abundance of the fusion protein) differs by a factor of five; this suggests that the overall activity of the respective pathways is at most moderately affected by Atg8 protein overexpression, thus supporting the validity of the approach. This is also true for the stably expressed Dendra2-GABARAP and Dendra2-LC3B proteins in fed and starved-blocked conditions. Therefore, development of cell lines stably expressing fluorescent fusion proteins under the control of endogenous promoters will be instrumental to avoid artefacts caused by protein overload while retaining the specificity of detection in both conventional and super resolution imaging modes. Attempts to develop such tools are under way in the research consortium of ICS-4 and ICS-6 working in autophagy research.

4.6. Interaction of GABARAP and LC3B during autophagosome-lysosome fusion

The proposed model of involvement of GABARAP subfamily mainly at late stages of autophagosome biogenesis, while LC3B plays a role at the early stages, led to the design of an experiment where the interaction of both Atg8 subfamilies with LAMP1 as a lysosomal marker was investigated (see figure 3.28-3.30 and appendices 7.5 and 7.6). The quantification of the number of EYFP-GABARAP or EYFP-LC3B structures co-localized with mCherry-LAMP1 was performed for size classes below and above 300 nm. This was mainly to relate the analysis to the diffraction limit size of the conventional fluorescence widefield microscopes. As depicted in figure 3.27, the average number of co-localized structures for EYFP-GABARAP and mCherry-LAMP1 above 300 nm is slightly higher than that for EYFP-LC3B and mCherry-LAMP1 (nearly a factor of 1.5). The average number of co-localized structures for EYFP-GABARAP and mCherry-LAMP1 below 300 nm is still slightly higher than that for EYFP-LC3B and mCherry-LAMP1 (nearly a factor of 1.2). Even though the variation of the number of co-localized structures below and above 300 nm is relatively high, in a way that one cannot statistically conclude, the results are still in conjunction with the idea that large roundish GABARAP labelled structures play a role at late stages of autophagosome biogenesis (here autophagosome-lysosome fusion) and less round structures of LC3B contribute more in early stages of autophagosome biogenesis. In figure 4.2, a very simplified cartoon illustrates early and late stages of autophagosome biogenesis.

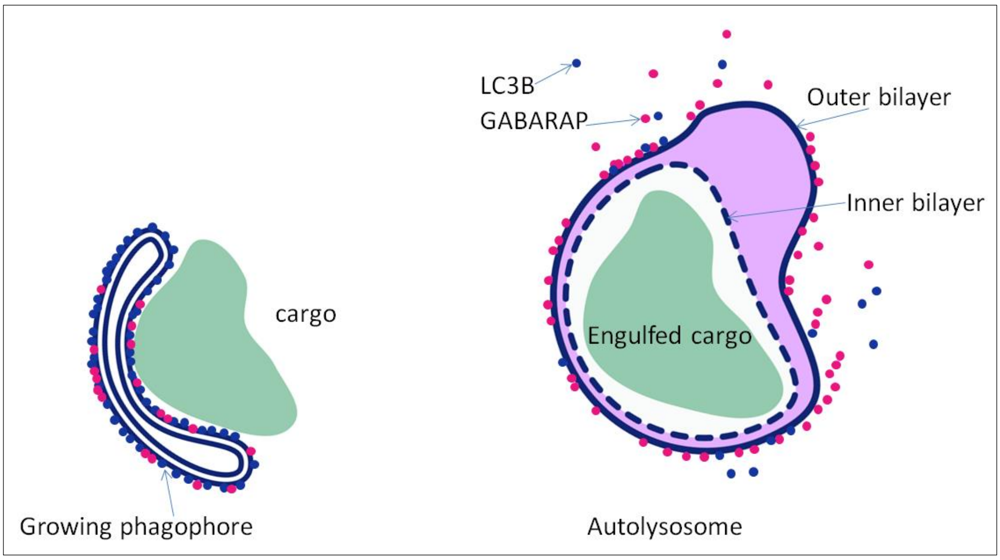

Figure 4.2. Simplified model for elongation of the growing phagophore around cargo (left) and degradation of the fully matured autophagosome after fusion with a lysosome to form an autolysosome (right). In the initial steps of autophagosome biogenesis (e.g. elongation phase), LC3B proteins are more involved, while at late stages (e.g. maturation and fusion phases), GABARAP proteins play a larger role.

5. Conclusions

Optimization of SMLM with EYFP: The basic idea of this thesis is the application of single molecule localization microscopy (SMLM) to investigate autophagy-relevant structures. A prerequisite is the choice of suitable fluorophores (here the fluorescent proteins EYFP, Dendra2 and mCherry) that are fused to the proteins of interest (GABARAP, LC3B and LAMP1). Optimal imaging conditions are also very important in single molecule imaging. In the first part of this thesis an optimization of SMLM-imaging of EYFP-labeled proteins is presented. It is shown quantitatively that excitation of EYFP at 514 nm leads to detection and localization of a significantly larger number of single EYFP emitters in an extended period of EYFP ON- and OFF-switching when compared to the more commonly used excitation of EYFP at 488 nm. The difference is explained by detrimental permanent EYFP photo-bleaching through excitation of metastable OFF-states of EYFP (with a protonated chromophore and an absorption maximum around 400 nm). The probability for this process is directly proportional to the absorption probability of these OFF-states, which is (naturally) considerably larger for 488 nm than 514 nm light. This is why, SMLM imaging of EYFP should be performed with 514 nm excitation, since it will for a given sample result in higher quality SMLM images when compared to 488 nm excitation.

SMLM is suitable when imaging autophagy processes: With the use of SMLM, it was shown that structures labeled with Atg8 proteins fused to FPs can be detected with sizes down to 30-50 nm, well below the diffraction limited resolution of ca. 200 nm when using conventional fluorescence microscopy techniques such as widefield or confocal fluorescence microscopy. The latter is a theoretical value, while the practical resolution is often considerably larger (ca. 300 nm). This nearly 10-fold improvement of spatial resolution was the motivation to investigate the localization of GABARAP and LC3B. SMLM is well suited to be used in autophagy and gives new impact by number, size and shape determination of vesicular structures in autophagy (and also the endo-lysosomal system).

Sizes of GABARAP and LC3B containing structures in the cytoplasm are similar: Size distributions for cytoplasmic, fluorescently labeled structures containing EYFP-GABARAP and EYFP-LC3B, respectively, showed a very similar behavior when proteins are transiently overexpressed in HEK-293 cells with enhanced autophagy (starved-blocked), with more than 1000 structures per cell that are mostly smaller than 300 nm. It can be concluded that EYFP-GABARAP and EYFP-LC3B containing structures are very much alike with respect to their size.

In cells with stable overexpression of Dendra2-GABARAP and Dendra2-LC3B, respectively, a clear and expected increase of “puncta” structures (autophagosomes) was found in conventional confocal fluorescence microscopy upon autophagy induction. This increase held only true for the large structures (> 300 nm and especially > 800 nm), though, when the same cell lines were investigated with SMLM. The overall number did not show this trend. The size distributions of cytosolic Dendra2- labeled GABARAP and LC3B structures under fed and starved-blocked conditions were found to be very similar with the majority of the structures with sizes well below the diffraction limited resolution. Again, the size distributions of the structures containing one or the other Atg8 protein do not show a difference. Apparently, GABARAP and LC3B containing vesicular structures cannot be distinguished by size.

Shapes of GABARAP and LC3B containing structures in the cytoplasm are largely different: On the other hand, shape determination of cytoplasmic FP-GABARAP and FP-LC3B containing structures showed very different behavior of the two proteins. For a more detailed analysis the shape distributions were generated for subsets of structures separated by the size (100, 300 and 800 nm splitting). FP-LC3B containing cytosolic structures are favorably located in asymmetric structures (ellipses, U-shapes), while FP-GABARAP is associated mostly with circular structures. This difference is the more obvious the larger the considered structures are. A direct consequence of these different shape distributions is that FP-LC3B and FP-GABARAP exist to a large extent in different cytosolic vesicular structures. The general model of autophagosome biogenesis together with the favorable shapes of FP-GABARAP and FP-LC3B containing structures supports the notion that LC3B is much more involved in the early stages of autophagosome formation while GABARAP is playing a role mainly in the late stages.

Conventional fluorescence microscopy delivers the WRONG shape information: An interesting and partially alarming result of our study originated from a direct comparison of conventional widefield and super-resolution SMLM fluorescence imaging. It was to be expected that with SMLM a much larger number of FP-GABARAP and FP-LC3B containing structures were detected, while in widefield fluorescence microscopy one observes only the largest and brightest structures. It came as a surprise, though, that the shapes determined in widefield fluorescence images were wrong for the majority of the structures as was shown in the corresponding SMLM fluorescence images. These obvious short-comings of imaging structures with limited or even insufficient detection efficiency and spatial resolution call into question the validity and completeness of the results in a number of previous studies of autophagy using conventional fluorescence imaging. One has to carefully check whether the results and conclusions might suffer from the fact that only the large and bright objects could have been considered, since only those are detected.

GABARAP and not LC3B associates to a higher degree with LAMP1-positive structures: A first attempt to elucidate the detailed localization of FP-GABARAP and FP-LC3B, respectively, with the help of SMLM was successfully carried out when two-colour SMLM fluorescence imaging was performed with EYFP-GABARAP/EYFP-LC3B and mCherry-LAMP1. To achieve SMLM images from mCherry a method from recent literature (Cloin 2017) was applied, where with a special buffer the nearly non-blinking mCherry FP was transformed into a photoactivatable FP. With this and the beforehand established EYFP-based SMLM-imaging two-colour SMLM imaging of a pair of very common FPs present in thousands of fusion protein constructs available in the scientific community has been established here. Using the marker protein mCherry-LAMP1, EYFP-GABARAP was found to co-localize with late endosomes and lysosomes with an even higher probability than EYFP-LC3B, but in both cases more than 50% of the mCherry-LAMP1 positive structures also contain the respective EYFP-Atg8 fusion protein. For EYFP-GABARAP, the co-localization with mCherry-LAMP1 structures ranges from 24% to up to 85% and the range of co-localization of EYFP-LC3B with mCherry-LAMP1 structures is 13% to 68%.

Drawbacks of overexpression: In the end one has to mention two experimental problems that should be solved in the future. The overexpression (transient or stable) with an unnatural promoter applied here - and in the vast majority of FP-fusion protein based fluorescence imaging studies - may lead to misguided localization of the fusion protein. The use of the CMV promoter (also here) to reach high expression levels – often much higher when compared to the endogenous expression level of the natural protein devoid of an FP under the control of its natural promoter – is problematic, since FP-GABARAP or FP-LC3B might associate with vesicular structures due to the abnormally high intracellular concentration and thus artefacts might be observed. Also, autophagy is a highly regulated process where upon stimulus higher numbers of proteins relevant for autophagy are needed and produced. Since the FP-fusion proteins are not regulated by the natural but the CMV promoter, important elements of the physiological response might be missing or distorted due to the absence of feedback signals. Another problem specific to FP-GABARAP and FP-LC3B (and also mCherry-LAMP1) stems from the same source, namely, the too high expression level. The latter may manifest in labelling of intracellular structures that are not autophagic or not even vesicular or membranous but large protein aggregates. Even with the high spatial resolution of SMLM these structures cannot be distinguished from the autophagic or endo-lysosomal structures on the basis of fluorescence images. A promising route is the generation of cell lines where the endogenous GABARAP or LC3B is knocked out and instead an FP-GABARAP or FP-LC3B fusion protein is expressed under control of the natural promoter, a research line that is currently under way in our research cooperation (ICS-4, ICS-6).

To summarize, SMLM has been proven to be valuable in studying autophagic and other vesicular structures in mammalian cells. GABARAP and LC3B localize to largely different but similarly sized structures.

6. References

[1] X. Zhang, E. Settembre, C. Xu, P. R. Dormitzer, R. Bellamy, S. C. Harrison and N. Grigorieff, "Near-atomic resolution using electron cryomicroscopy and single-particle reconstruction," *Proceedings of the National Academy of Sciences of the United States of America,* vol. 105, pp. 1867-1872, 2008.

[2] P. Zhang, A. A. Kiseleva, V. Korobeynikov, H. Liu, M. B. Einarson and E. A. Golemis, "Microscopy-Based automated live cell screening for small molecules that affect ciliation," *Frontiers in Genetics,* vol. 10, 2019.

[3] M. Zhang, H. Chang, Y. Zhang, J. Yu, L. Wu, W. Ji, J. Chen, B. Liu, J. Lu, Y. Liu, J. Zhang, P. Xu and T. Xu, "Rational design of true monomeric and bright photoactivatable fluorescent proteins," *Nature Methods,* vol. 9, pp. 727-729, 2012.

[4] G. Zhang, V. Gurtu and S. R. Kain, "An Enhanced Green Fluorescent Protein Allows Sensitive Detection of Gene Transfer in Mammalian Cells," vol. 711, pp. 707-711, 1996.

[5] A. Y. S. O.-O. Yukiko Kabeya, Y. O. Yoshimori and Tamotsu, "LC3, GABARAP and GATE16 localize to autophagosomal membrane depending on form-II formation," *Journal of Cell Science,* vol. 117, pp. 2805-2812, 2004.

[6] A. R. J. Young, "Starvation and ULK1-dependent cycling of mammalian Atg9 between the TGN and endosomes," *Journal of Cell Science,* vol. 119, pp. 3888-3900, 2006.

[7] A. G. York, S. H. Parekh, D. D. Nogare, R. S. Fischer, K. Temprine, M. Mione, A. B. Chitnis, C. A. Combs and H. Shroff, "Resolution doubling in live, multicellular organisms via multifocal structured illumination microscopy," *Nature Methods,* vol. 9, pp. 749-754, 2012.

[8] F. Yang, L. G. Moss and G. N. Phillips, "The Illolecular structure of green fluorescent protein," vol. 14, 1996.

[9] J. Yan, N. Okazaki, Y. Masuho, M.-A. Muramatsu, H. Kuroyanagi, T. Tomemori, Y.-I. Suzuki, T. Shirasawa, K. Asato, Y.-I. Matsuda, Y. Ohshima and S. Mitani, "Mouse ULK2, a novel member of the UNC-51-like protein kinases: Unique features of functional domains," *Oncogene,* vol. 18, pp. 5850-5859, 1999.

[10] I. V. Yampolsky, S. J. Remington, V. I. Martynov, V. K. Potapov, S. Lukyanov and K. A. Lukyanov, "Synthesis and properties of the chromophore of the asFP595 chromoprotein from Anemonia sulcata," *Biochemistry,* vol. 44, pp. 5788-5793, 2005.

[11] S. I. Yamashita, X. Jin, K. Furukawa, M. Hamasaki, A. Nezu, H. Otera, T. Saigusa, T. Yoshimori, Y. Sakai, K. Mihara and T. Kanki, "Mitochondrial division occurs concurrently with autophagosome formation but independently of Drp1 during mitophagy," *Journal of Cell Biology,* vol. 215, pp. 649-665, 2016.

[12] H. Yamamoto, S. Kakuta, T. M. Watanabe, A. Kitamura, T. Sekito, C. Kondo-Kakuta, R. Ichikawa, M. Kinjo and Y. Ohsumi, "Atg9 vesicles are an important membrane source during early steps of autophagosome formation," *Journal of Cell Biology,* vol. 198, pp. 219-233, 2012.

[13] X. Z. Xu, "Actin, spectrin and associated proteins form a periodic cytoskeletal structure in axons," *Science,* vol. 339, pp. 1-11, 2013.

[14] M. Xu, X. Li, J. Xiong, M. Xia, E. Gulbins, Y. Zhang and P. L. Li, "Regulation of autophagic flux by dynein-mediated autophagosomes trafficking in mouse coronary arterial myocytes," *Biochimica et Biophysica Acta - Molecular Cell Research,* vol. 1833, pp. 3228-3236, 2013.

[15] Xu and X. Zhuang, "Dual-objective STORM reveals three-dimensional filament organization in the actin cytoskeleton," *Nature methods,* vol. 9, pp. 185-188, 2012.

[16] Z. Xie, U. Nair and D. J. Klionsky, "Atg8 Controls Phagophore Expansion during Autophagosome Formation," *Molecular biology of the cell,* vol. 19, pp. 308-317, 2008.

[17] M. Xie, Y. Su, X. Lu, Y. Zhang, Z. Yang and Y. Zhang, "Blue and green photoluminescence graphene quantum dots synthesized from carbon fibers," *Materials Letters,* vol. 93, pp. 161-164, 2013.

[18] G. R. Wood V, L. M. Rajandream MA, S. A. Lyne R, P. N. Sgouros J, B. S. Hayles J, B. S. Basham D, B. D. Brooks K, C. T. Brown S, C. M. Churcher C, C. A. Connor R, F. T. Davis P, G. S. Fraser A and N. P. Gobl, "The genome sequence of Schizosaccharomyces pombe," *Nature,* vol. 415, pp. 871-880, 2002.

[19] S. Wolter, A. Löschberger, T. Holm, S. Aufmkolk, M.-c. Dabauvalle, S. V. D. Linde and M. Sauer, "correspondEnce rapi d STORM : accurate , fast open-source software for localization microscopy ORCAE : online resource for community annotation of eukaryotes," *Nature Methods,* vol. 9, pp. 1040-1041, 2012.

[20] M. Wirth, W. Zhang, M. Razi, L. Nyoni, D. Joshi, N. O'Reilly, T. Johansen, S. A. Tooze and S. Mouilleron, "Molecular determinants regulating selective binding of autophagy adapters and receptors to ATG8 proteins," *Nature Communications,* vol. 10, 2019.

[21] M. Winey, J. B. Meehl, E. T. O'Toole and T. H. Giddings, "Conventional transmission electron microscopy," *Molecular Biology of the Cell,* vol. 25, pp. 319-323, 2014.

[22] P. G. Wilmann, K. Turcic, J. M. Battad, M. C. J. Wilce, R. J. Devenish, M. Prescott and J. Rossjohn, "The 1.7 Å Crystal Structure of Dronpa: A Photoswitchable Green Fluorescent Protein," *Journal of Molecular Biology,* vol. 364, pp. 213-224, 2006.

[23] P. Wild, H. Farhan, D. G. McEwan, S. Wagner, V. V. Rogov, N. R. Brady, B. Richter, J. Korac, O. Waidmann, C. Choudhary, V. Dotsch, D. Bumann and I. Dikic, "Phosphorylation of the Autophagy Receptor Optineurin Restricts Salmonella Growth," *Science,* vol. 333, pp. 228-233, 2011.

[24] J. Wiedenmann, S. Ivanchenko, F. Oswald, F. Schmitt, C. Röcker, A. Salih, K. D. Spindler and G. U. Nienhaus, "EosFP, a fluorescent marker protein with UV-inducible green-to-red fluorescence conversion," *Proceedings of the National Academy of Sciences of the United States of America,* vol. 101, pp. 15905-15910, 2004.

[25] H. Weidberg, E. Shvets, T. Shpilka, F. Shimron, V. Shinder and Z. Elazar, "LC3 and GATE-16/GABARAP subfamilies are both essential yet act differently in autophagosome biogenesis," *EMBO Journal,* vol. 29, pp. 1792-1802, 2010.

[26] X. Wang, J. Dai, X. Min, Z. Yu, Y. Cheng, K. Huang, J. Yang, X. Yi, X. Lou and F. Xia, "DNA-Conjugated Amphiphilic Aggregation-Induced Emission Probe for Cancer Tissue Imaging and Prognosis Analysis," *Analytical Chemistry,* vol. 90, pp. 8162-8169, 2018.

[27] M. Walczak and S. Martens, "Dissecting the role of the Atg12-Atg5-Atg16 complex during autophagosome formation," *Autophagy,* vol. 9, pp. 424-425, 2013.

[28] D. Virant, B. Turkowyd, A. Balinovic and U. Endesfelder, "Combining primed photoconversion and UV-photoactivation for aberration-free, live-cell compliant multi-color single-molecule localization microscopy imaging," *International Journal of Molecular Sciences,* vol. 18, 2017.

[29] V. V. Verkhusha, "Spectra in Red Fluorescent Protein rsTagRFP," vol. 417, pp. 144-151, 2013.

[30] V. V. Verkhusha and A. Sorkin, "Conversion of the monomeric red fluorescent protein into a photoactivatable probe," *Chemistry and Biology,* vol. 12, pp. 279-285, 2005.

[31] a. R. H. N. Vedangi Sample and J. Zhang, "The structure and function of fluorescent proteins," 2009.

[32] J. J. Van Thor, T. Gensch, K. J. Hellingwerf and L. N. Johnson, "Phototransformation of green fluorescent protein with UV and visible light leads to decarboxylation of glutamate 222," *Nature Structural Biology,* vol. 9, pp. 37-41, 2002.

[33] S. Van De Linde, A. Löschberger, T. Klein, M. Heidbreder, S. Wolter, M. Heilemann and M. Sauer, "Direct stochastic optical reconstruction microscopy with standard fluorescent probes," *Nature Protocols,* vol. 6, pp. 991-1009, 2011.

[34] A. Vakili, D. Xiong, M. Rajadhyaksha and C. A. DiMarzio, "High brightness LED in confocal microscopy," *Three-Dimensional and Multidimensional Microscopy: Image Acquisition and Processing XXII,* vol. 9330, p. 933006, 2015.

[35] R. Y. Tsien, "Constructing and exploiting the fluorescent protein paintbox (Nobel Lecture).," *Angewandte Chemie (International ed. in English),* vol. 48, pp. 5612-5626, 2009.

[36] T. Torisu, K. Torisu, I. H. Lee, J. Liu, D. Malide, C. A. Combs, X. S. Wu, I. I. Rovira, M. M. Fergusson, R. Weigert, P. S. Connelly, M. P. Daniels, M. Komatsu, L. Cao and T. Finkel, "Autophagy regulates endothelial cell processing, maturation and secretion of von Willebrand

factor," *Nature Medicine,* vol. 19, pp. 1281-1287, 2013.

[37] M. Tomura and K. Kabashima, "Analysis of cell movement between skin and other anatomical sites in vivo using photoconvertible fluorescent protein "kaede"-transgenic mice," *Methods in Molecular Biology,* vol. 961, pp. 279-286, 2013.

[38] R. E. Thompson, D. R. Larson and W. W. Webb, "ThompsonJBiophys2002Precise nanometer localization analysis (Least Square Estimation).pdf," vol. 82, pp. 2775-2783, 2002.

[39] S. Thiberge, A. Nechushtan, D. Sprinzak, O. Gileadi, V. Behar, O. Zik, Y. Chowers, S. Michaeli, J. Schlessinger and E. Moses, "Scanning electron microscopy of cells and tissues under fully hydrated conditions," *PNAS,* vol. 260, p. 78, 2004.

[40] I. Tanida, M. Komatsu, T. Ueno and E. Kominami, "GATE-16 and GABARAP are authentic modifiers mediated by Apg7 and Apg3," *Biochemical and Biophysical Research Communications,* vol. 300, pp. 637-644, 2003.

[41] Y. Tang, L. Dai, X. Zhang, J. Li, J. Hendriks, X. Fan, N. Gruteser, A. Meisenberg, A. Baumann, A. Katranidis and T. Gensch, "SNSMIL, a real-time single molecule identification and localization algorithm for super-resolution fluorescence microscopy," *Scientific Reports,* vol. 5, pp. 1-13, 2015.

[42] Y. Tang, J. Hendriks, T. Gensch, L. Dai and J. Li, "Automatic Bayesian single molecule identification for localization microscopy," *Scientific Reports,* vol. 6, pp. 1-11, 2016.

[43] A. Tabor, S. Weisenburger, A. Banerjee, N. Purkayastha, J. M. Kaindl, H. Hübner, L. Wei, T. W. Grömer, J. Kornhuber, N. Tschammer, N. J. M. Birdsall, G. I. Mashanov, V. Sandoghdar and P. Gmeiner, "Visualization and ligand-induced modulation of dopamine receptor dimerization at the single molecule level," *Scientific Reports,* vol. 6, pp. 1-16, 2016.

[44] K. Suzuki, Y. Kubota, T. Sekito and Y. Ohsumi, "Hierarchy of Atg proteins in pre-autophagosomal structure organization," *Genes to Cells,* vol. 12, pp. 209-218, 2007.

[45] K. Suzuki, M. Akioka, C. Kondo-Kakuta, H. Yamamoto and Y. Ohsumi, "Fine mapping of autophagy-related proteins during autophagosome formation in Saccharomyces cerevisiae," *Journal of Cell Science,* vol. 126, pp. 2534-2544, 2013.

[46] K. Sugawara, N. N. Suzuki, Y. Fujioka, N. Mizushima, Y. Ohsumi and F. Inagaki, "The crystal structure of microtubule-associated protein light chain 3, a mammalian homologue of Saccharomyces cerevisiae Atg8," *Genes to Cells,* vol. 9, pp. 611-618, 2004.

[47] O. M. Subach, G. H. Patterson, L. M. Ting, Y. Wang, J. S. Condeelis and V. V. Verkhusha, "A photoswitchable orange-to-far-red fluorescent protein, PSmOrange," *Nature Methods,* vol. 8, pp. 771-780, 2011.

[48] O. M. Subach, D. Entenberg, J. S. Condeelis and V. V. Verkhusha, "A FRET-facilitated photoswitching using an orange fluorescent protein with the fast photoconversion kinetics,"

Journal of the American Chemical Society, vol. 134, pp. 14789-14799, 2012.

[49] F. V. Subach, G. H. Patterson, S. Manley, J. M. Gillette, J. Lippincott-Schwartz and V. V. Verkhusha, "Photoactivatable mCherry for high-resolution two-color fluorescence microscopy," *Nature Methods,* vol. 6, pp. 153-159, 2009.

[50] F. V. Subach, G. H. Patterson, M. Renz, J. Lippincott-Schwartz and V. V. Verkhusha, "Bright monomeric photoactivatable red fluorescent protein for two-color super-resolution sptPALM of live cells," *Journal of the American Chemical Society,* vol. 132, pp. 6481-6491, 2010.

[51] F. Ströhl and C. F. Kaminski, "Frontiers in structured illumination microscopy," *Optica,* vol. 3, p. 667, 2016.

[52] G. G. Stokes, "On the Change of Refrangibility of Light . [Abstract] Author (s): George G . Stokes Reviewed work (s): Source : Abstracts of the Papers Communicated to the Royal Society of London , Vol . 6 (1850 - Published by : The Royal Society Stable URL : http," *The Royal Society,* vol. 6, pp. 195-200, 1852.

[53] A. C. Stiel, M. Andresen, H. Bock, M. Hilbert, J. Schilde, A. Schönle, C. Eggeling, A. Egner, S. W. Hell and S. Jakobs, "Generation of monomeric reversibly switchable red fluorescent proteins for far-field fluorescence nanoscopy," *Biophysical Journal,* vol. 95, pp. 2989-2997, 2008.

[54] A. C. Stiel, S. Trowitzsch, G. Weber, M. Andresen, C. Eggeling, S. W. Hell, S. Jakobs and M. C. Wahl, "1.8 Å bright-state structure of the reversibly switchable fluorescent protein Dronpa guides the generation of fast switching variants," *Biochemical Journal,* vol. 402, pp. 35-42, 2007.

[55] O. V. Stepanenko, O. V. Stepanenko, D. M. Shcherbakova, M. Irina, K. K. Turoverov, V. V. Verkhusha and S. Biology, "HHS Public Access," vol. 51, 2015.

[56] O. V. Stepanenko, O. V. Stepanenko, I. M. Kuznetsova, V. V. Verkhusha and K. K. Turoverov, Beta-Barrel Scaffold of Fluorescent Proteins, 2013, pp. 221-278.

[57] C. M. St Croix, S. H. Shand and S. C. Watkins, "Confocal microscopy: comparisons, applications, and problems.," *BioTechniques,* vol. 39, 2005.

[58] M. D. Smith, M. E. Harley, A. J. Kemp, J. Wills, M. Lee, M. Arends, A. Kriegsheim, C. Behrends and S. Wilkinson, "CCPG1 is a noncanonical autophagy cargo receptor essential for reticulophagy and pancreatic ER proteostasis," *Autophagy,* vol. 14, pp. 1107-1109, 2018.

[59] J. D. Slocum and L. J. Webb, "A Double Decarboxylation in Superfolder Green Fluorescent Protein Leads to High Contrast Photoactivation," 2017.

[60] D. Sinnecker, P. Voigt, N. Hellwig and M. Schaefer, "Reversible photobleaching of enhanced green fluorescent proteins," *Biochemistry,* vol. 44, pp. 7085-7097, 2005.

[61] Y. Si, Y. Si, F. Nanomaterials, B. Application, Y. Si and N. Hildebrandt, "Fluorescent

Nanomaterials for Bioimaging and Biosensing : Application on E . coli Bacteria To cite this version : HAL Id : tel-01221690 DE L ' ECOLE NORMALE SUPERIEURE DE CACHAN Présentée par Sujet de la thése : Fluorescent Nanomaterials for Bioimaging an," 2015.

[62] O. SHIMOMURA, F. H. JOHNSON and Y. SAIGA, "Extraction, purification and properties of aequorin, a bioluminescent," *Journal of cellular and comparative physiology,* vol. 59, pp. 223-239, 1962.

[63] S. H. Shim, C. Xia, G. Zhong, H. P. Babcock, J. C. Vaughan, B. Huang, X. Wang, C. Xu, G. Q. Bi and X. Zhuang, "Super-resolution fluorescence imaging of organelles in live cells with photoswitchable membrane probes," *Proceedings of the National Academy of Sciences of the United States of America,* vol. 109, pp. 13978-13983, 2012.

[64] S. T. Shibutani and T. Yoshimori, "A current perspective of autophagosome biogenesis," *Cell Research,* vol. 24, pp. 58-68, 2014.

[65] S. Shibata, T. Iseda, T. Mitsuhashi, A. Oka, T. Shindo, N. Moritoki, T. Nagai, S. Otsubo, T. Inoue, E. Sasaki, C. Akazawa, T. Takahashi, R. Schalek, J. W. Lichtman and H. Okano, "Large-area fluorescence and electron microscopic correlative imaging with multibeam scanning electron microscopy," *Frontiers in Neural Circuits,* vol. 13, pp. 1-18, 2019.

[66] D. M. Shcherbakova, P. Sengupta, J. Lippincott-Schwartz and V. V. Verkhusha, "Photocontrolable Flourecent Proteins for Superresulution Imaging," *Annu Rev Biophys,* vol. 72, pp. 181-204, 2011.

[67] L. Shao, P. Kner, E. H. Rego and M. G. L. Gustafsson, "Super-resolution 3D microscopy of live whole cells using structured illumination," *Nature Methods,* vol. 8, pp. 1044-1048, 2011.

[68] N. C. Shaner, M. Z. Lin, M. R. McKeown, P. A. Steinbach, K. L. Hazelwood, M. W. Davidson and R. Y. Tsien, "Improving the photostability of bright monomeric orange and red fluorescent proteins," *Nature Methods,* vol. 5, pp. 545-551, 2008.

[69] N. C. Shaner, G. H. Patterson and M. W. Davidson, "Advances in fluorescent protein technology," *Journal of Cell Science,* vol. 120, pp. 4247-4260, 2007.

[70] N. C. Shaner, P. A. Steinbach and R. Y. Tsien, "A guide to choosing fluorescent proteins," *Nature Methods,* vol. 2, pp. 905-909, 2005.

[71] T. Sekito, T. Kawamata, R. Ichikawa, K. Suzuki and Y. Ohsumi, "Atg17 recruits Atg9 to organize the pre-autophagosomal structure," *Genes to Cells,* vol. 14, pp. 525-538, 2009.

[72] B. L. Scott, K. A. Sochacki, S. T. Low-Nam, E. M. Bailey, Q. A. Luu, A. Hor, A. M. Dickey, S. Smith, J. G. Kerkvliet, J. W. Taraska and A. D. Hoppe, "Membrane bending occurs at all stages of clathrincoat assembly and defines endocytic dynamics," *Nature Communications,* vol. 9, 2018.

[73] C. A. Schneider, W. S. Rasband and K. W. Eliceiri, "NIH Image to ImageJ: 25 years of image

analysis," *Nature Methods,* vol. 9, pp. 671-675, 2012.

[74] M. B. E. Schaaf, T. G. Keulers, M. A. Vooijs and K. M. A. Rouschop, "LC3/GABARAP family proteins: Autophagy-(un)related functions," *FASEB Journal,* vol. 30, pp. 3961-3978, 2016.

[75] M. Sauer and M. Heilemann, "Single-Molecule Localization Microscopy in Eukaryotes," *Chemical Reviews,* vol. 117, pp. 7478-7509, 2017.

[76] M. Sauer, "Reversible molecular photoswitches: A key technology for nanoscience and fluorescence imaging," *Proceedings of the National Academy of Sciences of the United States of America,* vol. 102, pp. 9433-9434, 2005.

[77] M. Sakoh-Nakatogawa, K. Matoba, E. Asai, H. Kirisako, J. Ishii, N. N. Noda, F. Inagaki, H. Nakatogawa and Y. Ohsumi, "Atg12-Atg5 conjugate enhances E2 activity of Atg3 by rearranging its catalytic site," *Nature Structural and Molecular Biology,* vol. 20, pp. 433-439, 2013.

[78] S. J. Sahl, S. W. Hell and S. Jakobs, "Fluorescence nanoscopy in cell biology," *Nature Reviews Molecular Cell Biology,* vol. 18, pp. 685-701, 2017.

[79] S. J. Sahl, L. E. Weiss, W. C. Duim, J. Frydman and W. E. Moerner, "Cellular inclusion bodies of mutant huntingtin exon 1 obscure small fibrillar aggregate species," *Scientific Reports,* vol. 2, pp. 1-7, 2012.

[80] M. J. Rust, M. Bates and X. Zhuang, "Sub-diffraction-limit imaging by stochastic optical reconstruction microscopy (STORM)," *Nature Methods,* vol. 3, pp. 793-795, 2006.

[81] R. C. Russell, Y. Tian, H. Yuan, H. W. Park, Y. Y. Chang, J. Kim, H. Kim, T. P. Neufeld, A. Dillin and K. L. Guan, "ULK1 induces autophagy by phosphorylating Beclin-1 and activating VPS34 lipid kinase," *Nature Cell Biology,* vol. 15, pp. 741-750, 2013.

[82] E. Ruska, "The Development of the Electron and of Electron Microscopy Microscope," *Bioscience Reports,* vol. 7, 1987.

[83] D. C. Rubinsztein, G. Mariño and G. Kroemer, "Autophagy and aging," *Cell,* vol. 146, pp. 682-695, 2011.

[84] A. B. Rosenbloom, S. H. Lee, M. To, A. Lee, J. Y. Shin and C. Bustamante, "Optimized two-color super resolution imaging of Drp1 during mitochondrial fission with a slow-switching Dronpa variant," *Proceedings of the National Academy of Sciences of the United States of America,* vol. 111, pp. 13093-13098, 2014.

[85] V. V. Rogov, H. Suzuki, E. Fiskin, P. Wild, A. Kniss, A. Rozenknop, R. Kato, M. Kawasaki, D. G. McEwan, F. Löhr, P. Güntert, I. Dikic, S. Wakatsuki and V. Dötsch, "Structural basis for phosphorylation-triggered autophagic clearance of Salmonella," *Biochemical Journal,* vol. 454, pp. 459-466, 2013.

[86] V. Rogov, V. Dötsch, T. Johansen and V. Kirkin, "Interactions between Autophagy Receptors and

Ubiquitin-like Proteins Form the Molecular Basis for Selective Autophagy," *Molecular Cell,* vol. 53, pp. 167-178, 2014.

[87] T. Robertson, F. Bunel and M. Roberts, "Fluorescein Derivatives in Intravital Fluorescence Imaging," *Cells,* vol. 2, pp. 591-606, 2013.

[88] L. G. Rikkert, R. Nieuwland, L. W. M. M. Terstappen and F. A. W. Coumans, "Quality of extracellular vesicle images by transmission electron microscopy is operator and protocol dependent," *Journal of Extracellular Vesicles,* vol. 8, 2019.

[89] E. Rieter, F. Vinke, D. Bakula, E. Cebollero, C. Ungermann, T. Proikas-Cezanne and F. Reggiori, "Atg18 function in autophagy is regulated by specific sites within its -propeller," *Journal of Cell Science,* vol. 126, pp. 593-604, 2013.

[90] U. Resch-genger, M. Grabolle, S. Cavaliere-jaricot, R. Nitschke and T. Nann, "Quantum dots versus organic dyes as fluorescent labels," vol. 5, pp. 763-775, 2008.

[91] W. Ren, S. Chen, S. Li, Y. Zhang, J. Liu, M. Guan, H. Yang, N. Li, C. Han, T. Li, Z. Zhao and J. Ge, "Photoluminescence Enhancement of Carbon Dots by Surfactants at Room Temperature," *Chemistry - A European Journal,* vol. 24, pp. 15806-15811, 2018.

[92] S. J. Remington, R. M. Wachter, D. K. Yarbrough, B. Branchaud, D. C. Anderson, K. Kallio and K. A. Lukyanov, "zFP538, a yellow-fluorescent protein from Zoanthus, contains a novel three-ring chromophore," *Biochemistry,* vol. 44, pp. 202-212, 2005.

[93] B. Ravikumar, S. Sarkar, J. E. Davies, M. Futter, M. Garcia-Arencibia, Z. W. Green-Thompson, M. Jimenez-Sanchez, V. I. Korolchuk, M. Lichtenberg, S. Luo, D. C. O. Massey, F. M. Menzies, K. Moreau, U. Narayanan, M. Renna, F. H. Siddiqi, B. R. Underwood, A. R. Winslow and D. C. Rubinsztein, "Regulation of Mammalian Autophagy in Physiology and Pathophysiology," *Physiological Reviews,* vol. 90, pp. 1383-1435, 2010.

[94] K. H. Rainey and G. H. Patterson, "Photoswitching FRET to monitor protein – protein interactions," vol. 116, 2019.

[95] M. L. Quillin, D. M. Anstrom, X. Shu, S. O'Leary, K. Kallio, D. M. Chudakov and S. J. Remington, "Kindling fluorescent protein from Anemonia sulcata: Dark-state structure at 1.38 Å resolution," *Biochemistry,* vol. 44, pp. 5774-5787, 2005.

[96] V. Quercioli, C. Bosisio, S. C. Daglio, F. Rocca, L. D'Alfonso, M. Collini, G. Baldini, G. Chirico, S. Bettati, S. Raboni and B. Campanini, "Photoinduced millisecond switching kinetics in the GFPMut2 E222Q mutant," *Journal of Physical Chemistry B,* vol. 114, pp. 4664-4677, 2010.

[97] D. C. Prasher, V. K. Eckenrode, W. W. Ward, F. G. Prendergast and M. J. Cormier, "Primary structure of the Aequorea victoria green-fluorescent protein," *Gene,* vol. 111, pp. 229-233, 1992.

[98] N. V. Pletneva, S. V. Pletnev, D. M. Chudakov, T. V. Tikhonova, V. O. Popov, V. I. Martynov, A. Wlodawer, Z. Dauter and V. Z. Pletnev, "Three-dimensional structure of yellow fluorescent protein zYFP538 from Zoanthus sp. at the resolution 1.8 angstrom," *Bioorganicheskaia khimiia,* vol. 33, pp. 421-430, 2007.

[99] V. Z. Pletnev, N. V. Pletneva, K. S. Sarkisyan, A. S. Mishin, K. A. Lukyanov, E. A. Goryacheva, R. H. Ziganshin, Z. Dauter and S. Pletnev, "Structure of the green fluorescent protein NowGFP with an anionic tryptophan-based chromophore," *Acta Crystallographica Section D: Biological Crystallography,* vol. 71, pp. 1699-1707, 2015.

[100] K. D. Piatkevich and V. V. Verkhusha, Guide to Red Fluorescent Proteins and Biosensors for Flow Cytometry, vol. 9, 2011, pp. 431-461.

[101] G. Pepe, J. M. Cole, P. G. Waddell and J. R. D. Griffiths, "Molecular engineering of fluorescein dyes as complementary absorbers in dye co-sensitized solar cells," *Molecular Systems Design and Engineering,* vol. 1, pp. 402-415, 2016.

[102] J. B. Pawley, "Fundamental limits in confocal microscopy," *Handbook of Biological Confocal Microscopy: Third Edition,* pp. 20-42, 2006.

[103] G. H. Patterson and J. Lippincott-Schwartz, "A photoactivatable GFP for selective photolabeling of proteins and cells," *Science,* vol. 297, pp. 1873-1877, 2002.

[104] D. Papinski and C. Kraft, "Regulation of Autophagy by Signaling Through the Atg1/ULK1 Complex," *Journal of Molecular Biology,* vol. 428, pp. 1725-1741, 2016.

[105] S. Pankiv, T. H. Clausen, T. Lamark, A. Brech, J. A. Bruun, H. Outzen, A. Øvervatn, G. Bjørkøy and T. Johansen, "p62/SQSTM1 binds directly to Atg8/LC3 to facilitate degradation of ubiquitinated protein aggregates by autophagy*[S]," *Journal of Biological Chemistry,* vol. 282, pp. 24131-24145, 2007.

[106] S. I. W. H. P. B. M. A. W. E. M. Ondrus and J. D. Bois, "Fluorescent Saxitoxins for Live Cell Imaging of Single Voltage- Gated Sodium Ion Channels beyond the Optical Diffraction Limit," *Chem Biol,* vol. 19, pp. 902-912, 2012.

[107] J. M. Oliver H. Weiergräber and D. Willbold, "We are IntechOpen , the world ' s leading publisher of Open Access books Built by scientists , for scientists TOP 1 %," *Long-Haul Travel Motivation by International Tourist to Penang,* vol. i, p. 13, 2018.

[108] K. Obara, T. Sekito, K. Niimi and Y. Ohsumi, "The Atg18-Atg2 complex is recruited to autophagic membranes via phosphatidylinositol 3-phosphate and exerts an essential function," *Journal of Biological Chemistry,* vol. 283, pp. 23972-23980, 2008.

[109] S. Nowotschin and A. K. Hadjantonakis, "Use of KikGR a photoconvertible green-to-red fluorescent protein for cell labeling and lineage analysis in ES cells and mouse embryos," *BMC Developmental Biology,* vol. 9, pp. 1-12, 2009.

[110] T. Noda, C. Tokunaga, Y. Ohsumi, J. Kim, W.-P. Huang, D. J. Klionsky and M. Baba, "Apg9p/Cvt7p is an integral membrane protein required for transport vesicle formation in the Cvt and autophagy pathways," *Journal of Cell Biology,* vol. 148, pp. 465-479, 2000.

[111] N. N. Noda, Y. Fujioka, T. Hanada, Y. Ohsumi and F. Inagaki, "Structure of the Atg12-Atg5 conjugate reveals a platform for stimulating Atg8-PE conjugation," *EMBO Reports,* vol. 14, pp. 206-211, 2013.

[112] J. D. Nicolas, M. Bernhardt, S. F. Schlick, M. Tiburcy, W. H. Zimmermann, A. Khan, A. Markus, F. Alves, K. Toischer and T. Salditt, "X-ray diffraction imaging of cardiac cells and tissue," *Progress in Biophysics and Molecular Biology,* vol. 144, pp. 151-165, 2019.

[113] T. N. Nguyen, B. S. Padman, J. Usher, V. Oorschot, G. Ramm and M. Lazarou, "Atg8 family LC3/GAB ARAP proteins are crucial for autophagosome-lysosome fusion but not autophagosome formation during PINK1/Parkin mitophagy and starvation," *Journal of Cell Biology,* vol. 215, pp. 857-874, 2016.

[114] N. Nguyen, V. Shteyn and T. J. Melia, "Sensing Membrane Curvature in Macroautophagy," *Journal of Molecular Biology,* vol. 429, pp. 457-472, 2017.

[115] A. C. Nascimbeni, F. Giordano, N. Dupont, D. Grasso, M. I. Vaccaro, P. Codogno and E. Morel, "ER–plasma membrane contact sites contribute to autophagosome biogenesis by regulation of local PI3P synthesis," *The EMBO Journal,* vol. 36, pp. 2018-2033, 2017.

[116] H. Nakatogawa, K. Suzuki, Y. Kamada and Y. Ohsumi, "Dynamics and diversity in autophagy mechanisms: Lessons from yeast," *Nature Reviews Molecular Cell Biology,* vol. 10, pp. 458-467, 2009.

[117] S. Nakamura and T. Yoshimori, "New insights into autophagosome–lysosome fusion," *Journal of Cell Science,* vol. 130, pp. 1209-1216, 2017.

[118] U. Nair, W. L. Yen, M. Mari, Y. Cao, Z. Xie, M. Baba, F. Reggiori and D. J. Klionsky, "A role for Atg8-PE deconjugation in autophagosome biogenesis," *Autophagy,* vol. 8, pp. 780-793, 2012.

[119] A. L. Morgado, J. M. Xavier, P. A. Dionísio, M. F. C. Ribeiro, R. B. Dias, A. M. Sebastião, S. Solá and C. M. P. Rodrigues, "MicroRNA-34a Modulates Neural Stem Cell Differentiation by Regulating Expression of Synaptic and Autophagic Proteins," *Molecular Neurobiology,* vol. 51, pp. 1168-1183, 2015.

[120] M. Mnisky, "Dec. 19, 1961 M. MNSKY," *United States Patent Office,* 1961.

[121] N. Mizushima, T. Yoshimori and Y. Ohsumi, "The Role of Atg Proteins in Autophagosome Formation," *Annual Review of Cell and Developmental Biology,* vol. 27, pp. 107-132, 2011.

[122] N. Mizushima, Y. Kobayashi, Y. Kabey, K. Suzuki, Y. Ohsumi, T. Yoshimori, A. Yamamoto, M. Hatano and T. Tokuhis, "Dissection of autophagosome formation using Apg5-deficient mouse

embryonic stem cells," *Journal of Cell Biology,* vol. 152, pp. 657-667, 2001.

[123] N. Mizushima, T. Noda and Y. Ohsumi, "Apg16p is required for the function of the Apg12p-Apg5p conjugate in the yeast autophagy pathway," *EMBO Journal,* vol. 18, pp. 3888-3896, 1999.

[124] N. Mizushima, T. Noda, T. Yoshimori, Y. Tanaka, T. Ishii, M. D. George, D. J. Klionsky, M. Ohsumi and Y. Ohsumi, "A protein conjugation system essential for autophagy.," *Nature,* vol. 395, pp. 395-8, 1998.

[125] H. Mizuno, P. Dedecker, R. Ando, T. Fukano, J. Hofkens and A. Miyawaki, "Higher resolution in localization microscopy by slower switching of a photochromic protein," *Photochemical and Photobiological Sciences,* vol. 9, pp. 239-248, 2010.

[126] M. Minsky, "Memoir on Inventing the Confocal Scanning Microscope," *Scanning,* vol. 10, pp. 128-138, 1987.

[127] X. Michalet, R. A. Colyer, G. Scalia, A. Ingargiola, R. Lin, J. E. Millaud, S. Weiss, O. H. W. Siegmund, A. S. Tremsin, J. V. Vallerga, A. Cheng, M. Levi, D. Aharoni, K. Arisaka, F. Villa, F. Guerrieri, F. Panzeri, I. Rech, A. Gulinatti, F. Zappa, M. Ghioni and S. Cova, "Development of new photon-counting detectors for single-molecule fluorescence microscopy," *Philosophical Transactions of the Royal Society B: Biological Sciences,* vol. 368, 2013.

[128] S. Michaeli, G. Galili, P. Genschik, A. R. Fernie and T. Avin-Wittenberg, "Autophagy in Plants - What's New on the Menu?," *Trends in Plant Science,* vol. 21, pp. 134-144, 2016.

[129] N. Mi, Y. Chen, S. Wang, M. Chen, M. Zhao, G. Yang, M. Ma, Q. Su, S. Luo, J. Shi, J. Xu, Q. Guo, N. Gao, Y. Sun, Z. Chen and L. Yu, "CapZ regulates autophagosomal membrane shaping by promoting actin assembly inside the isolation membrane," *Nature Cell Biology,* vol. 17, pp. 1112-1123, 2015.

[130] C. W. Merkle, S. P. Chong, A. M. Kho, J. Zhu, A. Dubra and V. J. Srinivasan, "Visible light optical coherence microscopy of the brain with isotropic femtoliter resolution in vivo," vol. 25, pp. 1032-1057, 2018.

[131] M. A. Mena, T. P. Treynor, S. L. Mayo and P. S. Daugherty, "enhanced brightness and targeted library," vol. 24, pp. 1569-1571, 2006.

[132] S. A. McKinney, C. S. Murphy, K. L. Hazelwood, M. W. Davidson and L. L. Looger, "A bright and photostable photoconvertible fluorescent protein," *Nature Methods,* vol. 6, pp. 131-133, 2009.

[133] A. L. McEvoy, H. Hoi, M. Bates, E. Platonova, P. J. Cranfill, M. A. Baird, M. W. Davidson, H. Ewers, J. Liphardt and R. E. Campbell, "mMaple: A Photoconvertible Fluorescent Protein for Use in Multiple Imaging Modalities," *PLoS ONE,* vol. 7, 2012.

[134] C. Mauvezin, P. Nagy, G. Juhász and T. P. Neufeld, "Autophagosome-lysosome fusion is

independent of V-ATPase-mediated acidification," *Nature Communications,* vol. 6, 2015.

[135] M. Mauthe and F. Reggiori, "ATG proteins: Are we always looking at autophagy?," *Autophagy,* vol. 12, pp. 2502-2503, 2016.

[136] O. S. Matusovsky, A. Mansson, M. Persson, Y.-S. Cheng and D. E. Rassier, "High-speed AFM reveals subsecond dynamics of cardiac thin filaments upon Ca 2+ activation and heavy meromyosin binding," *Proceedings of the National Academy of Sciences,* vol. 116, pp. 16384-16393, 2019.

[137] A. L. Mattheyses, S. M. Simon and J. Z. Rappoport, "Imaging with total internal reflection fluorescence microscopy for the cell biologist," *Journal of Cell Science,* vol. 123, pp. 3621-3628, 2010.

[138] T. Matsuda, A. Miyawaki and T. Nagai, "Direct measurement of protein dynamics inside cells using a rationally designed photoconvertible protein," *Nature Methods,* vol. 5, pp. 339-345, 2008.

[139] V. I. Martynov, A. A. Pakhomov, N. V. Popova, I. E. Deyev and A. G. Petrenko, "Synthetic Fluorophores for Visualizing Biomolecules in Living Systems," *Acta Naturae,* vol. 8, pp. 33-46, 2016.

[140] D. Marion, "An introduction to biological NMR spectroscopy," *Molecular and Cellular Proteomics,* vol. 12, pp. 3006-3025, 2013.

[141] D. T. Luu, A. Martiniãre, M. Sorieul, J. Runions and C. Maurel, "Fluorescence recovery after photobleaching reveals high cycling dynamics of plasma membrane aquaporins in Arabidopsis roots under salt stress," *Plant Journal,* vol. 69, pp. 894-905, 2012.

[142] X. Luo, L. Qian, Y. Xiao, Y. Tang, Y. Zhao, X. Wang, L. Gu, Z. Lei, J. Bao, J. Wu, T. He, F. Hu, J. Zheng, H. Li, W. Zhu, L. Shao, X. Dong, D. Chen, X. Qian and Y. Yang, "A diversity-oriented rhodamine library for wide-spectrum bactericidal agents with low inducible resistance against resistant pathogens," *Nature Communications,* vol. 10, 2019.

[143] A. Loudet and K. Burgess, "BODIPY dyes and their derivatives: Syntheses and spectroscopic properties," *Chemical Reviews,* vol. 107, pp. 4891-4932, 2007.

[144] A. Löschberger, S. Linde, M. C. Dabauvalle, B. Rieger, M. Heilemann, G. Krohne and M. Sauer, "Super-resolution imaging visualizes the eightfold symmetry of gp210 proteins around the nuclear pore complex and resolves the central channel with nanometer resolution," *Journal of Cell Science,* vol. 125, pp. 570-575, 2012.

[145] S. Lord Rayleigh Sec. R., "On the theory of optical images, with special reference to the microscope," *The London, Edinburgh, and Dublin Philosophical Magazine and Journal of Science,* vol. 42, pp. 167-195, 1896.

[146] Lische, Methods and protocols, vol. 47, 2005, pp. 407-421.

[147] L. Li, Z. V. Wang, J. A. Hill and F. Lin, "New autophagy reporter mice reveal dynamics of proximal tubular autophagy," *Journal of the American Society of Nephrology,* vol. 25, pp. 305-315, 2014.

[148] K. Li, W. Qin, D. Ding, N. Tomczak, J. Geng, R. Liu, J. Liu, X. Zhang, H. Liu, B. Liu and B. Z. Tang, "Photostable fluorescent organic dots with aggregation-induced emission (AIE dots) for noninvasive long-term cell tracing," *Scientific Reports,* vol. 3, pp. 1-10, 2013.

[149] M. D. Lew, S. F. Lee, J. L. Ptacin, M. K. Lee, R. J. Twieg, L. Shapiro and W. E. Moerner, "Three-dimensional superresolution colocalization of intracellular protein superstructures and the cell surface in live Caulobacter crescentus," *Proceedings of the National Academy of Sciences,* vol. 108, pp. E1102--E1110, 2011.

[150] C. Leterrier, P. Dubey and S. Roy, "The nano-architecture of the axonal cytoskeleton," *Nature Reviews Neuroscience,* vol. 18, pp. 713-726, 2017.

[151] M. Lelimousin, M. Noirclerc-savoye, C. Lazareno-saez, B. Paetzold, S. L. Vot, R. Chazal, P. Macheboeuf, M. J. Field, D. Bourgeois and A. Royant, "Intrinsic Dynamics in ECFP and Cerulean Control Fluorescence Quantum Yield †," pp. 10038-10046, 2009.

[152] R. J. T. J. R. Lee M.K and W. E. Moernera, "Enzymatic activation of nitro-aryl fluorogens in live bacterial cells for enzymatic turnover-activated localization microscopy," *Chem Sci,* vol. 42, pp. 220-225, 2013.

[153] S. F. Lee, M. A. Thompson, M. A. Schwartz, L. Shapiro and W. E. Moerner, "Super-resolution imaging of the nucleoid-associated protein HU in Caulobacter crescentus," *Biophysical Journal,* vol. 100, pp. L31--L33, 2011.

[154] L. D. Lavis and R. T. Raines, "Bright ideas for chemical biology-supplement," *ACS chemical biology,* vol. 3, pp. 142-55, 2008.

[155] L. D. Lavis and R. T. Raines, "Bright building blocks for chemical biology," *ACS Chemical Biology,* vol. 9, pp. 855-866, 2014.

[156] C. Laurent, L. Ricard, I. Buvat, O. Fain, A. Mekinian and M. Soussan, "AB0652 Pet/mr in large-vessel vasculitis: clinical value for the diagnosis and assessment of disease activity," pp. 1471.3--1472, 2018.

[157] A. Landajuela, J. H. Hervás, Z. Antón, L. R. Montes, D. Gil, M. Valle, J. F. Rodriguez, F. M. Goñi and A. Alonso, "Lipid Geometry and Bilayer Curvature Modulate LC3/GABARAP-Mediated Model Autophagosomal Elongation," *Biophysical Journal,* vol. 110, pp. 411-422, 2016.

[158] C. A. Lamb, J. Joachim and S. A. Tooze, Quantifying Autophagic Structures in Mammalian Cells Using Confocal Microscopy, 1 ed., vol. 587, Elsevier Inc., 2017, pp. 21-42.

[159] J. R. Lakowicz, Principles of fluorescence spectroscopy, 3rd Edition, Joseph R. Lakowicz, editor, 2006, p. 954.

[160] S. Kumar, J. Jia, Y. Gu, S. W. Choi, M. H. Mudd, A. Claude-Taupin, V. Deretic, A. Jain, T.-E. Rusten, F. Farzam, K. A. Lidke and M. J. Wester, "Mechanism of Stx17 recruitment to autophagosomes via IRGM and mammalian Atg8 proteins," *Journal of Cell Biology,* vol. 217, pp. 997-1013, 2018.

[161] H. Kuhn, "A quantum-mechanical theory of light absorption of organic dyes and similar compounds," *The Journal of Chemical Physics,* vol. 17, pp. 1198-1212, 1949.

[162] I. Koyama-Honda, E. Itakura, T. K. Fujiwara and N. Mizushima, "Temporal analysis of recruitment of mammalian ATG proteins to the autophagosome formation site," *Autophagy,* vol. 9, pp. 1491-1499, 2013.

[163] M. I. Koukourakis, D. Kalamida, A. Giatromanolaki, C. E. Zois, E. Sivridis, S. Pouliliou, A. Mitrakas, K. C. Gatter and A. L. Harris, "Autophagosome proteins LC3A, LC3B and LC3C have distinct subcellular distribution kinetics and expression in cancer cell lines," *PLoS ONE,* vol. 10, pp. 1-13, 2015.

[164] T. Kotani, H. Kirisako, M. Koizumi, Y. Ohsumi and H. Nakatogawa, "The Atg2-Atg18 complex tethers pre-autophagosomal membranes to the endoplasmic reticulum for autophagosome formation," *Proceedings of the National Academy of Sciences,* vol. 115, pp. 10363-10368, 2018.

[165] Koana, "Confocal Microscopy," *Journal of the Illumination Engineering Institute,* vol. 26, pp. 371-385, 1942.

[166] R. L. Knorr, H. Nakatogawa, Y. Ohsumi, R. Lipowsky, T. Baumgart and R. Dimova, "Membrane morphology is actively transformed by covalent binding of the protein Atg8 to PE-lipids," *PLoS ONE,* vol. 9, pp. 1-14, 2014.

[167] R. L. Knorr, R. Dimova and R. Lipowsky, "Curvature of double-membrane organelles generated by changes in membrane size and composition," *PLoS ONE,* vol. 7, 2012.

[168] D. J. Klionsky, Z. Elazar, P. O. Seglen and D. C. Rubinsztein, "Does bafilomycin A 1 block the fusion of autophagosomes with lysosomes?," *Autophagy,* vol. 4, pp. 849-850, 2008.

[169] N. V. Klementieva, K. A. Lukyanov, N. M. Markina, S. A. Lukyanov, E. V. Zagaynova and A. S. Mishin, "Green-to-red primed conversion of Dendra2 using blue and red lasers," *Chemical Communications,* vol. 52, pp. 13144-13146, 2016.

[170] T. A. Klar, S. Jakobs, M. Dyba, A. Egner and S. W. Hell, "Fluorescence microscopy with diffraction resolution barrier broken by stimulated emission," *Proceedings of the National Academy of Sciences of the United States of America,* vol. 97, pp. 8206-8210, 2000.

[171] T. Kirisako, Y. Ichimura, H. Okada, Y. Kabeya, N. Mizushima, T. Yoshimori, M. Ohsumi, T. Takao, T. Noda and Y. Ohsumi, "The reversible modification regulates the membrane-binding state of

Apg8/Aut7 essential for autophagy and the cytoplasm to vacuole targeting pathway," *Journal of Cell Biology,* vol. 151, pp. 263-275, 2000.

[172] J. Kim, M. Kundu, B. Viollet and K. L. Guan, "AMPK and mTOR regulate autophagy through direct phosphorylation of Ulk1," *Nature Cell Biology,* vol. 13, pp. 132-141, 2011.

[173] Kevin Range and D. M. Y. A. Moser, "基因的改变NIH Public Access," *Bone,* vol. 23, pp. 1-7, 2012.

[174] A. Kaufmann, V. Beier, H. G. Franquelim and T. Wollert, "Molecular mechanism of autophagic membrane-scaffold assembly and disassembly," *Cell,* vol. 156, pp. 469-481, 2014.

[175] T. Kato, R. P. Goodman, C. M. Erben, A. J. Turberfield and K. Namba, "High-resolution structural analysis DNA nanostructure by cryoEM," *Nano Letters,* vol. 9, pp. 2747-2750, 2009.

[176] D. J. Kast and R. Dominguez, "The Cytoskeleton–Autophagy Connection," *Current Biology,* vol. 27, pp. R318--R326, 2017.

[177] J. K. G. Karlsson, O. J. Woodford, H. Mustroph and A. Harriman, "Cyanine dyes as ratiometric fluorescence standards for the far-red spectral region," *Photochemical and Photobiological Sciences,* vol. 17, pp. 99-106, 2018.

[178] S. Karasawa, T. Araki, M. Yamamoto-Hino and A. Miyawaki, "A Green-emitting Fluorescent Protein from Galaxeidae Coral and Its Monomeric Version for Use in Fluorescent Labeling," *Journal of Biological Chemistry,* vol. 278, pp. 34167-34171, 2003.

[179] E. Karanasios, S. A. Walker, H. Okkenhaug, M. Manifava, E. Hummel, H. Zimmermann, Q. Ahmed, M. C. Domart, L. Collinson and N. T. Ktistakis, "Autophagy initiation by ULK complex assembly on ER tubulovesicular regions marked by ATG9 vesicles," *Nature Communications,* vol. 7, pp. 1-17, 2016.

[180] A. M. P. E. B. R. M. Kanchanawong, W. Davidson and C. M. Waterman, "Nanoscale architecture of integrin-based cell adhesions," *Nature,* vol. 468, 2010.

[181] C. H. Jung, C. B. Jun, S.-h. Ro, Y.-m. Kim, N. M. Otto, J. Cao, M. Kundu and D.-h. Kim, "ULK-Atg13-FIP200 Complexes Mediate mTOR Signaling to the Autophagy Machinery," vol. 20, pp. 1992-2003, 2009.

[182] F. M. Jradi and L. D. Lavis, "Chemistry of Photosensitive Fluorophores for Single-Molecule Localization Microscopy," *ACS Chemical Biology,* vol. 14, pp. 1077-1090, 2019.

[183] T. Johansen and T. Lamark, "Selective Autophagy: ATG8 Family Proteins, LIR Motifs and Cargo Receptors," *Journal of Molecular Biology,* 2019.

[184] J. Joachim, H. B. J. Jefferies, M. Razi, D. Frith, A. P. Snijders, P. Chakravarty, D. Judith and S. A. Tooze, "Activation of ULK Kinase and Autophagy by GABARAP Trafficking from the Centrosome Is Regulated by WAC and GM130," *Molecular Cell,* vol. 60, pp. 899-913, 2015.

[185] E. C. G. E. T. M. E. L. R. C. W. E. M. Jerod L. Ptacin1 and L. Shapiro1, "A spindle-like apparatus guides bacterial chromosome segregation," *Nat Cell Biol.,* vol. 12, pp. 791-798, 2010.

[186] A. B. Jaykumar, P. S. Caceres, I. Sablaban, B. A. Tannous and P. A. Ortiz, "Real-time monitoring of NKCC2 endocytosis by total internal reflection fluorescence (TIRF) microscopy," *American Journal of Physiology - Renal Physiology,* vol. 310, pp. F183--F191, 2016.

[187] M. S. Islam, M. Honma, T. Nakabayashi, M. Kinjo and N. Ohta, "pH dependence of the fluorescence lifetime of FAD in solution and in cells," *International Journal of Molecular Sciences,* vol. 14, pp. 1952-1963, 2013.

[188] T. Into, T. Horie, M. Inomata, J. Gohda, J. I. Inoue, Y. Murakami and S. Niida, "Basal autophagy prevents autoactivation or enhancement of inflammatory signals by targeting monomeric MyD88 /631/80/39 /631/80/86/2366 /631/250/516 /13/21 /13/89 /13/95 /13/109 /14/19 /38/77 /38/90 /82/80 /38/44 article," *Scientific Reports,* vol. 7, pp. 1-14, 2017.

[189] Ina Nemet and Y. Imanishi, "Applications of phototransformable fluorescent proteins for tracking dynamics of cellular components," *Photochem Photobiol Sci.,* vol. 14, pp. 1787-1806, 2015.

[190] T. T. Ichimura, N. I. Yoshinori Satomi, M. O. Noboru Mizushima and T. N. Y. Ohsumi, "Mediates, A ubiquitin-like system protein lipidation," *Nature,* vol. 408, pp. 488-492, 2000.

[191] L. P. Icart, E. Fernandes, L. Agüero, J. Ramón, D. Zaldivar and M. L. Dias, "Fluorescent microspheres of poly(ethylene glycol)-poly(lactic acid)-fluorescein copolymers synthesized by Ugi four-component condensation," *Journal of Applied Polymer Science,* vol. 133, pp. 1-9, 2016.

[192] Y. L. N. Hurley J. H., "Mechanisms of Autophagy," *Annual Review of Biophysics,* vol. 44, pp. 101-122, 2015.

[193] R. Huang, Y. Xu, W. Wan, X. Shou, J. Qian, Z. You, B. Liu, C. Chang, T. Zhou, J. Lippincott-Schwartz and W. Liu, "Deacetylation of nuclear LC3 drives autophagy initiation under starvation," *Molecular Cell,* vol. 57, pp. 456-466, 2015.

[194] N. Hosokawa, T. Hara, T. Kaizuka, C. Kishi, A. Takamura, Y. Miura, S.-i. Iemura, T. Natsume, K. Takehana, N. Yamada, J.-L. Guan, N. Oshiro and N. Mizushima, "Novel Roles of Hakai in Cell Proliferation and Oncogenesis," *Molecular Biology of the Cell,* vol. 20, pp. 1981-1991, 2008.

[195] H. Hoi, N. C. Shaner, M. W. Davidson, C. W. Cairo, J. Wang and R. E. Campbell, "A Monomeric Photoconvertible Fluorescent Protein for Imaging of Dynamic Protein Localization," *Journal of Molecular Biology,* vol. 401, pp. 776-791, 2010.

[196] S. T. Hess, T. P. K. Girirajan and M. D. Mason, "Ultra-high resolution imaging by fluorescence photoactivation localization microscopy," *Biophysical Journal,* vol. 91, pp. 4258-4272, 2006.

[197] A. Hense, K. Nienhaus and G. U. Nienhaus, "Exploring color tuning strategies in red fluorescent

proteins," *Photochemical and Photobiological Sciences,* vol. 14, pp. 200-212, 2015.

[198] J. N. Henderson, H. W. Ai, R. E. Campbell and S. J. Remington, "Structural basis for reversible photobleaching of a green fluorescent protein homologue," *Proceedings of the National Academy of Sciences of the United States of America,* vol. 104, pp. 6672-6677, 2007.

[199] R. Heintzmann and T. Huser, "Super-Resolution Structured Illumination Microscopy," *Chemical Reviews,* vol. 117, pp. 13890-13908, 2017.

[200] B. Hein, K. I. Willig and S. W. Hell, "Stimulated emission depletion (STED) nanoscopy of a fluorescent protein-labeled organelle inside a living cell," *Proceedings of the National Academy of Sciences of the United States of America,* vol. 105, pp. 14271-14276, 2008.

[201] R. Heim and R. Y. Tsien, "Engineering green fluorescent protein for improved brightness , longer wavelengths and fluorescence resonance energy transfer," pp. 178-182.

[202] M. Heilemann, S. Van De Linde, A. Mukherjee and M. Sauer, "Super-resolution imaging with small organic fluorophores," *Angewandte Chemie - International Edition,* vol. 48, pp. 6903-6908, 2009.

[203] M. Heilemann, S. Van De Linde, M. Schüttpelz, R. Kasper, B. Seefeldt, A. Mukherjee, P. Tinnefeld and M. Sauer, "Subdiffraction-resolution fluorescence imaging with conventional fluorescent probes," *Angewandte Chemie - International Edition,* vol. 47, pp. 6172-6176, 2008.

[204] C. He and K. J. Daniel, "Regulation Mechanisms and Signaling Pathways of Autophagy," *Annual review of Genetics,* vol. 43, pp. 67-93, 2010.

[205] T. Hara, A. Takamura, C. Kishi, S. I. Iemura, T. Natsume, J. L. Guan and N. Mizushima, "FIP200, a ULK-interacting protein, is required for autophagosome formation in mammalian cells," *Journal of Cell Biology,* vol. 181, pp. 497-510, 2008.

[206] T. Hanada, N. N. Noda, Y. Satomi, Y. Ichimura, Y. Fujioka, T. Takao, F. Inagaki and Y. Ohsumi, "The Atg12-Atg5 conjugate has a novel E3-like activity for protein lipidation in autophagy," *Journal of Biological Chemistry,* vol. 282, pp. 37298-37302, 2007.

[207] S. Hadipour-Lakmehsari, A. Driouchi, S. H. Lee, U. Kuzmanov, N. I. Callaghan, S. P. Heximer, C. A. Simmons, C. M. Yip and A. O. Gramolini, "Nanoscale reorganization of sarcoplasmic reticulum in pressure-overload cardiac hypertrophy visualized by dSTORM," *Scientific reports,* vol. 9, p. 7867, 2019.

[208] S. Habuchi, P. Dedecker, J. I. Hotta, C. Flors, R. Ando, H. Mizuno, A. Miyawaki and J. Hofkens, "Photo-induced protonation/deprotonation in the GFP-like fluorescent protein Dronpa: Mechanism responsible for the reversible photoswitching," *Photochemical and Photobiological Sciences,* vol. 5, pp. 567-576, 2006.

[209] S. Habuchi, H. Tsutsui, A. B. Kochaniak, A. Miyawaki and A. M. Oijen, "mKikGR, a monomeric

photoswitchable fluorescent protein," *PLoS ONE,* vol. 3, pp. 1-9, 2008.

[210] M. G. L. Gustafsson, "Surpassing the lateral resolution limit by a factor of two using structured illumination microscopy," *Journal of Microscopy,* vol. 198, pp. 82-87, 2000.

[211] N. G. Gurskaya, V. V. Verkhusha, A. S. Shcheglov, D. B. Staroverov, T. V. Chepurnykh, A. F. Fradkov, S. Lukyanov and K. A. Lukyanov, "Engineering of a monomeric green-to-red photoactivatable fluorescent protein induced by blue light," vol. 24, pp. 461-465, 2006.

[212] M. S. Gunewardene, F. V. Subach, T. J. Gould, G. P. Penoncello, M. V. Gudheti, V. V. Verkhusha and S. T. Hess, "Superresolution imaging of multiple fluorescent proteins with highly overlapping emission spectra in living cells," *Biophysical Journal,* vol. 101, pp. 1522-1528, 2011.

[213] P. Grumati and I. Dikic, "Ubiquitin signaling and autophagy," *Journal of Biological Chemistry,* vol. 293, pp. 5404-5413, 2018.

[214] T. Grotjohann, I. Testa, M. Reuss, T. Brakemann, C. Eggeling, S. W. Hell and S. Jakobs, "rsEGFP2 enables fast RESOLFT nanoscopy of living cells," *eLife,* vol. 2012, pp. 1-14, 2012.

[215] T. Grotjohann, I. Testa, M. Leutenegger, H. Bock, N. T. Urban, F. Lavoie-Cardinal, K. I. Willig, C. Eggeling, S. Jakobs and S. W. Hell, "Diffraction-unlimited all-optical imaging and writing with a photochromic GFP," *Nature,* vol. 478, pp. 204-208, 2011.

[216] L. A. Gross, G. S. Baird, R. C. Hoffman, K. K. Baldridge and R. Y. Tsien, "The structure of the chromophore within DsRed, a red fluorescent protein from coral," *Proceedings of the National Academy of Sciences of the United States of America,* vol. 97, pp. 11990-11995, 2000.

[217] D. Greenfield, A. L. McEvoy, H. Shroff, G. E. Crooks, N. S. Wingreen, E. Betzig and J. Liphardt, "Self-organization of the Escherichia coli chemotaxis network imaged with super-resolution light microscopy," *PLoS Biology,* vol. 7, 2009.

[218] F. L. GRAHAM and J. SMILEY, "Characteristics of a human cell line transformed by DNA from human adenovirus type 5," *Journal of General Virology,* vol. 36, pp. 59-72, 1977.

[219] M. Graef, J. R. Friedman, C. Graham, M. Babu and J. Nunnari, "ER exit sites are physical and functional core autophagosome biogenesis components," *Molecular Biology of the Cell,* vol. 24, pp. 2918-2931, 2013.

[220] B. Gottschalk, C. Klec, G. Leitinger, E. Bernhart, R. Rost, H. Bischof, C. T. Madreiter-Sokolowski, S. Radulović, E. Eroglu, W. Sattler, M. Waldeck-Weiermair, R. Malli and W. F. Graier, "MICU1 controls cristae junction and spatially anchors mitochondrial Ca2+ uniporter complex," *Nature Communications,* vol. 10, pp. 1-17, 2019.

[221] Goldmann, "Kopie von subito e.V., geliefert für Forschungszentrum Juelich GmbH (SLS02X00112)," *Ophtalmologiea,* vol. 98, pp. 257-270, 1940.

[222] H. M. Genau, J. Huber, F. Baschieri, M. Akutsu, V. Dötsch, H. Farhan, V. Rogov and C. Behrends,

"CUL3-KBTBD6/KBTBD7Ubiquitin Ligase Cooperates with GABARAP Proteins to Spatially Restrict TIAM1-RAC1 Signaling," *Molecular Cell,* vol. 57, pp. 995-1010, 2015.

[223] D. Gatica, V. Lahiri and D. J. Klionsky, "Cargo recognition and degradation by selective autophagy," *Nature Cell Biology,* vol. 20, pp. 233-242, 2018.

[224] I. G. Ganley, D. H. Lam, J. Wang, X. Ding, S. Chen and X. Jiang, "ULK1ATG13FIP200 complex mediates mTOR signaling and is essential for autophagy," *Journal of Biological Chemistry,* vol. 284, pp. 12297-12305, 2009.

[225] H.-J. Galla, "Spektroskopische Methoden in der Biochemie," pp. IX, 147 S., 1988.

[226] C. G. Galbraith and J. A. Galbraith, "Super-resolution microscopy at a glance," *Journal of Cell Science,* vol. 124, pp. 1607-1611, 2011.

[227] A. Gahlmann, J. L. Ptacin, G. Grover, S. Quirin, A. R. S. Von Diezmann, M. K. Lee, M. P. Backlund, L. Shapiro, R. Piestun and W. E. Moerner, "Quantitative multicolor subdiffraction imaging of bacterial protein ultrastructures in three dimensions," *Nano Letters,* vol. 13, pp. 987-993, 2013.

[228] N. Fujita, M. F. ‡. T. N. Takashi Itoh and T. Yoshimori, "The Atg16L Complex Specifies the Site of LC3 Lipidation for Membrane Biogenesis in Autophagy Naonobu," *Molecular biology of the cell,* vol. 19, pp. 2092-2100, 2008.

[229] Y. Fujioka, N. N. Noda, K. Fujii, K. Yoshimoto, Y. Ohsumi and F. Inagaki, "In vitro reconstitution of plant Atg8 and Atg12 conjugation systems essential for autophagy," *Journal of Biological Chemistry,* vol. 283, pp. 1921-1928, 2008.

[230] Förster, "Zwischenmolekulare Energiewanderung und Fluoreszenz," *Annalen. der. Physik,* vol. 6, pp. 55-75, 1948.

[231] K. N. Fish, "Total Internal Reflection Fluorescence (TIRF) Microscopy," *Curr Protoc Cytom,* vol. 12, 2009.

[232] N. Feiner-Gracia, M. Beck, S. Pujals, S. Tosi, T. Mandal, C. Buske, M. Linden and L. Albertazzi, "Super-Resolution Microscopy Unveils Dynamic Heterogeneities in Nanoparticle Protein Corona," *Small,* vol. 13, pp. 1-11, 2017.

[233] G. Fazeli and A. M. Wehman, "Safely removing cell debris with LC3-associated phagocytosis," *Biology of the Cell,* vol. 109, pp. 355-363, 2017.

[234] J. Falco, C. Cavallo, I. G. Vetrano, C. Laurentis, L. Siozos, M. Schiariti, M. Broggi, P. Ferroli and F. Acerbi, "Fluorescein Application in Cranial and Spinal Tumors Enhancing at Preoperative MRI and Operated With a Dedicated Filter on the Surgical Microscope: Preliminary Results in 279 Patients Enrolled in the FLUOCERTUM Prospective Study," *Frontiers in Surgery,* vol. 6, pp. 1-13, 2019.

[235] U. Endesfelder, S. Linde, S. Wolter, M. Sauer and M. Heilemann, "Subdiffraction-resolution

fluorescence microscopy of myosin-actin motility," *ChemPhysChem,* vol. 11, pp. 836-840, 2010.

[236] 2. L. U. C. I. E. N. E. W. E. I. S. S. 2. T. O. M. E. R. M. I. C. H. A. E. L. I. 1. ELIAS NEHME and Y. O. A. V. SHECHTMAN2, "Deep-STORM: super-resolution single-molecule microscopy by deep learning," vol. 5, 2018.

[237] D. F. Egan, D. B. Shackelford, M. M. Mihaylova, S. Gelino, R. a. Kohnz, W. Mair, D. S. Vasquez, A. Joshi, D. M. Gwinn, R. Taylor, J. M. Asara, J. Fitzpatrick, A. Dillin, B. Viollet, M. Kundu, M. Hansen and R. J. Shaw, "Energy Sensing to Mitophagy," *Science,* vol. 331, pp. 456-461, 2010.

[238] Efe and S. D. Emr, "Atg18 Regulates Organelle Morphology and Fab1 Kinase Activity Independent of Its Membrane Recruitment by Phosphatidylinositol 3,5-Bisphosphate," *Molecular Biology of the Cell,* vol. 18, pp. 4232-4244, 2007.

[239] M. Dyba, S. Jakobs and S. W. Hell, "Immunofluorescence stimulated emission depletion microscopy," *Nature Biotechnology,* vol. 21, pp. 1303-1304, 2003.

[240] K. Dunster, B. H. Toh and J. W. Sentry, "Early endosomes, late endosomes, and lysosomes display distinct partitioning strategies of inheritance with similarities to Golgi-derived membranes," *European Journal of Cell Biology,* vol. 81, pp. 117-124, 2002.

[241] W. C. Duim, Y. Jiang, K. Shen, J. Frydman and W. E. Moerner, "Super-resolution fluorescence of huntingtin reveals growth of globular species into short fibers and coexistence of distinct aggregates," *ACS Chemical Biology,* vol. 9, pp. 2767-2778, 2014.

[242] S. K. Dove, R. C. Piper, R. K. McEwen, J. W. Yu, N. C. King, D. C. Hughes, J. Thuring, A. B. Holmes, F. T. Cooke, R. H. Michell, P. J. Parker and M. A. Lemmon, "Svp1p defines a family of phosphatidylinositol 3,5-bisphosphate effectors," *EMBO Journal,* vol. 23, pp. 1922-1933, 2004.

[243] I. Dikic and Z. Elazar, "Mechanism and medical implications of mammalian autophagy," *Nature Reviews Molecular Cell Biology,* vol. 19, pp. 349-364, 2018.

[244] R. M. Dickson, A. B. Cubittt, R. Y. Tsient and W. E. Moerner, "On/off blinking and switching behaviour of single molecules of green fluorescent protein," *Nature,* vol. 388, pp. 355-358, 1997.

[245] R. N. Day and M. W. Davidson, "The Fluorescent protein palette," *Online,* vol. 366, pp. 1772-1775, 2007.

[246] P. Davidovits and M. D. Egger, "Scanning laser microscope," *Nature,* vol. 223, p. 831, 1969.

[247] A. Dani, B. Huang, J. Bergan, C. Dulac and X. Zhuang, "Superresolution Imaging of Chemical Synapses in the Brain," *Neuron,* vol. 68, pp. 843-856, 2010.

[248] J. Dancourt and T. J. Melia, "Lipidation of the autophagy proteins LC3 and GABARAP is a membrane-curvature dependent process," *Autophagy,* vol. 10, pp. 1470-1471, 2014.

[249] T. D. Craggs, "Green fluorescent protein: Structure, folding and chromophore maturation," *Chemical Society Reviews,* vol. 38, pp. 2865-2875, 2009.

[250] S. Cox, E. Rosten, J. Monypenny and T. Jovanovic-talisman, "UKPMC Funders Group Bayesian localisation microscopy reveals nanoscale podosome dynamics," *Nature Methods,* vol. 9, pp. 195-200, 2012.

[251] L. M. Costantini, M. Baloban, M. L. Markwardt, M. Rizzo, F. Guo, V. V. Verkhusha and E. L. Snapp, "A palette of fluorescent proteins optimized for diverse cellular environments," *Nature Communications,* vol. 6, 2015.

[252] R. Conrad, G. Stölting, J. Hendriks, G. Ruello, D. Kortzak, N. Jordan, T. Gensch and P. Hidalgo, "Rapid Turnover of the Cardiac L-Type CaV1.2 Channel by Endocytic Recycling Regulates Its Cell Surface Availability," *iScience,* vol. 7, pp. 1-15, 2018.

[253] V. Cohen-Kaplan, I. Livneh, N. Avni, B. Fabre, T. Ziv, Y. T. Kwon and A. Ciechanover, "p62- and ubiquitin-dependent stress-induced autophagy of the mammalian 26S proteasome," *Proceedings of the National Academy of Sciences of the United States of America,* vol. 113, pp. E7490--E7499, 2016.

[254] N. S. Claxton, T. J. Fellers and M. W. Davidson, "Laser Scanning Confocal Microscopy," *Developments in ophthalmology,* vol. 45, p. 37, 2005.

[255] J. Claßen, A. Graf, F. Aupert, D. Solle, M. Höhse and T. Scheper, "A novel LED-based 2D-fluorescence spectroscopy system for in-line bioprocess monitoring of Chinese hamster ovary cell cultivations—Part II," *Engineering in Life Sciences,* vol. 19, pp. 341-351, 2019.

[256] R. Ciuffa, T. Lamark, A. K. Tarafder, A. Guesdon, S. Rybina, W. J. H. Hagen, T. Johansen and C. Sachse, "The Selective Autophagy Receptor p62 Forms a Flexible Filamentous Helical Scaffold," *Cell Reports,* vol. 11, pp. 748-758, 2015.

[257] D. M. Chudakov, S. Lukyanov and K. A. Lukyanov, "Tracking intracellular protein movements using photoswitchable fluorescent proteins PS-CFP2 and Dendra2," *Nature Protocols,* vol. 2, pp. 2024-2032, 2007.

[258] D. M. Chudakov, V. V. Verkhusha, D. B. Staroverov, E. A. Souslova, S. Lukyanov and K. A. Lukyanov, "Photoswitchable cyan fluorescent protein for protein tracking," *Nature Biotechnology,* vol. 22, pp. 1435-1439, 2004.

[259] D. M. Chudakov, V. V. Belousov, A. G. Zaraisky, V. V. Novoselov, D. B. Staroverov, D. B. Zorov, S. Lukyanov and K. A. Lukyanov, "Kindling fluorescent proteins for precise in vivo photolabeling," *Nature Biotechnology,* vol. 21, pp. 191-194, 2003.

[260] X. T. Cheng, Y. X. Xie, B. Zhou, N. Huang, T. Farfel-Becker and Z. H. Sheng, "Characterization of LAMP1-labeled nondegradative lysosomal and endocytic compartments in neurons," *Journal of Cell Biology,* vol. 217, pp. 3127-3139, 2018.

[261] H. Chang, M. Zhang, W. Ji, J. Chen, Y. Zhang, B. Liu, J. Lu, J. Zhang, P. Xu and T. Xu, "A unique series of reversibly switchable fluorescent proteins with beneficial properties for various applications," *Proceedings of the National Academy of Sciences of the United States of America,* vol. 109, pp. 4455-4460, 2012.

[262] E. Y. W. Chan, A. Longatti, N. C. McKnight and S. A. Tooze, "Kinase-Inactivated ULK Proteins Inhibit Autophagy via Their Conserved C-Terminal Domains Using an Atg13-Independent Mechanism," *Molecular and Cellular Biology,* vol. 29, pp. 157-171, 2009.

[263] M. Chalfie, "Green Fluorescent Protein," *Photochemistry and Photobiology,* vol. 62, pp. 651-656, 1995.

[264] F. Z. Chakrama, S. Seguin-Py, J. N. Le Grand, A. Fraichard, R. Delage-Mourroux, G. Despouy, V. Perez, M. Jouvenot and M. Boyer-Guittaut, "GABARAPL1 (GEC1) associates with autophagic vesicles," *Autophagy,* vol. 6, pp. 495-505, 2010.

[265] L. Casares-Crespo, I. Calatayud-Baselga, L. García-Corzo and H. Mira, "On the role of Basal autophagy in adult neural stem cells and neurogenesis," *Frontiers in Cellular Neuroscience,* vol. 12, pp. 1-9, 2018.

[266] S. R. Carlsson and A. Simonsen, "Membrane dynamics in autophagosome biogenesis," *Journal of Cell Science,* vol. 128, pp. 193-205, 2015.

[267] L. Buetow and D. T. Huang, "Structural insights into the catalysis and regulation of E3 ubiquitin ligases," *Nature Reviews Molecular Cell Biology,* vol. 17, pp. 626-642, 2016.

[268] T. Brakemann, G. Weber, M. Andresen, G. Groenhof, A. C. Stiel, S. Trowitzsch, C. Eggeling, H. Grubmüller, S. W. Hell, M. C. Wahl and S. Jakobs, "Molecular basis of the light-driven switching of the photochromic fluorescent protein padron," *Journal of Biological Chemistry,* vol. 285, pp. 14603-14609, 2010.

[269] T. Brakemann, A. C. Stiel, G. Weber, M. Andresen, I. Testa, T. Grotjohann, M. Leutenegger, U. Plessmann, H. Urlaub, C. Eggeling, M. C. Wahl, S. W. Hell and S. Jakobs, "A reversibly photoswitchable GFP-like protein with fluorescence excitation decoupled from switching," *Nature Biotechnology,* vol. 29, pp. 942-950, 2011.

[270] M. Boyer-Guittaut, L. Poillet, Q. Liang, E. Bôle-Richard, X. Ouyang, G. A. Benavides, F. Z. Chakrama, A. Fraichard, V. M. Darley-Usmar, G. Despouy, M. Jouvenot, R. Delage-Mourroux and J. Zhang, "The role of GABARAPL1/GEC1 in autophagic flux and mitochondrial quality control in MDA-MB-436 breast cancer cells," *Autophagy,* vol. 10, pp. 986-1003, 2014.

[271] D. Bourgeois and V. Adam, "Reversible photoswitching in fluorescent proteins: A mechanistic view," *IUBMB Life,* vol. 64, pp. 482-491, 2012.

[272] A. Bogner, P. H. Jouneau, G. Thollet, D. Basset and C. Gauthier, "A history of scanning electron microscopy developments: Towards "wet-STEM" imaging," *Micron,* vol. 38, pp. 390-401, 2007.

[273] N. Boens, V. Leen, W. Dehaen, L. Wang, K. Robeyns, W. Qin, X. Tang, D. Beljonne, C. Tonnelé, J. M. Paredes, M. J. Ruedas-Rama, A. Orte, L. Crovetto, E. M. Talavera and J. M. Alvarez-Pez, "Visible absorption and fluorescence spectroscopy of conformationally constrained, annulated BODIPY dyes," *Journal of Physical Chemistry A,* vol. 116, pp. 9621-9631, 2012.

[274] J. S. Biteen, M. A. Thompson, N. K. Tselentis, G. R. Bowman, L. Shapiro and W. E. Moerner, "Super-resolution imaging in live Caulobacter crescentus cells using photoswitchable EYFP," *Nature Methods,* vol. 5, pp. 947-949, 2008.

[275] O. Biskou, V. Casanova, C. Stevens, P. G. Barlow, G. P. Wright, K. M. Hooper, S. Kemp and J. Satsangi, "The type III intermediate filament vimentin regulates organelle distribution and modulates autophagy," *Plos One,* pp. 1-20, 2019.

[276] Å. B. Birgisdottir, T. Lamark and T. Johansen, "The LIR motif - crucial for selective autophagy," *Journal of Cell Science,* vol. 126, pp. 3237-3247, 2013.

[277] E. Betzig, G. H. Patterson, R. Sougrat, O. W. Lindwasser, S. Olenych, J. S. Bonifacino, M. W. Davidson, J. Lippincott-Schwartz and H. F. Hess, "Imaging intracellular fluorescent proteins at nanometer resolution," *Science,* vol. 313, pp. 1642-1645, 2006.

[278] J. E. Berlier, A. Rothe, G. Buller, J. Bradford, D. R. Gray, B. J. Filanoski, W. G. Telford, S. Yue, J. Liu, C. Y. Cheung, W. Chang, J. D. Hirsch, J. M. Beechem, R. P. Haugland and R. P. Haugland, "Quantitative Comparison of Long-wavelength Alexa Fluor Dyes to Cy Dyes: Fluorescence of the Dyes and Their Bioconjugates," *Journal of Histochemistry and Cytochemistry,* vol. 51, pp. 1699-1712, 2003.

[279] A. Benke and S. Manley, "Live-Cell dSTORM of Cellular DNA Based on Direct DNA Labeling," *ChemBioChem,* vol. 13, pp. 298-301, 2012.

[280] G. M. J. Beaudoin, C. M. Schofield, T. Nuwal, K. Zang, E. M. Ullian, B. Huang and L. F. Reichardt, "Afadin, A Ras/Rap effector that controls cadherin function, promotes spine and excitatory synapse density in the hippocampus," *Journal of Neuroscience,* vol. 32, pp. 99-110, 2012.

[281] V. Bayer, "Ueber eine neue Klaese von Farbetoffen," *Ber. Dtsch. Chem. Ges.,* vol. 4, pp. 555-558, 1871.

[282] K. A. Bauckman, N. Owusu-Boaitey and I. U. Mysorekar, "Selective autophagy: Xenophagy," *Methods,* vol. 75, pp. 120-127, 2015.

[283] M. Bates, S. A. Jones and X. Zhuang, "Stochastic optical reconstruction microscopy (STORM): A method for superresolution fluorescence imaging," *Cold Spring Harbor Protocols,* vol. 8, pp. 498-520, 2013.

[284] T. N. Baldering, J. T. Bullerjahn, G. Hummer, M. Heilemann and S. Malkusch, "Molecule counts in complex oligomers with single-molecule localization microscopy," *Journal of Physics D: Applied Physics,* vol. 52, p. 474002, 2019.

[285] J. Backer, "The regulation and function of Class III PI3Ks: novel roles for Vps34," *Biochemical Journal,* vol. 410, pp. 1-17, 2008.

[286] C. Baarlink, M. Plessner, A. Sherrard, K. Morita, S. Misu, D. Virant, E. M. Kleinschnitz, R. Harniman, D. Alibhai, S. Baumeister, K. Miyamoto, U. Endesfelder, A. Kaidi and R. Grosse, "A transient pool of nuclear F-actin at mitotic exit controls chromatin organization," *Nature Cell Biology,* vol. 19, pp. 1389-1399, 2017.

[287] D. Axelrod, "Total Internal Reflection Fluorescence Microscopy," *Encyclopedia of Cell Biology,* vol. 2, pp. 62-69, 2016.

[288] P. Atkins and J. Paula, ATKINS' PHYSICAL CHEMISTRY, 8 ed., New York: Great Britain by Oxford University Press, 2006.

[289] M. Andresen, A. C. Stiel, J. Fölling, D. Wenzel, A. Schönle, A. Egner, C. Eggeling, S. W. Hell and S. Jakobs, "Photoswitchable fluorescent proteins enable monochromatic multilabel imaging and dual color fluorescence nanoscopy," *Nature Biotechnology,* vol. 26, pp. 1035-1040, 2008.

[290] R. Ando, H. Mizuno and A. Miyawaki, "Regulated fast nucleocytoplasmic shuttling observed by reversible protein highlighting," *Science,* vol. 306, pp. 1370-1373, 2004.

[291] R. Ando, C. Flors, H. Mizuno, J. Hofkens and A. Miyawaki, "Highlighted generation of fluorescence signals using simultaneous two-color irradiation on Dronpa mutants," *Biophysical Journal,* vol. 92, pp. 97-99, 2007.

[292] R. Ando, H. Hama, M. Yamamoto-Hino, H. Mizuno and A. Miyawaki, "An optical marker based on the UV-induced green-to-red photoconversion of a fluorescent protein," *Proceedings of the National Academy of Sciences of the United States of America,* vol. 99, pp. 12651-12656, 2002.

[293] J. R. Allen, S. T. Ross and M. W. Davidson, "Sample preparation for single molecule localization microscopy," *Physical Chemistry Chemical Physics,* vol. 15, pp. 18771-18783, 2013.

[294] N. O. Alieva, K. A. Konzen, S. F. Field, E. A. Meleshkevitch, M. E. Hunt, V. Beltran-Ramirez, D. J. Miller, J. Wiedenmann, A. Salih and M. V. Matz, "Diversity and evolution of coral fluorescent proteins," *PLoS ONE,* vol. 3, 2008.

[295] b. M. D. a. B. Adam Lassak, B. Dorota Wyczechowska, b. E. Anna Wilk, a. B. Luis Marrero, D. A. Hamid Boulares, B. Luis Del Valle, B. Francesca Peruzzi, B. Augusto Ochoa and B. Krzysztof Reissa, "Molecular and Structural Traits of Insulin Receptor Substrate 1/LC3 Nuclear Structures and Their Role in Autophagy Control and Tumor Cell Survival," *Molecular and Cellular Biology,* vol. 38, pp. 1-23, 2017.

[296] I. Abdollahzadeh, M. Schwarten, T. Gensch, D. Willbold and O. H. Weiergräber, "The Atg8 family of proteins-modulating shape and functionality of autophagic membranes," *Frontiers in Genetics,* vol. 8, 2017.

[297] S. L. d. R. N. B. S. C. V. Abbruzzetti and F. Beltram, "Engineered photoreceptors as novel optogenetic tools," *Photochemical and Photobiological Sciences,* vol. 9, pp. 1286-1300, 2010.

[298] E. Abbe, "Beiträge zur Theorie des Mikroskops und der mikroskopischen Wahrnehmung," *Archiv für Mikroskopische Anatomie,* vol. 9, pp. 440-456, 1873.

[299] Jusuk I., Vietz C., Raab M., Dammeyer T. and Tinnefeld P. "Super-Resolution Imaging Conditions for enhanced Yellow Fluorescent Protein (eYFP) Demonstrated on DNA Origami Nanorulers," *Scientific Reports ,* vol. 5, 2015.

7. Appendices

7.1. Excitation of EYFP with 514 nm and with 488 nm

In this section, three typical examples of the measurement of HEK-293 cells stably expressing EYFP-GEC1 with SMLM using 488 nm excitation at high- and two examples at low-power and two examples for 514 nm excitation at high- and two examples at high-power conditions are given. In each example the number of localizations per frame for that particular measurement is depicted and mono- and bi-exponential fitted decay curves together with their residuals are represented.

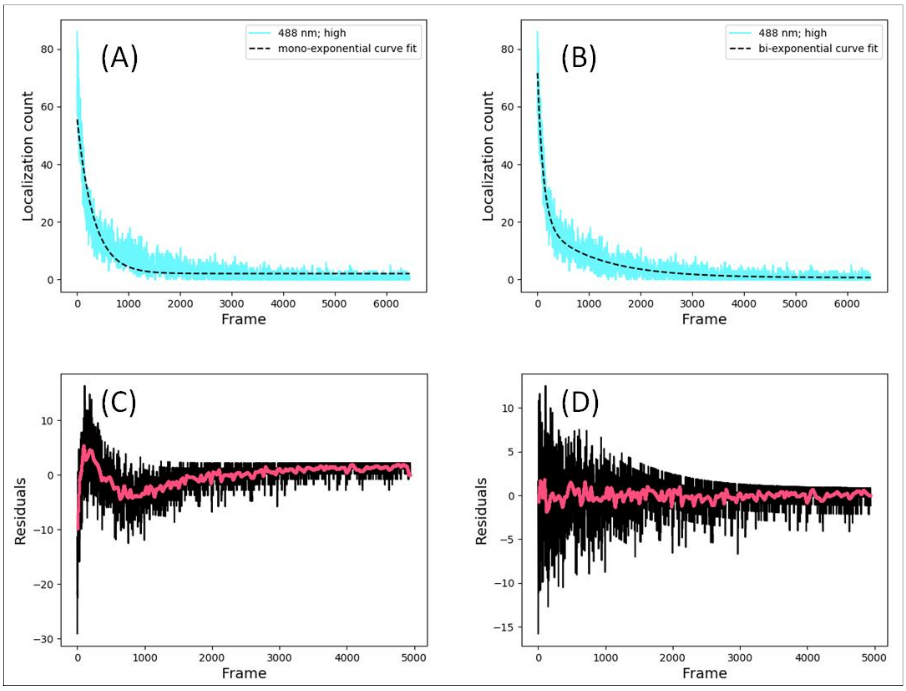

Figure 7.1.1. Number of localizations per frame for the measurement of HEK-293 cells stably expressing EYFP-GEC1 with 488 nm high power (55.4 mW) excitation. A mono-exponential decay fitted curve and its residuals are given in (A) and (C), respectively. A bi-exponential fitted curve and its residuals are given in (B) and (D), respectively. The red curves in (C) and (D) are the rolling average curves for every 50 frames.

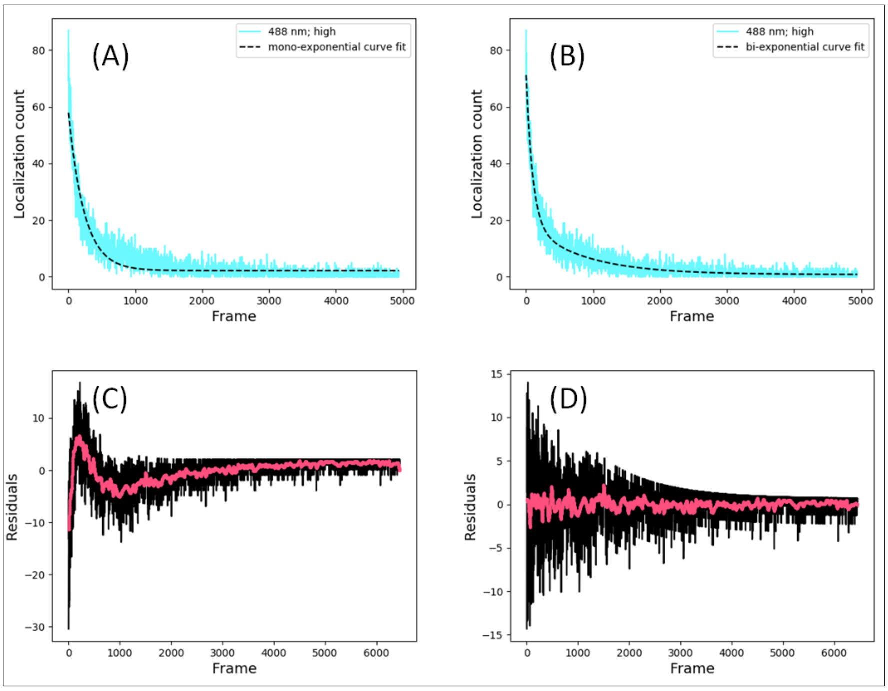

Figure 7.1.2. Number of localizations per frame for the measurement of HEK-293 cells stably expressing EYFP-GEC1 with 488 nm high power (55.4 mW) excitation. A mono-exponential decay fitted curve and its residuals are given in (A) and (C), respectively. A bi-exponential fitted curve and its residuals are given in (B) and (D), respectively. The red curves in (C) and (D) are the rolling average curves for every 50 frames.

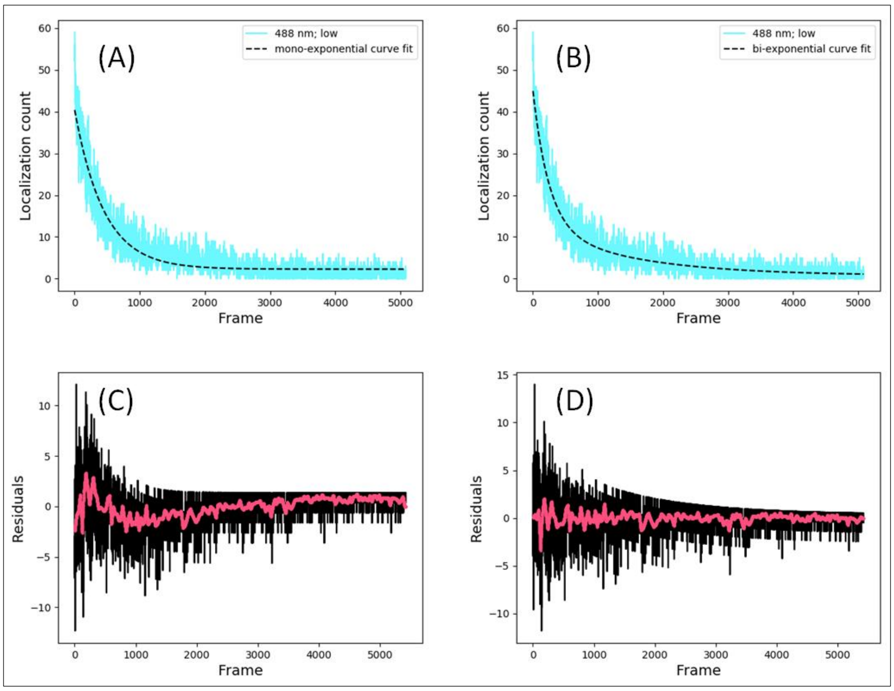

Figure 7.1.3. Number of localizations per frame for the measurement of HEK-293 cells stably expressing EYFP-GEC1 with 488 nm low power (23.6 mW) excitation. A mono-exponential decay fitted curve and its residuals are given in (A) and (C), respectively. A bi-exponential fitted curve and its residuals are given in (B) and (D), respectively. The red curves in (C) and (D) are the rolling average curves for every 50 frames.

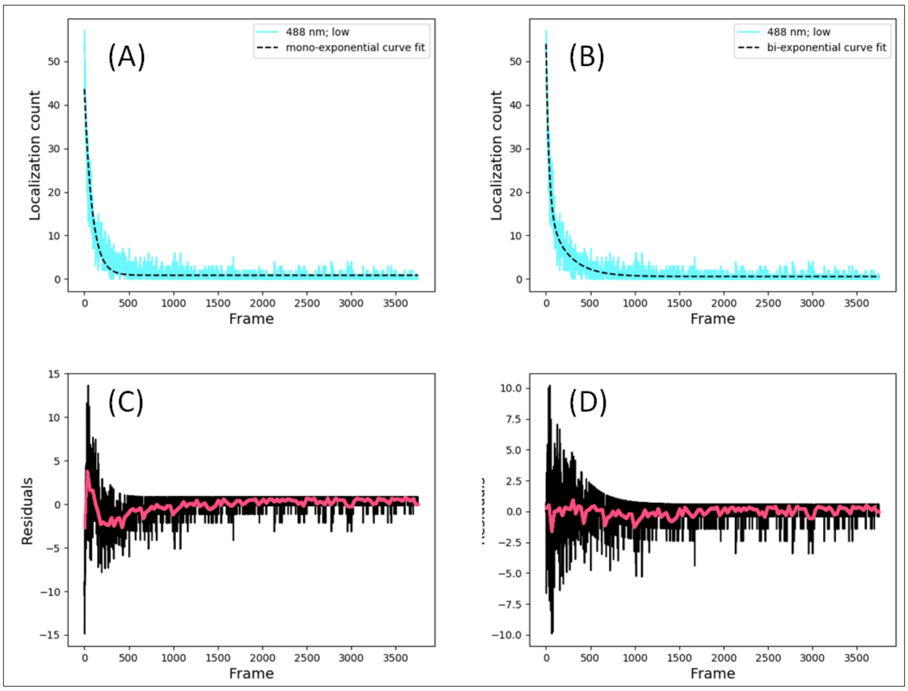

Figure 7.1.4. Number of localizations per frame for the measurement of HEK-293 cells stably expressing EYFP-GEC1 with 488 nm low power (23.6 mW) excitation. A mono-exponential decay fitted curve and its residuals are given in (A) and (C), respectively. A bi-exponential fitted curve and its residuals are given in (B) and (D), respectively. The red curves in (C) and (D) are the rolling average curves for every 50 frames.

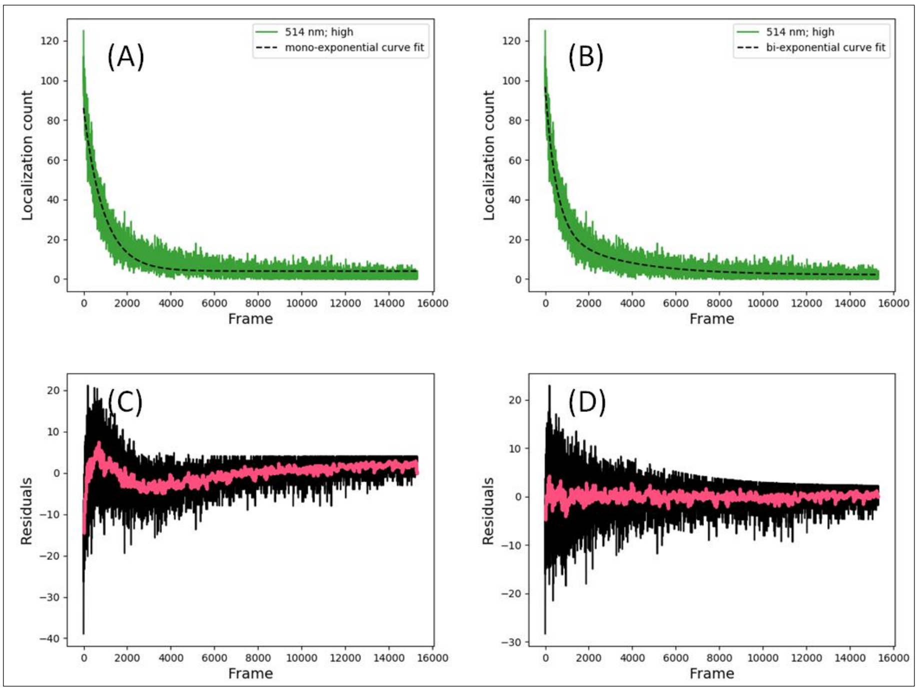

Figure 7.1.5. Number of localizations per frame for the measurement of HEK-293 cells stably expressing EYFP-GEC1 with 514 nm high power (55.4 mW) excitation. A mono-exponential decay fitted curve and its residuals are given in (A) and (C), respectively. A bi-exponential fitted curve and its residuals are given in (B) and (D), respectively. The red curves in (C) and (D) are the rolling average curves for every 50 frames.

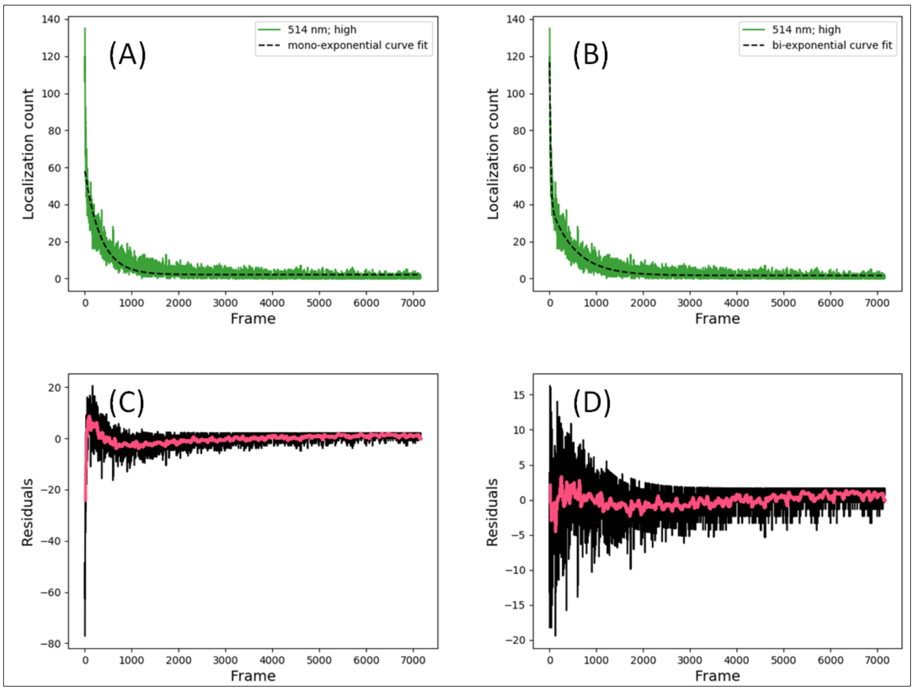

Figure 7.1.6. Number of localizations per frame for the measurement of HEK-293 cells stably expressing EYFP-GEC1 with 514 nm high power (55.4 mW) excitation. A mono-exponential decay fitted curve and its residuals are given in (A) and (C), respectively. A bi-exponential fitted curve and its residuals are given in (B) and (D), respectively. The red curves in (C) and (D) are the rolling average curves for every 50 frames.

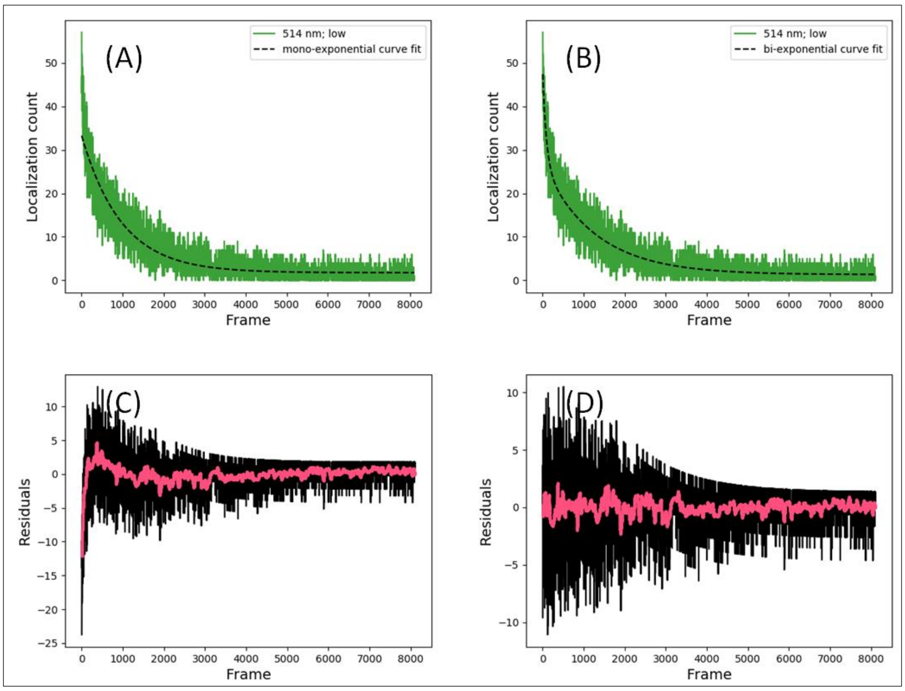

Figure 7.1.7. Number of localizations per frame for the measurement of HEK-293 cells stably expressing EYFP-GEC1 with 514 nm low power (23.6 mW) excitation. A mono-exponential decay fitted curve and its residuals are given in (A) and (C), respectively. A bi-exponential fitted curve and its residuals are given in (B) and (D), respectively. The red curves in (C) and (D) are the rolling average curves for every 50 frames.

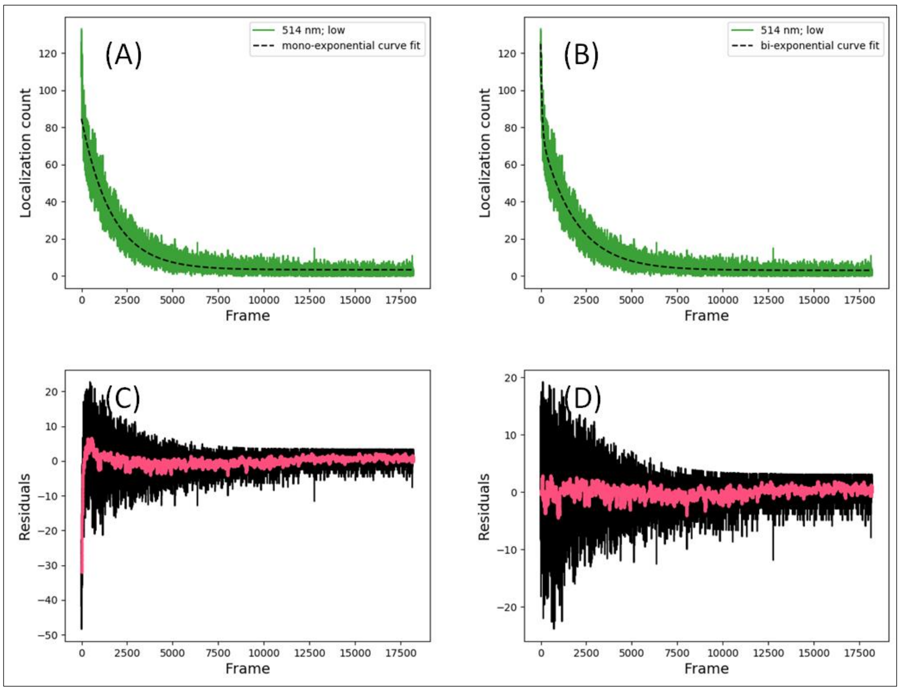

Figure 7.1.8. Number of localizations per frame for the measurement of HEK-293 cells stably expressing EYFP-GEC1 with 514 nm low power (23.6 mW) excitation. A mono-exponential decay fitted curve and its residuals are given in (A) and (C), respectively. A bi-exponential fitted curve and its residuals are given in (B) and (D), respectively. The red curves in (C) and (D) are the rolling average curves for every 50 frames.

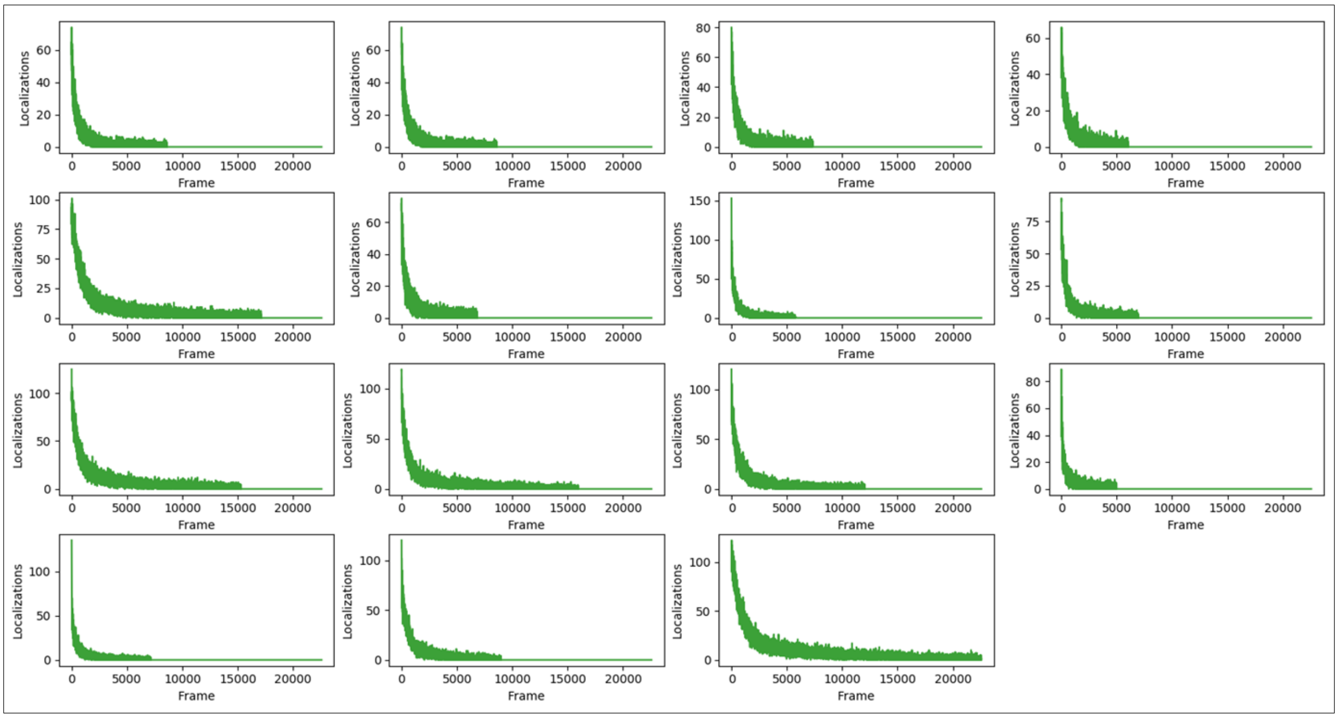

Figure 7.1.9. Number of detected localizations per frame of all 15 measurements of HEK-293 cells stably expressing EYFP-GEC1 excited with 55.4 mW 514 nm laser light.

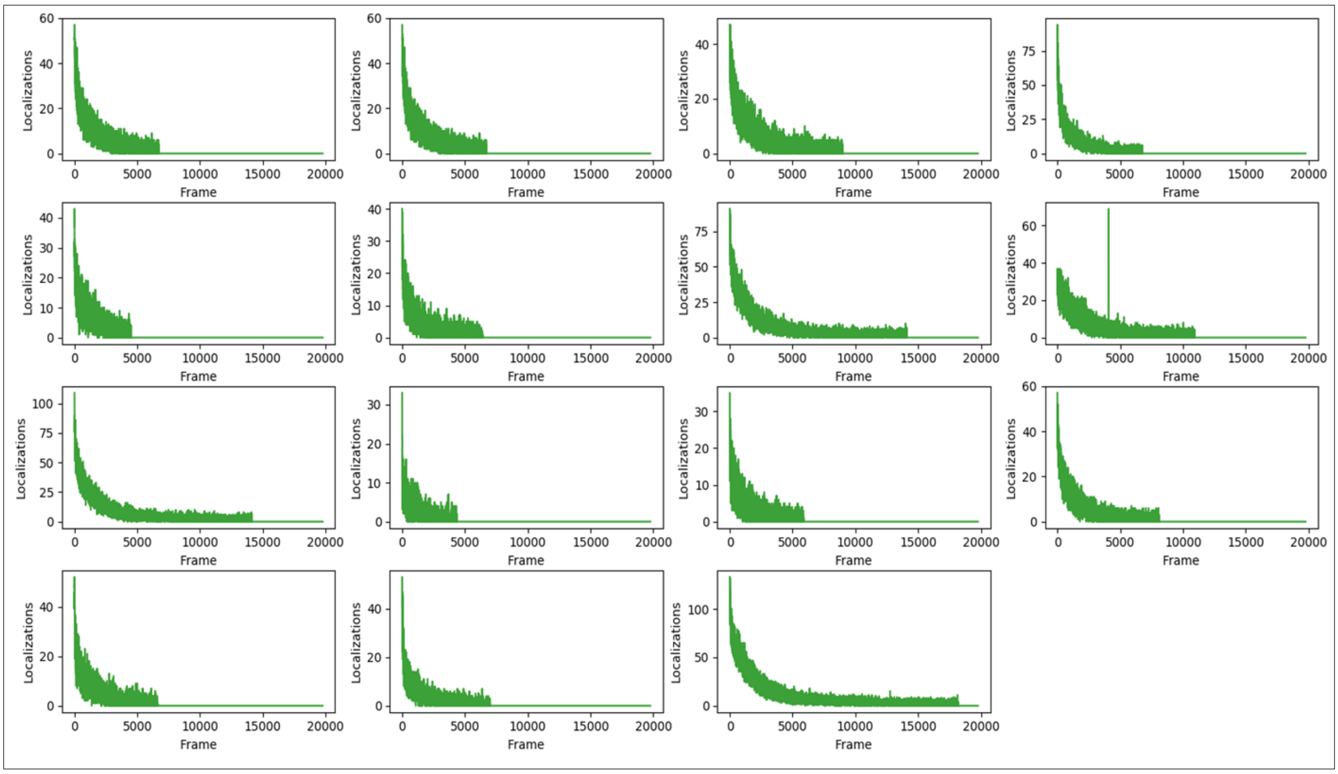

Figure 7.1.10. Number of detected localizations per frame of all 15 measurements of HEK-293 cells stably expressing EYFP-GEC1 excited with 23.6 mW 514 nm laser light.

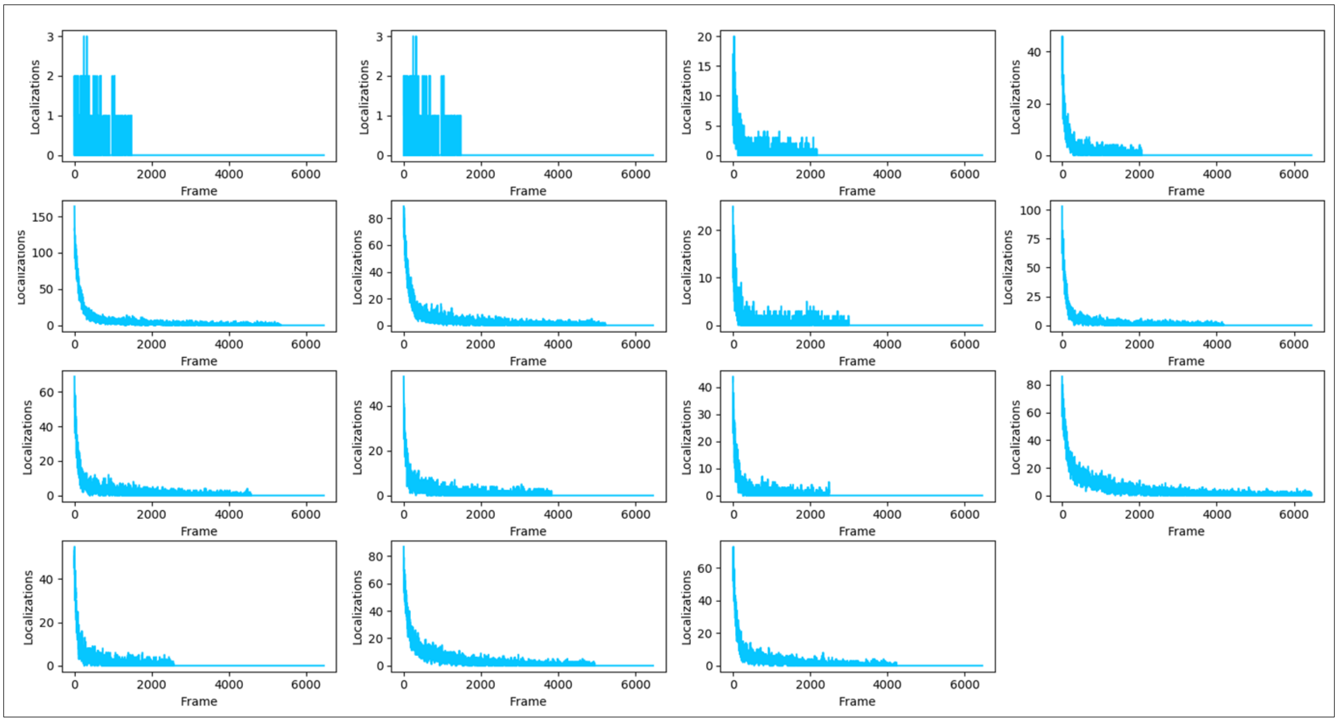

Figure 7.1.11. Number of detected localizations per frame of all 15 measurements of HEK-293 cells stably expressing EYFP-GEC1 excited with 55.4 mW 488 nm laser light.

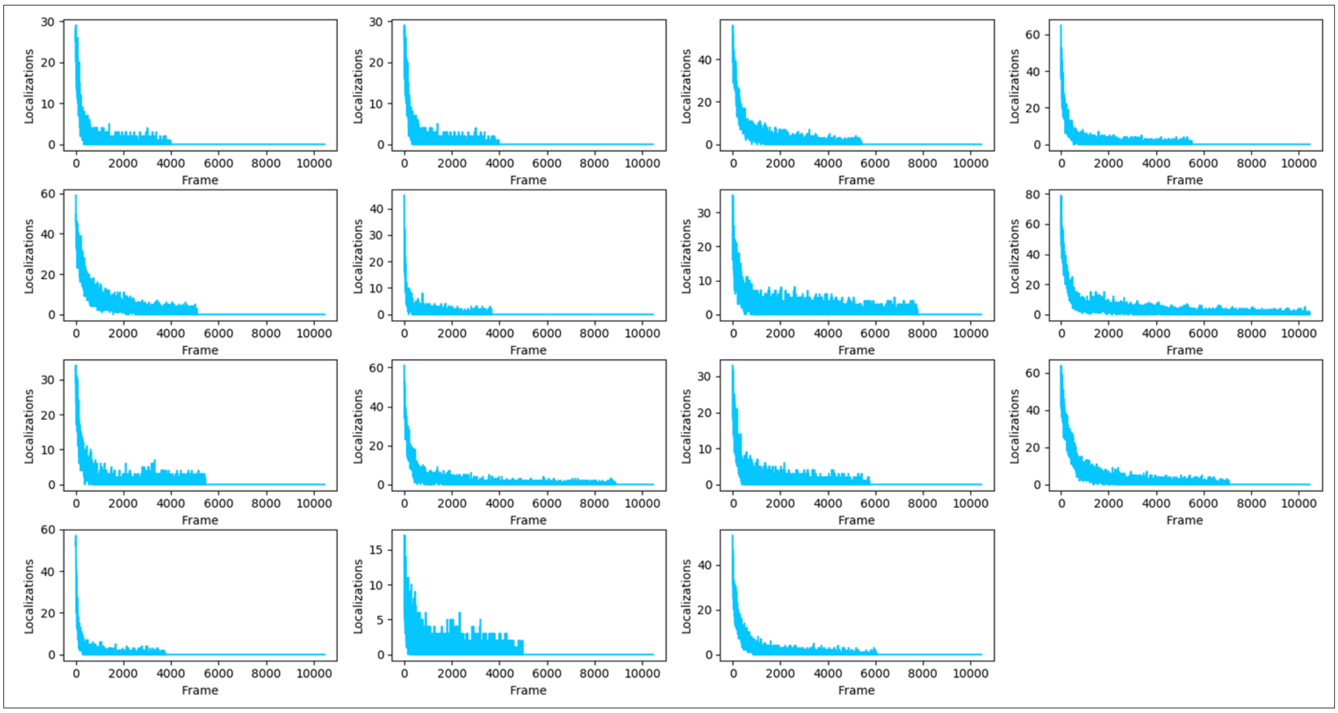

Figure 7.1.12. Number of detected localizations per frame of all 15 measurements of HEK-293 cells stably expressing EYFP-GEC1 excited with 23.6 mW 488 nm laser light.

Table 7.1. The parameter "weighted characteristic frame" for all 15 measurements of HEK-293 cells stably expressing EYFP-GEC1 excited with 488 nm at low and high power, and 514 nm at low and high power, respectively. The average value of 15 measurements and the standard error of mean (SEM) are given for each condition.

488 nm; high power	488 nm; low power	514 nm; high power	514 nm; low power
200	262	481	804
113	378	423	1113
85	206	449	538
201	576	1450	779
223	91	437	525
79	918	204	971
150	554	330	1672
172	226	1103	934
161	329	895	270
85	322	702	544
366	550	284	741
87	87	187	569
283	844	443	392
184	248	1848	1147
124	85	381	1089
Average/SEM	Average/SEM	Average/SEM	Average/SEM
167.5/20.16	378.4/64.98	641.13/120.6	805.87/90.02

7.2. Images of HEK-293 cells transiently transfected with EYFP-GABARAP and EYFP-LC3B widefield and super-resolution images used in this thesis

In this section, the transmission, widefield and SMLM images of all ten samples used for the data analysis shown in figures 3.10-3.15 are given.

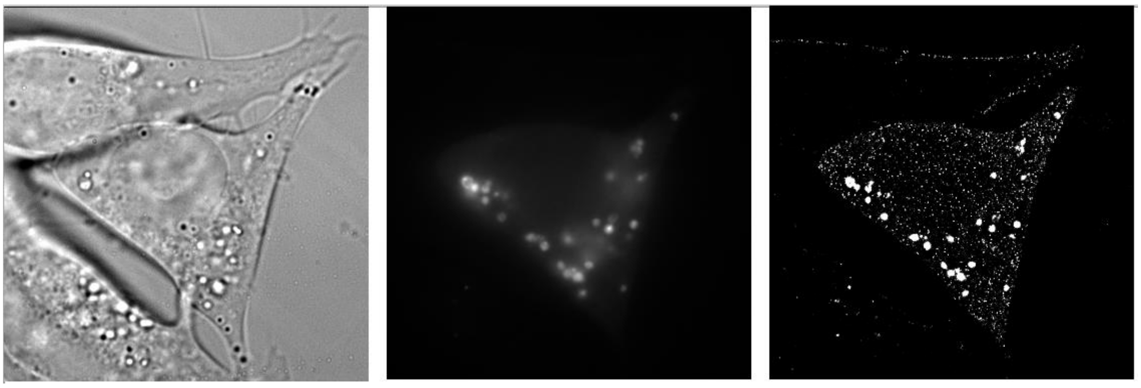

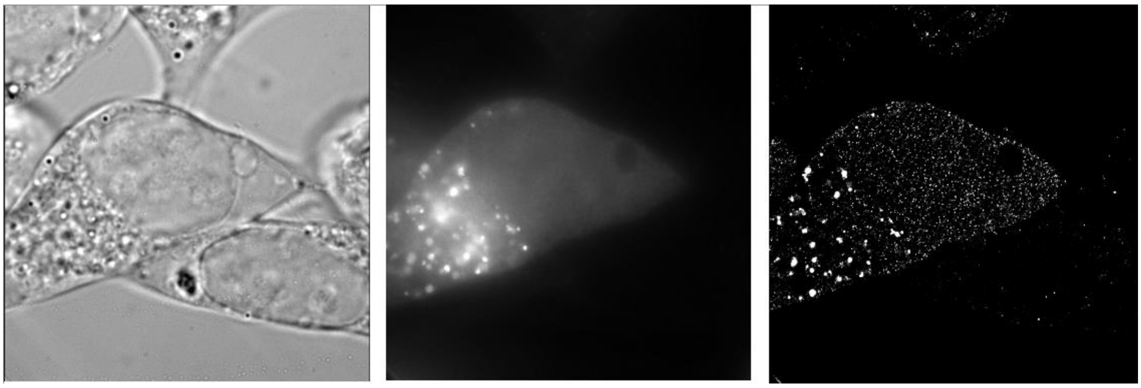

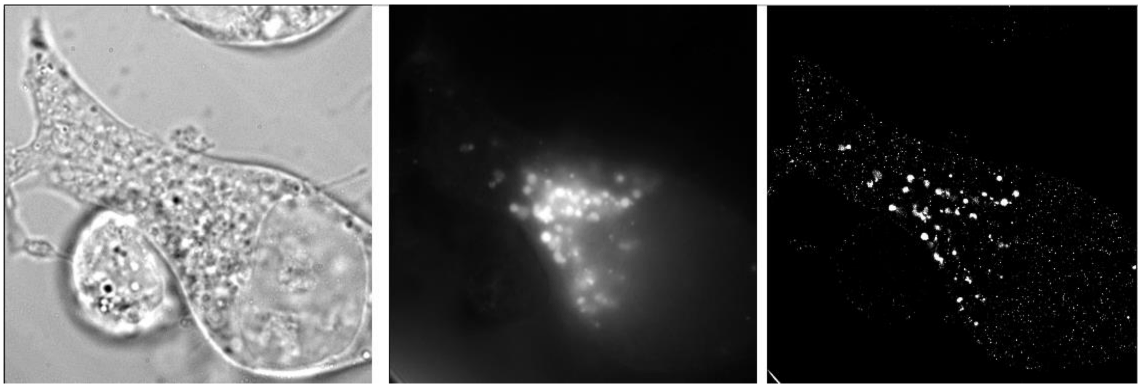

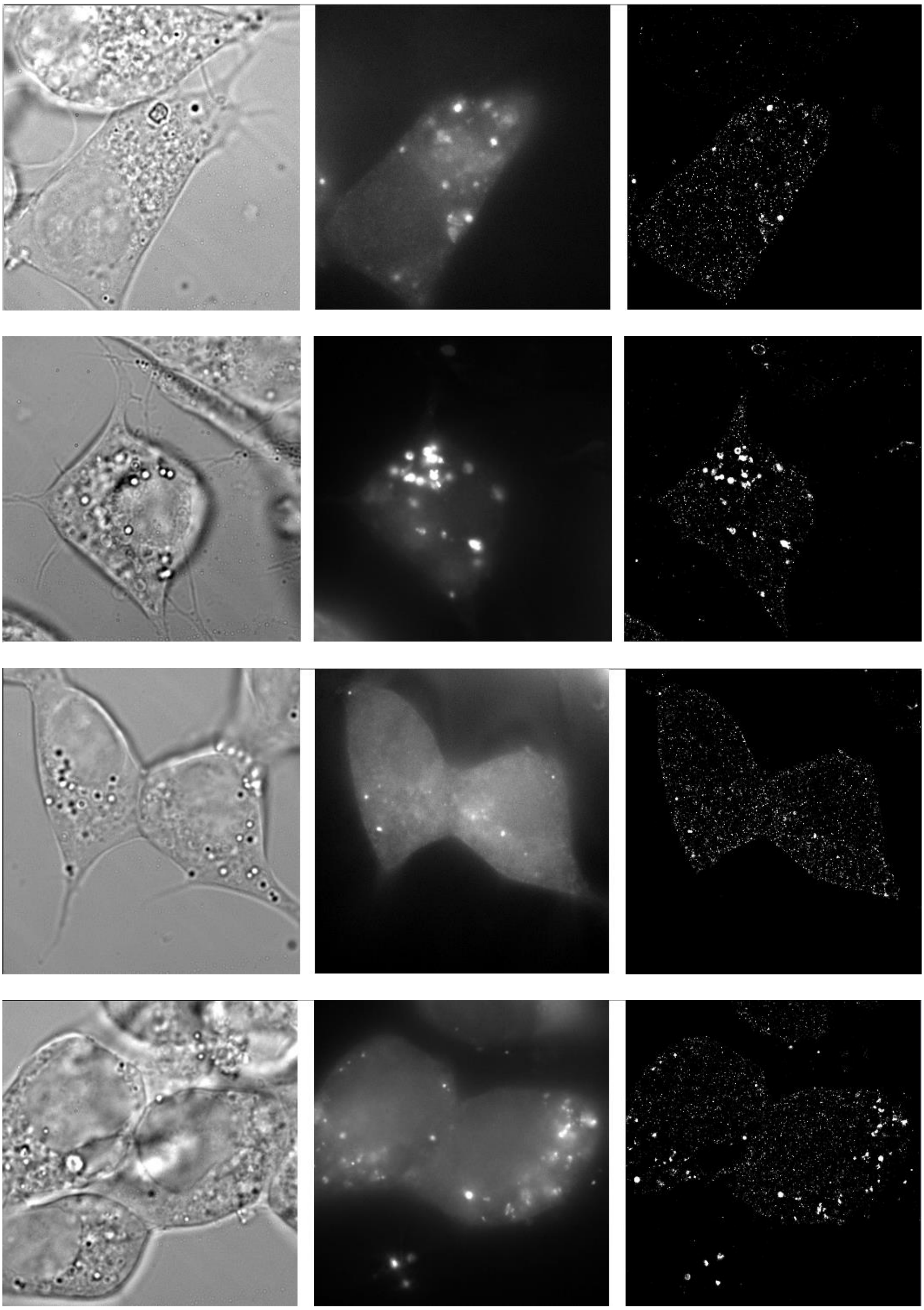

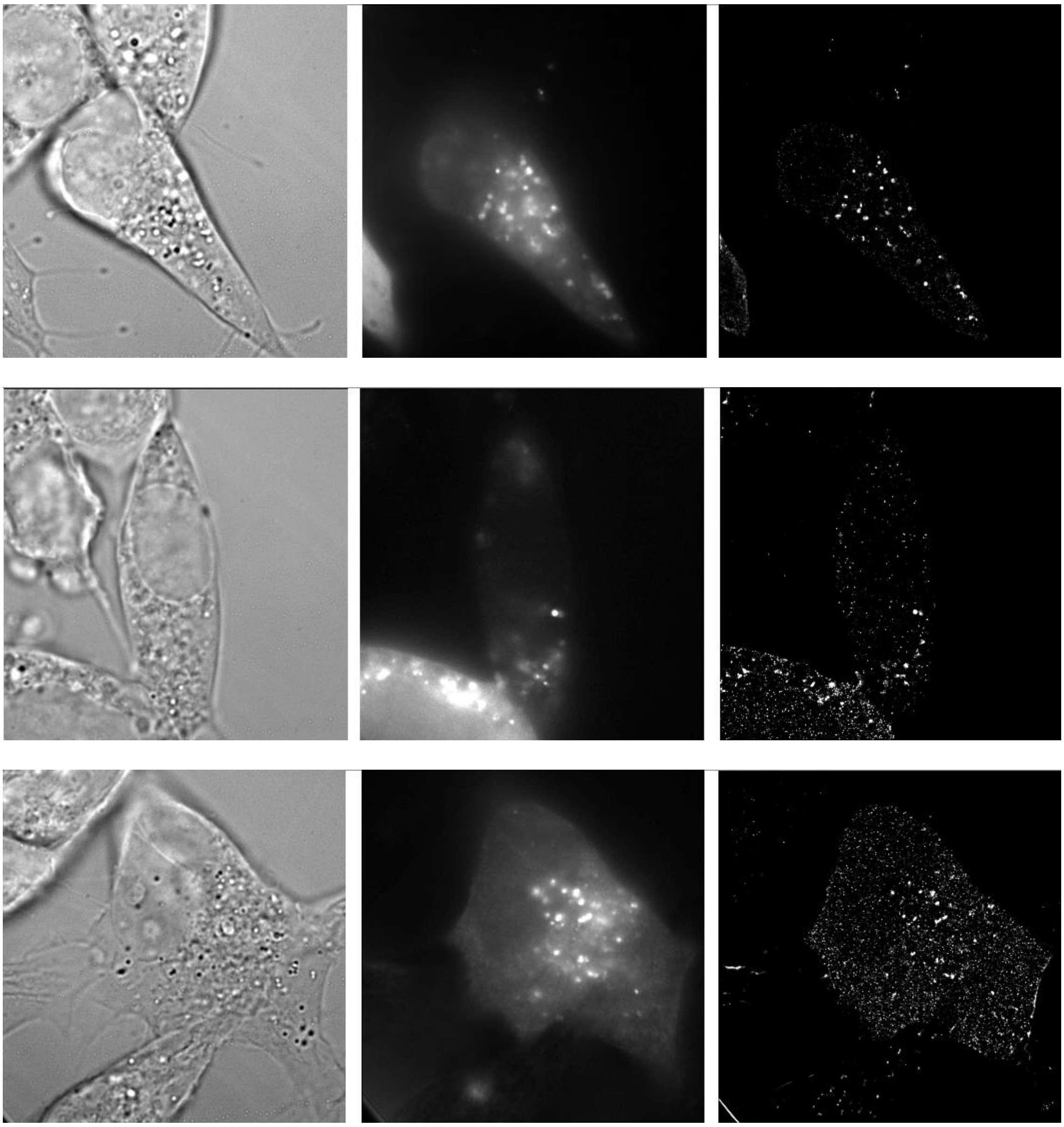

Figure 7.2.1. Ten images featuring HEK-293 cells transiently transfected with EYFP-GABARAP; starved-blocked condition; scale bar is 5 µm.

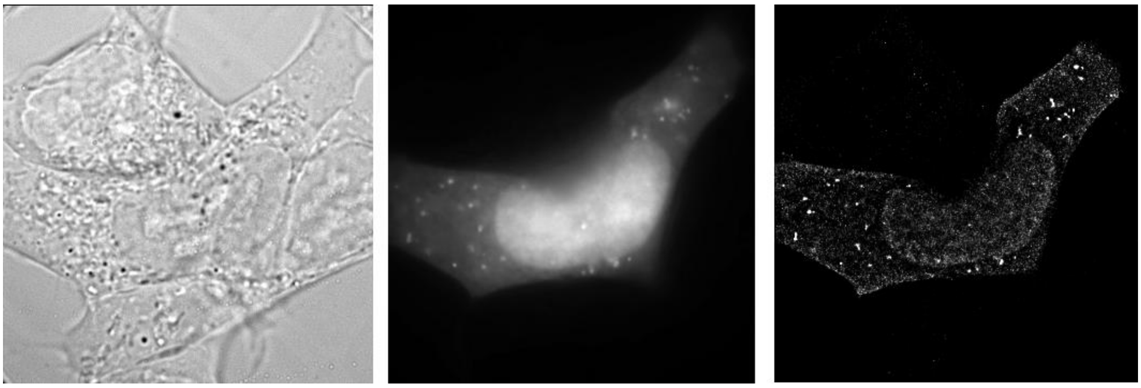

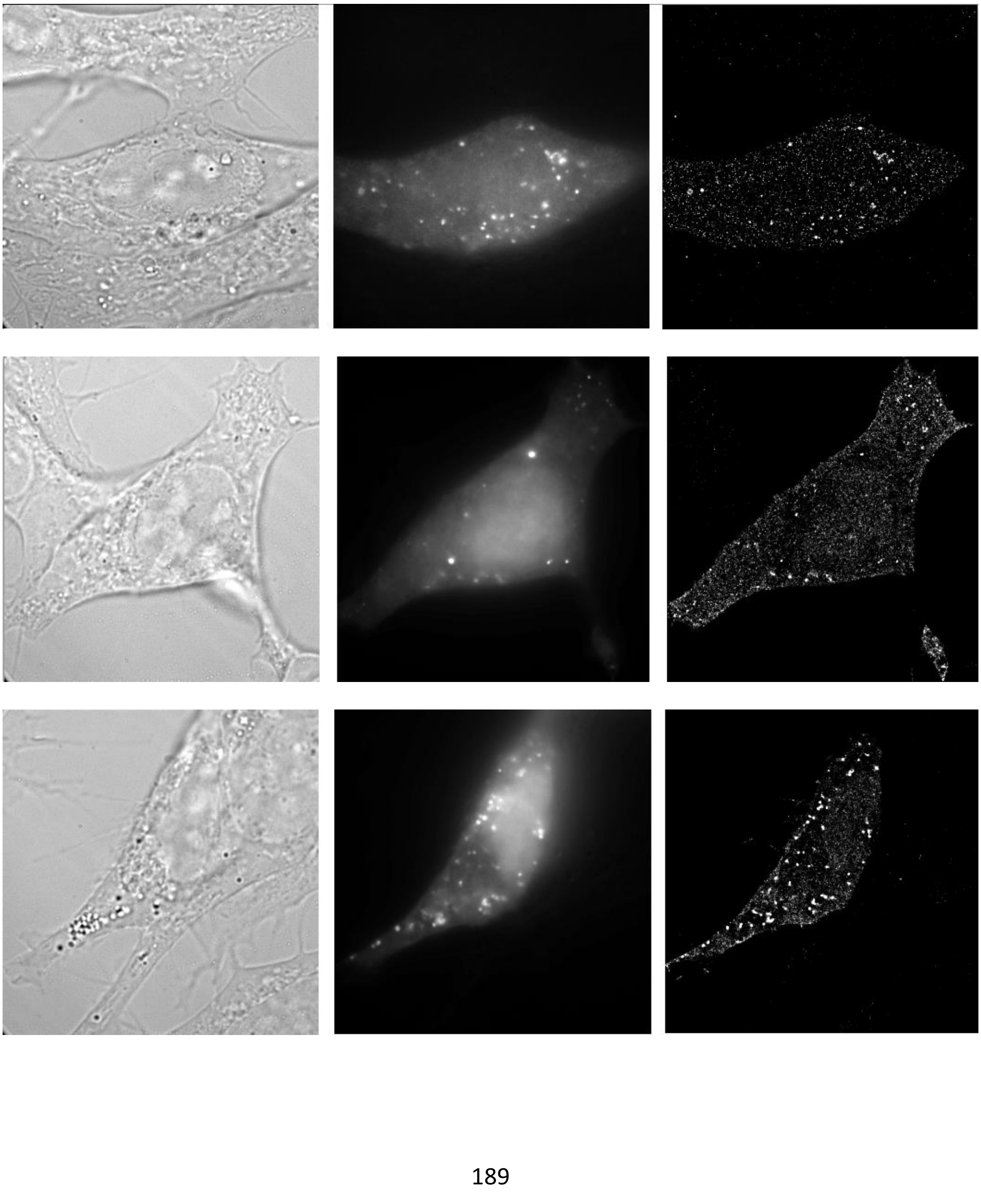

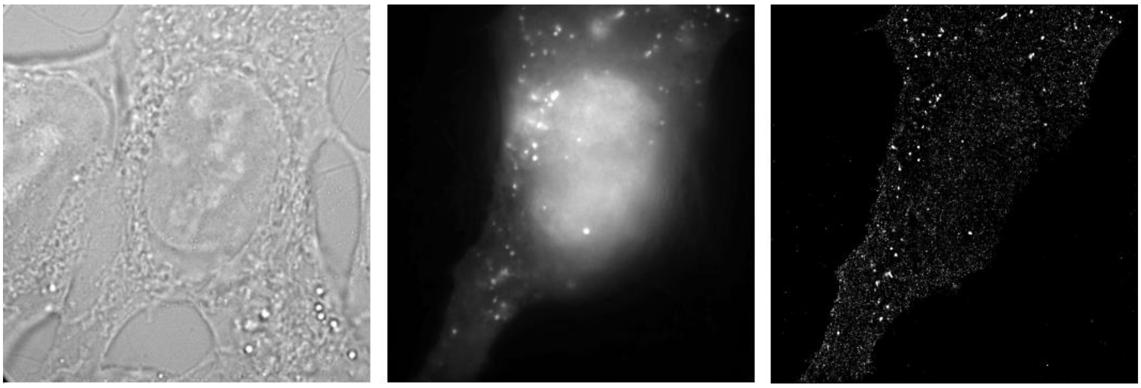

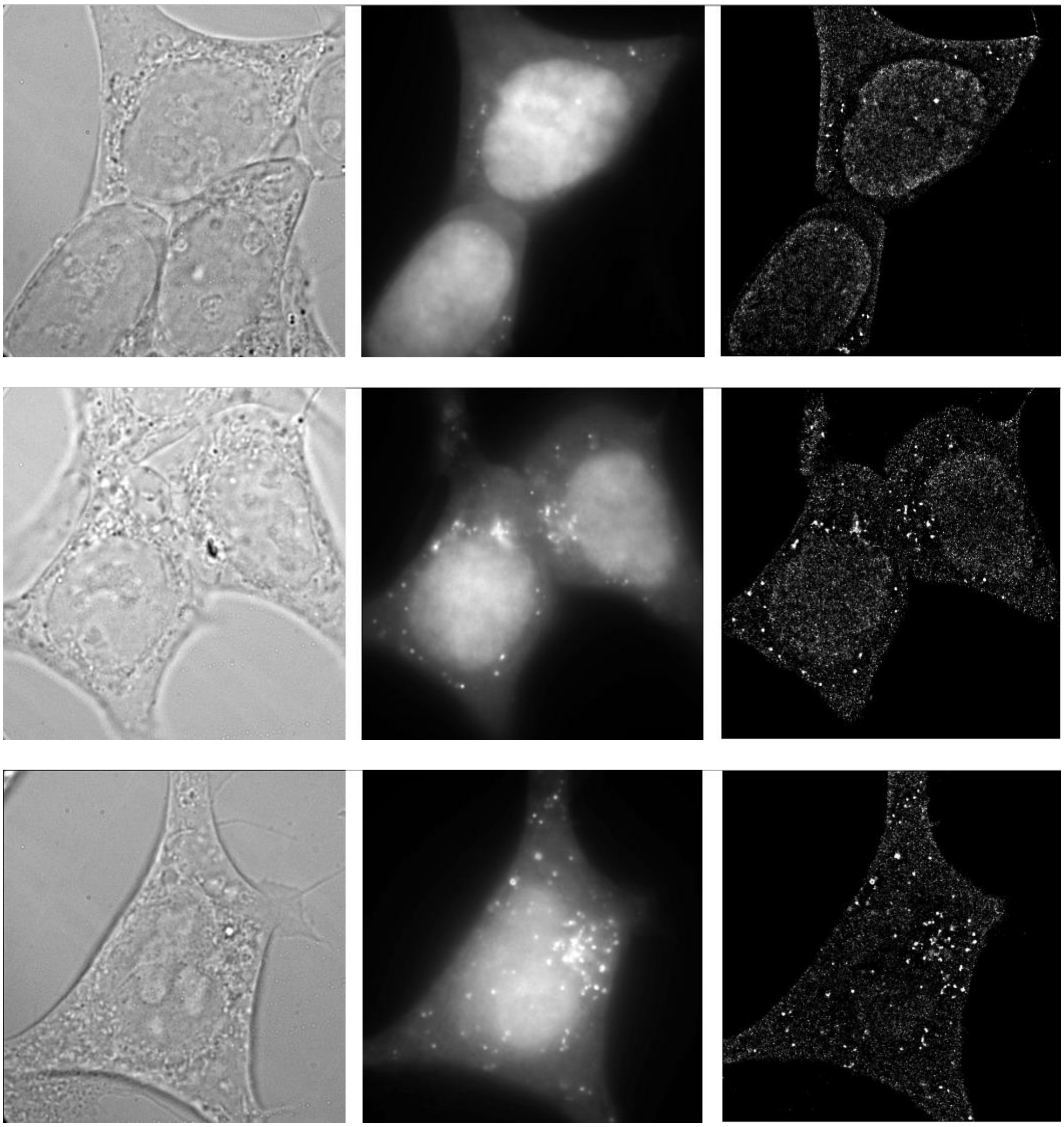

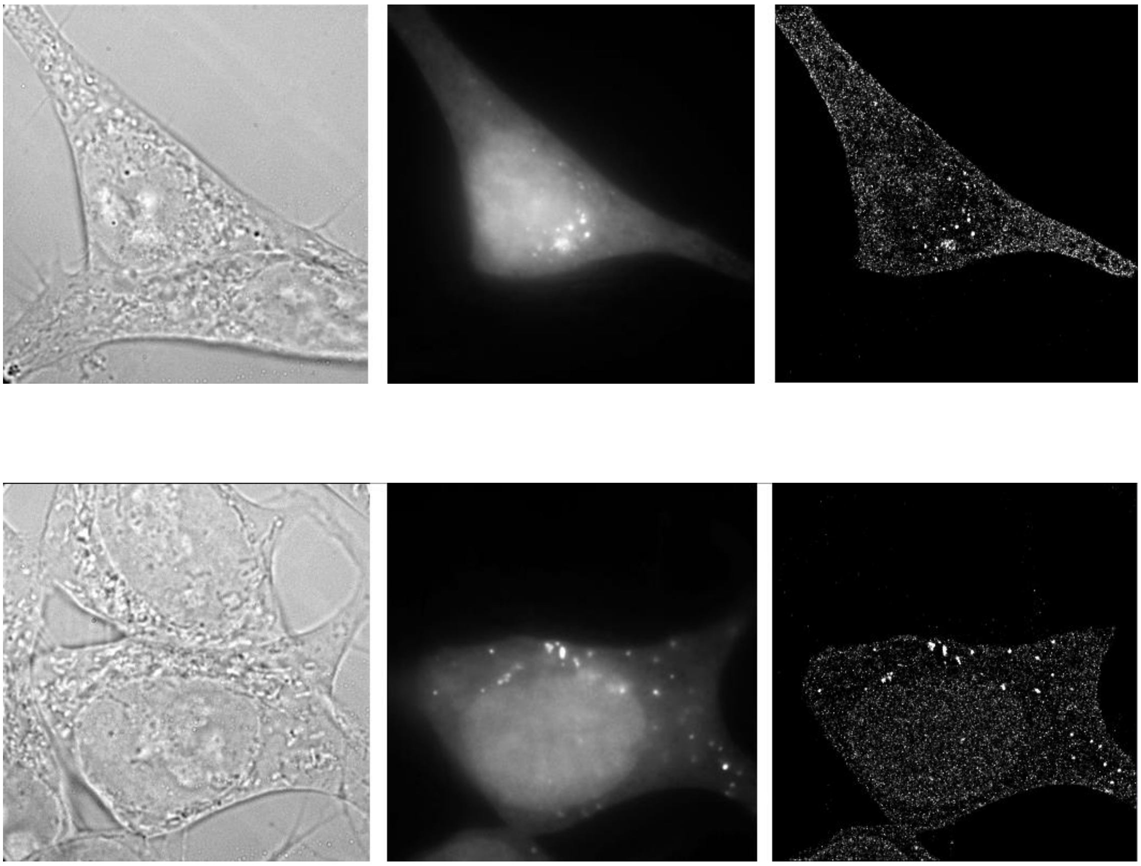

Figure 7.2.2. Ten images featuring HEK-293 cells transiently transfected with EYFP-LC3B; starved-blocked condition; scale bar is 5 µm.

7.3. HEK-293 cells stably expressing Dendra2-GABARAP and Dendra2-LC3B images obtained from laser scanning confocal microscope (LSM)

The availability of HEK-293 cell lines stably expressing Dendra2-GABARAP and Dendra2-LC3B motivated us to measure their expression level under fed and starved-blocked conditions by exciting Dendra2 FPs. Since in our group several HEK-293 cell lines transiently or stably expressing different FP-fused Atg8s have been imaged previously under fed, starved, or starved-blocked conditions by a laser scanning confocal microscope (LSM), this imaging setup used for the first measurement of HEK-293 cell lines stably expressing Dendra2-GABARAP or Dendra2-LC3B under fed and starved-blocked conditions.

In contrast to widefield microscopy, which images signals from object planes above or below the focal plane, the development of confocal laser scanning microscopy offers determinative advantages. The confocal microscopy allows detection of only one sample plane and creates an optical section through the specimen. In a conventional microscope the object is illuminated by an incoherent light source (e.g., a lamp), while in confocal microscopy, often a laser is used.

Starting from the light source, the excitation light is directed to the sample via a dichroic mirror. A detailed explanation of light absorption by the fluorophore in excitation and emission of fluorescence is given in the introduction chapter. The dichroic mirror acts as a color distributor. As a result, the emission light is not reflected to the laser, but passes through a system of other filters to a photomultiplier, where even a few photons can be detected. The so-called pinhole is installed in front of the actual detector. This pinhole ensures that only light from one plane is detected and thus at a time only a single point is detected in the preparation. A line-by-line probing (scanning) of the specimen results in a complete picture of the desired plane in a short time (in several seconds to minute time scale).

All images and measurements were taken on the Zeiss LSM 710 Confocal Laser Scanning Microscope (Jena, Germany), using a 63 X objective with oil corrected immersion lens and equipped with Zen controller software.

For the measurement of HEK-293 cells stably expressing Dendra2-GABARAP or Dendra2-LC3B, the settings were selected as follows in the Zen controller software:

1. The filter set:

- MBS 488/543
- Plate
- Normal LSM
- T-PMT (checked)

2. The power status:

- power = 3.0
- pinhole = 134.3
- Gain (master) = 690
- T_PMT gain (master) = 272

3. Acquisition:

- averaging number = 16

Normally, all cell images were recorded as z-stacks with an interval between 1 and 12 µm.

In this section, the LSM images of all ten samples for HEK-293 cells stably expressing Dendra2-GABARAP or Dendra2-LC3B in fed and starved-blocked conditions are given.

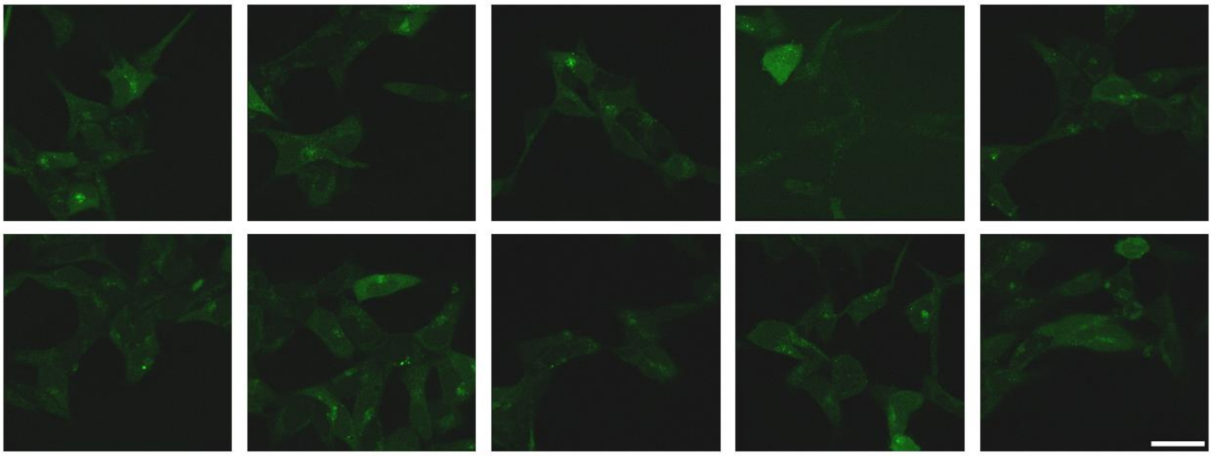

Figure 7.3.1. Ten images containing HEK-293 cells stably expressing Dendra2-GABARAP; fed condition; scale bar is 30 µm.

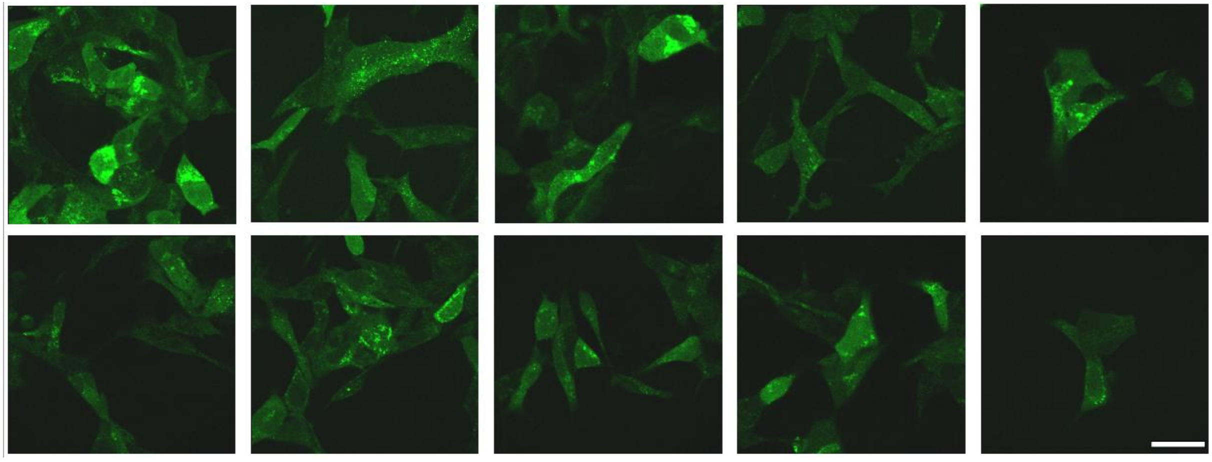

Figure 7.3.2. Ten images containing HEK-293 cells stably expressing Dendra2-GABARAP; starved-blocked condition; scale bar is 30 µm.

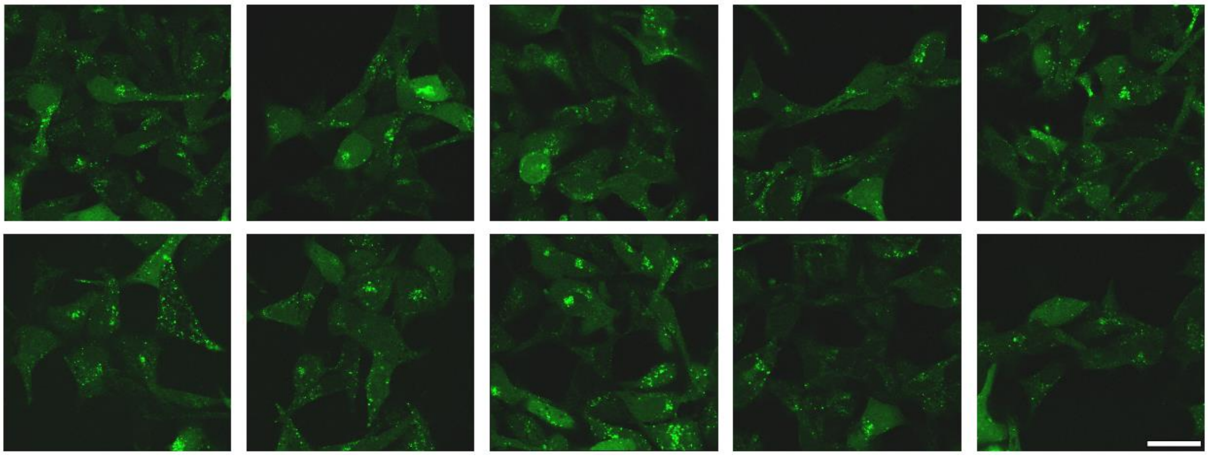

Figure 7.3.3. Ten images containing HEK-293 cells stably expressing Dendra2-LC3B; fed condition; scale bar is 30 µm.

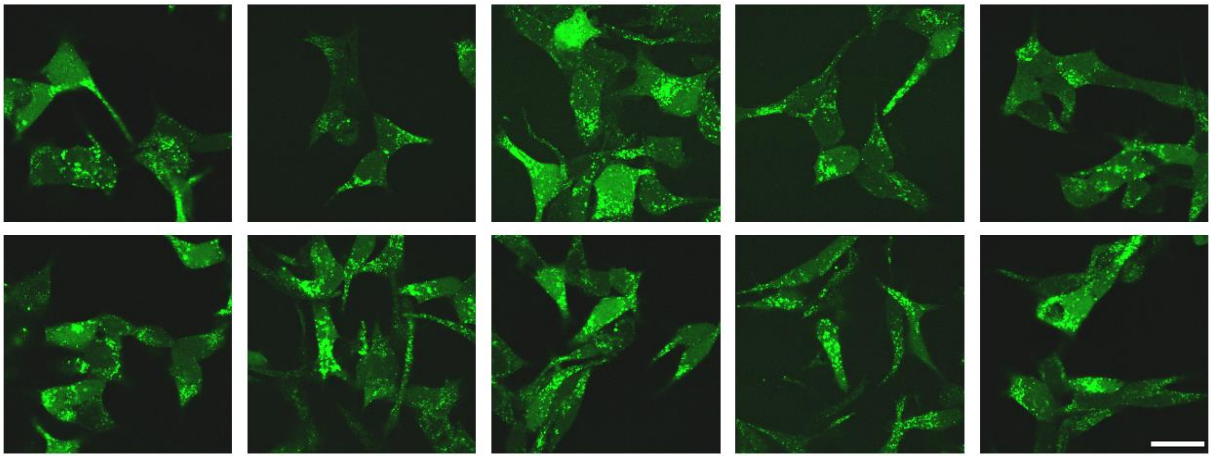

Figure 7.3.4. Ten images containing HEK-293 cells stably expressing Dendra2-LC3B; starved-blocked condition; scale bar is 30 µm.

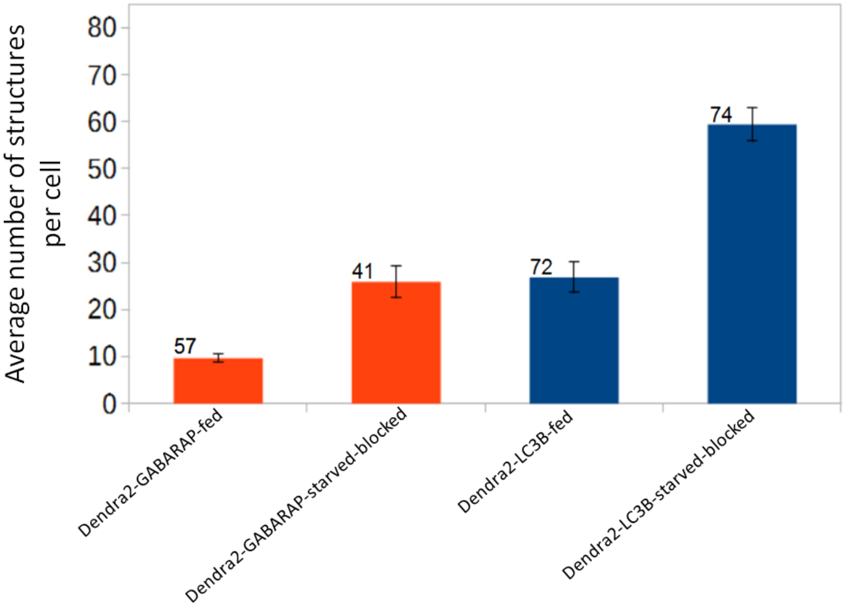

Figure 7.3.5. Average number of structures per cell for the cells shown in figures 3.7.1-3.7.4. The given numbers on top of each bar represent the total number of cells for the particular cell shown at x axis. Error bars show the standard error of mean (SEM).

7.4. HEK-293 cells stably expressing Dendra2-GABARAP and Dendra2-LC3B- widefield and super-resolution images used in this thesis

In this section, the transmission, the widefield and the SMLM images of all ten samples used for the data analysis shown in figures 3.17-3.27 are given.

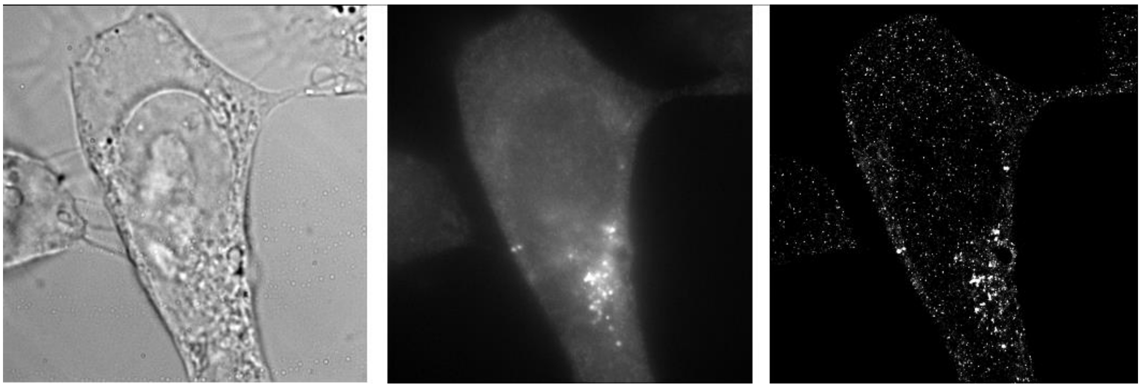

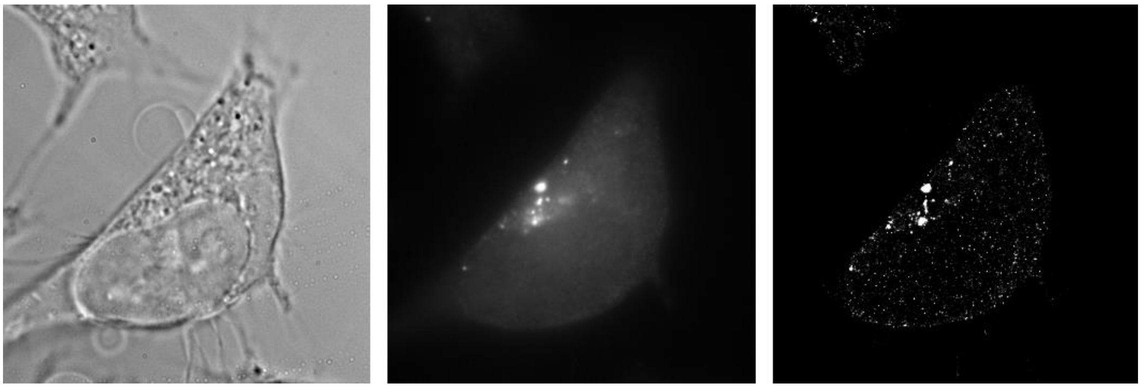

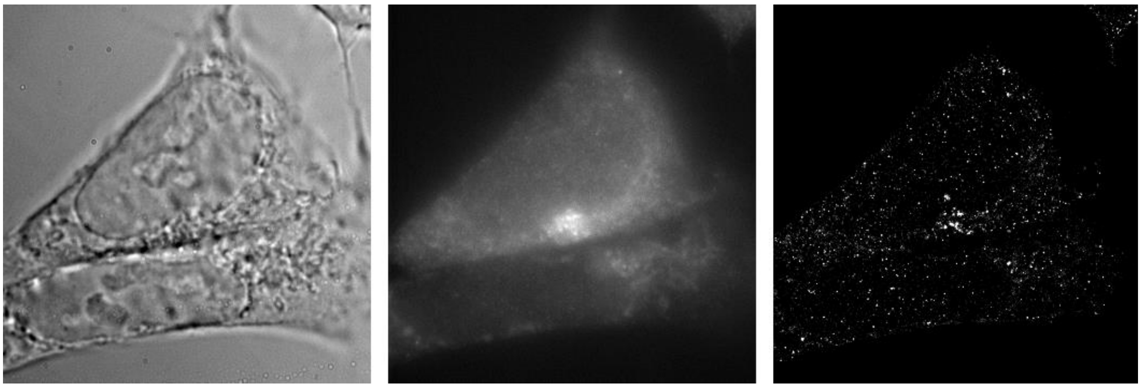

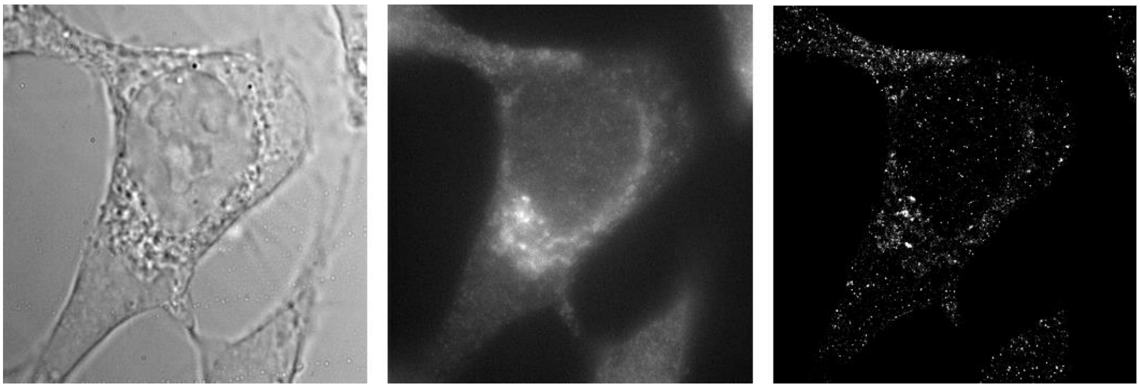

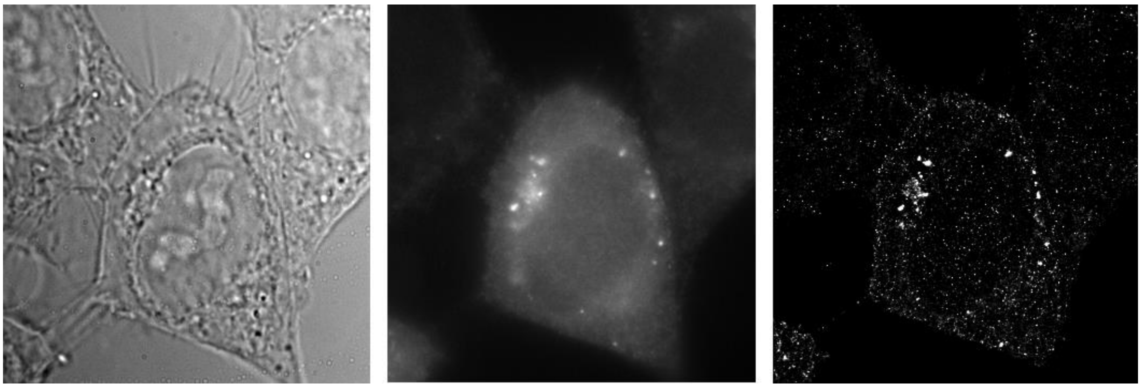

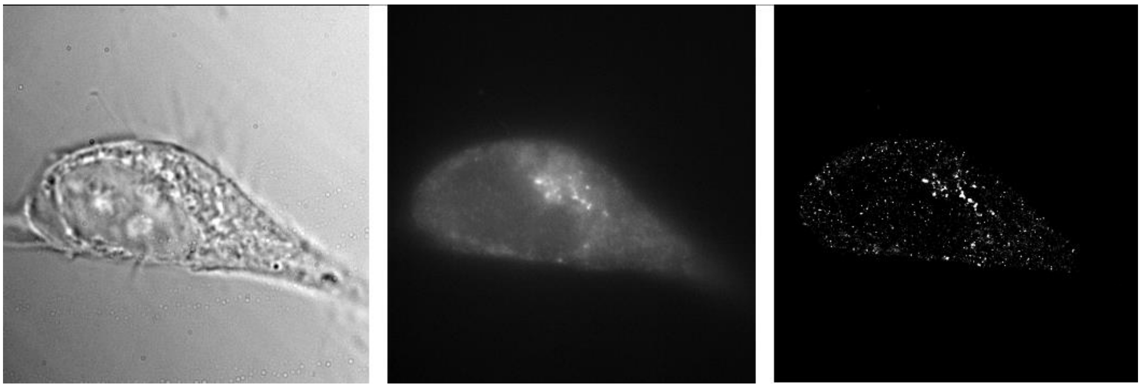

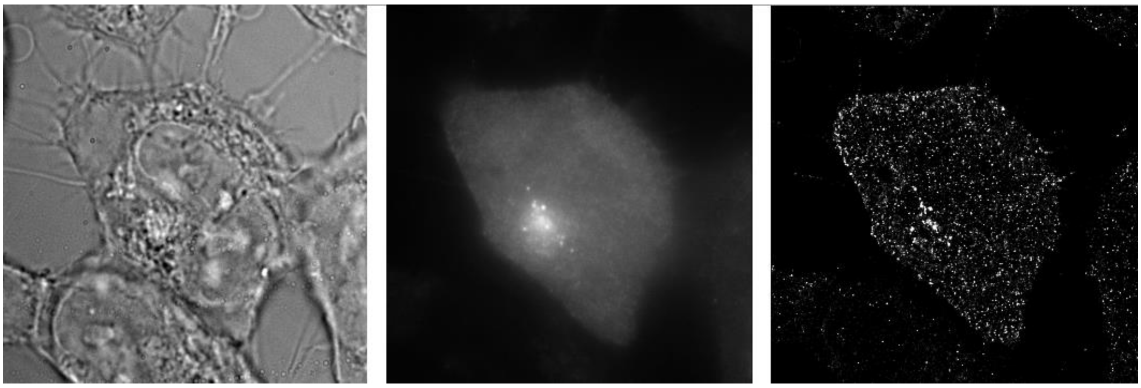

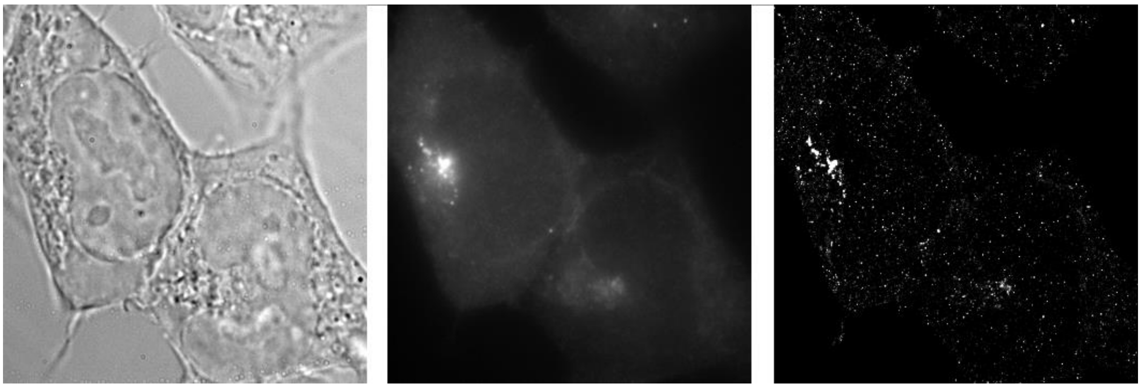

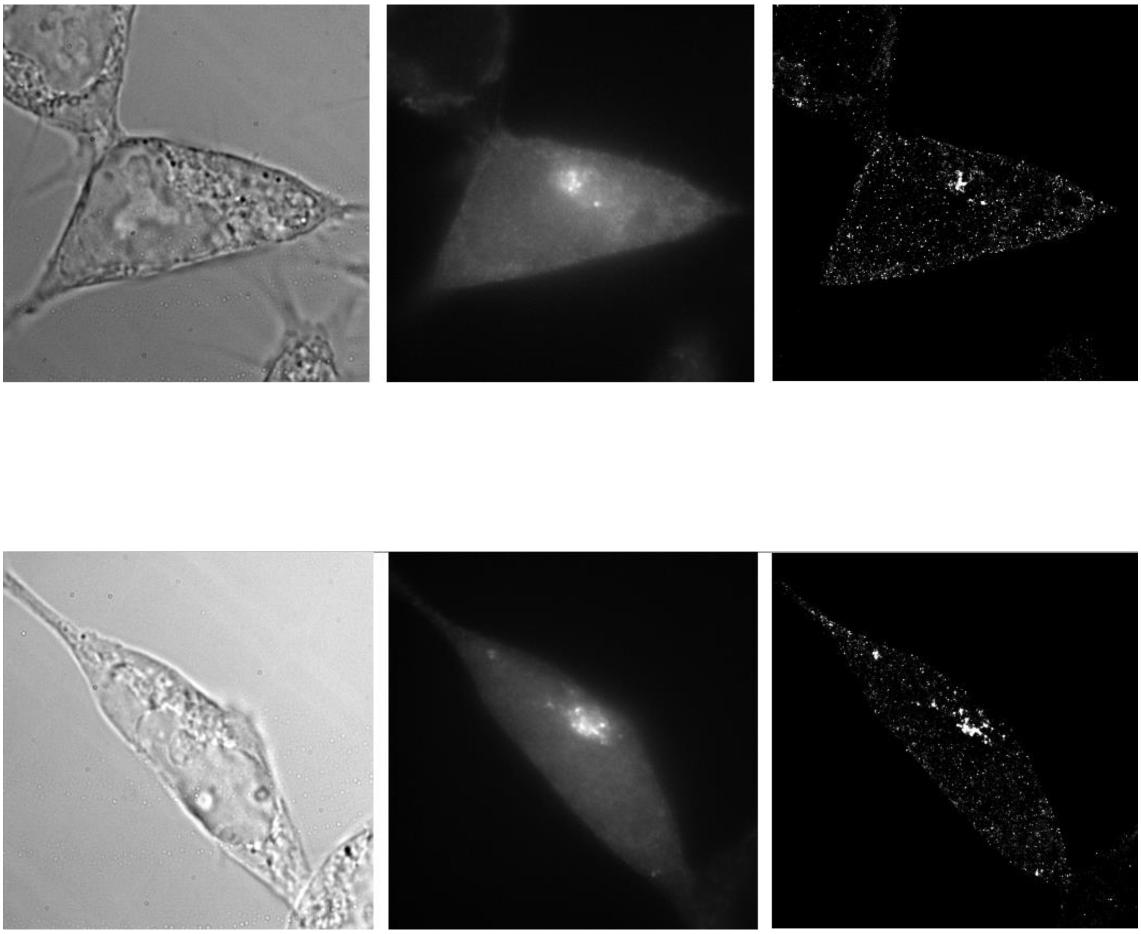

Figure 7.4.1. Ten images featuring HEK-293 cells stably expressing Dendra2-GABARAP; fed condition; scale bar is 5 µm.

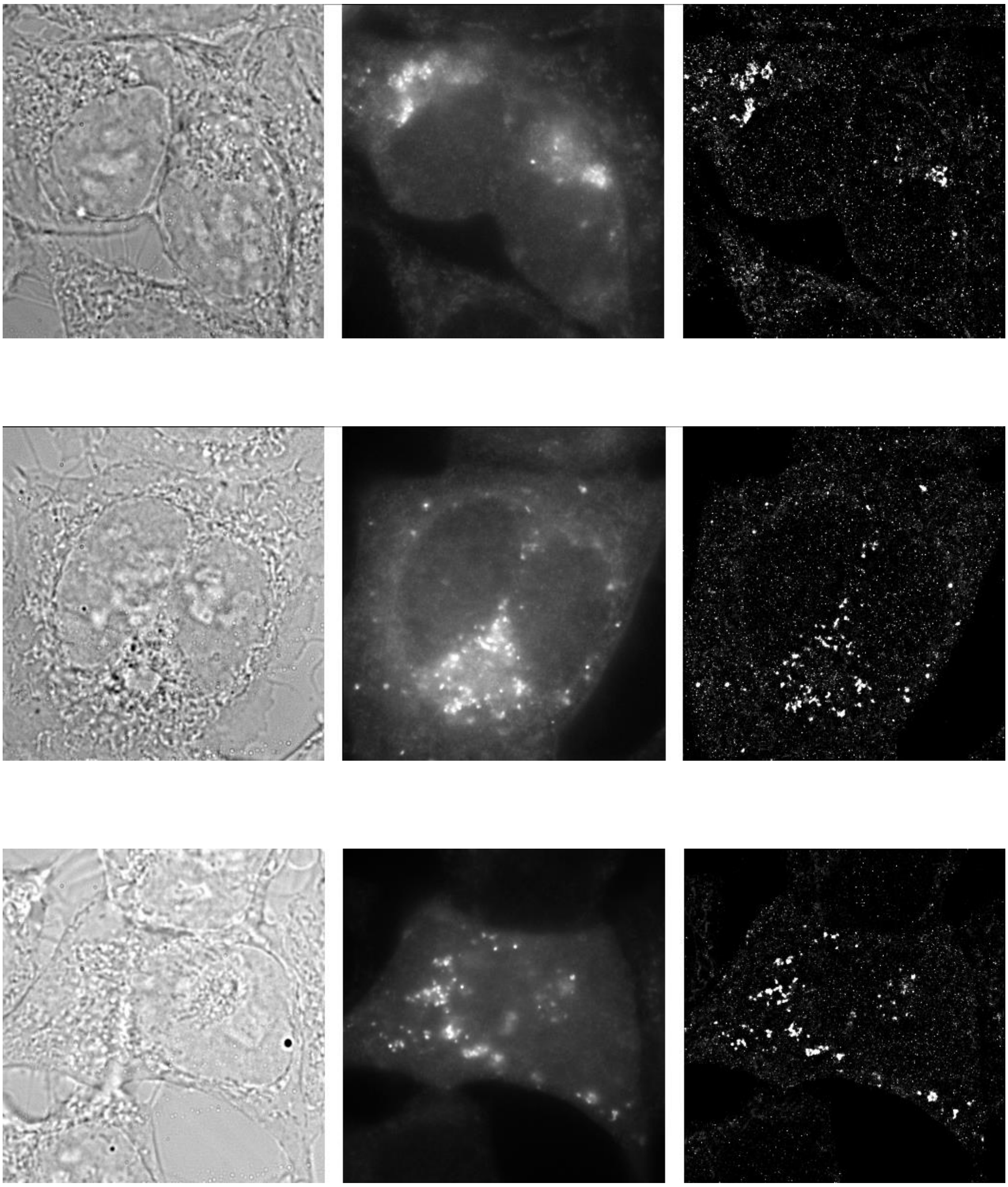

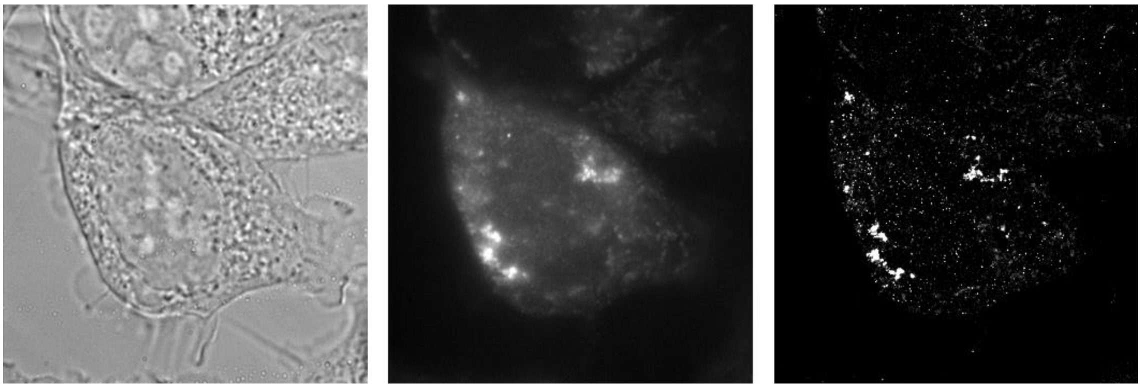

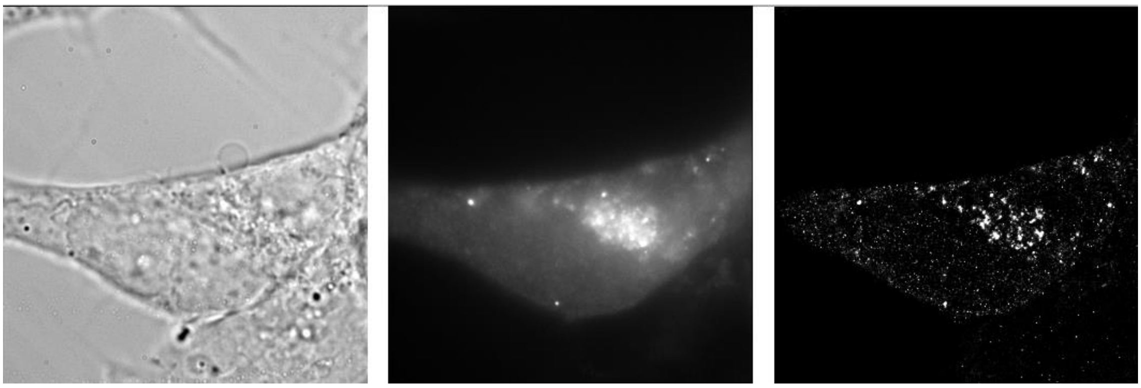

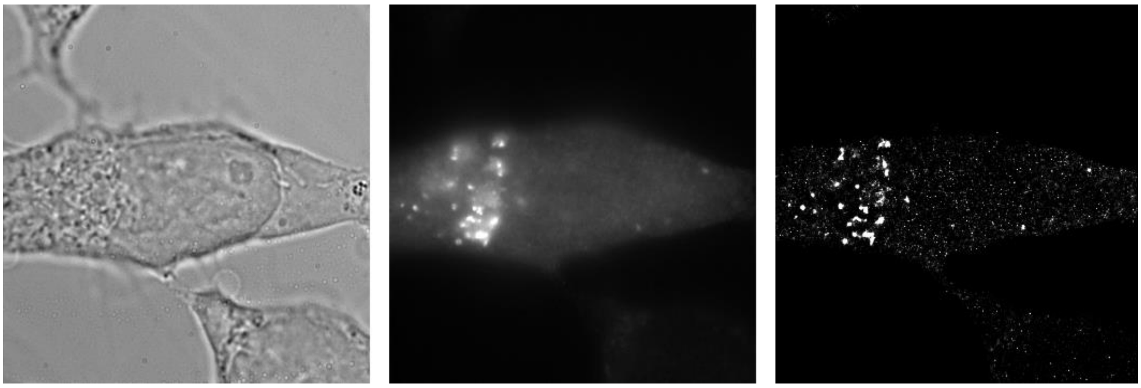

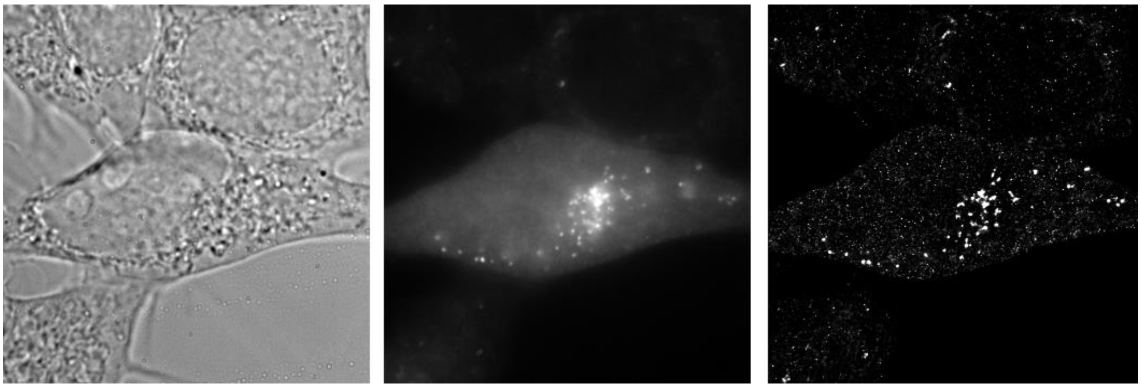

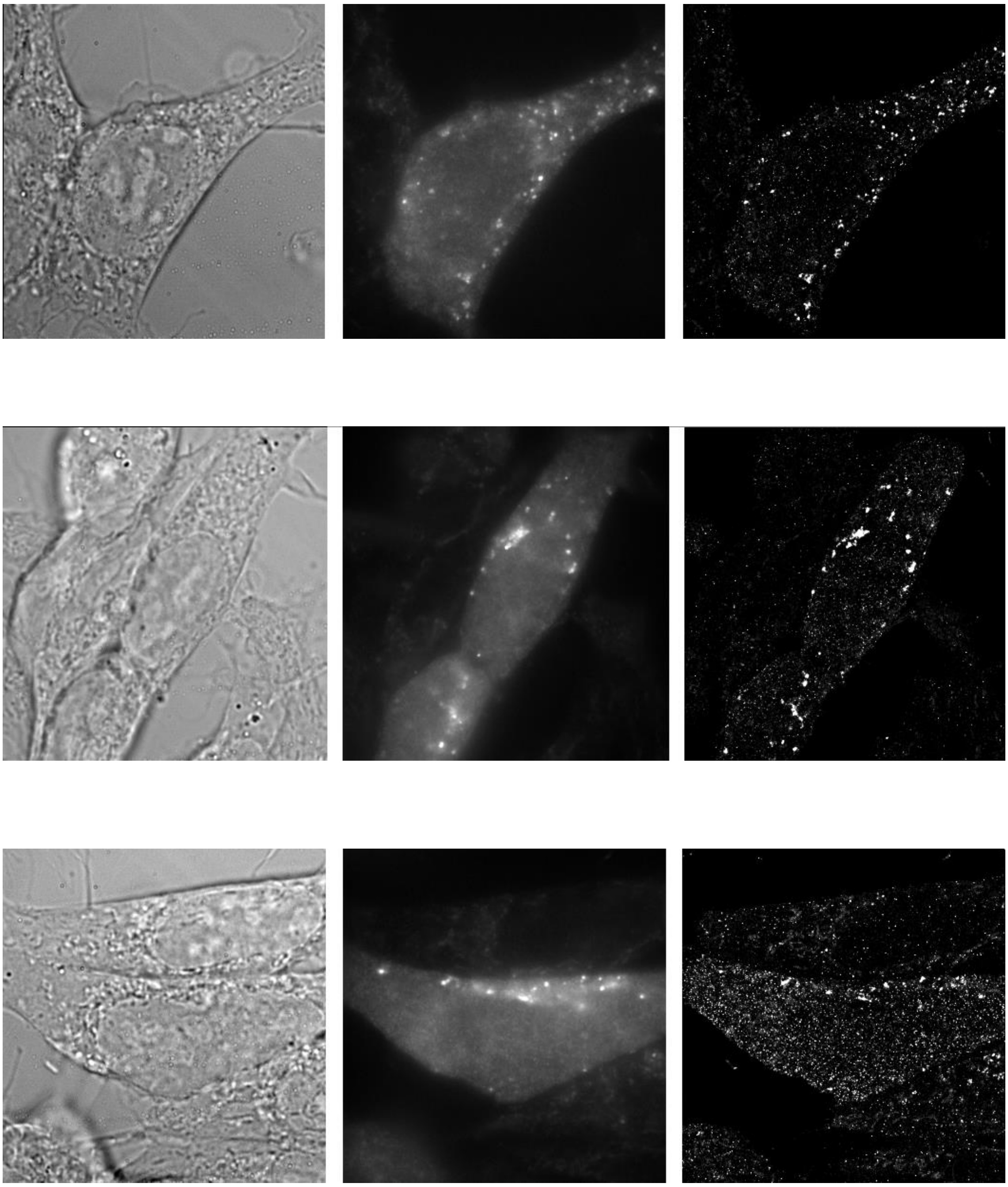

Figure 7.4.2. Ten images featuring HEK-293 cells stably expressing Dendra2-GABARAP; starved-blocked condition; scale bar is 5 µm.

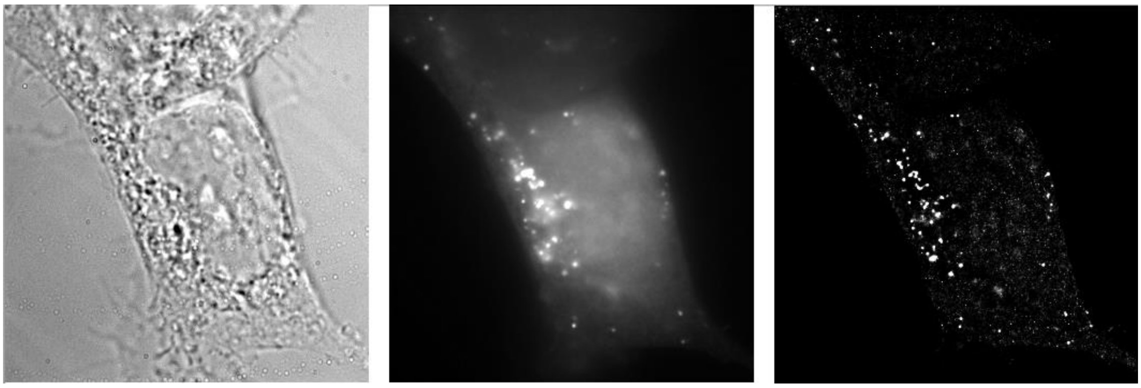

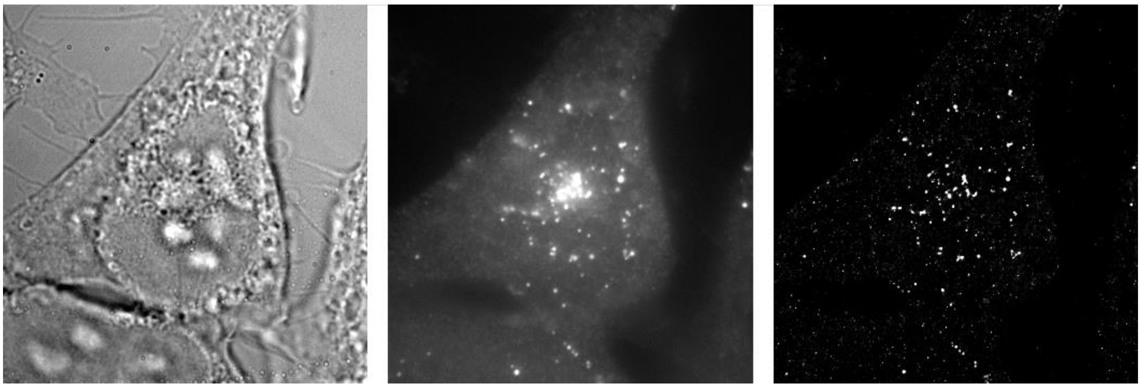

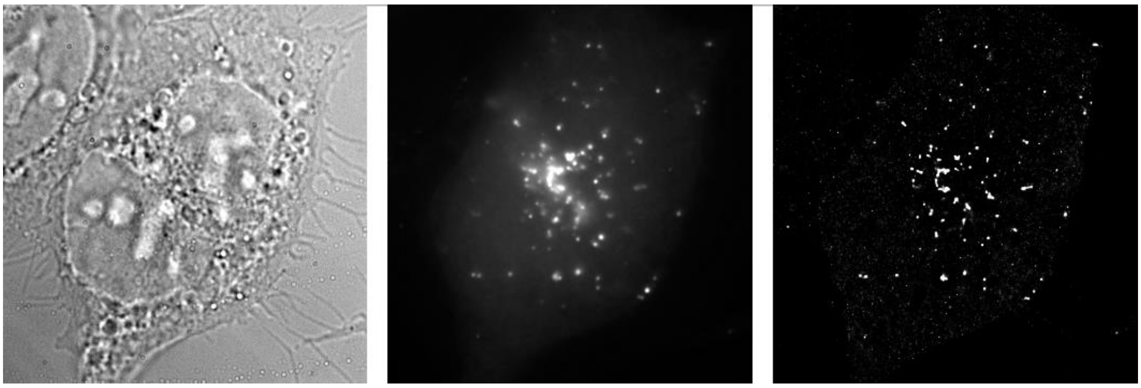

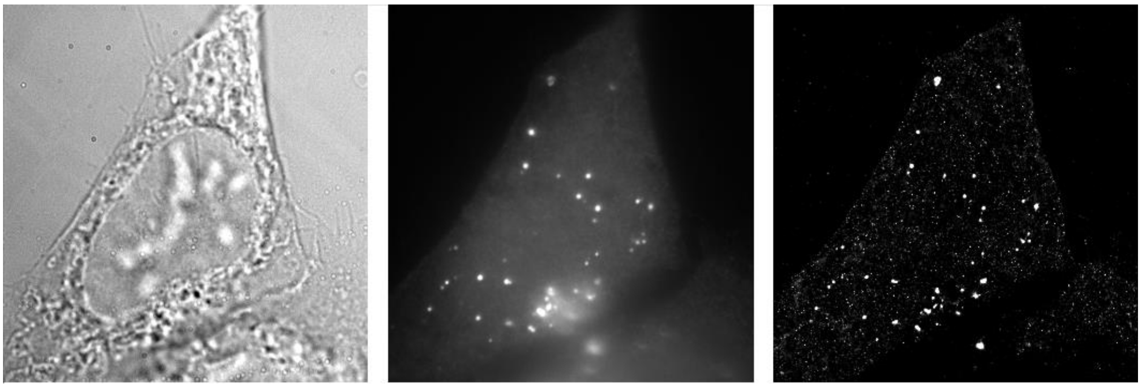

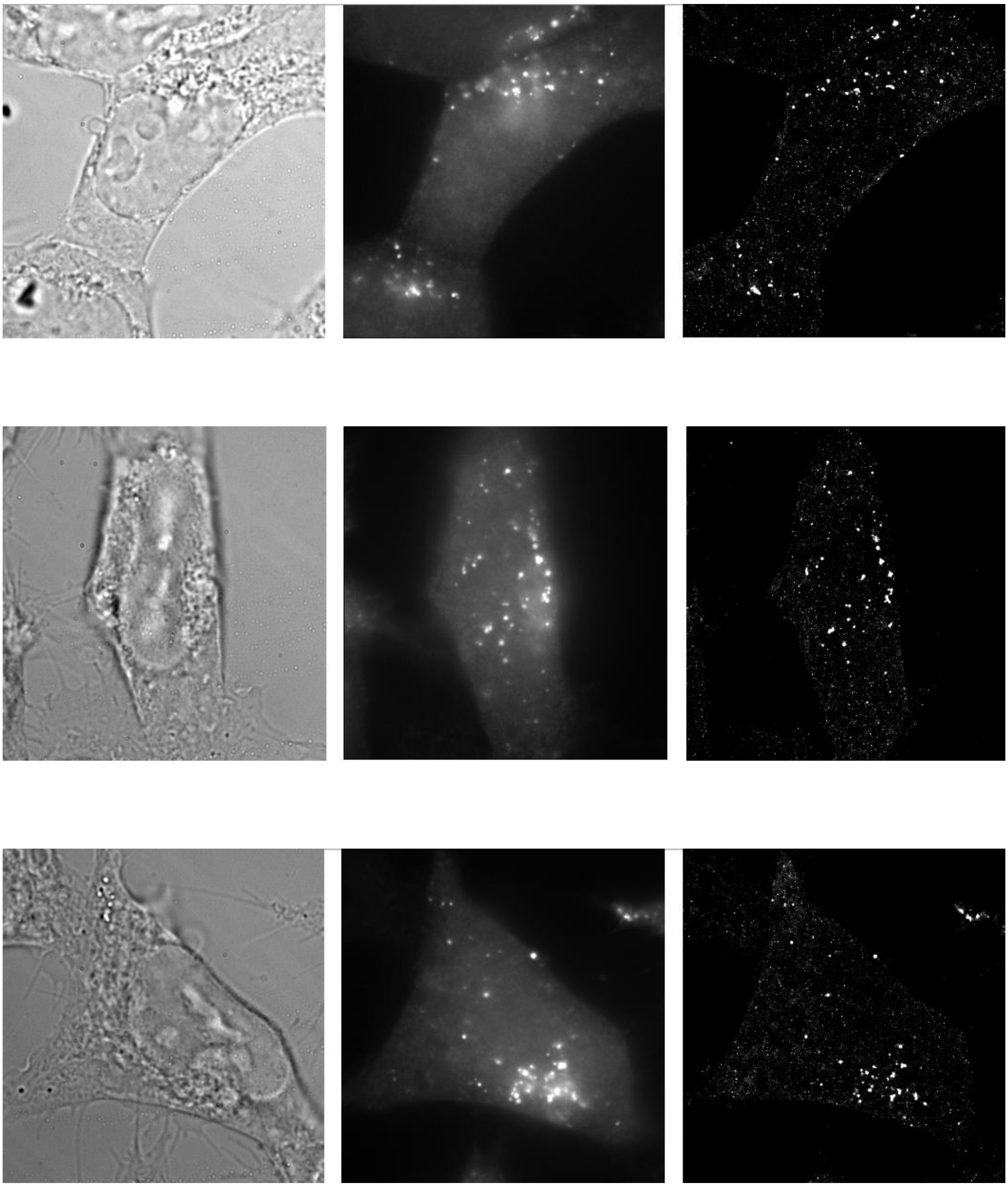

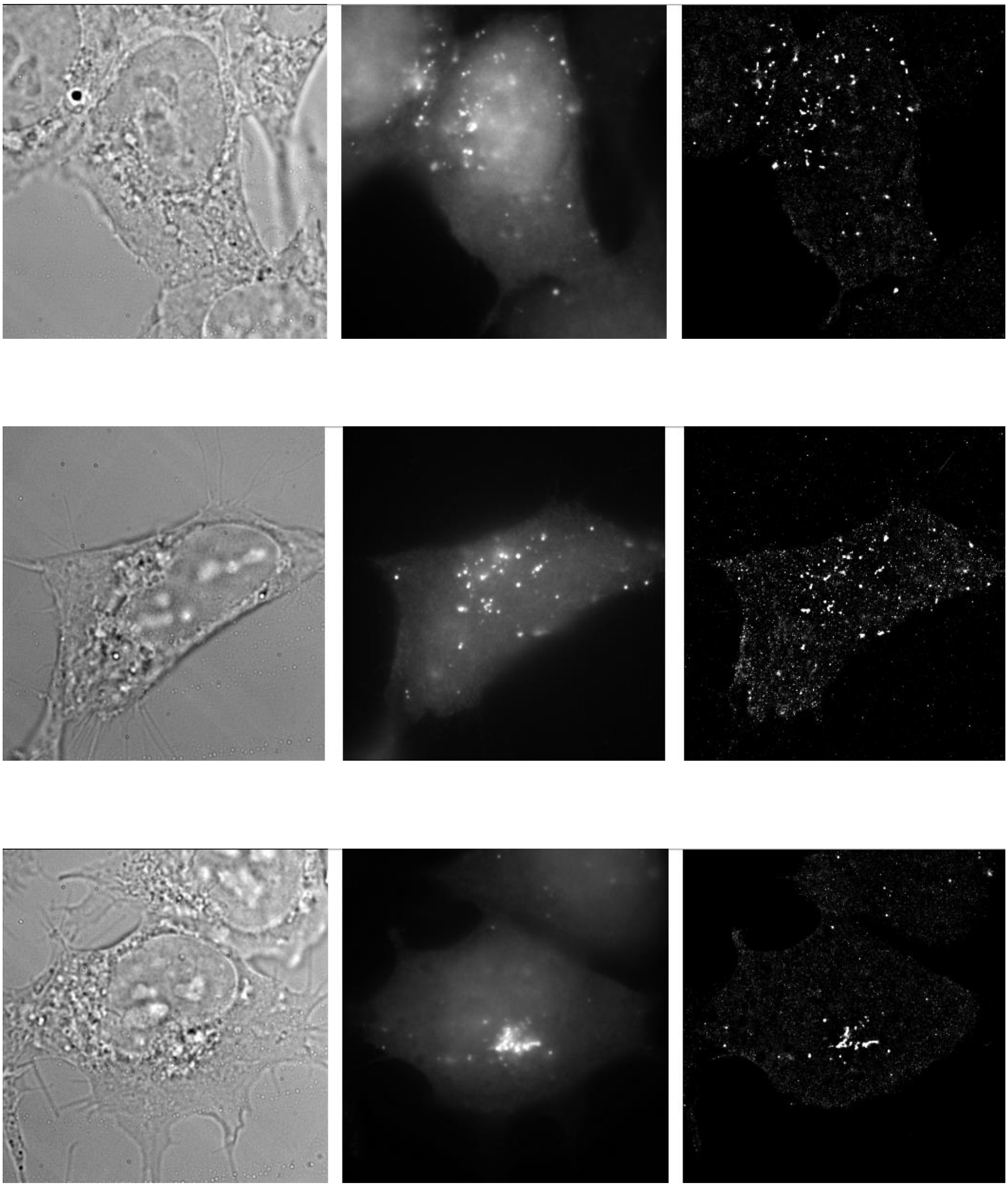

Figure 7.4.3. Ten images featuring HEK-293 cells stably expressing Dendra2-LC3B; fed condition; scale bar is 5 μm.

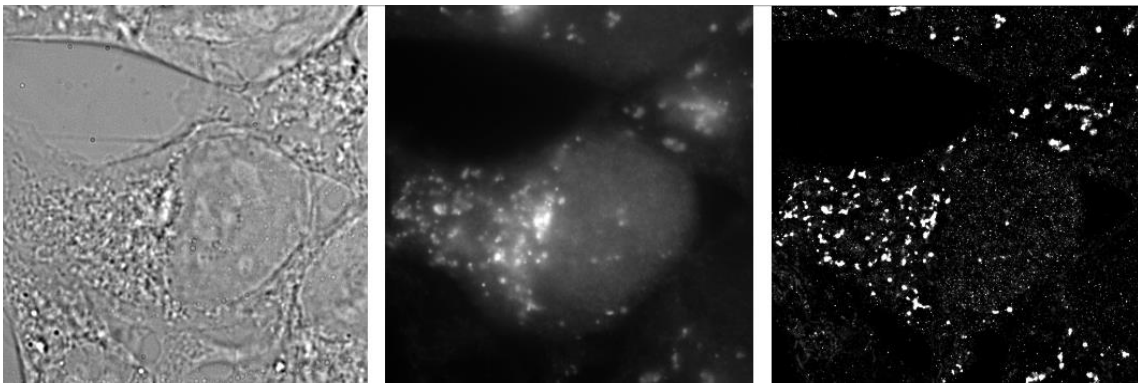

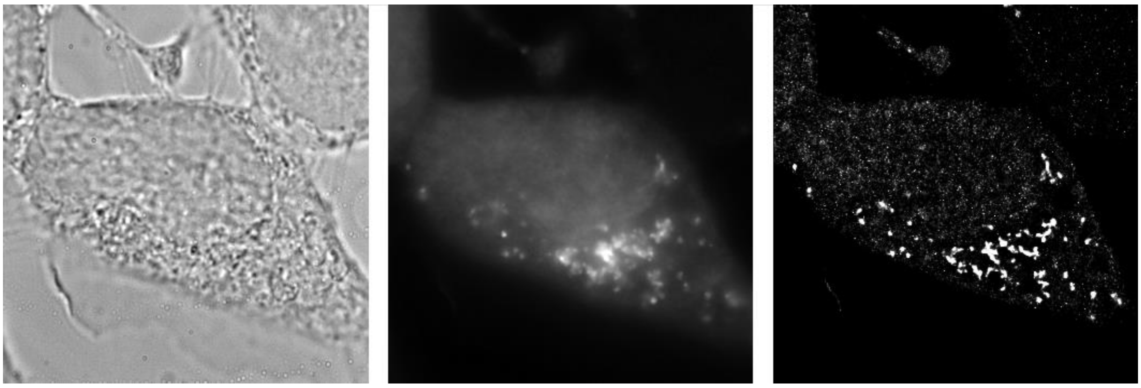

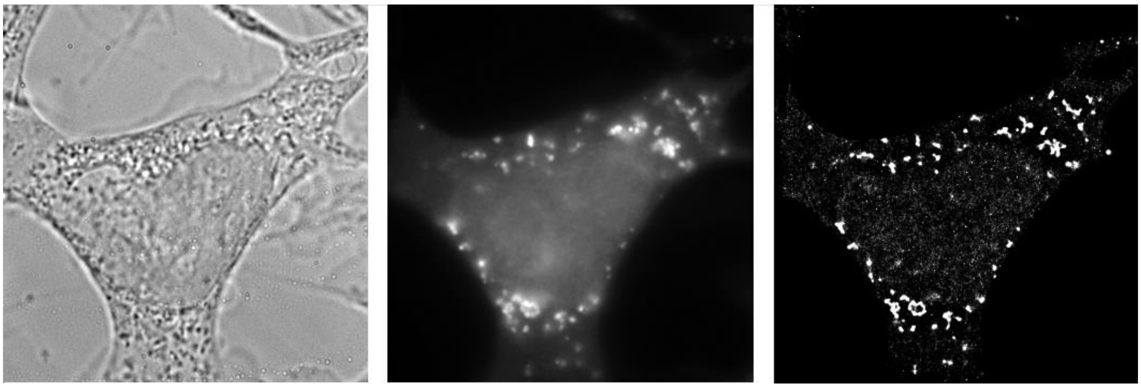

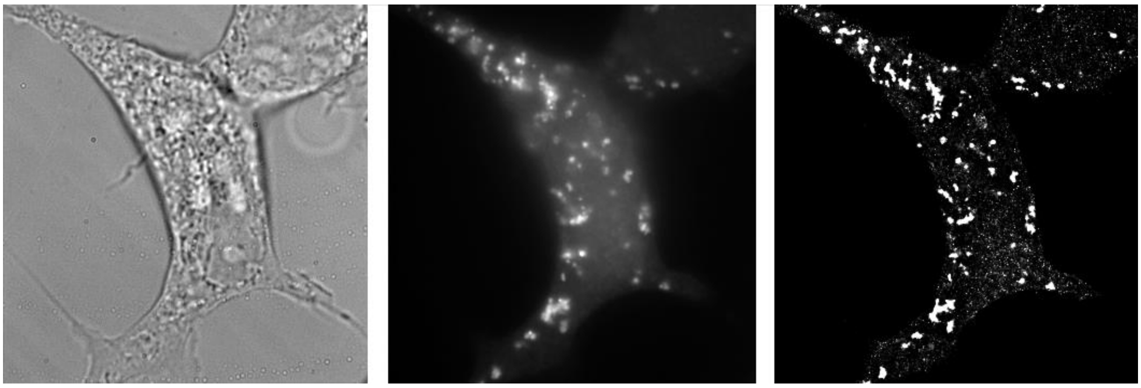

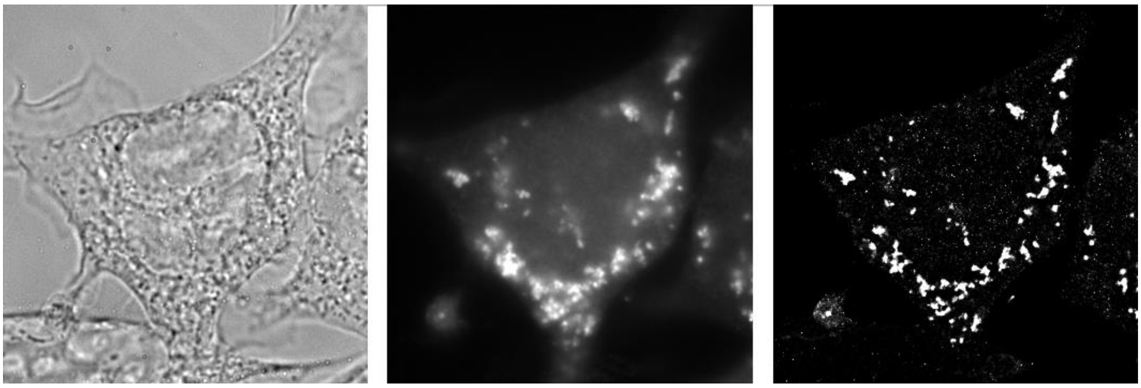

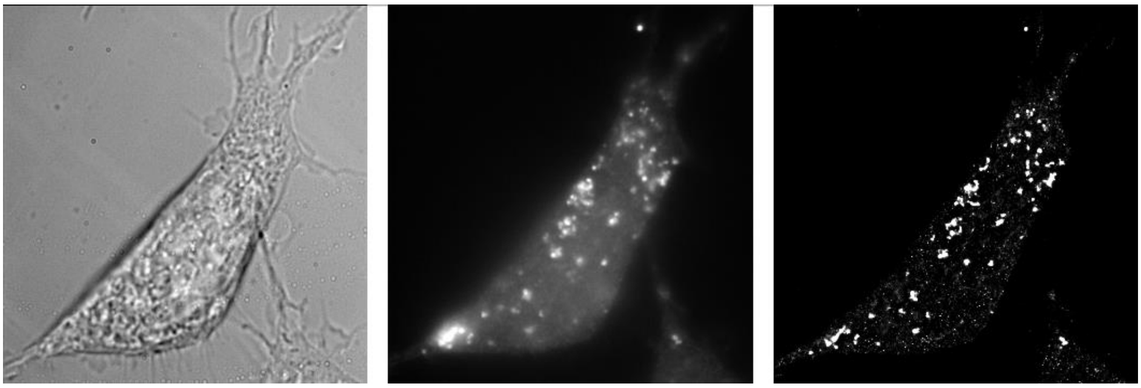

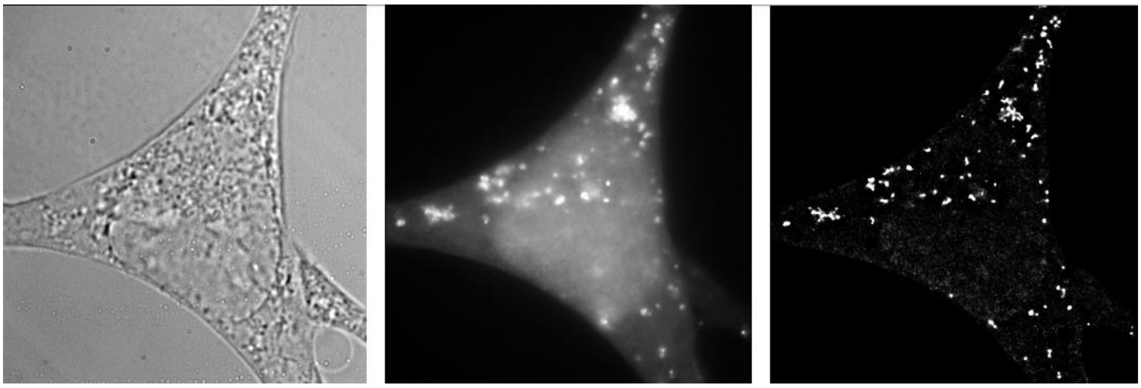

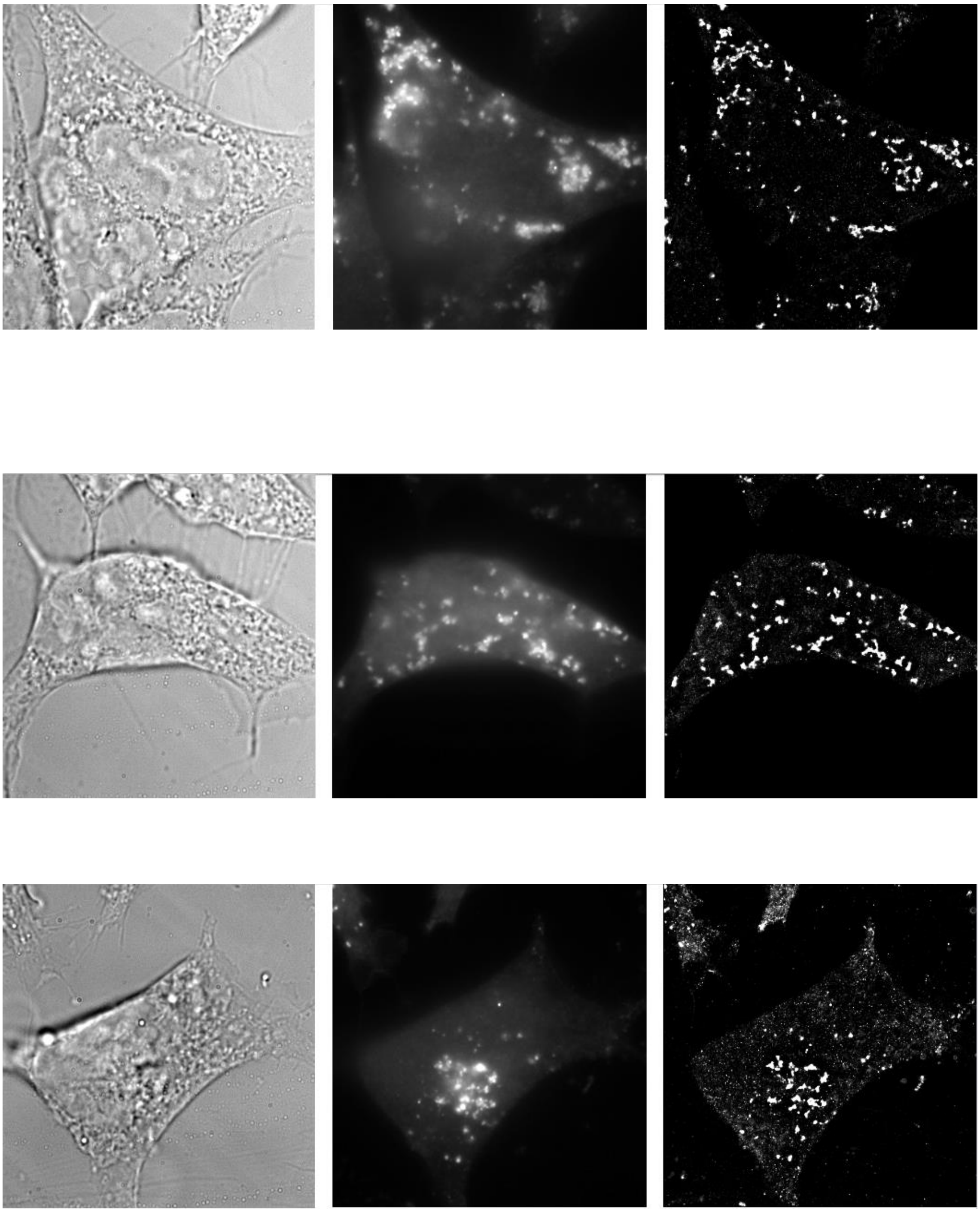

Figure 7.4.4. Ten images featuring HEK-293 cells stably expressing Dendra2-LC3B; starved-blocked condition; scale bar is 5 μm.

7.5. HEK-293 cells transiently transfected with EYFP-GABARAP and mCherry-LAMP1- widefield and super-resolution images

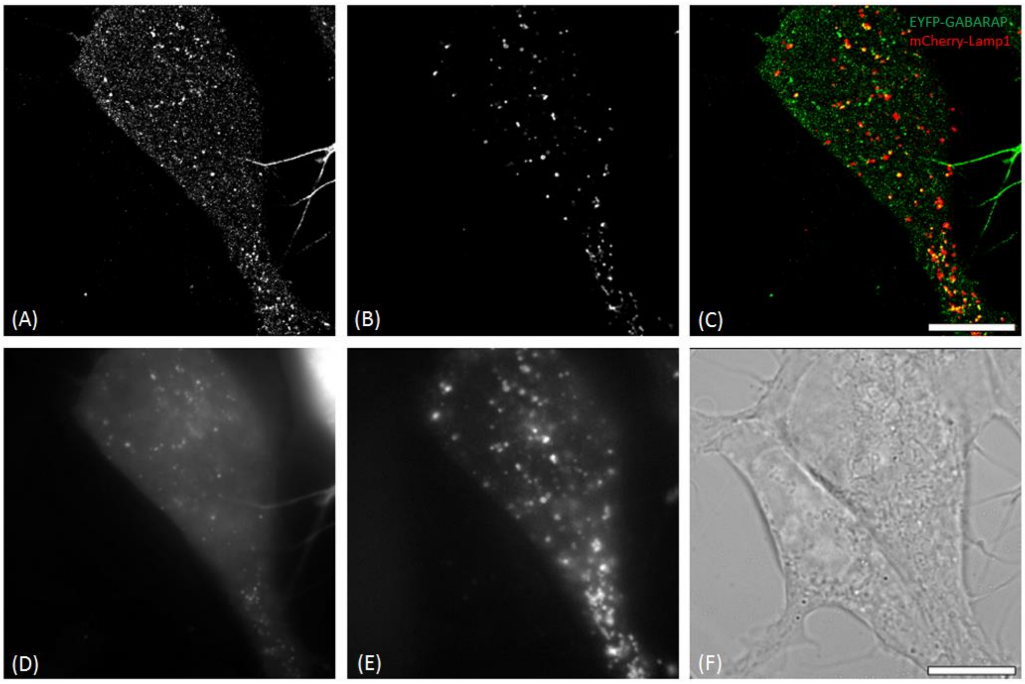

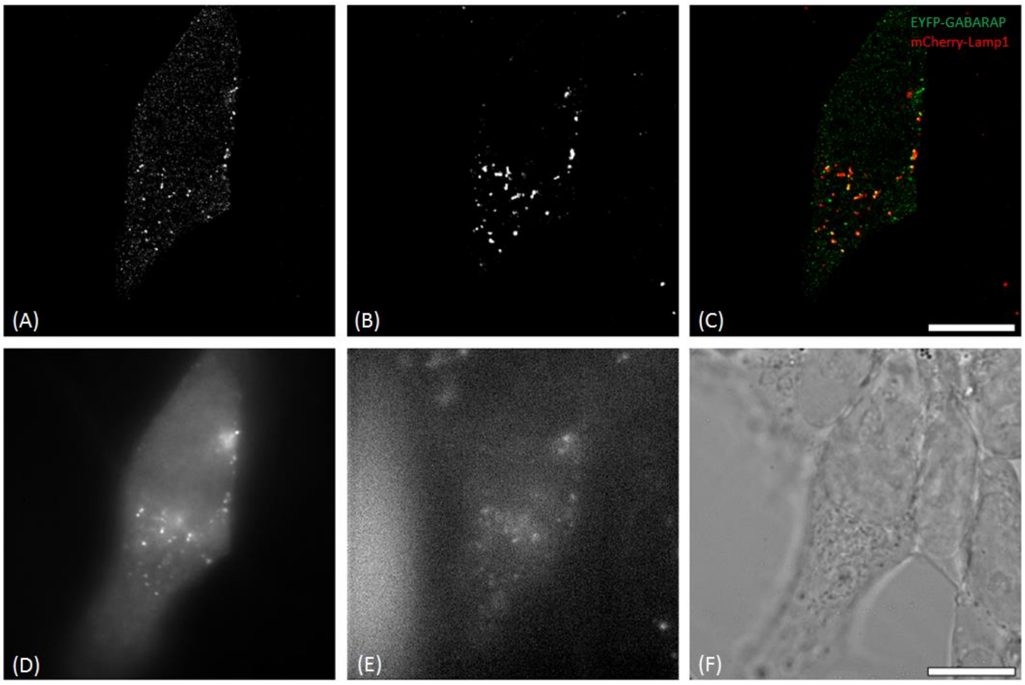

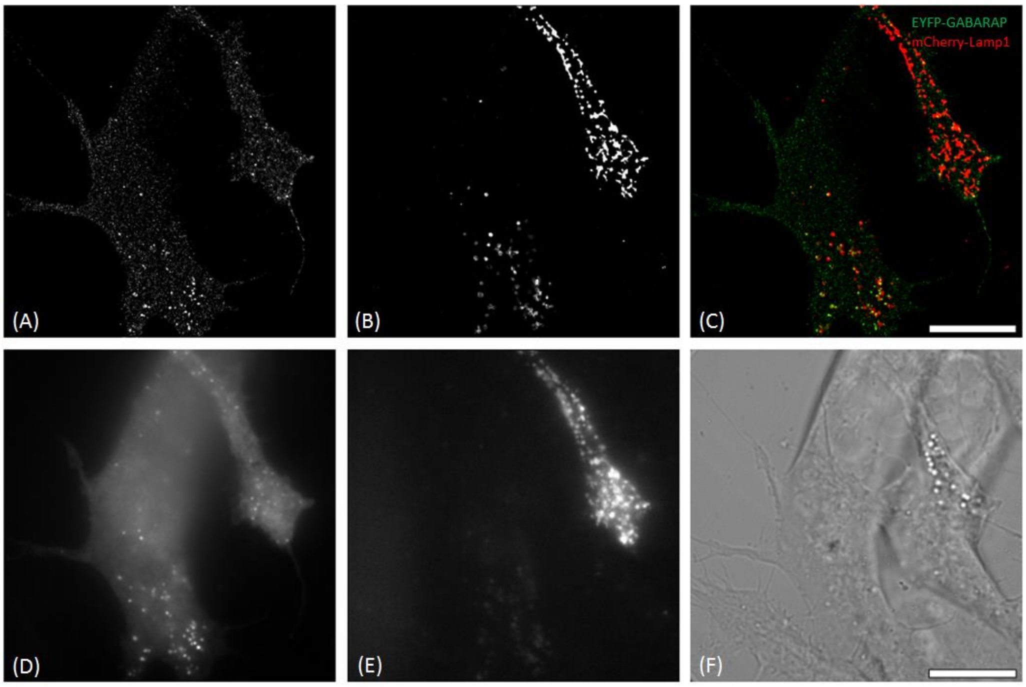
EYFP-GABARAP
mCherry-Lamp1
(A)
(B)
(C)
(D)
(E)
(F)

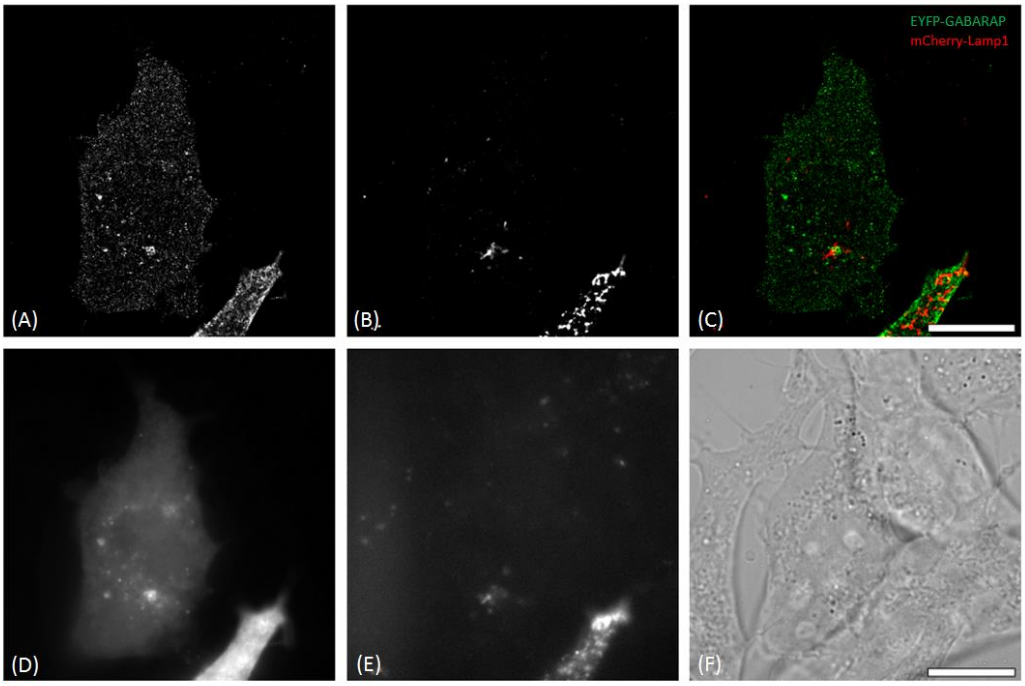
EYFP-GABARAP
mCherry-Lamp1
(A)
(B)
(C)
(D)
(E)
(F)

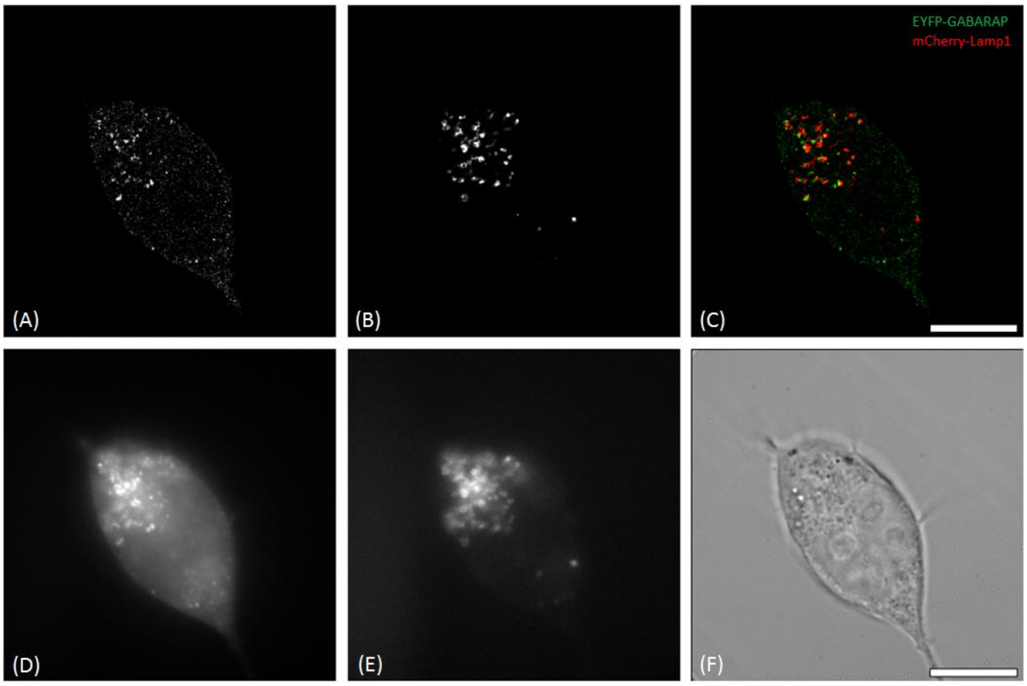

Figure 7.5.1. Images featuring HEK-293 cells transiently co-transfected with EYFP-GABARAP and LAMP1-mCherry; starved-blocked condition. (A): super-resolution image of EYFP-GABARAP structures. (B): super-resolution image of mCherry-LAMP1 structures. (C): overlap of (A) and (B), while (A) was given the green color and (B) the red color. (D): widefield image of EYFP-GABARAP structures. (D): widefield of mCherry-LAMP1 structures. (E): transmission image of the cell. The scale bar is 10 µm.

7.6. HEK-293 cells transiently transfected with EYFP-LC3B and mCherry-LAMP1- widefield and super-resolution images

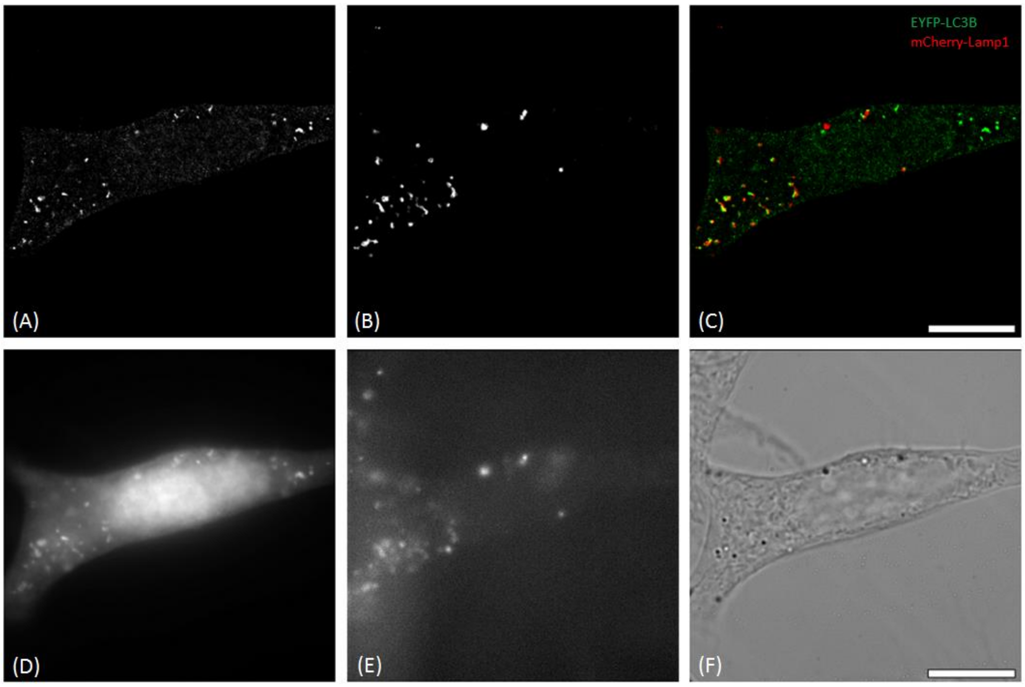

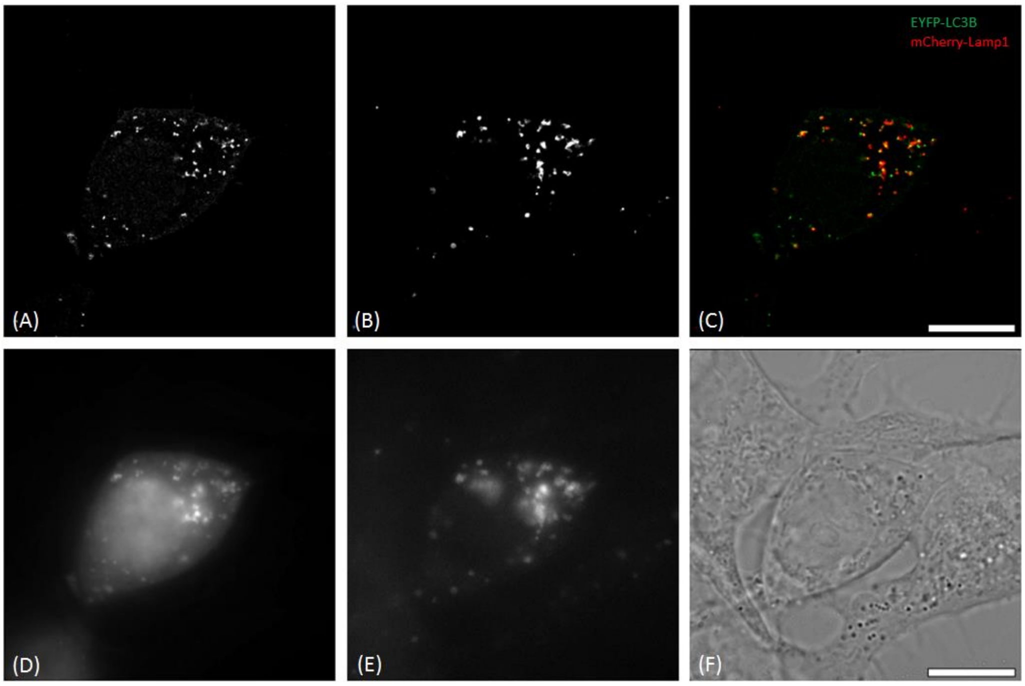
EYFP-LC3B
mCherry-Lamp1
(A)
(B)
(C)
(D)
(E)
(F)

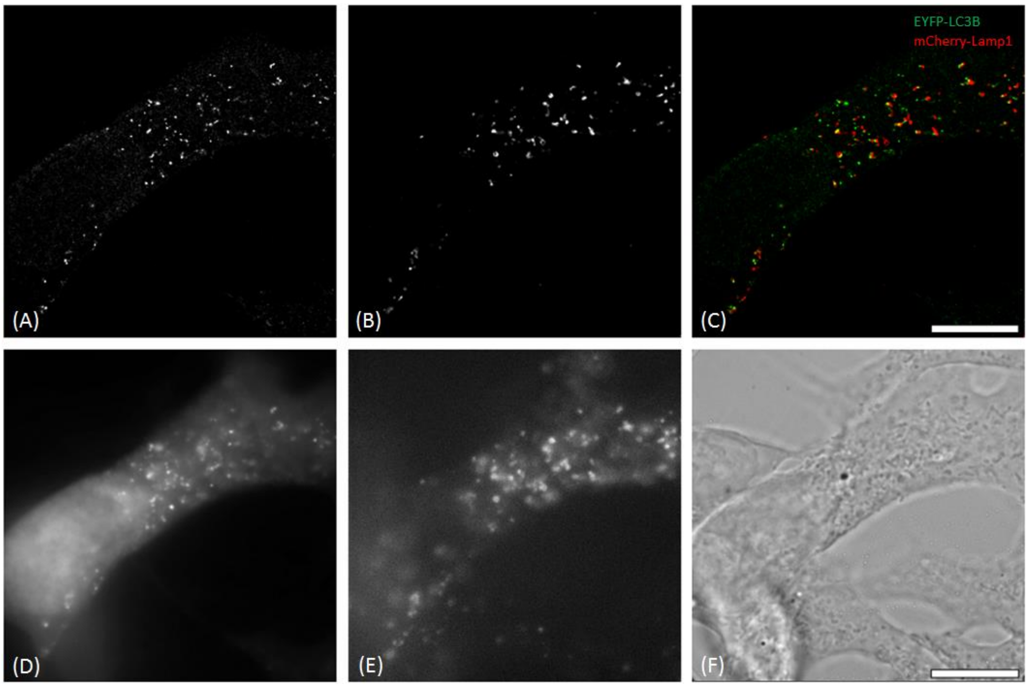
EYFP-LC3B
mCherry-Lamp1
(A)
(B)
(C)
(D)
(E)
(F)

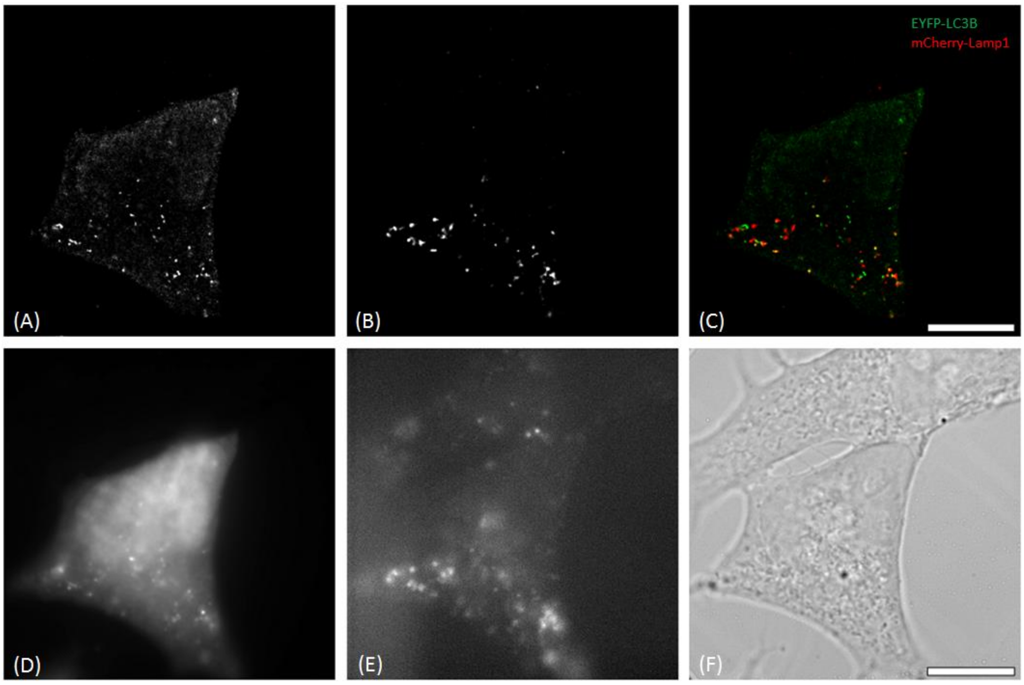

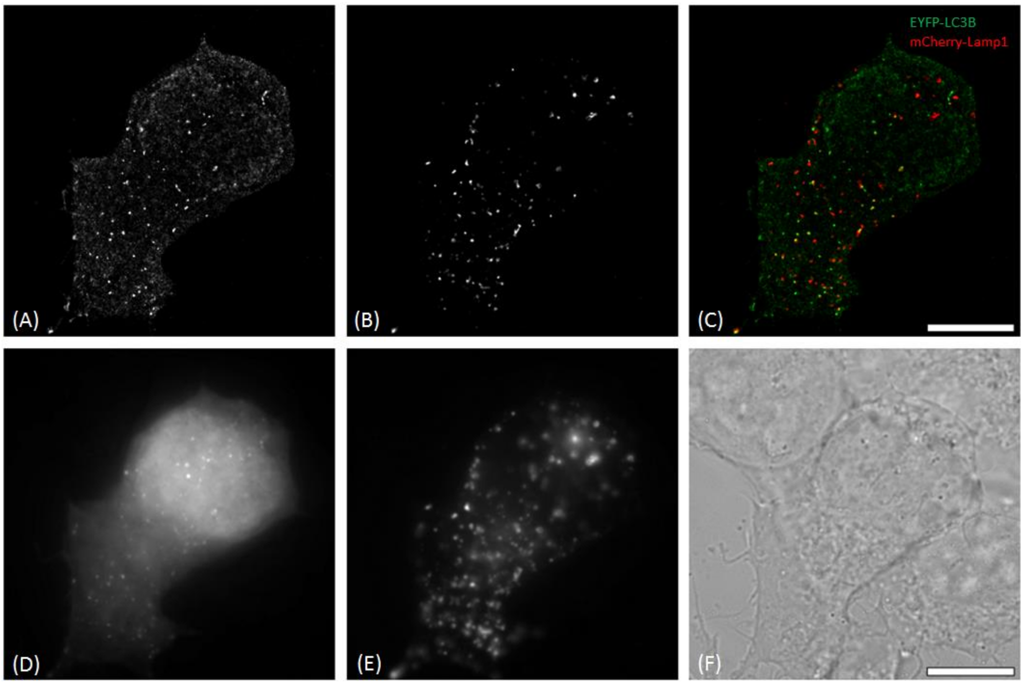

Figure 7.6.1. Images featuring HEK-293 cells transiently co-transfected with EYFP-LC3B and LAMP1-mCherry; starved-blocked condition. (A): super-resolution image of EYFP-LC3B structures. (B): super-resolution image of mCherry-LAMP1 structures. (C): overlap of (A) and (B), while (A) was given the green color and (B) the red color. (D): widefield image of EYFP-LC3B structures. (D): widefield of mCherry-LAMP1 structures. (E): transmission image of the cell. The scale bar is 10 µm.

7.7. SMLM imaging of HEK-293 cells transiently transfected with EYFP-GABARAP in dSTORM imaging buffer vs. PBS

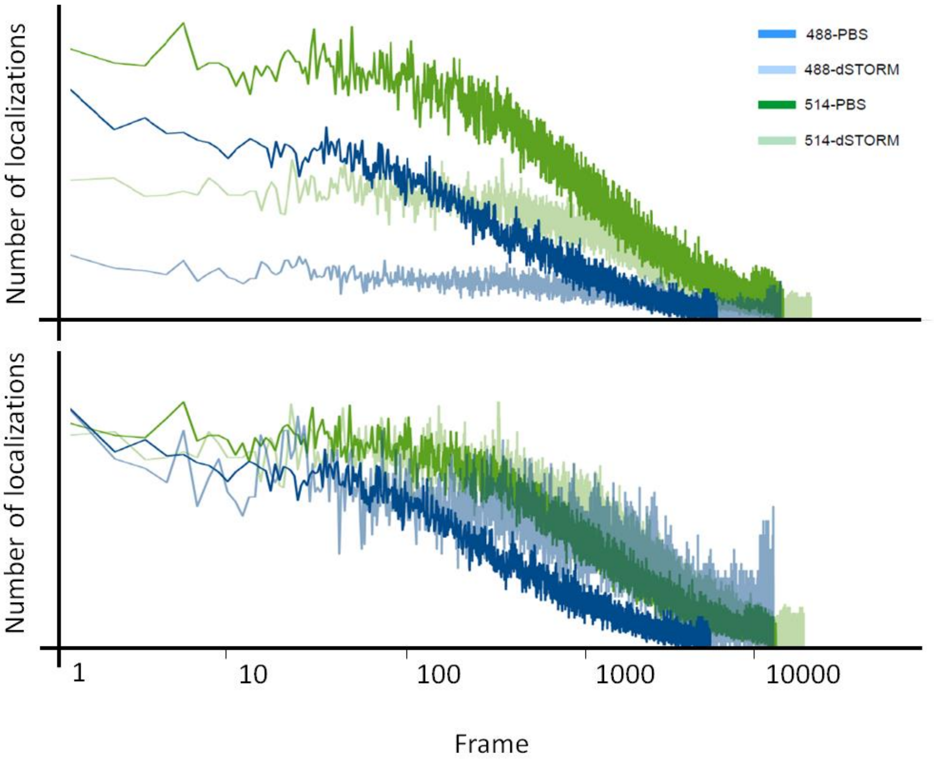

Figure 7.7.1. The average number of localizations vs. frame for three HEK-293 cells transiently transfected with EYFP-GABARAP measured in PBS pH7.4 and excited at 488 nm (dark blue), and at 514 nm (dark green), and measured in dSTORM buffer excited at 488 nm (light blue), and at 514 nm (light green).

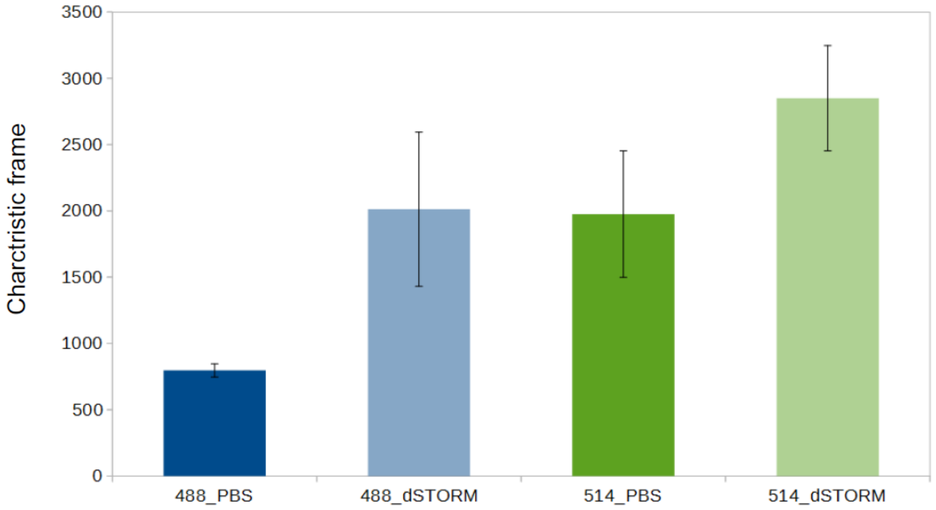

Figure 7.7.2. The Characteristic frame number for three HEK-293 cells transiently transfected with EYFP-GABARAP measured in PBS pH7.4 and excited at 488 nm (dark blue), and at 514 nm (dark green), and measured in dSTORM buffer excited at 488 nm (light blue), and at 514 nm (light green).

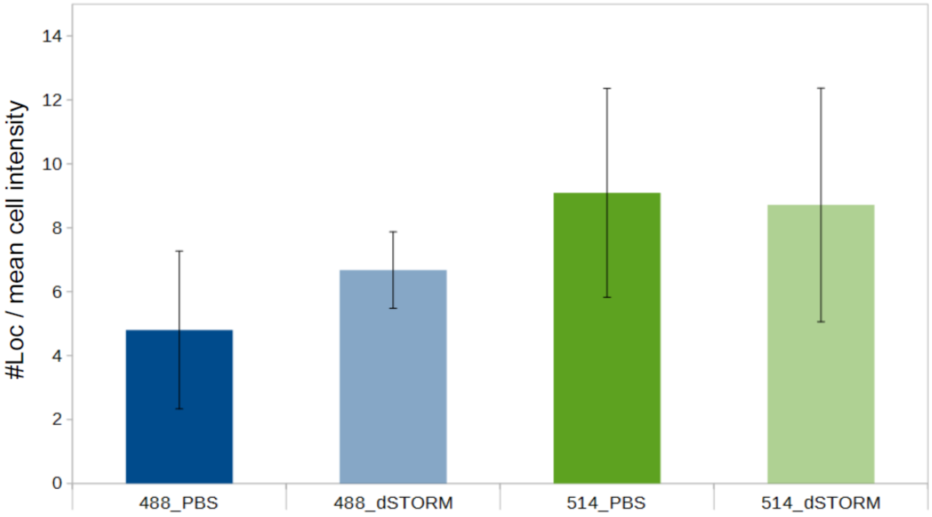

Figure 7.7.3. The number of localizations per average cell intensity for three HEK-293 cells transiently transfected with EYFP-GABARAP measured in PBS pH7.4 and excited at 488 nm (dark blue), and at 514 nm (dark green), and measured in dSTORM buffer excited at 488 nm (light blue), and at 514 nm (light green).

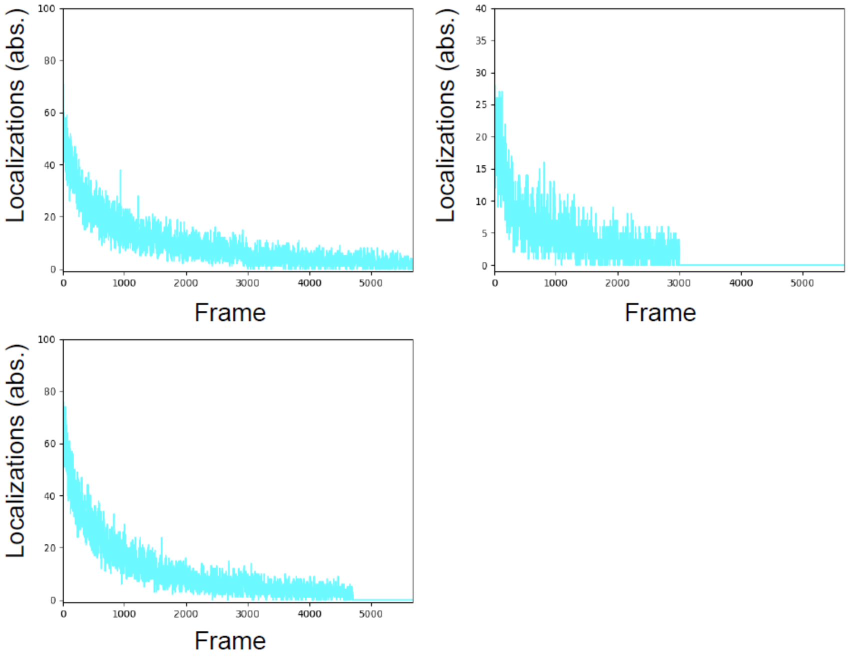

Figure 7.7.4. The number of localizations per frame for three HEK-293 cells transiently transfected with EYFP-GABARAP measured in PBS pH7.4 and excited at 488 nm.

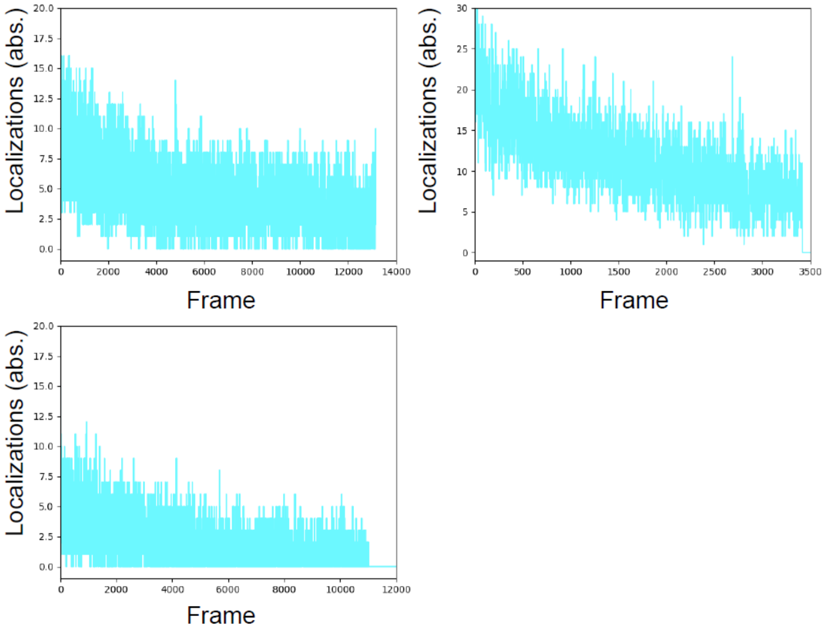

Figure 7.7.5. The number of localizations per frame for three HEK-293 cells transiently transfected with EYFP-GABARAP measured dSTORM buffer and excited at 488 nm.

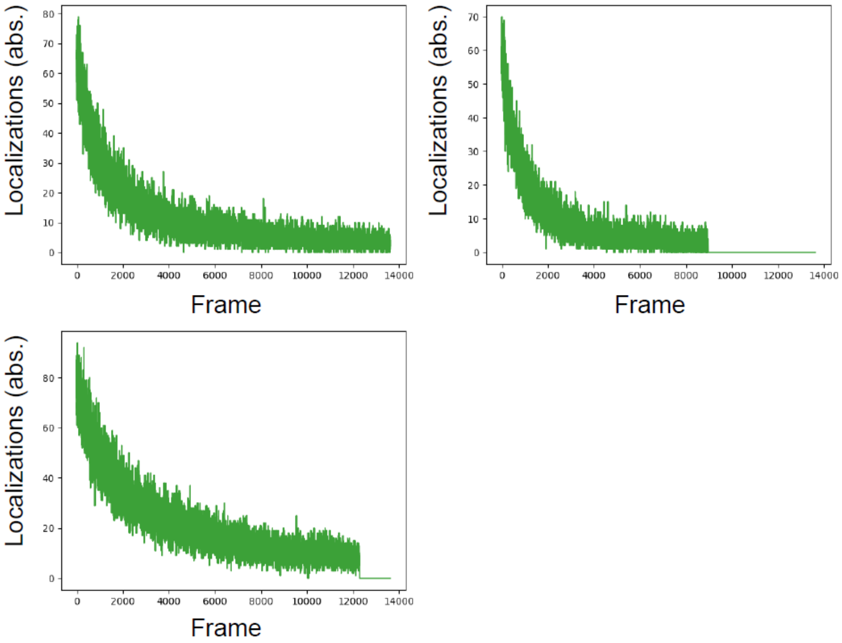

Figure 7.7.6. The number of localizations per frame for three HEK-293 cells transiently transfected with EYFP-GABARAP measured in PBS pH7.4 and excited at 514 nm.

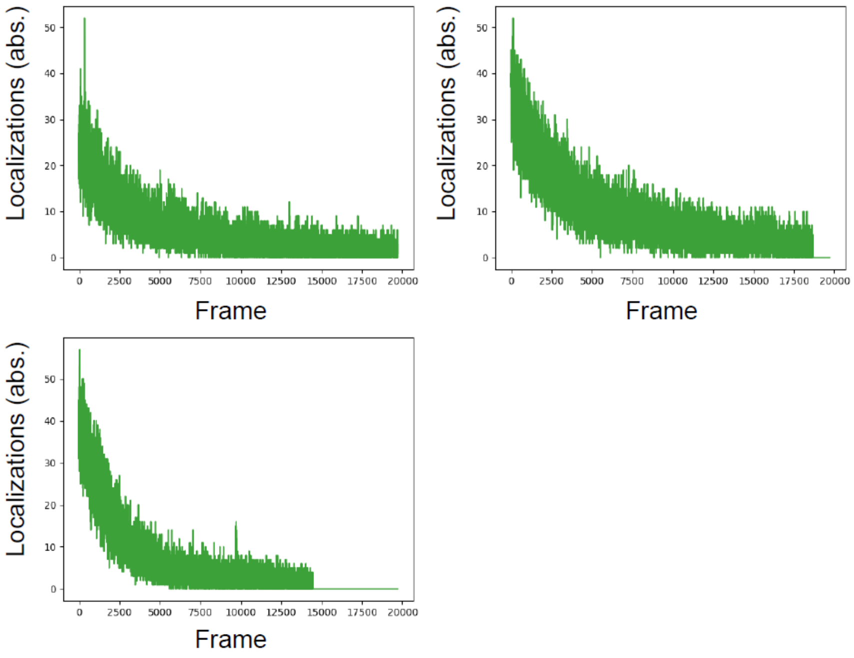

Figure 7.7.7. The number of localizations per frame for three HEK-293 cells transiently transfected with EYFP-GABARAP measured in dSTORM buffer and excited at 514 nm.

7.8. Macros and codes used for the shape and size analysis

```
//------------------------------------------------------------------------------

Initialize.ijm

run("Set Scale...", "distance=0 known=0 pixel=1 unit=pixel");
run("ROI Manager...");
roiManager("Associate", "false");
roiManager("Centered", "true");
roiManager("UseNames", "false");
selectWindow("ROI Manager");
run("Close");
run("Options...", "iterations=1 count=1 black");

//------------------------------------------------------------------------------

Isolate_Structures.ijm

run("Set Scale...", "distance=0 known=0 pixel=1 unit=pixel");
run("8-bit");
setOption("BlackBackground", false);
run("Make Binary");
run("Set Scale...", "distance=0 known=0 pixel=1 unit=pixel");
run("Analyze Particles...", "show=Outlines size=9-35000 add");
run("Close");
roiManager("Associate", "false");
roiManager("Centered", "true");
roiManager("UseNames", "false");
for(i = 0; i < 100000; i++) {
        newImage("Untitled", "8-bit white", 100, 100, 1);
        roiManager("Select", i);
        roiManager("Set Fill Color", "black");
        run("Flatten");
        saveAs("Png", "F:\\SMLM_Data\\...\\"+i+".png");
        run("Close");
        run("Close");

}
```

```
//----------------------------------------------------------
```

Classification.ijm

```
Counter = 0;
Lower   = 0;
for(i = Lower; i < Lower + 1000; i++)
{
      open("F:\\SMLM_Data\\...\\"+i+".png");
       Counter = i;
       run("Set... ", "zoom=500 x=50 y=50");
       run("In [+]");
       run("In [+]");
       exec("cmd","/c","start","\"Window  Title\"","C:\\Users\\...\\__SASA_HELPER.exe");
       if((Counter != Lower) && (Counter % 250 == 0))
              print(Counter);
       close();
       Counter++;
}
```

```
//----------------------------------------------------------
```

MAIN.C

```
#include <stdio.h>
#include <conio.h>
#define _CRT_SECURE_NO_WARNINGS
#pragma warning(disable:4996)
char ENTER = '\n';

int main(void)
{
       char inp = 0;
       FILE* fp = fopen("F:\\SMLM_Data\...\\__SASA_HELPER.txt", "a");
       inp = getch();
       fwrite(&inp,   1, 1, fp);
       fwrite(&ENTER, 1, 1, fp);
       fclose(fp);
}
```

```
//----------------------------------------------------------
```

The contribution of the doctorate candidate, Iman Abdollahzadeh, in the publications directly utilized and cited in the PhD thesis.

1. Autophagy-Related Proteins GABARAP and LC3B Label Structures of Similar Size but Different Shape in Super-Resolution Imaging, *Molecules* - 2019 – DOI: 10.3390/molecules24091833, **Abdollahzadeh I.**, Hendriks J., Sanwald J.L., Simons I.M., Hoffmann S., Weiergräber O.H., Willbold D., Gensch T.

Iman Abdollahzadeh (hereafter as IA) performed the super-resolution microscopy experiments and developed the image analysis methodology in a semi-automatic approach. IA performed the statistical analysis of all the data presented in this publication. As the first author, IA was responsible for the initial steps in the text writing before revision by other co-authors and he was also responsible for the final evaluation of the text body after receiving all other co-authors revision and comments. The idea and motivation behind this work was initially introduced by IA to the other members of the group and were developed with all other members. The discussion and the results of the final manuscript were divided between all co-authors and as such IA was also involved in both. All the cell culture, cell sample preparation, and imaging techniques were performed by IA under supervision of supervisors.

2. The Atg8 Family of Proteins—Modulating Shape and Functionality of Autophagic Membranes- *Frontiers in Genetics* - 2017 – DOI: 10.3389/fgene.2017.00109, **Abdollahzadeh I.**, Schwarten M., Gensch T., Willbold W., Weiergräber O.H.

Iman Abdollahzadeh (hereafter as IA) was responsible for the literature review and the initial text writing for the entire sub-chapter "Involvement in Phagophore Membrane Curvature". The whole article and the mentioned sub-chapter then discussed with the other co-authors and IA was also equally contributed for the discussion.

Jülich, 10/01/2020, Iman Abdollahzadeh

Abdollahzadeh

I herewith declare that I have produced this thesis without the prohibited assistance of third parties and without making use of aids other than those specified; notions taken over directly or indirectly from other sources have been identified as such. This work has not previously been presented in identical or similar form to any other German or foreign examination board. I have not previously failed a doctoral examination procedure.

Jülich, 10.01.2020
Iman Abdollahzadeh
Abdollahzadeh